NBS TECHNICAL NOTE 1178

U.S. DEPARTMENT OF COMMERCE/National Bureau of Standards

NBS Reactor: Summary of Activities July 1981 Through June 1982

NATIONAL BUREAU OF STANDARDS

The National Bureau of Standards[1] was established by an act of Congress on March 3, 1901. The Bureau's overall goal is to strengthen and advance the Nation's science and technology and facilitate their effective application for public benefit. To this end, the Bureau conducts research and provides: (1) a basis for the Nation's physical measurement system, (2) scientific and technological services for industry and government, (3) a technical basis for equity in trade, and (4) technical services to promote public safety. The Bureau's technical work is performed by the National Measurement Laboratory, the National Engineering Laboratory, and the Institute for Computer Sciences and Technology.

THE NATIONAL MEASUREMENT LABORATORY provides the national system of physical and chemical and materials measurement; coordinates the system with measurement systems of other nations and furnishes essential services leading to accurate and uniform physical and chemical measurement throughout the Nation's scientific community, industry, and commerce; conducts materials research leading to improved methods of measurement, standards, and data on the properties of materials needed by industry, commerce, educational institutions, and Government; provides advisory and research services to other Government agencies; develops, produces, and distributes Standard Reference Materials; and provides calibration services. The Laboratory consists of the following centers:

Absolute Physical Quantities[2] — Radiation Research — Chemical Physics — Analytical Chemistry — Materials Science

THE NATIONAL ENGINEERING LABORATORY provides technology and technical services to the public and private sectors to address national needs and to solve national problems; conducts research in engineering and applied science in support of these efforts; builds and maintains competence in the necessary disciplines required to carry out this research and technical service; develops engineering data and measurement capabilities; provides engineering measurement traceability services; develops test methods and proposes engineering standards and code changes; develops and proposes new engineering practices; and develops and improves mechanisms to transfer results of its research to the ultimate user. The Laboratory consists of the following centers:

Applied Mathematics — Electronics and Electrical Engineering[2] — Manufacturing Engineering — Building Technology — Fire Research — Chemical Engineering[2]

THE INSTITUTE FOR COMPUTER SCIENCES AND TECHNOLOGY conducts research and provides scientific and technical services to aid Federal agencies in the selection, acquisition, application, and use of computer technology to improve effectiveness and economy in Government operations in accordance with Public Law 89-306 (40 U.S.C. 759), relevant Executive Orders, and other directives; carries out this mission by managing the Federal Information Processing Standards Program, developing Federal ADP standards guidelines, and managing Federal participation in ADP voluntary standardization activities; provides scientific and technological advisory services and assistance to Federal agencies; and provides the technical foundation for computer-related policies of the Federal Government. The Institute consists of the following centers:

Programming Science and Technology — Computer Systems Engineering.

[1] Headquarters and Laboratories at Gaithersburg, MD, unless otherwise noted; mailing address Washington, DC 20234.

[2] Some divisions within the center are located at Boulder, CO 80303.

NBS Reactor:
Summary of Activities
July 1981 Through June 1982

Frederick J. Shorten, Editor

Reactor Radiation Division
National Measurement Laboratory
National Bureau of Standards
Washington, DC 20234

NBS technical note

U.S. DEPARTMENT OF COMMERCE, Malcolm Baldrige, Secretary
NATIONAL BUREAU OF STANDARDS, Ernest Ambler, Director

Issued June 1983

National Bureau of Standards Technical Note 1178
Natl. Bur. Stand. (U.S.), Tech. Note 1178, 231 pages (June 1983)
CODEN: NBTNAE

U.S. GOVERNMENT PRINTING OFFICE
WASHINGTON: 1983

For sale by the Superintendent of Documents, U.S. Government Printing Office, Washington, DC 20402
Price $6.50
(Add 25 percent for other than U.S. mailing)

FOREWORD

The National Bureau of Standards Reactor was built not only to serve the needs of the NBS but also those of other government agencies as a National Center for the application of neutron methods to problems of national interest. The Reactor Radiation Division was established to operate the reactor and to foster its scientific and technological use. Toward this end, the Division has a small nucleus of scientists experienced in the use of reactors for a wide range of scientific and technical problems. In addition to pursing their own research and developing sophisticated experimental facilities, they actively seek out and encourage collaboration with other scientists engaged in challenging programs whose work can benefit from use of the reactor, but who as yet do not have the reactor experience necessary to take full advantage of the facilities available. The Division also provides irradiation services to a wide variety of users as well as engineering and other technical services.

The reactor operates at 10 MW and is designed to provide more than 25 experimental facilities ranging from intense neutron beams to extensive irradiation facilities, making it one of the most versatile high flux research reactors in the country. Thus, it is able to serve a large number of scientists and engineers in a broad range of activities both within and outside the NBS.

This report attempts to summarize all the work done which is dependent on the reactor including a large number of programs outside the Division. The first section summarizes these programs carried out by scientists in the Reactor Radiation Division and their collaborators. The second section summarizes NBS work originating entirely outside the RRD which requires no collaboration with RRD scientists. The section entitled, "Service Programs," covers those programs originating outside NBS but for which RRD provides irradiation services. The remaining sections are self-explanatory.

FOREWORD

Appreciation is extended to F. J. Shorten of the Reactor Radiation Division for his extensive contributions to the editing, organization, and preparation of this report, and T. Mangum, S. Long, and N. Phelps for efforts in typing manuscripts.

R. S. Carter
Chief, Reactor Radiation Division
National Bureau of Standards

ABSTRACT

This report summarizes all those programs which depend on the NBS reactor. It covers the period from July 1981 through June 1982. The programs range from the use of neutron beams to study the structure and dynamics of materials through nuclear physics and neutron standards to sample irradiations for activation analysis, isotope production, radiation effects studies, neutron radiography, and nondestructive evaluation.

Key words: Activation analysis; crystal structure; diffraction; isotopes; molecular dynamics; neutron; neutron radiography; nondestructive evaluation; nuclear reactor; radiation.

DISCLAIMER

TABLE OF CONTENTS

TABLE OF CONTENTS

TABLE OF CONTENTS

A. REACTOR RADIATION DIVISION AND COLLABORATIVE PROGRAMS

NBS CRYSTAL DATA IDENTIFICATION FILE

A. D. Mighell and J. K. Stalick

A crystal data identification file is available for lease[1] in magnetic tape form. This data base permits the user rapidly to identify unknown crystalline materials using x-ray diffractometer measurements. These data were collected from the published literature and were evaluated by the NBS Crystal Data Center and cooperating data centers. The work was supported by the Office of Standard Reference Data at NBS.

1. Description of the Data Base

The data base contains evaluated crystallochemical data on approximately 60,000 materials. Each entry consists of the reduced cell, cell volume, crystal system, space group, space group number, calculated density, chemical name, chemical formula, and journal reference.

2. Use of the Data Base

The data base will prove to be a practical analytical tool for compound characterization and identification because the reduced cell (i.e., the lattice) is unique for most compounds. Unknowns can conveniently be identified by the following sequence:

1. Determine a primitive or centered cell for unknown crystal.
2. Calculate the reduced cell.
3. Check the NBS Crystal Data Identification File.

In addition to routine analytical work, the data base will be useful in preventing redeterminations of published structures. The data base can also be used in conjunction with other data for materials characterization.

3. Coverages and Updates

The data base contains data for commonly occurring materials. With respect to the published literature, it is current (1980) for organic and organometallic materials and is complete to 1970 for inorganic materials. New entries are being added on a regular basis and a revised version of the data base will be made available annually to all subscribers.

4. Use of the NBS Crystal Data Identification File

Our research and data center work have demonstrated the desirability of routinely characterizing crystalline materials by cell parameters as determined from x-ray diffraction experiments in addition to the traditional chemical analyses. Cell parameters can be determined either by single-crystal techniques or by powder techniques in conjunction with indexing programs. We have found that identification procedures based on lattice-formula matching are extremely effective. The reduced cell may be used to determine if two crystals, known and unknown, have the same lattice. Usually a simple comparison of the reduced cells and cell volumes is sufficient to identify a compound. This is easy to do as the cells on the tape are ordered on the magnitude of the reduced cell parameters. The match can be done by hand by using a computer listing of the tape, or it can be carried out using a computer search procedure.

Lattice-matching can be enhanced by using software that allows one to match derivative lattices. This is desirable because in some cases cell centering is not published (e.g., a face-centered cubic cell reported as a primitive cell) or a subcell or supercell may have been determined experimentally. Consequently, one sometimes needs to match cells with volume ratios of 1/2, 2, 1/3, 3, 1/4, 4, etc. In other cases (e.g., in the cells determined by indexing procedures using powder data), one may obtain a cell that defines a lattice that bears a composite relationship to the correct lattice. In spite of these errors, identification is still possible by using a mattrix approach.[2] In this approach, the nature of the lattice relationship is deduced from the transformation matrix relating the reduced cells of the known and the unknown lattice. Alternatively, the matching of a lattice against a sublattice or superlattice, but not a composite lattice, can be accomplished by systematically calculating appropriate sub- and superlattice.[3]

The routine use of the NBS Crystal Data Identification File coupled with modern cell determination procedures offers a new approach for materials identification and characterization. The entire procedure of cell determination and file search can be automated. The method would have practical applications in any industrial analytical laboratory and can be used independently or in conjunction with powder diffraction identification techniques.

---

1. From the JCPDS--International Centre for Diffraction Data, 1601 Park Lane, Swarthmore, Pennsylvania, 19081.

2. A. Santoro, A. D. Mighell, and J. R. Rodgers, *Acta Cryst.* A36, 796 (1980).

3. A. Santoro and A. D. Mighell, *Acta Cryst.* A29, 169 (1973).

A MATRIX METHOD FOR LATTICE SYMMETRY DETERMINATION (AN APPLICATION OF THE B-MATRIX ALGORITHM)

V. L. Himes
(Catholic University of America, Washington, DC)
and
(National Bureau of Standards, Washington, DC)

and

A. D. Mighell

A previous study based on classification according to reduced form has shown that the crystal lattice symmetry and the metric lattice symmetry are usually identical for molecular compounds (Mighell and Rodgers, 1980). Although reduction procedures can reliably be used to determine metric symmetry, there are several non-trivial problems with the method when used automatically without human interaction. First, when calculating the reduced cell, experimental errors cause problems in treating the inequalities inherent in the special conditions for reduction. Occasionally, more than one "reduced" cell is possible depending on how the errors are treated. Second, one must transform an experimentally determined cell to the reduced cell and properly identify the form of the reduced cell matrix. Third, it is difficult to establish all possible pseudo-symmetries when using reduction procedures. Having recognized the problem of experimental error, Clegg (1981) offers an alternative method to obtain the correct Bravais lattice from the reduced cell. However, we recommend a new, general approach to determine metric lattice symmetry. The central focus of the method described herein is on determining matrices that relate any primitive unit cell to itself rather than on obtaining reduced cells and conventional cells.

In a recent paper, it was shown that properties of lattices can be derived from the nature of the transformation matrices relating unit cells in the same or in different lattices (Santoro, Mighell & Rodgers, 1980). An algorithm ($\underset{\sim}{B}$-matrix) was presented that will determine the matrices $\underset{\sim}{B}$ in the following equation:

$$\underset{\sim}{a}_i = \sum_j B_{ij}\underset{\sim}{a}_j (i,j = 1, 2, 3)$$

where $\underset{\sim}{a}_i$ and $\underset{\sim}{a}_j$ define two primitive triplets of noncoplanar translations (a triplet is called <u>primitive</u> when it defines a primitive cell; <u>International Tables for X-ray Crystallography</u>, 1969). We have found that the $\underset{\sim}{B}$-matrix algorithm can be used routinely to determine metric lattice symmetry. To determine symmetry using the algorithm, one selects a primitive cell and then determines how many ways it can be transformed into itself to within any specified tolerance of the unit cell parameters. Only $\underset{\sim}{B}$-matrices with integer elements and a determinant of +1 are considered. The greater the number of matrices found, the higher the symmetry. Using the algorithm, the number of matrices for the seven lattice metric symmetries are: triclinic, 1; monoclinic, 2; orthorhombic, 4; rhombohedral, 6; tetragonal, 8; hexagonal, 12; and cubic 24. The 24 matrices listed in table 1 for a primitive cubic cell were output from the computer program used to calculate $\underset{\sim}{B}$-matrices. Multiplication of the matrices in table 1 by -1 generates a set of 48 matrices which are identical to those listed for the 48 symmetry operations compatible with a cubic lattice (Rigault, 1980).

In contrast to reduction techniques, one can deduce the lattice symmetry from any primitive cell that has been determined, without transformation to a standard cell. Consider the example of the primitive unit cell which was determined for potassium antimony tartrate hydrate.

The matrix procedure yielded a set of four matrices with integer elements ranging from 0 to ± 4. When the original cell was reduced and analyzed by the matrix procedure, a different set of four integer-only matrices was obtained with elements of 0 and ± 1. In each case, the orthorhombic symmetry of the conventional unit cell (C-centered) was predicted. Table 2 gives a summary of these results.

The most important features of this method are that one can determine the highest possible metric symmetry within a specified tolerance and that pseudo-symmetries are immediately apparent. The treatment of experimental error using the matrix method is conceptually simpler than in reduction as one does not need to worry about the inequalities inherent in reduction theory. When using reduction techniques, it is not uncommon for the computer program or the person to miss the highest possible metric symmetry because of the effects of experimental errors in the unit cell parameters, round-off errors in computations and the assessment of the equality or inequality of numbers. This is especially true for those cases when the experimental error in the unit cell parameters is large or unknown. In contrast, experience has shown that the matrix procedure correctly predicts the metric symmetry even when the experimental error is large. To ensure that all potentially interesting matrices are generated, a relatively large tolerance for cell parameter errors should be used.

Recently, it was reported that several crystal structure analyses have been, "almost certainly described in space groups of unnecessarily low symmetry" (Marsh & Shomaker, 1979; see also Herbstein & Marsh, 1982; Marsh & Shomaker, 1980; Schomaker & Marsh, 1979). In several instances, the crystal structures were reported to have been described in the wrong crystal system. For example, the compound dichlorobis(4-vinylpyridine) zinc(II) was originally reported in the triclinic space group P1 with unit cell parameters

$$a = 7.501(4) \quad b = 7.522(5) \quad c = 14.482(6)\ \text{Å}$$
$$\alpha = 90.41(4) \quad \beta = 90.53(4) \quad \gamma = 105.29(5)^\circ .$$

Marsh and Schomaker (1979) found that the triclinic unit cell could be transformed by the matrix (1 1 0/ -1 1 0 / 0 0 1) to a monoclinic C-centered unit cell with

$$a = 9.115 \qquad b = 11.942 \qquad c = 14.482\ \text{Å}$$
$$\alpha = 89.93 \qquad \beta = 90.77 \qquad \gamma = 89.83^\circ .$$

Although the angles α and γ have large deviations relative to the e.s.d.'s of the originally reported unit cell, the atomic coordinates conform more closely to the monoclinic symmetry. The monoclinic lattice symmetry for the Zn(II) compound is predicted by the matrix procedure to determine metric symmetry. The following matrices and "error" matrices were found using the originally reported triclinic cell and tolerances of 0.2 Å for the cell edges and 0.5° for the cell angles:

$$\begin{array}{ccc}
 & \underset{\sim}{B}\text{-matrices} & \text{Error matrices} \\
\text{I} & \begin{bmatrix} 0 & 1 & 0 \\ -1 & 0 & 0 \\ 0 & 0 & -1 \end{bmatrix} & \begin{matrix} 0.021 & -0.021 & 0.000 \\ 0.120 & -0.120 & 0.000 \\ & & \end{matrix} \\
\text{II} & \begin{bmatrix} 1 & 0 & 0 \\ 0 & 1 & 0 \\ 0 & 0 & 1 \end{bmatrix} & \begin{matrix} 0.000 & 0.000 & 0.000 \\ 0.000 & 0.000 & 0.000\ . \\ & & \end{matrix}
\end{array}$$

The "error" matrices represent the tolerances in the unit cell parameters required to transform the cell into itself by the specified matrix. Suppose cell A is defined by lattice parameters, a, b, c, α, β, γ. If the matrix procedure to determine metric lattice symmetry for cell A yields the matrix $\underset{\sim}{M}$ with the error matrix

$$\begin{bmatrix} \text{tol } a & \text{tol } b & \text{tol } c \\ \text{tol } \alpha & \text{tol } \beta & \text{tol } \gamma \end{bmatrix} ,$$

then the transformation of cell A by the matrix $\underset{\sim}{M}$ will give cell B having lattice parameters

$$a' = a + \text{tol } a \qquad b' = b + \text{tol } b \qquad c' = c + \text{tol } c$$
$$\alpha' = \alpha + \text{tol } \alpha \qquad \beta' = \beta + \text{tol } \beta \qquad \gamma' = \gamma + \text{tol } \gamma\ .$$

In the case of the Zn(II) compound, matrix I will transform the initial triclinic cell into a second cell with

$$a = 7.522 \qquad b = 7.501 \qquad c = 14.482\ \text{Å}$$
$$\alpha = 90.53 \qquad \beta = 90.41 \qquad \gamma = 105.29°.$$

If the Zn(II) compound has crystallized in the monoclinic system, the two unit cells are symmetrically equivalent. An average of the lattice parameters for the two symmetry-related unit cells gives

$$a = 7.5115 \qquad b = 7.5115 \qquad c = 14.482\ \text{Å}$$
$$\alpha = 90.47 \qquad \beta = 90.47 \qquad \gamma = 105.29°.$$

Transformation of the average cell by the matrix (1 1 0 / -1 1 0 / 0 0 1) gives an ideal centered-monoclinic cell with

$$a = 9.115 \qquad b = 11.942 \qquad c = 14.482\ \text{Å}$$
$$\alpha = 90.00 \qquad \beta = 90.77 \qquad \gamma = 90.00°.$$

Thus, an analysis of the error matrices provides an indication of the extent to which the original triclinic cell parameters must be changed to make the cell reflect the exact monoclinic metric symmetry. It should be mentioned that the above analysis of the error matrices is only one of many possible interpretations.

The previous discussion concerning the use of the matrix procedure to determine metric symmetry for dichlorobis(4-vinylpyridine)zinc(II) was based on the results of an analysis using tolerances for cell parameter errors which were smaller than those normally recommended for routine structure work. Although the tolerances specified may vary considerably depending on the individual problem, the recommended values typically range from 0.5 to 1.0 Å for the cell edges and 1.0 to 4.0° for the cell angles. The matrix method reveals that the Zn(II) compound could be metrically orthorhombic depending on the interpretation of experimental error. The set of four matrices and error matrices found for the original triclinic cell using tolerances of 1.0 Å and 4.0° are given in Table 3. When the four error matrices are averaged and the resulting error matrix is applied to the triclinic cell, the following cell parameters are obtained:

$a = 7.5115 \quad b = 7.5115 \quad c = 14.482\ \text{Å}$

$\alpha = 90.00 \quad \beta = 90.00 \quad \gamma = 105.29°.$

This cell may be transformed by the matrix (1 1 0 / -1 1 0 / 0 0 1) to a centered-orthorhombic unit cell with

$a = 9.115 \quad b = 11.942 \quad c = 14.482\ \text{Å}$

$\alpha = 90.00 \quad \beta = 90.00 \quad \gamma = 90.00°.$

The matrix procedure yields all possible lattice symmetries within a specified tolerance. The actual selection of the highest possible symmetry of the lattice is dependent on the assessment of the experimental error. An advantage of the matrix procedure to determine metric lattice symmetry is that an analysis of the error matrices output from the computer program enables a direct comparison of the calculated errors (i.e. those related to the specified tolerances) with the experimental errors determined for the primitive unit cell. The triclinic unit cell for the Zn(II) compound is metrically monoclinic since the calculated errors correspond to approximately twice the e.s.d.'s for the cell edges a and b and the cell angles α and β. In order to have exact orthorhombic metric symmetry, the original triclinic cell parameters must be changed by a maximum of approximately 13 e.s.d.'s.

Thus, in addition to the determination of metric lattices symmetry, the matrix procedure offers a direct and convenient way to find all possible pseudo-symmetries within a specified range of cell parameter errors. To determine metric pseudo-symmetry using the matrix procedure, one simply increases the magnitudes of the tolerances acceptable for the cell parameters and analyzes the sets of matrices and error matrices obtained. The interpretation of the error matrices (i.e. symmetry versus pseudo-symmetry) will vary considerably depending upon the compound being studied.

The matrix method may be used on a problem-to-problem basis to determine symmetry or it can be used to critically evaluate lattice symmetry in large sets of data. In our routine structure work, the matrix procedure has been used to determine symmetry as soon as a refined primitive cell has been obtained; in every case, the method gave the correct symmetry. When the unit cell is highly skewed, one must allow the computer program to seek matrices with integer elements typically as high as ± 10. In contrast, when the matrix procedure is used to analyze the lattice symmetry of a standard cell based on the 3 shortest lattice translations, a standard set of matrices having matrix elements of -1, 0, 1 is produced. Thus, one may be certain that the proper matrix elements have been considered when the reduced cell is analyzed by the matrix procedure. This eliminates the possibility that the correct lattice symmetry has been missed because the expermentalist misjudged the matrix elements which were required to analyze a skewed unit cell.

Computer analyses of approximately 30,000 lattices from the NBS Crystal Data Identification File (NBS*ID File) have proved that the matrix method for metric symmetry determination is fast, efficient and reliable. The method predicts a lattice symmetry which, in most cases, is consistent with the crystal symmetry reported by the authors in the original reference. In a relatively low percentage of cases, the matrix procedure predicts a higher symmetry. The percentages of compounds where the matrix method predicted a higher symmetry are given in Table 4. For example, using tolerances of 0.15 Å and 1.5°, 12.4% of the compounds reported to have monoclinic crystal symmetry were found to have higher metric symmetry. Similarly, 5.4% of all organic compounds in the 1-line file have higher metric symmetry when tolerances of 0.09Å and 0.9° are specified in the computer program to calculate B-matrices. As expected since the cubic symmetry is the highest possible symmetry of the lattice, the matrix method never found more than 24 matrices for any of the 30,232 entries analyzed.

The computer analyses of the NBS*ID File using the matrix procedure have revealed that the unit cell parameters with higher metric symmetry commonly involve a transformation to or from a centered cell. The most frequently encountered examples include the transformations from a primitive triclinic cell to a centered monoclinic cell, a primitive monoclinic cell to a centered orthorhombic cell, and a centered monoclinic cell to a primitive rhombohedral cell. There are, however, numerous compounds in the 1-line file that do not require a transformation to or from a centered cell to reveal higher metric symmetry. Among other examples, there are many substances which have been characterized by primitive monoclinic unit cells which are metrically orthorhombic with $a \neq b \neq c$ and $\alpha = \beta = \gamma = 90°$. Presumably, the higher metric symmetry and any structural implications have been noted by the authors. Further discussions are planned concerning the cases for which the metric symmetry exceeds the reported crystal symmetry.

It has become apparent that metric symmetry and possibly crystal symmetry is often missed by diffraction techniques currently being employed. In view of the recent trend toward the determination of a unit cell solely from diffractometer data, the use of metric methods to indicate probable lattice symmetry is especially important. Ideally, the check for metric symmetry should be carried out as soon as a refined unit cell has been determined. Experience has shown that the matrix procedure offers a direct and convenient way to determine the highest possible symmetry of the lattice. On a practical basis, algorithms to determine metric symmetry (such as the $\underset{\sim}{B}$-matrix and reduction algorithms) could be incorporated into the software for modern, automated diffractometers. However, the need to critically evaluate all stages of crystallographic work should not be eliminated by the availability of sophisticated automation.

Table 1. Matrices found for a cubic primitive cell

1	-1	0	0	0	-1	0	0	0	1	13	0	0	1	-1	0	0	0	-1	0
2	-1	0	0	0	0	-1	0	-1	0	14	0	0	1	0	-1	0	1	0	0
3	-1	0	0	0	0	1	0	1	0	15	0	0	1	0	1	0	-1	0	0
4	-1	0	0	0	1	0	0	0	-1	16	0	0	1	1	0	0	0	1	0
5	0	-1	0	-1	0	0	0	0	-1	17	0	1	0	-1	0	0	0	0	1
6	0	-1	0	0	0	-1	1	0	0	18	0	1	0	0	0	-1	-1	0	0
7	0	-1	0	0	0	1	-1	0	0	19	0	1	0	0	0	1	1	0	0
8	0	-1	0	1	0	0	0	0	1	20	0	1	0	1	0	0	0	0	-1
9	0	0	-1	-1	0	0	0	1	0	21	1	0	0	0	-1	0	0	0	-1
10	0	0	-1	0	-1	0	-1	0	0	22	1	0	0	0	0	-1	0	1	0
11	0	0	-1	0	1	0	1	0	0	23	1	0	0	0	0	1	0	-1	0
12	0	0	-1	1	0	0	0	-1	0	24	1	0	0	0	1	0	0	0	1

Table 2. Lattice symmetry determination for potassium anitmony tartrate hydrate.

	Unit Cell Parameters			
	a	b	c (Å)	$\underset{\sim}{B}$-Matrices
	α	β	γ (°)	
Initial primitive cell	8.095(6)	8.096(6)	30.667(25)	$\begin{bmatrix}-1 & 0 & 0\\ 0 & -1 & 0\\ -4 & 0 & 1\end{bmatrix}\begin{bmatrix}0 & -1 & 0\\ -1 & 0 & 0\\ 2 & -2 & -1\end{bmatrix}\begin{bmatrix}0 & 1 & 0\\ 1 & 0 & 0\\ 2 & 2 & -1\end{bmatrix}\begin{bmatrix}1 & 0 & 0\\ 0 & 1 & 0\\ 0 & 0 & 1\end{bmatrix}$
	88.69(6)	57.95(5)	87.48(6)	
	(1 0 0 / 0 -1 0 / 2 0 -1)			
Reduced cell	8.095	8.096	25.993	$\begin{bmatrix}-1 & 0 & 0\\ 0 & -1 & 0\\ 0 & 0 & 1\end{bmatrix}\begin{bmatrix}0 & -1 & 0\\ -1 & 0 & 0\\ 0 & 0 & -1\end{bmatrix}\begin{bmatrix}0 & 1 & 0\\ 1 & 0 & 0\\ 0 & 0 & -1\end{bmatrix}\begin{bmatrix}1 & 0 & 0\\ 0 & 1 & 0\\ 0 & 0 & 1\end{bmatrix}$
(reduced form #13)	90.02	90.18	92.52	
orthorhombic-C)				
	(-1 1 0 / 1 1 0 / 0 0 -1)			
Refined conventional	11.694(5)	11.192(5)	25.961(9)	
cell (space group $C222_1$)	89.97(3)	90.04(3)	89.97(4)	

Table 3. Matrices and error matrices found for dichlorobis-(4-vinylpyridine) zinc(II) when tolerances of 1.0 Å and 4.0° were specified.

	-1	0	0	0.000	0.000	0.000
I	0	-1	0	-0.820	-1.060	0.000
	0	0	1			
II	0	-1	0	0.021	-0.021	0.000
	-1	0	0	0.120	-0.120	0.000
	0	0	-1			
III	0	1	0	0.021	-0.021	0.000
	1	0	0	-0.940	-0.940	0.000
	0	0	-1			
IV	1	0	0	0.000	0.000	0.000
	0	1	0	0.000	0.000	0.000
	0	0	1			

Table 4. Percentages of organic compounds having higher metric symmetry. Of the 30,232 entries analyzed, there were 4526 triclinic(A), 15926 monoclinic(M), 7816 orthorhombic(O), 301 rhombohedral(R), 945 tetragonal(T), 484 hexagonal(H), and 234 cubic entries.

Tolerence		A	M	O	R	T	H	Total
Å	°							
0.01	0.1	0.8	1.8	0.6	<0.5	<0.5	<0.5	1.2
0.02	0.2	1.2	2.9	0.9	<0.5	<0.5	<0.5	1.9
0.03	0.3	1.3	3.4	1.3	1.0	<0.5	<0.5	2.3
0.04	0.4	1.6	4.2	1.7	1.0	0.5	<0.5	2.9
0.05	0.5	1.7	4.8	2.0	1.0	0.7	<0.5	3.3
0.06	0.6	2.1	5.8	2.4	1.0	0.6	<0.5	4.0
0.07	0.7	2.2	6.2	2.7	1.3	0.7	<0.5	4.3
0.08	0.8	2.5	7.2	2.9	1.3	1.1	<0.5	5.0
0.09	0.9	2.8	7.7	3.1	1.7	1.3	<0.5	5.4
0.10	1.0	3.2	8.9	3.5	1.7	1.4	<0.5	6.1
0.11	1.1	3.4	9.4	3.7	1.7	1.7	<0.5	6.5
0.12	1.2	3.9	10.4	4.0	2.0	1.7	<0.5	7.2
0.13	1.3	4.2	10.9	4.2	2.0	1.7	<0.5	7.6
0.14	1.4	4.8	11.9	4.6	2.7	1.9	<0.5	8.3
0.15	1.5	5.3	12.4	4.8	3.3	1.9	<0.5	8.7

---

1. W. Clegg, *Acta Cryst.* A37, 913-915 (1981).

2. F. H. Herbstein and R. E. Marsh, *Acta Cryst.* B38, 1051-1055 (1982).

3. *International Tables for X-ray Crystallography*, Vol. I, 3rd. ed., p. 8, Birmingham: Kynoch Press (1969).

4. R. E. Marsh and V. Schomaker, *Inorg. Chem.* 18, 2331-2336 (1979).

5. R. E. Marsh and V. Schomaker, *Acta Cryst.* B36, 219-220 (1980).

6. A. D. Mighell and J. R. Rodgers, *Acta Cryst.* A36, 321-326 (1980).

7. G. Rigault, "Metric Tensor and Symmetry Operations in Crystallography." Published for the International Union of Crystallography Commission on Crystallographic Teaching by University College Cardiff Press; Cardiff, Wales.

8. A. Santoro, A. D. Mighell, and J. R. Rodgers, *Acta Cryst.* A36, 796-800 (1980).

9. V. Schomaker and R. E. Marsh, *Acta Cryst.* B35, 1094-1099 (1979).

SYNTHESIS AND STRUCTURE OF $Cu_5(BTA)_6(t\text{-}C_4H_9NC)_4$, A MIXED-VALENT COPPER-NITROGEN CLUSTER CONTAINING η^3-BENZOTRIAZOLATE

V. L. Himes
(The Catholic University of America, Washington, DC)
and
(National Bureau of Standards, Washington, DC)

and

A. D. Mighell

and

A. R. Siedle
(3M Central Research Laboratories, St. Paul, MN)

and

G. F. Kokosaka
(State University of New York, Plattsburgh, NY)

Protection of metals with reactive materials capable of forming surface-phase coordination compounds is an area of chemistry which is of considerable scientific and technological importance. In view of the extensive use of benzotriazole as a corrosion inhibitor for copper and its alloys (Reekijk, Roelofsen, Siedle, and Spek, 1979, and references cited therein), it is remarkable that, to our knowledge, no copper-benzotriazole complex has been structurally characterized by x-ray diffraction. The synthesis and crystal structure of a neutral, highly symmetric complex containing a three-dimensional copper-nitrogen cluster formed by the coordination of η^3-benzotriazolate to copper(I) and copper(II) is described herein. The central cluster is composed of interconnected copper-nitrogen cycles (azametallocycles) which vary in size and spatial orientation.

The reaction of copper(I) thiophenoxide, benzotriazole, and alkyl isocyanides in dichloromethane at room temperature produces $Cu_5(BTA)_6(RNC)_4$ [BTA = benzotriazolate (1-)]. Since the benzotriazolate ion has a charge of -1, the pentacopper compounds are mixed-valent materials which contain four Cu(I) ions and one Cu(II) ion. The reaction does not occur in the absence of air. Evidently, oxygen oxidizes some of the Cu(I) to Cu(II), which acts as a template for the assembly of the rather complex product. The rate of reaction can be controlled by regulating the partial pressure of oxygen and, in this way, red-orange crystals of $Cu_5(BTA)_6(\underline{t}-C_4H_9NC)_4$ suitable for x-ray analysis were obtained. Analysis calculated for $C_{56}H_{60}Cu_5N_{22}$: C,49.49; H,4.45; Cu,23.38; N,22.68; S,0.0. Found: C,49.3; H,4.4; Cu,23.8; N,22.7; S, < 0.3. The infrared spectrum shows a strong band at 2140 cm^{-1} due to <u>tert</u>-butylisocyanide coordinated to the metal. This complex crystallizes in the tetragonal crystal system, space group $P\bar{4}2_1c$, unit cell parameters a = 13.836(4), c = 16.686(4) Å; Z = 2, D_{calc} = 1.413, D_{obsd} = 1.41(2) Mg m^{-3} (flotation). A total of 1196 unique reflections were measured on an automated 4-circle diffractometer using graphite-monochromated MoKα radiation (λ = 0.71069 Å) and the θ-2θ scan mode in the range $3.0 \leq 2\theta \leq 45.0°$. Intensity data were corrected for Lorentz and polarization effects, but not for absorption (crystal size = 0.10 x 0.11 x 0.11 mm, μ = 16.9 cm^{-1}). The positions of the two independent copper atoms were determined by direct methods and were verified in a 3-dimensional Patterson map. Successive least-squares refinement and Fourier syntheses revealed the positions of the remaining non-hydrogen atoms. Full matrix least-squares refinement gave a conventional agreement factor R = 0.063 for 903 observed reflections with $F_o > 3\sigma$ (Fo).

1. Discussion

The crystal structure consists of neutral complexes with crystallographic $\bar{4}$ symmetry in which an octahedrally coordinated copper(II) ion is surrounded by four tetrahedrally coordinated copper(I) ions. Tridentate BTA ligands bridge each copper(I) ion to three symmetry-related copper(I) ions and to the central copper(II) ion. Figure 1 gives a view of the complex down a $\bar{4}$ axis. A stereoview of the complex is illustrated in figure 2; the labeling scheme is presented in figure 3. Table 1 lists selected interatomic distances and angles.

There are two complexes in the unit cell with the central Cu2 ions in special positions (0, 0, 0) and (1/2, 1/2, 1/2) with $\bar{4}$ symmetry. Each

Cu2 ion is coordinated to four equatorial and two axial BTA ligands at the N1 and N4 positions, respectively. The four Cu1 ions surrounding the central Cu2 ion are each coordinated to one tert-butyl isocyanide ligand and to three different BTA ligands (two equatorial and one axial) at the N2, N3, and N5 positions. The four equatorial BTA ligands illustrated in figure 1 occupy general positions in the unit cell; within experimental error, their central nitrogen atoms (N1 positions) are in the $z = 1/2$ plane ($z = 0$ plane for the complex at the origin) and are coplanar with Cu2. Because N4 lies on a crystallographic $\overline{4}$ axis, a two-fold axis relates the two halves of the axial BTA ligands. The four equatorial BTA ligands define planes which make acute angles of 41.7° with the Cu2 basal plane. Because of symmetry considerations, the two planes defined by the axial BTA ligands are normal to the Cu2 basal plane.

The geometry about Cu2 is unusual in that it is an undistorted octahedron of a compressed form $[(Cu2)(N1)_4(N4)_2]$. While the two Cu2-N4 bond distances are typical, the four Cu2-N1 distances are longer than those usually found for nitrogen coordinated to copper(II) (Hamalainen, Turpeinen, and Ahlargen, 1979; van Niekerk and Nassimbeni, 1979). Similar copper(II)-nitrogen distances have been observed in $Cu(diethylenetriamine)_2(NO_3)_2$ (Stephens, 1969) and in $Cu(4\text{-formyl-2-methoxyphenolato})_2$(tetramethylethylenediamine) (Greenhough and Ladd, 1978), compounds in which the copper(II) ion has distorted, compressed octahedral geometry.

The coordination geometry about Cu1 is approximately tetrahedral but there are significant deviations from the ideal angles. The Cu1-C10 distance of 1.882(17) Å and Cu1-C10-N6 angle of 175.8(1.6)° are in general agreement with the respective values of 1.81(15) Å and 180(2)° found for $CuI(CNCH_3)$ (Fisher, Taylor, and Harding, 1960). The coordination distances to Cu1 are close to those reported for copper(I)-cyanide complexes in which Cu-N distances are typically 2.0 Å and Cu-C distances are approximately 1.9 Å with a nearly linear Cu-C-N angle (Vrabel, Garaj, and Kutschabsky, 1979; Williams, Cromer, and Larson, 1971).

The nature of the bridging between the copper ions is such that a three-dimensional copper-nitrogen cluster is formed in the center of the complex. As a tridentate ligand, BTA is involved in two types of copper-nitrogen-copper bridges. Bridging between Cu2 and Cu1 is accomplished via the central and an adjacent nitrogen atom of a BTA ligand. The four symmetry-related Cu1 ions are bridged by the two nitrogen atoms adjacent to the central nitrogen of a BTA ligand in a manner analogous to the imidazolate bridge in $[Cu_2(bpim)(imidazolate)]_2(NO_3)_4 \cdot 4H_2O$, where bpim = 4,5-bis$\left[\left[[2\text{-}(2\text{-pyridyl})\text{ethyl}]\text{imino}\right]\text{methyl}\right]$imidazolate (Kolks, Frihart, Rabinowitz, and Lippard, 1976). The axial BTA ligands bridge two Cu1 ions situated on the same side of the Cu2 basal plane (i.e., the plane defined by Cu2 and the four N1 atoms) while the equatorial BTA ligands bridge Cu1 ions on opposite sides of the Cu2 basal plane. Thus, the central cluster is composed of interconnected copper-nitrogen cycles (azametallocycles) which vary in size and spatial orientation.

The four symmetry-related Cu1 ions lie 2.02 Å alternatively above and below the Cu2 basal plane forming a copper(I) tetrahedron $[(Cu2)(Cu1)_4]$ about Cu2. Thus, the core of the copper-nitrogen cluster consists of an octahedron $[(Cu2)(N1)_2(N4)_2]$ that is inscribed in a tetrahedron (figure 4). The nitrogen atoms at the vertices of the octahedron lie very close to the midpoints of the edges of the circumscribed tetrahedron; each of the central nitrogen atoms of the BTA ligands are close to one copper(II) and two copper(I) ions (see table 1). The complex $Cu_5(BTA)_6(\underline{t}\text{-}C_4H_9NC)_4$ is slightly distorted from ideal cubic symmetry ($\bar{4}3m$) because of the chemical nature of the bonding to the central copper(II) ion. The stereochemistry about Cu2 is a compressed octahedron with two axial Cu2-N4 bonds of 2.03(2) Å and four symmetry-equivalent Cu2-N1 bonds of 2.24(1) Å. This axial compression (parallel to the z axis of the unit cell) explains the slight distortion of the $(Cu2)(Cu1)_4$ tetrahedron. The two Cu1 - Cu2 - Cu1 angles along the line of compression are 112.50(5)° while the other four angles are 107.98(5)°. The two edges of the $(Cu2)(Cu1)_4$ tetrahedron normal to the line of compression are 6.050(3) Å while the remaining four edges are 5.886(3) Å.

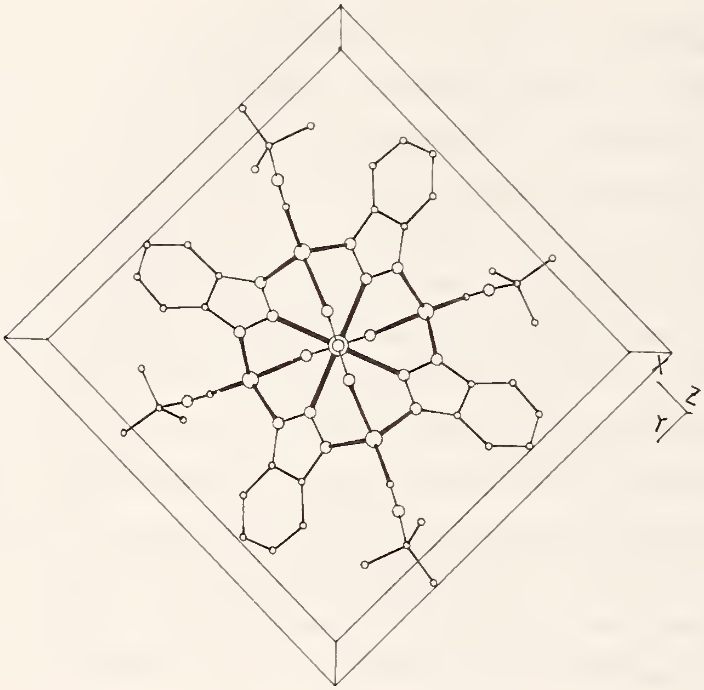

Figure 1. Structure of $Cu_5(BTA)_6(\underline{t}-C_4H_9NC)_4$ viewed down a crystallographic $\bar{4}$-axis (parallel to the z axis of the unit cell). For clarity, the benzene moieties of the axially coordinated BTA ligands, as well as the entire complex at the origin, have been omitted.

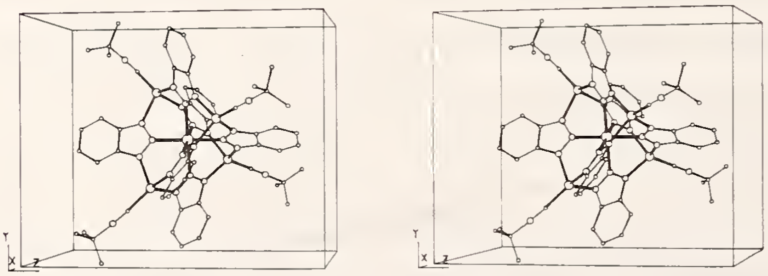

Figure 2. Stereoview of the complex viewed approximately down the x-axis (10° rotation about y).

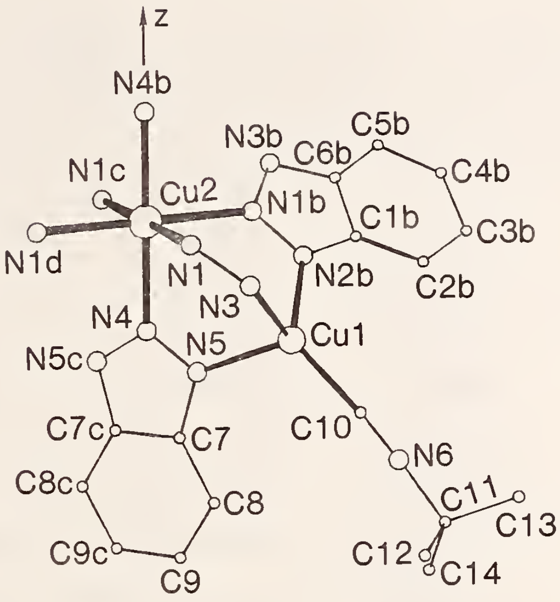

Figure 3. Perspective drawing showing the labeling scheme used. Unique atoms are labeled with atom type and number, while the letters b, c, d refer to the equivalent positions defined in table 1.

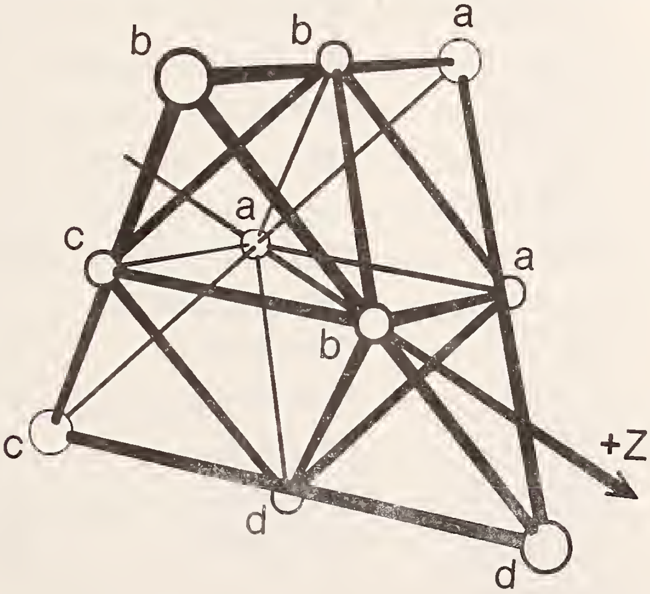

Figure 4. Geometric drawing showing that the core of the copper-nitrogen cluster may be viewed as a (Cu2)(Cu1)$_4$ tetrahedron with an inscribed (Cu2)(N1)$_4$(N4)$_2$ octahedron. The central Cu2 ion has not been drawn; the two N4 atoms lie along the z-axis. The equivalent positions a, b, c, and d are defined in table 1.

Table 1. Selected interatomic distances (Å) and angles (°) with estimated standard deviations in parentheses. The letters a, b, c, d refer to the following equivalent positions: a (no symbol) = x, y, z; b = 1 - y, x, 1 - z; c = 1 - x, 1 - y, z; d = y, 1 - x, 1 - z.

Cu2...Cu1	3.638(2)	Cu1-N3	2.013(14)
Cu2-N1	2.241(13)	Cu1...N4	3.026(2)
Cu2-N4	2.085(16)	Cu1-N5	2.087(12)
Cu1...Cu1b	5.886(3)	Cu1-C10	1.882(17)
Cu1...Cu1c	6.050(3)	N1...N1b	3.169(19)
Cu1...N1	2.949(13)	N1...N4	3.064(17)
Cu1...N1b	2.941(13)	N4...N1b	3.058(17)
Cu1-N2b	2.024(12)		
Cu1...Cu2..Cu1b	107.98(5)	Cu2-N4-N5	122.8(8)
Cu1...Cu2...Cu1c	112.50(5)	Cu1...N4...Cu1c	177.6(6)
N1-Cu2-N1b	90.0(5)	N1...N4...N1b	62.3(4)
N1-Cu2-N1c	179.8(5)	N5-Cu1-C10	117.0(6)
N1-Cu2-N4	90.1(3)	Cu2-N1-N2	123.8(10)
N1b-Cu2-N4	89.9(3)	Cu2-N1-N3	124.1(10)
Cu1b...Cu1...Cu1c	59.07(3)	Cu1...N1...Cu1d	176.0(5)
Cu1b...Cu1...Cu1d	61.85(4)	N1b...N1...N1d	90.0(5)
N1...Cu1...N1b	65.1(4)	N1b...N1...N4	58.7(4)
N1...Cu1...N4	61.7(4)	N1d...N1...N4b	58.9(4)
N1b...Cu1...N4	61.6(3)	Cu1d-N2-N1	121.9(10)
N2b-Cu1-N3	98.3(5)	Cu1d-N2-C1	131.0(11)
N2b-Cu1-N5	94.7(5)	Cu1-N5-N4	125.5(9)
N2b-Cu1-C10	123.9(7)	Cu1-N5-C7	127.9(9)
N3-Cu1-N5	95.3(5)	Cu1-C10-N6	175.8(16)
N3-Cu1-C10	121.2(6)		

By studying the geometric nature of the central copper-nitrogen cluster, a variety of complexes of the type (Metal A)(Metal B)$_4$(BTA)$_6$ could be prepared in which tridentate BTA ligands bridge the octahedrally coordinated metal A and the surrounding tetrahedral array of metal B ions. As the complex is not required to be neutral, the valences of the metal ions may vary. The structure proposed by Marshall (1978) contains a copper-nitrogen cluster in which copper (II) is substituted for copper(I); the structure may be viewed as a $[Cu(II)_5(BTA)_6]^{4+}$ cation neutralized by four 2,4-pentanedionato(1-) anions. In addition, similar metal-nitrogen clusters could be prepared using two different metal ions. It is conceivable that the symmetry of the resulting complex may be higher than the tetragonal symmetry found for $Cu_5(BTA)_6(\underline{t}\text{-}C_4H_9NC)_4$. If the central copper(II) ion (Cu2) were replaced by a metal ion which has six equivalent metal-nitrogen coordinate bonds, it is possible that the symmetry of the complex would be cubic with point symmetry $\bar{4}3m$. Thus, by changing the valences of the metal ions and by using metals other than copper, a broad class of new metal-nitrogen clusters may be synthesized.

The reaction of benzotriazole with metallic copper leads initially to copper(I) benzotriazolate (Siedle, Velapoldi, and Erickson, 1978 and 1979) which subsequently oxidizes in air. The structure described herein shows how the benzotriazolate anion, acting as tridentate ligand, can bridge multiple sites containing both copper(I) and copper(II). It is possible that similar bonding is involved in the corrosion-resistant surface phase produced on the bulk metal.

2. On-Going and Planned Work

The geometric nature of the copper-nitrogen cluster in $Cu_5(BTA)_6(\underline{t}\text{-}C_4H_9NC)_4$ gives rise to highly unusual electron paramagnetic resonance (EPR) spectra. The compressed octahedral configuration of Cu(II) requires that the room temperature EPR spectrum be interpreted in terms of a dynamic Jahn-Teller effect. The EPR spectra at low temperatures indicate that the complex undergoes a reversible phase change at -120 °C. Furthermore, low temperature EPR spectroscopic studies predict that the copper-nitrogen coordinate bonds at Cu(II) will be elongated by approximately 0.01 Å. If the phase change observed in the EPR spectra is correlated with a crystallographic phase change, the low temperature crystal structure of the complex would be cubic. In addition to the tert-butyl isocyanide derivative, the three related complexes $Cu_5(BTA)_6(R\text{-}NC)_4$, where R = isopropyl, cyclohexyl, and phenyl, have been synthesized. It is expected in these complexes that the geometry of the copper-nitrogen cluster will remain essentially the same. The EPR spectra for these compounds are currently being recorded and analyzed. It is planned to carry out x-ray and neutron diffraction studies on these compounds to further correlate the EPR spectra with any structural changes.

---

1. P. J. Fisher, N. E. Taylor, and M. M. Hardin, *J. Chem. Soc.*, 2303-2309 (1960).

2. T. J. Greenhough and M. F. C. Ladd, *Acta Cryst.* B34, 2744-2752 (1978).

3. R. Hämäläinen, U. Turpeinen, and M. Ahlgrén, *Acta Cryst.* B35, 2408-2410 (1979).

4. G. F. Kokoszka, et al. (1982). In preparation.

5. G. Kolks, C. R. Frihart, H. N. Rabinowitz, and S. J. Lippard, *J. Am. Chem. Soc.* 98, 5720-5721 (1976).

6. J. H. Marshall, *Inorg. Chem.* 17, 3711-3 (1978).

7. J. Reedijk, G. Roelofsen, A. R. Siedle, and A. L. Spek, *Inorg. Chem.* 18, 1947-1951 (1979).

8. A. R. Siedle, R. A. Velapoldi, and N. Erickson, *Inorg. Nucl. Chem. Lett.* 15, 33 (1978).

9. A. R. Siedle, R. A. Velapoldi, and N. Erickson, *Appl. Surf. Sci.* 3, 229-235 (1979).

10. F. S. Stephens, *J. Chem. Soc.* (A), 883-890 (1969).

11. J. C. van Niekerk and L. R. Nassimbeni, *Acta Cryst.* B35, 1221-1223 (1979).

12. V. Vrabel, J. Garaj, and L. Kutschabsky, *Acta Cryst.* B35, 357-360 (1979).

13. R. J. Williams, D. T. Cromer, and A. C. Larson, *Acta Cryst.* B27, 1701-1706 (1971).

NEUTRON DIFFRACTION STUDY OF SODIUM SESQUICARBONATE DIHYDRATE

C. S. Choi
(Energetic Materials Division, LCWSL, ARRADCOM, Dover, NJ)
and
(National Bureau of Standards, Washington, DC)

and

A. D. Mighell

$Na_2CO_3 \cdot NaHCO_3 \cdot 2H_2O$ crystallizes in the monoclinic space group C2/c with a = 20.36(2), b = 3.48(1), c = 10.29(1) Å, β = 106.48(1)°, Z = 4, Dx = 2.147 Mg m^{-3}. The final R value after full matrix least-squares refinement was 0.040 for 742 observed reflections. In this structure, water molecules and $(CO_3 \cdot H \cdot CO_3)^{3-}$ anions form a two-dimensional hydrogen-bonded network (figure 1). The $(HC_2O_6)^{3-}$ anion is almost planar and consists of two CO_3^{2-} anions linked by a hydrogen atom which lies at a center of symmetry with an $\overline{\mathrm{O...H...O}}$ distance of 2.46 Å. Analysis of thermal ellipsoids (figure 2) from a conventional anisotropic refinement and a least-squares refinement of a split-hydrogen model revealed that this hydrogen atom is dynamically disordered between two equivalent sites separated by 0.211(9) Å.

To further study the nature of the disorder, it is planned to collect neutron powder diffraction data at room and low temperatures. Various models will be refined using the technique of neutron profile analysis.

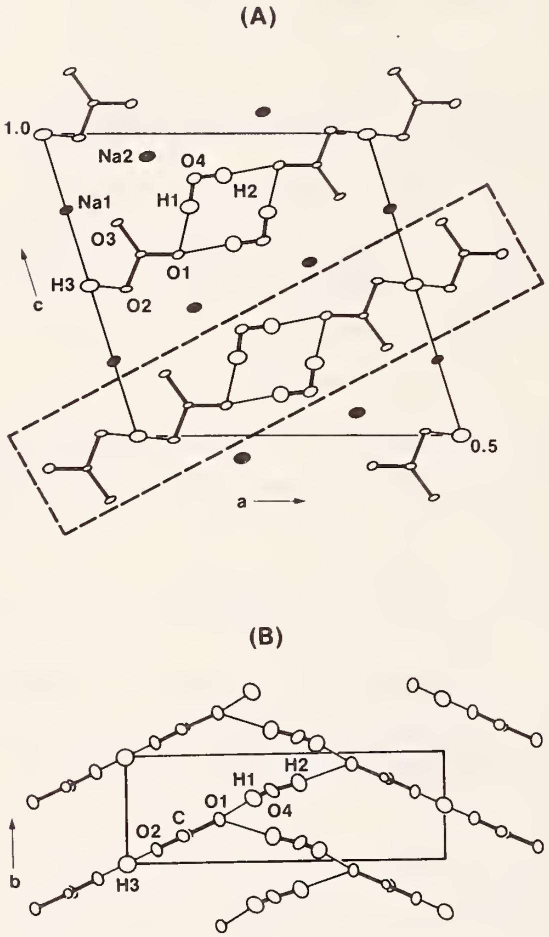

Figure 1. Packing and hydrogen bonding in sodium sesquicarbonate dihydrate. Figure (A) is the (0 1 0) projection of one half of the unit cell. This figure shows that the Na cation layer and the anion layer (marked by broken lines and consisting of $(CO_3 \cdot H \cdot CO_3)^{3-}$ ions and water molecules) are oriented parallel to the (1 0 1) plane and interleave each other. Figure (B) is the projection of the anion layer onto the (1 0 1) plane, showing a two-dimensional hydrogen-bonded network.

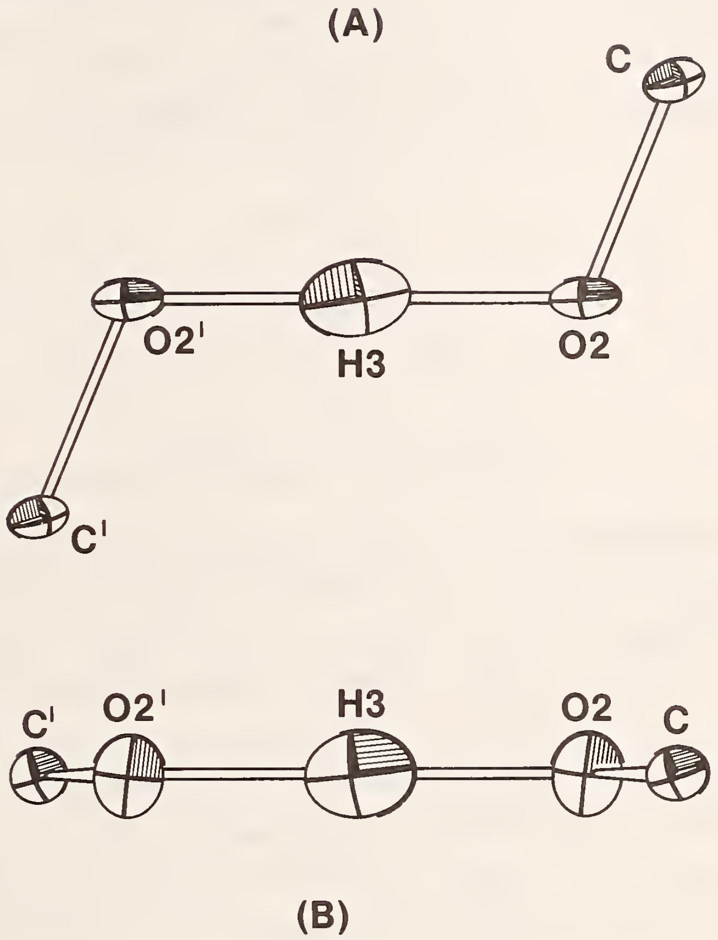

Figure 2. The thermal ellipsoid of the H(3) atom: (A) view along the normal to the plane C-O(2)...H(3); and (B) view parallel to the plane.

SINGLE CRYSTAL X-RAY STRUCTURE DETERMINATION OF THE DIMETHYL OXIME OF PHOSPHORAMIDE MUSTARD, $C_7H_{16}N_3O_2PCl_2$

V. L. Himes
(The Catholic University of America, Washington, DC)
and
(National Bureau of Standards, Washington, DC)

and

A. D. Mighell

and

S. Takagi
(American Dental Association Health)

and

G. Zon and S. M. Ludeman
(The Catholic University of America, Washington, DC)

Cyclophosphamide (1) is a well-known drug which exhibits antineoplastic activity against a relatively broad spectrum of human cancers. Consequently, there is considerable interest in understanding the mechanism of action which underlies the oncostatic specificity of cyclophosphamide.[1] Rationally designed test compounds should provide indirect evidence concerning the mechanism of action of CP. In addition, it is possible that such studies could lead to the synthesis of new compounds with anti-cancer activity superior to that of CP. These investigations have been greatly assisted by single-crystal x-ray structure determinations of CP, CP metabolites, and CP analogs.[2]

A new drug-design strategy which is based on the "pro-metabolite" delivery concept is being applied to the CP system. The application of the pro-metabolite delivery concept to derivatives of phosphoramide mustard has lead to the synthesis of (2). This novel anti-cancer prodrug has a

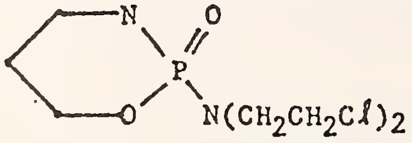
(1)

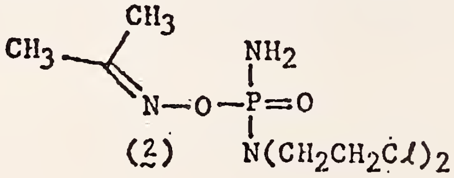
(2)

proposed mechanism of action involving enzymatic N-O bond reduction to generate the phosphoramide mustard which is the active metabolite produced from CP. The P(O)ON=C moiety common to this class of compounds has no structural precedent.

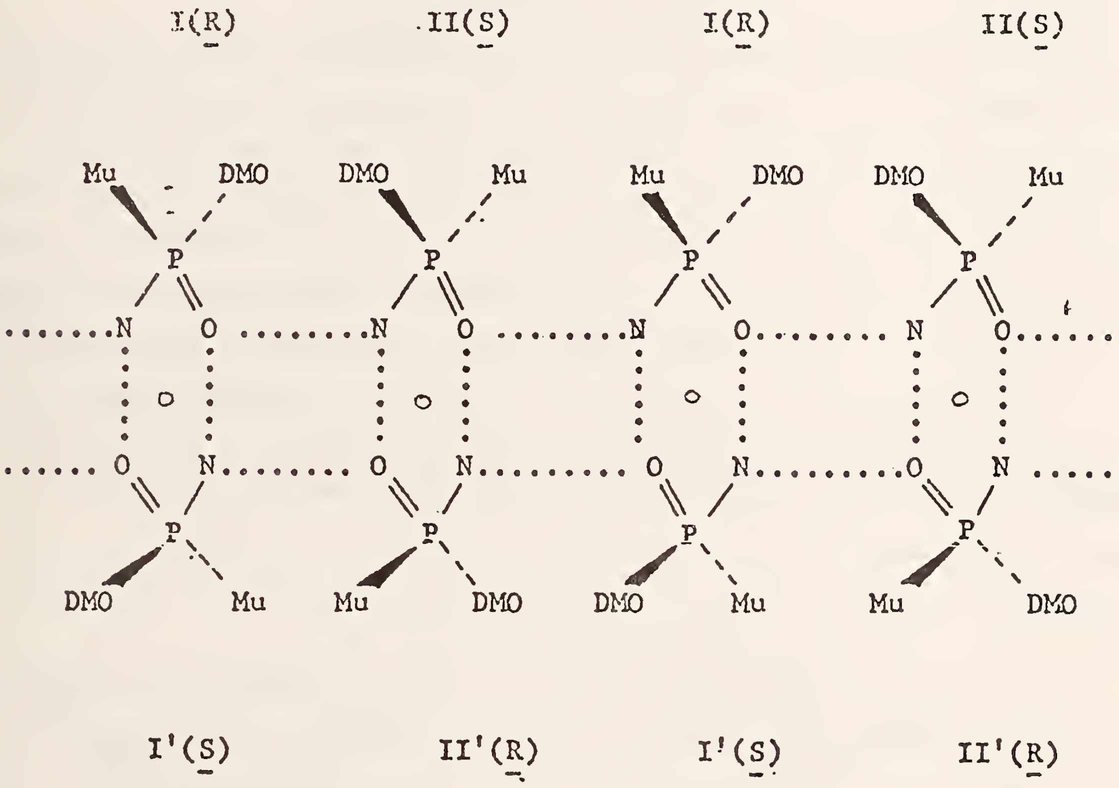

Mu = $-N(CH_2CH_2Cl)_2$

DMO = $-ON{=}C(CH_3)_2$

Figure 1. Schematic representation of the hydrogen bonding in the dimethyl oxime of phosphoramide mustard.

The dimethyl oxime of phosphoramide mustard (2), $C_7H_{16}N_3O_2PCl_2$, crystallizes in the triclinic space group $P\bar{1}$ with Z = 4, unit cell parameters a = 9.517(3), b = 10.872(3), c = 14.345(3) Å, α = 92.01(1), β = 103.66(1), γ = 115.69(1)° and d_{calc} = 1.42 g/cm^3. The structure was solved by a combination of phasing techniques. The positions of the P and

Cl atoms were determined by direct methods while successive least-squares refinements and Fourier syntheses revealed the positions of the remaining nonhydrogen atoms. Full-matrix anisotropic refinement of the model (which did not include hydrogen atoms) gave a conventional agreement factor of $R = 0.077$ for 2562 observed reflections with $I \geq 3\sigma(I)$.

There are two crystallographically independent molecules (I and II) in the asymmetric unit. Comparison of the bond distances, angles, and dihedral angles reveals that the conformations of molecules I and II are very similar. Each molecule participates in four hydrogen bonds which are almost identical in length (~ 2.94 Å). A schematic representation of the hydrogen bonding is shown in figure 1. In each molecule, the amide nitrogen atom is the donor in two hydrogen bonds while the phosphoryl oxygen atom is the acceptor in two hydrogen bonds. Molecule I is hydrogen bonded to molecule II which has the opposite absolute configuration at phosphorous. In addition, molecules I and II are each hydrogen bonded to a centrosymmetrically related molecule to form the dimers I. . .I' and II. . .II'. The hydrogen bonding in the structure is such that a ladder is formed which is parallel to the (1,1,0) direction in the unit cell.

The packing in the structure is interesting not only from the point of view of the hydrogen bonding, but also with respect to the orientations of the $-N(CH_2CH_2Cl)_2$ and $-ON=C(CH_3)_2$ moieties in the two independent molecules. Parallel to the ladder of hydrogen bonds are two rows of two chlorine atoms and four rows of alternating chlorine atoms and methyl groups from molecules I and II. The distances from the phosphorous atom to the chlorine atoms and to one methyl carbon atom are approximately equal (~ 5.0 Å) in each molecule. Thus, in terms of spatial considerations, it appears that the $-ON=C(CH_3)$ moiety has "substituted" for an $-NCH_2CH_2Cl$ moiety in the structure.

---

1. O. M. Friedman, A. Myles, and M. Colvin, "*Advances in Cancer Chemotherapy,*" 143-204 and references therein (1979).

2. G. Zon, *Progr. Med. Chem.,* in press.

STUDY OF HYDROGEN BONDS IN $Ca_2KH_7(PO_4)_4\cdot 2H_2O$

S. Takagi and M. Mathew
(American Dental Association)
and
E. Prince

The crystal structures of the isomorphous compounds $Ca_2(NH_4)H_7(PO_4)_4\cdot 2H_2O$ and $Ca_2KH_7(PO_4)_4\cdot 2H_2O$ have been determined previously from x-ray diffraction data. A unique feature of these structures is that, if the crystal is assumed to be centrosymmetric, three pairs of oxygen atoms in phosphate groups are hydrogen bonded across centers of symmetry, forming an infinite $[H_3(PO_4)_2]_n^{3-}$ sheet structure. Because x-ray diffraction data do not permit a detailed analysis of the hydrogen bond structure, a neutron diffraction study was undertaken.

The unit cell is triclinic, with cell parameters, as determined by x-rays, equal to $\underline{a} = 5.676(1)$, $\underline{b} = 12.210(2)$, $\underline{c} = 6.292(1)$ Å, $\alpha = 104.10(2)°$,

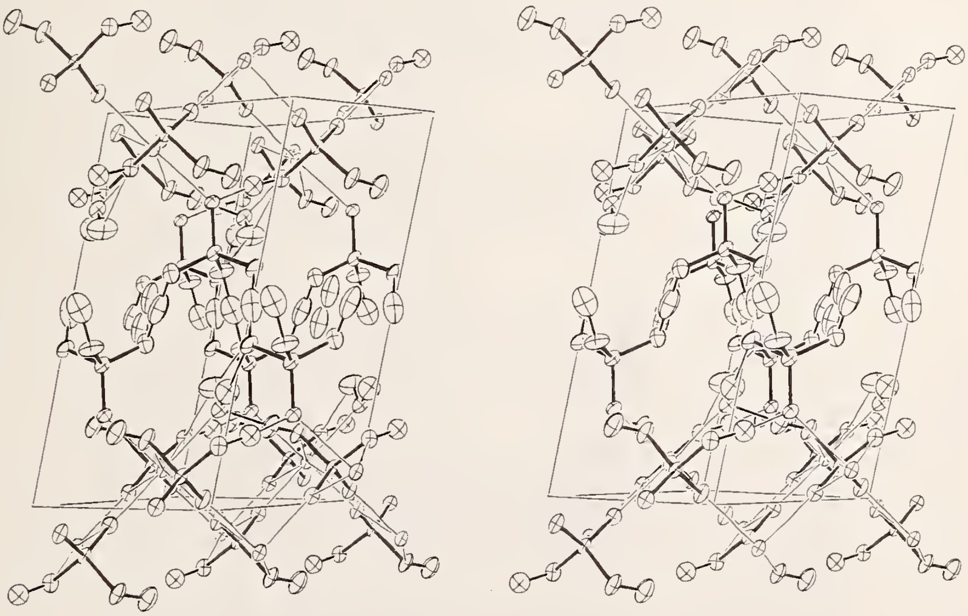

Figure 1. Stereoscopic view of the structure of $CaKH_3(PO_4)_4\cdot 2H_2O$

TABLE 1

$Ca_2KH_7(PO_4)_4 \cdot 2H_2O$ in Space Group PI

One half of a potassium atom occupies each of two disordered positions across a center of symmetry.

Atom	x	y	z	U_{11}	U_{22}	U_{33}	U_{12}	U_{13}	U_{23}
Ca	0.0008(7)	0.0990(3)	0.2983(6)	0.0085(17)	0.0235(2)	0.0089(17)	0.0041(16)	-0.0004(13)	0.0038(16)
K	0.4989(32)	0.5389(13)	-0.0131(30)	0.0172(52)	0.0974(157)	0.0279(64)	0.0002(04)	0.0073(46)	0.0035(101)
P(1)	0.1519(7)	0.6374(3)	0.3794(6)	0.0215(19)	0.0246(18)	0.0124(17)	0.0045(15)	0.0038(14)	0.0037(14)
P(2)	0.4971(6)	-0.0970(3)	0.2113(5)	0.0086(15)	0.0226(18)	0.0058(15)	0.0043(13)	-0.0012(11)	0.0023(13)
O(11)	0.1045(8)	0.5948(3)	0.1097(6)	0.0437(23)	0.0291(19)	0.0134(16)	0.0002(17)	0.0115(15)	-0.0033(14)
O(12)	0.1391(6)	0.7642(3)	0.4353(5)	0.0208(16)	0.0194(16)	0.0161(15)	0.0050(12)	0.0062(12)	0.0049(12)
O(13)	0.4214(7)	0.5982(3)	0.5381(7)	0.0226(18)	0.0239(19)	0.0355(21)	0.0057(15)	-0.0038(15)	0.0026(16)
O(14)	-0.0619(7)	0.5848(3)	0.4136(7)	0.0256(19)	0.0393(22)	0.0313(20)	0.0039(17)	0.0119(15)	0.0136(17)
O(21)	0.2447(6)	-0.0350(3)	0.1428(5)	0.0091(14)	0.0331(17)	0.0107(14)	0.0079(12)	-0.0010(11)	0.0052(13)
O(22)	0.7455(6)	-0.0326(3)	0.3187(5)	0.0109(15)	0.0275(16)	0.0132(14)	0.0015(13)	-0.0012(11)	0.0045(13)
O(23)	0.5324(7)	-0.1685(3)	0.3983(6)	0.0141(17)	0.0306(18)	0.0164(15)	0.0045(14)	0.0010(12)	0.0103(14)
O(24)	0.4649(7)	-0.1829(3)	-0.0321(6)	0.0158(18)	0.0410(21)	0.0152(15)	-0.0009(15)	0.0042(13)	-0.0076(14)
O(3)	0.1431(7)	0.2484(3)	0.1744(6)	0.0217(17)	0.0281(19)	0.0152(17)	0.0020(16)	0.0029(15)	0.0025(16)
H(23)	0.3631(12)	-0.1907(5)	0.4114(10)	0.0276(32)	0.0385(33)	0.0217(27)	-0.0028(26)	0.0019(23)	0.0068(24)
H(24)	0.6205(12)	-0.2015(6)	-0.0667(11)	0.0259(33)	0.0531(44)	0.0341(33)	0.0040(30)	0.0137(27)	-0.0017(29)
H(31)	0.0311(13)	0.2919(6)	0.0622(12)	0.0384(37)	0.0575(43)	0.0325(34)	0.0074(33)	0.0035(29)	0.0164(34)
H(32)	0.2487(16)	0.3016(6)	0.3161(13)	0.0644(49)	0.0434(39)	0.0285(37)	-0.0089(35)	-0.0066(35)	-0.0019(33)
H(11)	0.0	0.5	0.0	0.0361(58)	0.1071(110)	0.0518(67)	0.0215(65)	0.0187(50)	0.0463(77)
H(13)	0.5	0.5	0.5	0.0464(61)	0.0797(87)	0.0389(56)	-0.0184(59)	0.0042(46)	-0.0148(55)
H(14)	0.5	0.5	0.5	0.0434(58)	0.0874(87)	0.0302(51)	0.0057(57)	0.0166(44)	-0.0058(56)

TABLE 2

Selected Bond Distances and Angles in $Ca_2KH_7(PO_4)_4\ 2H_2O$, Neutron Results

Ca...O(12)	2.389(5)Å		
Ca...O(21)	2.345(5)		
Ca...O(21)	2.475(4)		
Ca...O(22)	2.323(6)		
Ca...O(22)	2.513(5)		
Ca...O(23)	2.604(14)		
Ca...O(24)	2.709(5)		
Ca...O(3)	2.477(6)		
P(1)-O(11)	1.560(5)	O(11)-P(1)-O(12)	108.6(3)
P(1)-O(12)	1.504(5)	O(11)-P(1)-O(13)	109.0(3)
P(1)-O(13)	1.534(5)	O(11)-P(1)-O(14)	107.3(3)
P(1)-O(14)	1.541(7)	O(12)-P(1)-O(13)	110.1(3)
		O(12)-P(1)-O(14)	111.5(3)
		O(13)-P(1)-O(14)	110.2(3)
P(2)-O(21)	1.492(4)	O(21)-P(2)-O(22)	119.6(3)
P(2)-O(22)	1.489(5)	O(21)-P(2)-O(23)	111.8(3)
P(2)-O(23)	1.567(6)	O(21)-P(2)-O(24)	103.0(2)
P(2)-O(24)	1.580(5)	O(22)-P(2)-O(24)	103.9(2)
		O(22)-P(2)-O(24)	111.0(3)
		O(23)-P(2)-O(24)	107.2(3)
O(23)-H(23)	1.065(9)Å	P(2)-O(23)-H(23)	118.2(4)
O(24)-H(24)	0.989(9)	P(2)-O(24)-H(24)	118.2(4)
O(3)-H(31)	0.959(8)	H(31)-O(3)-H(32)	106.3(7)
O(3)-H(32)	0.958(7)		
O(11)-H(11)	1.252(4)		
O(13)-H(13)	1.240(4)		
O(14)-H(14)	1.237(4)		

		O-H	H..O	<O-H
O(11)...O(11)	2.504	1.252(4)	1.252(4)	180
O(13)...O(13)	2.479(5)	1.240(4)	1.240(4)	180
O(14)...O(14)	2.474(6)	1.237(4)	1.237(4)	180
O(23)...O(12)	2.572(6)	1.065(9)	1.512(9)	173.0(6)
O(24)...O(3)	2.717(6)	0.989(9)	1.737(9)	170.0(5)
O(3) ...O(11)	2.799(6)	0.959(8)	1.867(9)	163.3(7)
O(3) ...O(23)	2.877(5)	0.958(7)	2.556(9)	99.7(6)
O(3) ...O(13)	2.893(5)	0.958(7)	2.073(9)	142.5(9)
O(3) ...O(14)	3.055(6)	0.958(7)	2.455(10)	120.5(8)

$\beta = 115.16(2)°$, $\gamma = 84.25(2)°$. Of 1945 reflections measured within a limiting sphere defined by a maximum 2θ of 117° and a wavelength of 1.273 Å, 1293 had intensities significantly above background. The parameters from an x-ray refinement were used as the starting point for a refinement of the structure with the neutron data in space group $P\overline{1}$. The refinement proceeded to $R = 0.073$, $R_w = 0.065$. Table 1 gives the refined parameters and table 2 gives selected bond distances and angles. Figure 1 is a stereoscopic pair giving a view of the structure. An attempt will be made to refine the structure in space group P1 to see if this gives an indication that the potassium atom and three of the hydrogen atoms that appear to occupy symmetry centers or disordered positions near them actually occupy asymmetric positions.

EFFECTS OF INTERSTITIAL ELEMENTS ON PHASE RELATIONSHIPS IN THE TITANIUM-ALUMINUM SYSTEM

R. M. Waterstrat
(American Dental Association)

and

E. Prince

The objective of this research is to determine the effect of interstitial solute elements, such as oxygen, nitrogen and carbon on the $\alpha/\alpha + \alpha_2/\alpha_2$ phase boundaries in the Ti-Al system. These influences must be adequately defined since the interstitial elements are ubiquitous contaminants in titanium alloys beginning with the initial starting material (titanium sponge) and accumulating through various stages of fabrication to the final product. Once present, they cannot be easily removed. Furthermore, some contamination of titanium alloys by these elements is virtually unavoidable since hot titanium is capable of scavenging them from an ultra high vacuum (pressures $<10^{-6}$ torr) or from the highest purity inert gases (impurity contents <5 ppm). The only practical solution to these problems of interstitial contamination

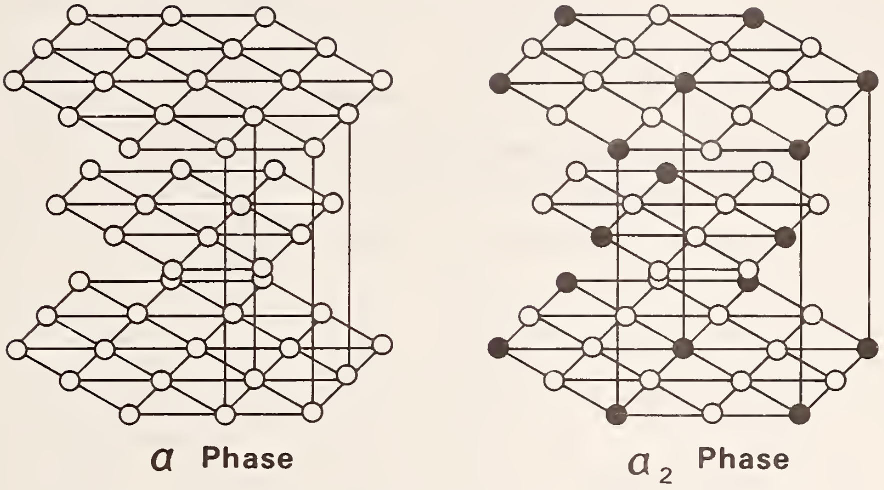

Figure 1. Schematic representation of the structures of the α phase and the α_2 phase. Open circles represent Ti atoms, dark circles represent Al atoms and grey circles represent a statistically random occupancy by both Ti and Al atoms in the ratio called for by the phase composition. Darker lines outline the respective unit cell for each structure. The α_2 phase structure actually involves slight displacements of the Ti atoms from the ideal positions shown here (see ref. 3).

is to set maximum allowable limits for it and then impose effective controls on it. This requires a knowledge of its effect on alloy properties and behavior.

It is well known that oxygen, for example, can be a source of embrittlement in titanium and its alloys. In pure titanium the mechanism of embrittlement probably involves an interaction between oxygen atoms and dislocations which tends to immobilize the dislocations and produce a ductile/brittle transition (1). In titanium-aluminum alloys, however, oxygen seems to act by promoting the formation of the brittle α_2 phase (Ti_3Al), an atomically ordered version of the more ductile α phase structure (2). There is a lack of precise information about how oxygen stabilizes the α_2 phase since phase relationships in the Ti-Al-O system have not been well defined. Attempts to determine the relevant portion of this ternary diagram have been plagued by the same experimental problems which have hindered the development of the binary Ti-Al phase diagram for so many years. The most serious of these problems are: an inability to prevent decomposition of quenched alloys, an inability to discriminate quantitatively between the α and α_2 phases in two-phase alloys, an inability to estimate the effects of coherent/incoherent interactions and persistent problems with alloy contamination at high temperatures.

The first three lines (100, 101, 110) are called "superlattice lines" since they exist only when long-range atomic ordering is present while the last three lines (200, 002, 201) are "fundamental lines" common to both ordered (α_2) and disordered (α) phases. Actual neutron diffraction patterns which we obtained from α and α_2 phases are shown in Figure 2. It is estimated that, using neutrons, less than 1% α_2 phase in a matrix of α phase would be detectable whereas, using X-rays one would be fortunate to detect 10% α_2 in α phase. The extraordinary intensities of the "superlattice lines" for neutrons result from an exceptionally large difference in neutron scattering potentials (b) for the Ti and Al sublattices relative to the average potential for a random occupancy of these sublattices. This can be calculated from the known scattering potentials for neutrons (b_{Ti}, b_{Al}) and for X-rays (f_{Ti}, f_{Al}). (The latter are proportional to the respective atomic numbers.) A unique feature of b_{Ti} and b_{Al} is that they are of equal magnitude by opposite sign. This means that Ti and Al atoms scatter the incident neutrons 180° out of phase with each other. Such phase differences do not occur with x-ray scattering.

The relative intensities seen in figure 2 are not in complete agreement with those calculated in table 1. This indicates that the sample had some preferred crystalline orientations. The (110) superlattice line seemed to be particularly affected since its intensity is about twice as strong as would be expected. However, the sample was not rotated during the experiment and proper rotation could be expected to reduce or even eliminate such orientation effects. Furthermore our samples will contain various amounts of oxygen and other interstitial elements which are known

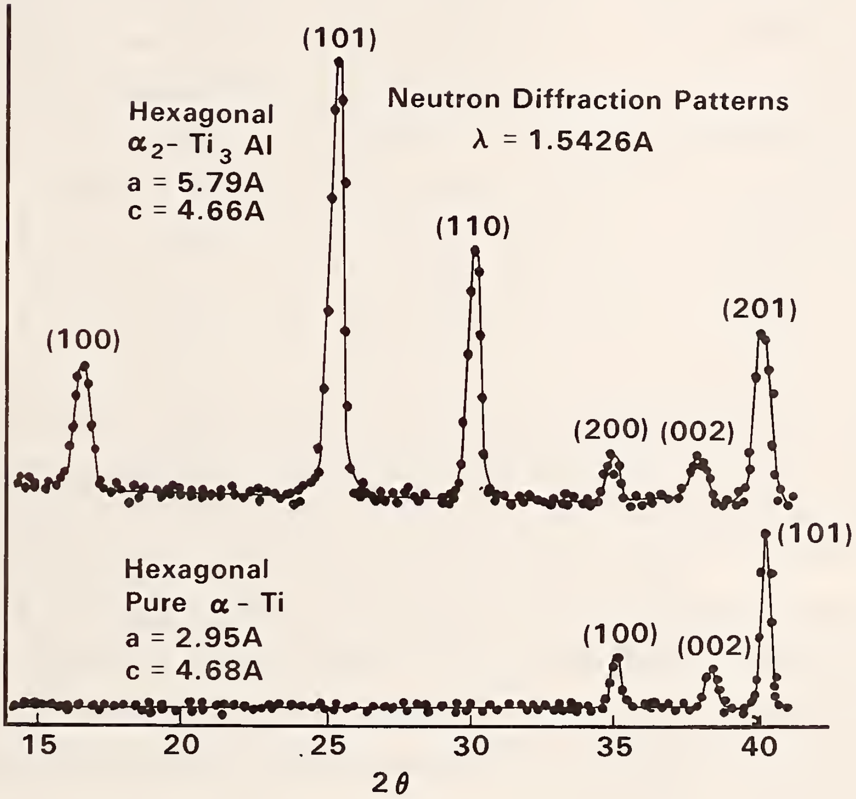

Figure 2. Neutron diffraction patterns for α phase (annealed Ti powder) and α_2 phase (annealed Ti_3 Al). Lines are identified with their Miller indices. The patterns were obtained at room temperature using unrotating samples.

to produce strong grain-size refinement in titanium alloys. This would also act to reduce grain orientation effects. Complete randomness is not essential in our studies, however, since we are more interested in detecting the presence of the α and α_2 phases rather than in measuring the precise percentages. The expected width of the two-phase ($\alpha + \alpha_2$) regions is approximately 10 at.% Al and this contributes to a high sensitivity, since a 1 at.% variation in Al content will produce approximately a 10% variation in the volume percentage of these phases. Thus the phase boundaries should be locatable with an accuracy of better than ± 1 at.%.

Table 1. Calculated Relative Intensities of Diffraction Peaks in Fully Ordered α_2 Phase (Ti_3Al) Using X-rays and Neutrons.

hkl	X-rays	neutrons
100	2	76
101	5	253
110	2	123
200	24	22
002	27	26
201	100	100

Another possible complication in our samples would be the presence of rather fine (optically unresolvable) particles in samples annealed at low temperatures (∿600°C, for example). This may produce appreciable broadening of our diffraction peaks if the particles are ∿50 Å in diameter or less. In most of our samples we expect the second phase particles to be much larger than this. However, our inherently high sensitivity will help to overcome the slight reduction caused by particle-size broadening of the diffraction lines and we do not expect this to be a serious problem.

It may be of some interest for this study to apply neutron diffraction techniques to locate oxygen atom positions in the α and α_2 phase structures. This has already been done for α phase alloys in the binary Ti-O system (14). It was found that the oxygen atoms tend to occupy octahedral interstices in this structure. They do so in a random manner at high temperatures (700°C), but an ordering of the oxygen atoms occurs in these sites at lower temperatures. The ordering is centered around the stoichiometries Ti_6O, Ti_3O, and Ti_2O. It is unlikely that exactly the same type of ordering will be found in α_2 phase (Ti_3Al) since its solubility for oxygen is lower than any of these compositions. A random occupancy of the octahedral sites by oxygen in the α_2 phase is conceivable, however, and it is noteworthy that the lattice parameters of both α and α_2 phases show a similar behavior with respect to additions of oxygen. The hexagonal (a) axis is affected our samples will contain various amounts of oxygen and other interstitial elements which are known to produce strong grain-size refinement in titanium alloys. This would also act to reduce grain orientation effects. Complete randomness is not essential in our separation during cooling at lower temperatures. Further work is needed to settle this question. Our results, however, lead us to conclude that our first samples in the α- α_2 two-phase region should be a ternary series at the 6 at.% 0 level where we will locate both the α and α_2 phase boundaries in the ternary system and can then estimate the boundaries at lower oxygen contents by extrapolating to the known binary system. Similar procedures can subsequently be followed at other oxygen levels and at various temperatures until the necessary data have been obtained.

1. Preliminary Neutron Diffraction Experiments

The α phase is a substitutional solid solution of Al in hexagonal Ti in which the Ti and Al atoms are distributed at random among the available atomic sites in the structure (Fig. 1a). The α_2 phase structure is a "superlattice" in which the Ti and Al atoms take up an ordered arrangement with respect to each other (Fig. 3b). The onset of atomic ordering will produce extra lines in the diffraction patterns for X-rays or neutrons and these will be detected the more readily as the average scattering potentials of the Ti and Al sublattices become appreciably different. This will occur, for example, as the degree of long-range atomic ordering increases. It will also occur when neutrons replace

Table II. Percent Difference in Atomic Scattering Potentials for Ti and Al Relative to the Average Potential (wieghted for composition).

X-rays	$\frac{4(f_{Ti} - f_{Al})}{3f_{Ti} + f_{Al}}$	=	$\frac{4(22 - 13)}{79}$	=	46%
Neutrons	$\frac{4(b_{Ti} + b_{Al}}{3b_{Ti} + b_{Al}}$		$\frac{4(-.34 - .35)}{-.67}$	=	412%

x-rays as the diffracting radiation since the difference in scattering potential for Ti and Al atoms is much greater using neutrons than when using x-rays. We have calculated the relative intensities to be expected for a fully ordered α_2 phase structure (Ti_3Al) with x-rays and with neutrons for the first six lines in the pattern (Table 1).
very little while the (c) axis undergoes a pronounced expansion. The oxygen solubilities in co-existing α and α_2 phases are of considerable interest since it has been postulated that a partitioning of oxygen occurs in favor of the α_2 phase which tends to stabilize this brittle constituent (2).

---

1. D. Gupta and S. Weinig, "The Dislocation-Oxygen Interaction in Alpha Titanium and its Effect on the Ductile to Brittle Transition," *Trans. Aime* 215 (1959) pp. 209-216.

2. J. Y. Lim, C. J. McMahon, Jr., D. P. Pope, and J. C. Williams, "The Effect of Oxygen on the Structure and Mechanical Behavior of Aged Ti-8 Wt. Pct. Al," *Met. Trans.* 7A (1976) pp. 139-144.

3. P. C. Gehlen, "The Crystallographic Structure of Ti_3Al," *The Science, Technology and Application of Titanium,* pp. 349-357; Pergamon Press, New York, NY 1970.

STUDIES OF ZEOLITE STRUCTURE BY NEUTRON POWDER DIFFRACTION

J. B. Parise
(E. I. duPont de Nemours and Co., Wilmington, DE)
and
E. Prince

Zeolites are a class of commercially important reactant and product selective absorbants and catalysts whose selectivity arises from the sizes and configurations of pores and channels within aluminosilicate frameworks. By choosing zeolites with specific channel sizes it is possible to select only those products that are smaller than the channel sizes. A knowledge of the sizes and configurations of the pores under the conditions at which the zeolites usually operate is crucial to an understanding of their

Table 1. Atomic parameters for dehydrated (K, Cs)-ZK5 at room temperature.

Atom	x	y	z	B($\mathring{A}^2$)
Si	0.0831(3)*	0.2021(3)	0.3208(4)	0.4(2)
O1	0.1284(2)	x	0.3156(4)	2.3(2)
O2	0.2518(3)	x	0.4082(4)	1.8(2)
O3	0.0	0.1792(4)	0.3364(4)	2.1(2)
O4	1/4	0.1080(2)	0.3920(2)	2.2(2)
Cs1	0.0	0.0	0.31	
Cs2	1/4	0	1/2	

---

*esd's in parenthesis.

chemical properties.

The structure of a typical small pore zeolite, designated ZK-5, has been studied at 25°C and 220°C using the NBS high resolution powder diffractometer. Although there is some uncertainty due to variations in framework geometry upon hydration and heating, the positions of the metal atoms (in this case Co and K) have been determined in this study. A list of refined parameters is given in table 1.

The analysis of these data sets is continuing. Further studies of ZK-5, in its hydrogen and metal exchanged forms, will help in the interpretation of adsorption data collected on small pore zeolites at du Pont. It is hoped that by studying changes of geometry with temperature in "simple" small pore zeolites we may establish a basis for predicting such changes in more complex systems.

STRUCTURE REFINEMENT OF COMPOSITIONS IN THE NASICON SOLID SOLUTION SYSTEM

L. J. Schioler and B. J. Wuensch
(Massachusetts Institute of Technology, Cambridge, MA)
and
E. Prince

Increasing interest in solid state fast ion conductors led to the discovery (Goodenough, et al. 1976) of the NASICON solid solution system, which can be represented by the formula $Na_{1+x}Zr_2Si_xP_{3-x}O_{12}$, with $0 < x < 3$. The composition with $x = 2$ was christened NASICON for NA Super Ionic CONductor. It was found to have an ionic conductivity at 300°C of 0.2 $(\text{ohm-cm})^{-1}$, which is comparable to the best beta"-alumina. NASICON has advantages over the beta aluminas in that it can be sintered to a high density at a lower temperature (1200°C as compared with 1500°C). It is insensitive to moisture, which reduces the conductivity of beta alumina, and the ion migration occurs through channels which are linked three dimensionally in the structure as opposed to beta alumina, where the ions are mobile only within planes.

The structure of the end members of this solid solution system, $NaZr_2P_3O_{12}$ ($x = 0$) and $Na_4Zr_2Si_3O_{12}$ ($x = 3$), were first determined by Hagman and Kierkegaard (1968) and Sizova et al. (1973), respectively. These were found to be rhombohedral with space group $R\bar{3}c$. The structure is based on a "lantern" shaped unit consisting of two octahedra and three tetrahedra linked at the corners. These "lantern" units form a three-dimensional framework, with the sodium ions occupying interstices. Figure 1 shows this "lantern" unit as well as a projection of the $NaZr_2P_3O_{12}$ structure on [001].

Hong (1976), in work done in conjunction with that of Goodenough et al., studied several compositions in this system using x-ray powder diffraction techniques. He found that the powder patterns of all compositions except those in the range $1.8 < x < 2.2$, could be indexed on a rhombohedral lattice (space group $R\bar{3}c$). The compositions with

$1.8 < x < 2.2$ could be indexed on a monoclinic lattice (space group C2/c, which is a subgroup of R3c). Table 1 gives the space group parameters for $R\bar{3}c$ and C2/c. Attempts to determine the structures of other compositions in the solid solution were not successful due to the inability to grow single crystals. From x-ray powder data, Hong postulated the structure parameters of the highly conducting composition NASICON ($x = 2.0$). In this monoclinic structure he assumed that the silicon and phosphorous are ordered on the 8f and 4e sites, respectively. This ordering could be one of the reasons the structure changes from rhomohedral to monoclinic and back as x increases.

Hong found a variation in lattice parameters with composition (figure 2). The a lattice parameter increases with x, while the c parameter goes through a maximum, resulting in the cell volume also exhibiting a maximum. Interestingly enough, the conductivity vs. composition plot also exhibits a maximum for a composition near where the cell volume is maximized (figure 3). The reasons for the unusual behavior of the lattice constants and the conductivity has not yet been explained. The most likely reasons for this behavior are the changes in the geometry of the framework, the size of the "bottleneck" between the sodium sites, and the concentration of the mobile sodium, all of which vary with the composition. Which of these has the greatest effect on the lattice parameters and the conductivity will remain unclear until structure refinements have been carried out on the intermediate compounds in the system.

For two reasons the information obtainable from x-ray powder diffraction techniques is not sufficient for a structure refinement to determine the causes for the unusual behavior. The main reason is that the peaks in the x-ray powder pattern are difficult to model in a profile analysis, resulting in a poor fit. The second reason is that in x-ray diffraction, the scattering is dominated by the heavy elements in the material, in the NASICON system the zirconium. These problems can be overcome by the use of neutron diffraction techniques, because the peak

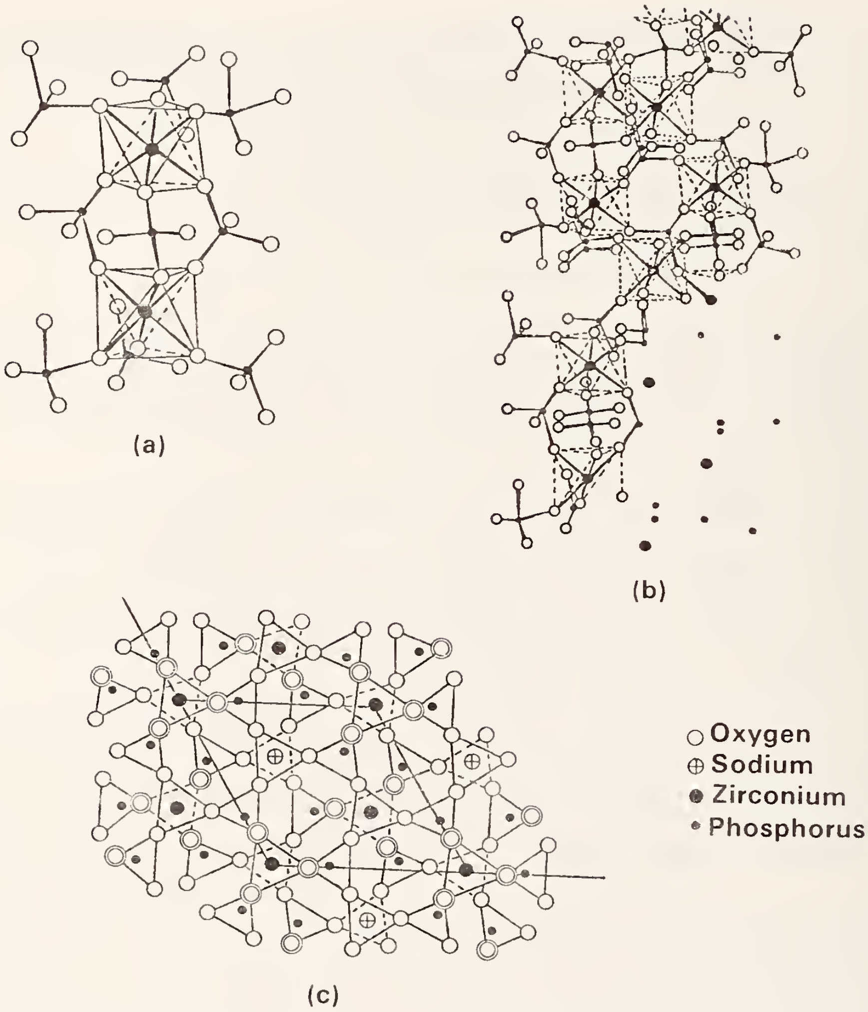

Figure 1. "Latern" unit upon which the NASICON type structure is based (upper). Projection of NaZr$_2$P$_3$O$_{12}$ an [001], after Hagman and Kierkegaard, (1968) (lower).

of a neutron powder pattern are well described by a Gaussian shape, and the scattering powers of the elements are more nearly equal.

Four samples in the NASICON solid solution system were brought to NBS for study using neutron diffraction. The compositions of the samples were selected to give structural information near critical changes in the lattice parameters. Two of the compositions selected, $x = 1.6$ and $x = 2.5$, bracket the high conductivity composition region as found by Kafalas and Cava (1979). Another composition was NASICON per se ($x = 2.0$). The last composition ($x = 1.0$) was selected to be

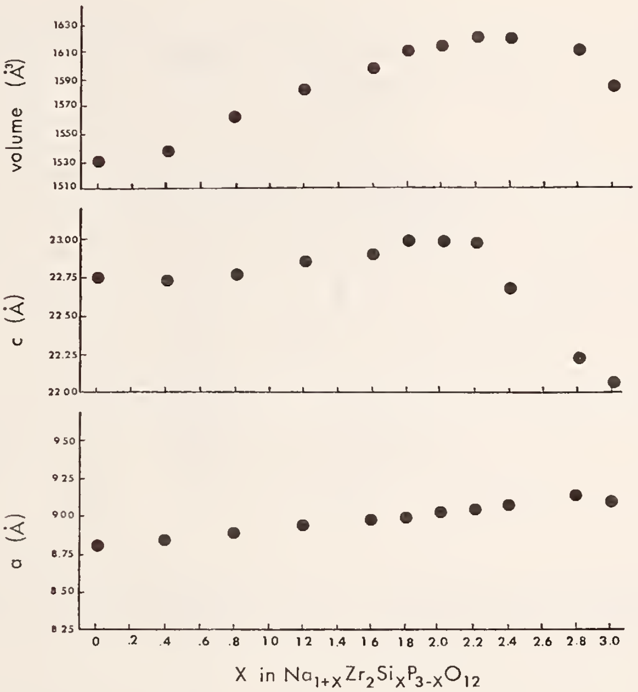

Figure 2. Variation of cell parameters with composition in the NASICON solid solution system. For $1.8 \leq x \leq 2.2$, these are the hexagonal equivalent parameters. (From Hong, 1976.)

outside the region of high conductivity. Neutron powder patterns were obtained at room temperature on the multidetector powder diffractometer. Refinements of the four patterns were carried out using the Rietveld method.

Initially the compositions with x = 1.0, 1.6, and 2.5 were refined on a rhombohedral lattice, and that with x = 2.0 on a monoclinic lattice. Refinement of the x = 1.6 sample did not give a good fit. The x-ray powder diffraction pattern of this sample was reexamined and it was noticed that the peak at 27.5 degrees 2θ, which should be a single peak if the lattice is rhombohedral, had a slight shoulder, indicating that the structure was actually monoclinic. Refinement on the monoclinic lattice proceeded smoothly. The final lattice parameters are given in table 2 and the refined structure parameters are given in table 3.

Refinement on the sodium occupancies in the four samples show that the Na(1) site (6b) in the rhombohedral structures (x = 1.0 and 2.5) is

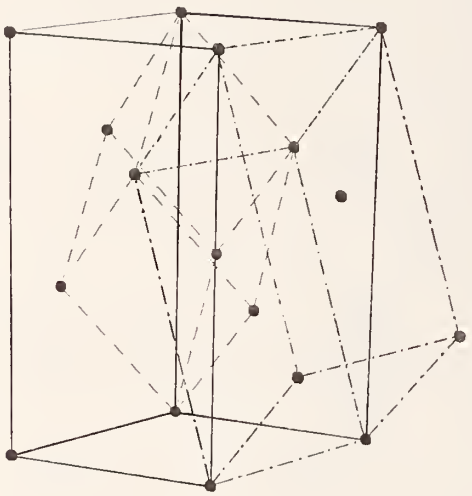

Figure 3. Variation of conductivity with composition in the NASICON solid solution system.

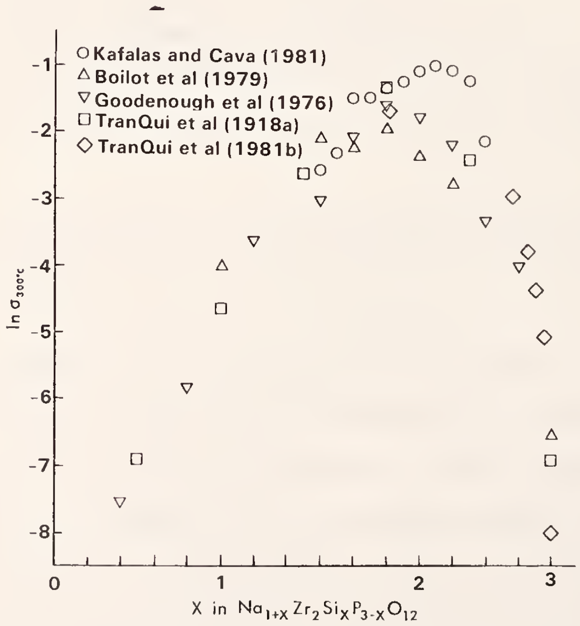

Figure 4. Relationship between the rhombohedral, hexagonal, and monoclinic cells.

Table 1. Space group parameters.

$R\bar{3}c$

Atom	Position	Point Symmetry	Equipoint 1		
Na(1)	6b	$\bar{3}$	0	0	0
Na(2)	18e	2	x	0	1/4
Zr	12c	3	0	0	z
Si/P	18e	2	x	0	1/4
O(1) & O(2)	36f	1	x	y	z

C2/c

Atom	Position	Point Symmetry	Equipoint 1		
Na(1)	4d	$\bar{1}$	1/4	1/4	1/2
Na(2)	4e	2	0	y	1/4
Na(3)	8f	1	x	y	z
Zr	8f	1	x	y	z
Si/P	8f	1	x	y	z
P/Si	4e	2	0	y	1/4
O(1) - O(6)	8f	1	x	y	z

fully occupied at room temperature, as is the equivalent Na(1) site (4d) in the monoclinic structure of the compositions with x = 1.6 and 2.0. The occupancies of the Na(2) and Na(3) sites (4e and 8f) of x = 1.6 are not random; site 4e has a greater and site 8f has a lower occupancy than would be expected for random occupancy. This is also observed in the sample with x = 2.0.

The silicon and phosphorous occupancies show a significant shift from random in the sample with x = 1.6. In this composition the occupanices of the Si in the 8f and the P in the 4e site are greater than would be expected for random occupancy of these two elements over the two sites. For x = 2.0, refinement on the occupancies indicated that for this composition the Si and P are almost completely ordered over sites 8f and 4e, respectively, thus confirming Hong's assumption of complete ordering in the ideal structure.

Table 2. Lattice parameters of compositions in the NASICON system.

Composition	A	B	C	Alpha	Beta	Gamma	Reference
Hexagonal Axes							
NZSP-0	8.815(1)		22.746(7)	90.	90.	120.	Hong (1976)
NZSP-10	8.9346(1)		22.8363(7)	90.	90.	120.	
NZSP-16	8.9954		22.9716	90.44	89.56	119.999	
NZSP-20	9.0351		22.9870	90.95	89.05	119.892	
NZSP-25	9.1115(3)		22.6513(16)	90.	90.	120.	
NZSP-30	9.1963(5)		22.181(2)	90.	90.	120.	TranQui et al. (1981)
Monoclinic Axes							
NZSP-0	15.268	8.815	9.132	90.	123.871	90.	Hong (1976)
NZSP-10	15.475	8.935	9.222	90.	124.010	90.	
NZSP-16	15.5805(9)	8.9956(5)	9.2137(5)	90.	123.795(4)	90.	
NZSP-20	15.6407(6)	9.0498(3)	9.2102(4)	90.	123.709(3)	90.	
NZSP-25	15.782	9.112	9.202	90.	124.866	90.	
NZSP-30	15.911	9.186	9.099	90.	125.653	90.	TranQui et al. (1981)

Table 3. Refined parameters.

Space Group $R\bar{3}c$ (167) $Na_2Zr_2SiP_2O_{12}$ (x = 1.0)

R Weighted = 7.70
R Expected = 5.07

Atom	Position	x	y	z	Occupancy	B_{11}	B_{22}	B_{33}	B_{12}	B_{13}	B_{23}
Na(1)	6b	0	0	0	.167(5)	21.0(18)	B11	3.0(11)	1/2 B11	0	0
Na(2)	18c	.642(2)	0	1/4	.166(5)	-.5(6)	2.0(10)	14.9(26)	1/2 B22	1/2 B23	-.8(11)
Zr	12c	0	0	.1468(2)	.3333	.66(8)	.66(8)	.60(16)	1/2 B11	0	0
Si	18e	.2915(4)	0	1/4	.1667	1.17(16)	.6(2)	1.6(2)	1/2 B22	1/2 B23	.59(57)
P	18e				.3333						
O(1)	36f	.1787(4)	-.0252(4)	.1950(1)	1.0	2.3(2)	2.8(2)	2.5(2)	1.8(1)	-1.0(2)	.26(14)
O(2)	36f	.1931(4)	.1706(3)	.0892(1)	1.0	1.6(2)	1.0(1)	1.8(1)	.4(1)	.4(1)	.5(1)

Space Group C^2/c (15) $Na_{2.6}Zr_2Si_{1.6}P_{1.4}O_{12}$

R Weighted = 6.45
R Expected = 5.20

Atom	Position	x	y	z	Occupancy	B_{11}	B_{22}	B_{33}	B_{12}	B_{13}	B_{23}
Na(1)	4d	1/4	1/4	1/2	.5	51.7(78)	12.9(55)	10.5(25)	9.5(69)	4.7(38)	-9.0(42)
Na(2)	4e	0	.398(2)	1/4	.406(15)	2.4(11)	1.2(10)	15.7(26)	0	4.1(14)	0
Na(3)	8f	.833(2)	.076(4)	.797(4)	.393(15)	2.0(23)	2.7(19)	4.6(16)	-3.2(16)	1.4(17)	2.8(15)
Zr	8f	.1011(4)	.253(1)	.0571(6)	1.0	1.0(2)	.6(2)	2.8(2)	-1.4(3)	1.8(2)	-.8(3)
Si(1)	8f	.3622(9)	.102(1)	.263(2)	.60(7)	3.5(6)	1.6(6)	3.0(6)	1.5(5)	1.8(6)	1.0(4)
P(1)					.40(7)						
Si(2)	4e	0	.039(2)	1/4	.20(7)	3.2(8)	1.3(9)	.7(7)	0	.6(6)	0
P(2)					.30(7)						
O(1)	8f	.1493(9)	.436(1)	.222(1)	1.0	3.1(5)	1.6(5)	.05(54)	-.2(5)	.2(5)	-1.2(4)
O(2)	8f	.4335(8)	.446(1)	.083(1)	1.0	3.8(4)	2.4(5)	.6(4)	-.5(4)	1.6(4)	.1(3)
O(3)	8f	.2560(7)	.183(1)	.217(1)	1.0	2.1(5)	.3(4)	2.0(4)	-.2(4)	.6(3)	-.7(3)
O(4)	8f	.4504(7)	.183(1)	.433(1)	1.0	1.6(4)	3.7(5)	2.2(4)	-1.3(4)	1.6(4)	-1.0(4)
O(5)	8f	.3726(7)	.1361(1)	.106(1)	1.0	3.4(4)	1.5(5)	3.5(5)	-1.5(4)	3.1(4)	.05(36)
O(6)	8f	.0789(7)	.146(1)	.238(1)	1.0	2.3(4)	.1(4)	1.2(4)	-.6(3)	1.2(3)	-1.2(3)

Table 3. (Continued).

Space Group C^2/c (15) $Na_3Zr_2Si_2PO_{12}$

R Weighted = 6.24
R Expected = 5.23

Atom	Position	x	y	z	Occupancy	B_{11}	B_{22}	B_{33}	B_{12}	B_{13}	B_{23}
Na(1)	4d	1/4	1/4	1/2	.5	53.(8)	71.(10)	27.(5)	55.(6)	-22.(4)	-41.(6)
Na(2)	4e	0	.398(2)	1/4	.37(1)	4.(1)	-2.5(7)	5.(1)	0	5.(1)	0
Na(3)	8f	.822(2)	.054(4)	.759(8)	.63(1)	4.(2)	28.(3)	65.(5)	14.(1)	21.(2)	44.(4)
Zr	8f	.0999(4)	.249(1)	.0556(6)	1.0	1.1(2)	1.1(2)	1.0(2)	-2.0(2)	.8(1)	-.8(2)
Si(1) P(1)	8f	.3650(7)	.107(1)	.268(1)	.87(6) .13(6)	1.5(4)	-2.0(4)	1.0(5)	3.(3)	-.9(3)	.9(3)
Si(2) P(2)	4e	0	.048(2)	1/4	.13(6) .37(6)	5.2(8)	3.3(8)	4.5(8)	0	2.3(8)	0
O(1)	8f	.1449(7)	.4364(9)	.2176(9)	1.0	2.8(5)	1.2(4)	1.1(4)	.1(4)	.9(3)	-.1(3)
O(2)	8f	.4352(6)	.443(1)	.081(1)	1.0	.9(3)	1.9(4)	2.6(4)	-1.0(3)	.1(3)	-1.4(3)
O(3)	8f	.2536(6)	.1840(9)	.212(1)	1.0	-.1(4)	2.5(4)	1.5(4)	-.2(3)	-1.4(3)	.4(3)
O(4)	8f	.4499(6)	.1827(9)	.439(1)	1.0	1.7(4)	3.2(4)	.7(4)	-.9(4)	1.1(3)	-1.0(3)
O(5)	8f	.3776(7)	.134(1)	.113(1)	1.0	5.1(6)	2.1(5)	2.6(5)	-.7(4)	3.5(5)	.7(4)
O(6)	8f	.0824(5)	.1431(9)	.2415(9)	1.0	-.2(4)	1.6(4)	1.5(3)	.9(3)	.5(3)	-.4(2)

Space Group $R\bar{3}c$ (167) $Na_{3.5}Zr_2Si_{2.5}P_{0.5}O_{12}$

R Weighted = 8.38
R Expected = 5.09

Atom	Position	x	y	z	Occupancy	B_{11}	B_{22}	B_{33}	B_{12}	B_{13}	B_{23}
Na(1)	6b	0	0	0	.164(5)	22.3(32)	B11	7.9(26)	1/2 B11	0	0
Na(2)	18e	.634(1)	0	1/4	.419(5)	.3(4)	.9(6)	10.0(11)	1/2 B22	1/2 B23	1.9(6)
Zr	12c	0	0	.1478(2)	.3333	.1(1)	B11	1.8(3)	1/2 B11	0	0
Si P	18e	.292(1)	0	1/4	.4167 .0833	3.9(4)	1.4(4)	2.7(5)	1/2 B22	1/2 B23	1.2(4)
O(1)	36f	.1787(5)	-.0266(5)	.1935(2)	1.0	2.2(2)	1.5(2)	4.4(3)	1.1(2)	-2.2(2)	-.1(2)
O(2)	36f	.1916(5)	.1667(5)	.0896(2)	1.0	.4(2)	.6(2)	3.0(2)	.04(18)	.5(2)	.6(2)

The framework does change as the composition changes across the solid solution range. The sizes and distortions of the tetrahedra change as x changes. In the rhombohedral structure the tetrahedra are fairly regular, and are larger in the structure with x = 2.5 than in the structure with x = 1.0, as would be expected when the larger Si^{+4} is substituted for the P^{+5}. In the monoclinic structure there are two types of tetrahedron: one with the central atom in site 4e and one with the central atom in site 8f. The tetrahedron with the central atom in site 4e has a larger range of bond distances and angles than the tetrahedron in the rhombohedral structure, but is less distorted than the second type of tetrahedron in the monoclinic structure. The other changes in the framework and the size of the "bottlenecks" between sodium sites remain for further analysis of the refinement on these structures.

---

1. J. B. Goodenough, H. Y. P. Hong, and J. A. Kafalas, "Fast Na^+-Ion Transport in Skeleton Structures," *Mat. Res. Bull.* 11, 203-220.

2. L. O. Hagman and P. Kierkegaard, "The Crystal Structure of $NaMe^{IV}(PO_4)_3$; Me^{IV} = Ge, Ti, Zr," *Acta. Chem. Scand.* 22, 1822-1832 (1968).

3. R. G. Sizova, A. A. Voronkov, R. G. Shumyatskaya, V. V. Ilyukhin, and N. V. Belov, "Crystal Structure of $Na_4Zr_2(SiO_4)_3$," *Sov. Phys. Dokl.* 17. 718-620 (1973).

4. H. Y. P. Hong, "Crystal Structures and Crystal Chemistry in the System $Na_{1+x}Zr_2Si_xP_{3-x}O_{12}$," *Mat. Res. Bull.* 11, 173-182 (1976).

5. J. A. Kafalas and R. J. Cava, "Effects of Pressure and Composition on Fast Na^+-Ion Conductivity in the System $Na_{1+x}Zr_2Si_xP_{3-x}O_{12}$," *Fast Ion Transport in Solids*, (P. Vashista, J. N. Mundy, and G. K. Shenoy, eds.) Elsevier North-Holland, Inc. NY, 419-422 (1979).

THE STRUCTURE OF AMMONIUM PARATUNGSTATE TETRAHYDRATE

H. T. Evans
(U. S. Geological Survey, Reston, VA)
and
E. Prince

Ammonium paratungstate tetrahydrate is a "heteropoly" tungstate salt in which the hetero atom is hydrogen. An x-ray structure study by D'Amour and Allmann (1972) established the structure of the heteropoly anion, which has the composition $H_2W_{12}O_{42}$, except for the hydrogen positions. It also located the nitrogen atoms of the ammonium groups and the oxygen atoms of the water molecules, but, because the x-ray diffraction intensities are dominated by the tungsten, no hydrogen atoms could be located. A neutron diffraction study was undertaken to determine the positions of the hydrogen atoms, of which there are 25 out of a total of 59 atoms in the asymmetric unit.

Ammonium paratungstate tetrahydrate, $(NH_4)_{10}H_2W_{12}O_{42}\cdot 4H_2O$, crystallizes in the monoclinic system, space group $P2_1/n$, cell constants $\underline{a}$ = 15.079(2) Å, $\underline{b}$ = 14.450(2) Å, $\underline{c}$ = 10.968(1) Å, β = 109.24(1)°, with two formula units in the unit cell. Data were collected on the four-circle neutron diffractometer from a crystal with approximate dimensions 3.0 x 2.0 x 1.3 mm. Because of the large unit cell and the large amount of hydrogen in the crystal an unusually small number of the accessible Bragg reflections had observable intensities. Of 5256 unique reflections measured within the limiting sphere defined by a 2θ of 120° and a wavelength of 1.273 Å, only 1553 had observable intensities. The structure parameters for the non-hydrogen atoms reported by D'Amour and Allmann were used to determine phases to compute an F_o Fourier density map. Seventeen of the twenty-five hydrogen atoms in the asymmetric unit were easily located in this density map and their positions were used to determine phases for a second map. Six, and possibly a seventh, of the remaining hydrogen atoms were located on this new map, so that the positions of all hydrogen atoms except those on one of the water molecules were determined. The structure was

TABLE 1

Preliminary Atom Parameters for Ammonium Paratungstate Tetrahydrate, $(NH_4)_{10}H_2W_{12}O_{42} \cdot 4H_2O$

Atom	x	y	z	β_{11}	β_{22}	β_{33}	β_{12}	β_{13}	β_{23}
W(1)	−0.01178	−0.04690	0.24291	0.00062	0.00139	0.00369	0.00207	0.00346	0.00037
W(2)	−0.00860	0.18429	0.22514	0.00236	0.00200	0.00620	−0.00057	−0.00335	0.00074
W(3)	0.16800	0.05842	0.18737	−0.00072	−0.00069	0.01383	−0.00031	0.00109	−0.00275
W(4)	−0.06330	−0.26198	0.03800	0.00099	0.00131	0.01006	−0.00039	0.00143	0.00062
W(5)	−0.24351	0.07880	0.05292	0.00145	0.00410	0.00155	0.00007	−0.00066	−0.00094
W(6)	−0.24545	−0.14812	0.07361	−0.00087	0.00095	0.00153	−0.00062	0.00104	−0.00108
O(1)	0.11996	−0.01453	0.30302	0.00085	0.00077	0.00074	0.00056	−0.00013	−0.00075
O(2)	−0.02396	0.08317	0.31617	0.00187	0.00153	0.00431	−0.00020	0.00175	0.00178
O(3)	0.12256	0.16646	0.27693	0.00075	0.00395	0.00030	−0.00086	−0.00058	0.00083
O(4)	−0.02235	−0.11105	0.37411	0.00259	−0.00052	0.00817	−0.00002	0.00396	0.00034
O(5)	0.28615	0.07314	0.29660	0.00084	0.00113	0.00392	−0.00089	−0.00007	0.00070
O(6)	−0.02993	0.27236	0.31969	0.00175	0.00514	0.00717	0.00111	−0.00013	−0.00566
O(7)	0.01135	0.05988	0.10558	0.00138	0.00232	0.00445	0.00038	−0.00038	−0.00330
O(8)	0.00775	−0.13608	0.13035	0.00162	0.00007	0.00186	−0.00043	0.00049	0.00094
O(9)	−0.13925	−0.03156	0.14890	0.00388	0.00160	−0.00006	0.00000	0.00078	−0.00099
O(10)	−0.14202	0.15863	0.10945	0.00115	0.00096	0.00803	−0.00075	0.00196	−0.00089
O(11)	−0.00394	0.24314	0.07146	0.00128	0.00283	0.00516	0.00150	0.00177	0.00108
O(12)	0.16805	0.14763	0.06328	0.00269	0.00010	0.00345	−0.00057	−0.00052	0.00192

TABLE 1 (cont.)

Atom	x	y	z	β_{11}	β_{22}	β_{33}	β_{12}	β_{13}	β_{23}
O(13)	0.17480	-0.03781	0.09216	0.00269	0.00083	0.00733	-0.00052	0.00431	-0.00238
O(14)	-0.14683	-0.22883	0.15191	0.00172	0.00024	0.00111	0.00123	-0.00247	0.00015
O(15)	0.30580	0.03802	0.01437	-0.00032	0.00177	0.00655	-0.00094	0.00122	0.00126
O(16)	-0.28954	0.08483	0.18576	0.00072	0.00481	0.00230	0.00116	0.00091	0.00050
O(17)	0.31968	-0.15138	0.06429	0.00251	0.00238	0.00451	0.00013	-0.00148	0.00173
O(18)	0.01470	-0.32591	0.16413	0.00336	0.00164	0.00367	0.00051	0.00025	0.00262
O(19)	0.14649	0.34758	0.04752	0.00356	0.00140	0.00163	-0.00033	0.00114	-0.00066
O(20)	-0.27797	-0.13505	0.21408	0.00297	0.00274	0.00521	-0.00101	0.00260	0.00261
O(21)	0.33425	0.22580	0.01858	0.00617	0.00068	0.00130	-0.00137	0.00049	-0.00085
N(1)	0.06986	0.45709	0.21308	0.00425	0.00420	0.00486	0.00044	-0.00133	0.00107
N(2)	0.33435	0.40970	-0.06717	0.00288	0.00402	0.00654	0.00210	0.00119	0.00258
N(3)	-0.23294	0.33260	0.03338	0.00910	0.00253	0.01014	0.00078	0.00453	0.00071
N(4)	-0.46279	0.19801	0.09452	0.00452	0.00376	0.00611	-0.00197	-0.00145	0.00185
N(5)	0.30321	0.28376	0.26991	0.00239	0.00214	0.00771	0.00056	0.00301	0.00236
OW(1)	0.13229	0.49909	-0.11998	4.28933	0.00000	0.00000	0.00000	0.00000	0.00000
OW(2)	-0.45368	-0.03295	0.11413	6.17735	0.00000	0.00000	0.00000	0.00000	0.00000
H(1)	-0.02281	0.06795	0.01442	0.00164	0.00559	0.00469	-0.00014	0.00283	-0.00517
H(11)	-0.00033	0.45495	0.17925	0.00486	0.00867	0.01706	0.00119	0.00326	-0.00396
H(12)	0.09289	0.42781	0.30052	0.00126	0.03366	0.01804	0.00726	-0.00240	-0.00284

TABLE 1 (cont.)

Atom	x	y	z	β_{11}	β_{22}	β_{33}	β_{12}	β_{13}	β_{23}
H(13)	0.09128	0.52295	0.21948	0.01084	0.01593	0.01401	0.00135	-0.00355	-0.01863
H(14)	0.09560	0.42265	0.15306	0.00325	0.00808	0.01004	0.00031	0.00002	-0.00669
H(21)	0.34492	0.45289	0.00752	0.01181	0.00731	0.00684	0.00940	0.00043	-0.00182
H(22)	0.27167	0.42258	-0.13305	0.00453	0.00582	0.00662	-0.00074	0.00426	-0.00625
H(23)	0.38469	0.41896	-0.10676	0.00085	0.00484	0.01339	-0.00072	-0.00076	-0.00078
H(24)	0.33612	0.34437	-0.03639	0.01395	0.00583	0.03274	0.00863	0.01882	0.01059
H(31)	-0.21199	0.39726	0.02511	0.00811	0.00291	0.01833	-0.00102	-0.00214	0.00563
H(32)	-0.18257	0.28816	0.03150	0.00646	0.00698	0.01005	0.00253	0.00430	-0.00239
H(33)	-0.24559	0.32602	0.11691	0.00960	0.00449	0.00433	0.00050	-0.00274	0.00137
H(34)	-0.29161	0.31896	-0.04000	0.00296	0.01082	0.00428	-0.00019	-0.00422	0.00404
H(41)	-0.40170	0.16602	0.13796	0.01780	0.01781	0.01586	0.01785	0.00804	0.01232
H(42)	-0.50951	0.17932	0.13682	0.04416	0.00428	0.02843	0.01108	0.03591	0.01017
H(43)	-0.45324	0.26653	0.10206	0.01330	0.00668	0.05860	-0.00707	0.02604	-0.01843
H(44)	-0.48670	0.18017	0.00124	0.00856	0.00964	0.00408	-0.00382	0.00880	-0.00800
H(51)	0.33825	0.22404	0.27844	0.01248	0.00092	0.02753	0.00273	0.00674	-0.00069
H(52)	0.25820	0.27991	0.31932	0.00920	0.01123	0.04248	-0.00023	0.01877	0.01299
H(53)	0.34866	0.33534	0.30513	0.00704	0.02361	-0.00245	0.00516	-0.00256	-0.00756
H(54)	0.26773	0.29575	0.17675	0.02737	0.00324	0.00543	-0.00589	-0.00001	-0.00053
HW(11)	-0.35476	0.01947	0.28996	8.07190	0.00000	0.00000	0.00000	0.00000	0.00000
HW(12)	-0.36559	0.04721	0.42028	6.01987	0.00000	0.00000	0.00000	0.00000	0.00000
HW(21)	-0.07596	0.47158	0.38839	9.20383	0.00000	0.00000	0.00000	0.00000	0.00000
HW(22)	0.02074	0.50010	0.40123	37.67000	0.00000	0.00000	0.00000	0.00000	0.00000

refined by conventional methods to a weighted R of 12.8%. The relatively poor fit is probably due to large curvilinear thermal motions, and a constrained, rigid body model will therefore be used in further refinement. table 1 gives preliminary values for the atom parameters.

---

1. D'Amour, H. and Allmann, R., Z. *Krist* 136, 23-47 (1972).

THE STRUCTURES OF LITHIUM-INSERTED METAL OXIDES: $LiReO_3$ AND Li_2ReO_3

R. J. Cava, D. W. Murphy, and S. Zahurak
(Bell Laboratories, Murray Hill, NJ)

and

A. Santoro

and

R. S. Roth
(National Measurement Laboratory)

There has been significant interest in recent years in materials which undergo topotactic insertion of lithium because of their potential use as electrode materials in secondary batteries. Lithium is ionic in these compounds, and the charge is compensated by a reduction of the host cations (chalcogen-chalcogen bonds may be reduced in some compounds). Host structures may be of the layer or framework type. In the layer type, the Li^+ ions are accommodated in the van der Waals gap between layers, and in framework structures, Li^+ions occupy formerly vacant cations sites. ReO_3 and shear structures related to it are suitable hosts for lithium, with stoichiometries (5) $0.0 \leq x \leq 0.35$, $x = 1.0$, and $1.8 \leq 2.0$. Structural characterization of insertion compounds has lagged far behind the preparation of new compounds due to the unavailability of single srystals for standard crystallographic structure analysis. Lithium insertion inevitably involves significant changes in structural dimensions which pulverize starting materials. Neutron diffraction powder profile analysis is the best

TABLE 1

Atom	Position	x	y	z	B (λ^2)
Re	6a	0	0	0	0.18(6)
Li	6a	0	0	0.273(1)	1.6(3)
O	18b	-0.3801(7)	0.012(1)	0.2460(9)	0.27(6)

m = 1.5(12, R_N = 5.66, R_P = 5.55, R_W = 7.04, R_E = 5.00. Space group R3c, Z = 6. Number of observations: 2464. Number of independent Bragg reflections: 49.

Atom	Position	x	y	z	B (λ^2)
Re	6a	0	0	0	0.21(6)
Li1	6a	0	0	0.312(1)	1.4(3)
Li2	6a	0	0	0.169(1)	1.4(3)
O	18b	-0.3580(9)	-0.008(2)	0.2551(8)	0.21(6)

m = 3(12), R_N = 8.5, R_P = 7.58, R_W = 9.77, R_E - 7.71. Space group: R3c, Z = 6. Number of observations: 2505. Number of independent Bragg reflections: 65.

technique for structure determination, as it requires only a polycrystalline, powdered sample, and is more sensitive than x-ray diffraction in the characterization of light atoms such as Li in structures which contain atoms of higher atomic number.

Neutron diffraction measurements were performed on a powder diffractometer at the NBS Reactor. The samples were loaded into 1-cm-diameter vanadium cans sealed with wax to avoid decomposition of the compounds, which are air sensitive.

The powder profile refinement was performed with the Rietveld method adapted to the five-detector diffractometer design and modified to allow the refinement of background intensity. In the course of this analysis, it became apparent that the peaks produced by samples of the two compounds did not conform to a Gaussian distribution. This effect cannot be attributed to instrumental factors, since the diffractometer, used with identical conditions and with standard materials such as Al_2O_3, gives Gaussian diffraction lines over the entire 2Θ angular range within very good approximation (X between 1.1 and 1.2, by fitting single peaks). The program was then further modified to describe the line profiles with the Pearson Type VII distribution, which allows the lineshape to be changed continuously from Gaussian to Lorentzian through one additional profile parameter.

Atomic positions and thermal parameters for the $LiReO_3$ and Li_2ReO_3 structure are presented in Table 1.

There is a close relationship between the structures of ReO_3, and Li_2ReO_3. The ReO_3 host lattice in the lithium-inserted phases can be derived from that of ReO_3 by a rotation of approximately 60° about a cubic (111) direction, with the shared corners of the ReO_6 octahedra acting as hinges. No bonds are broken. For a rotation of exactly 60°, the transformation is from a 3/4 CCP and HCP. The resulting phases have rhombohedral symmetry, with the cubic (111) rotation axis becoming the hexagonal c axis.

The twist in the ReO_3 host lattice occurs to accommodate the coordination preferred by the Li ions, and is possible because of the exclusive corner sharing. In ReO_3 the cavity is a cubo-octahedron, and the center is 12-coordinated. The (111) twist converts the 12-coordinate cavity into two 6-coordinate (octahedral) cavities sharing faces. The volume per formula unit decreases in going from ReO_3 to $Li_{0.35}ReO_3$, stays approximately the same on further lithium insertion and twisting to the rhombohedral cell, and then increases on further Li insertion so that the volume of Li_2ReO_3 is approximately equal to that of

ReO_3. These volume changes reflect both the increased packing density of the anion array and the changes in the sizes of the cation coordination polyhedra.

Compounds which have been observed to undergo twists of the type described here are relatively few. In addition to the present examples, compounds of stoichiometry $M^{II}M^{IV}F_6$ (ordered ReO_3 type) have been observed to undergo cubic-to-hexagonal transitions, and $LiNbO_3$ and $LiTaO_3$ (rhombohedral) have been observed to become cubic on ion exchange of hydrogen for lithium.

NEUTRON PROFILE REFINEMENT OF THE STRUCTURES OF Li_2SnO_3 AND Li_2ZrO_3

J. L. Hodeau and M. Marenzo
(CNRS, Grenoble, Cedex, France)

and

A. Santoro and R. S. Roth
(National Measurement Laboratory)

Compounds of the type Li_2BO_3 (B Ti, Mo, Pd, etc.) are of interest as possible Li^+ ion conductors if nonstoichiometry can be introduced into their structures. Li_2SnO_3 and Li_2ZrO_3 are important representatives of this class of compounds.

The specimens of Li_2SnO_3 and Li_2ZrO_3 were prepared for neutron diffraction examination by mixing and grinding together the appropriate quantities of Li_2CO_3 and the corresponding oxides to give a final 30-g batch. All materials were of commercial grade and were designated chemically pure. The mixtures were first calcined at 700°C for 24 hr to obtain preliminary reaction and to release most of the CO_2, then reground and reheated repeatedly, first at 1000°C for 16 hr and then at 1400°C for several hours in a tightly covered Pt crucible. After each hour at 1400°C, the material was removed from the furnace and a portion was examined by x-ray diffraction to determine crystallinity and the degree of combination.[1] When all of the peaks of the oxide and/or other phases had disappeared and the diffraction peaks of the desired phase were strong and sharp with distinct α_1-α_2 doublets at 30-40° 2θ, the specimens were deemed ready for final study.

Neutron diffraction data were collected for both compounds, at room temperature with a five-detector diffractometer at the National Bureau of Standards Reactor. The neutron intensities were analyzed with the Rietveld method, modified by Prince to simultaneously process the data from the five counters of the diffractometer. The background was assumed to be a straight line of finite slope and was refined for each of the five channels of the diffractometer together with the profile and structural parameters. The results of the refinements are shown in Tables 1 and 2.

The structural arrangement of Li_2ZrO_3 and Li_2SnO_3 is NaCl-like. In both compounds, therefore, the oxygen atoms form a distorted cubic close-packed network, and the cations occupy, in an ordered fashion, all octahedral site present in this network. The distribution of the lithium also form a cubic close-packed network. The distribution of the lithium and of the tetravalent cations is different in the two compounds, and for this reason, these cannot be considered isostructural.

In the structure of Li_2SnO_3 there exist two types of layers, one composed of lithium-occupied octahedra only and the other composed of lithium- and tin-occupied octahedra in a 1:2 ratio, stacked alternately along the perpendicular to the ab plane. The cations of the mixed layers are ordered in such a way that they form hexagonal close-packed planes in which the tin atoms occupy the vertices of the hexagons and the lithium atoms the centers. A given layer repeats every six levels, namely, after a double cubic close-packed AB'CA'BC' (where B'A'C' refer to lithium-occupied octahedron layers).

In the structure of Li_2ZrO_3, all the layers parallel to the ab monoclinic plane have the same cation distribution: namely, they are composed of lithium- and zirconium-occupied octahedra in a 2:1 ratio. The cations belonging to one octahedral layer form hexagonal close-packed

TABLE 1

Results of the Profile Refinement of the Structure of Li_2SnO_3

Atom	Position	x	y	z	B (λ^2)	Multiplicity
Sn(1)	4e2	0	0.418(1)	1/4	0.2	0.5
Sn(2)	4e2	0	0.750(1)	1/4	0.2	0.5
O(1)	8f1	0.1387(7)	0.2610(7)	0.1339(3)	0.48(8)	1.0
O(2)	8f1	0.1118(6)	0.5853(7)	0.1340(2)	0.19(6)	1.0
O(3)	8f1	0.1343(6)	0.9078(7)	0.1322(3)	0.15(6)	1.0
Li(1)	8f1	0.231(2)	0.073(1)	-0.0006(7)	1.5	1.0
Li(2)	4d1	1/4	1/4	1/2	1.5	0.41(1)
Li(3)	4c2	0	0.083(6)	1/4	1.5	0.394(8)

Note: R=5.27, R_N=6.68, R_W=8.67, R_E=6.73. Space group C2/c, Z=8.a=5.2889(2), b=9.1872(3), c=10.0270(3) A, β=100.348(2)°. Number of observations:3272. Number of independent Bragg reflections:358.

TABLE 2

Results of the Profile Refinement of the Structure of Li_2ZrO_3

Atom	Position	x	y	z	B (λ^2)	Multiplicity
Zr	4e2	0	0.0916(5)	1/2	0.16(5)	0.5
O(1)	4d1	1/4	1/4	1/4	0.40(5)	0.5
O(2)	8f1	0.2721(4)	0.5754(3)	0.4863(4)	0.31(4)	1.0
Li(1)	4e2	0	0.423(2)	1/4	1.4(3)	0.45(1)
Li(2)	4e2	0	0.742(2)	1/4	1.1(3)	0.46(1)

Note: R=5.01, R_N=6.35, R_W=8.82, R_E=5.09. Space group C2/c, Z=4, a=5.4218(2), b=9.021614, c=5.4187(2) Å, β=112.709(2). Number of observations: 2505. Number of independent Bragg reflections: 186.

planes as in the previous case. However, in Li_2ZrO_3, the lithium atoms occupy the vertices of the hexagons while the zirconium atoms occupy the centers. As in the case of Li_2SnO_3, a given octahedral layer repeats every six layers.

The reason why the cation arrangement is different in the two structures seems to be related to the difference in size between Sn^{4+} and Zr^{4+}. All $Li_2M^{4+}O_3$ compounds reported so far, with the exception of Li_2ZrO_3 have a cation ordering similar to that of Li_2SnO_3. Of all the tetravalent cations forming these compounds. Zr^{1+} has the largest ionic radius, and therefore it is logical to surmise that the factor deciding the cation ordering is the $r(Li^{+1}/r(M^{4+})$ ratio. The cation order found in Li_2ZrO_3 can be regarded as a three-dimensional order, whereas that found in Li_2SnO_3 is of a lower dimensionality since it contains layers of lithium-occupied octahedra alternating with layers composed of lithium- and tin-occupied octahedra.

A NEUTRON POWDER DIFFRACTION STUDY OF A- AND B-PbO_2 IN THE POSITIVE ELECTRODE MATERIAL OF LEAD-ACID BATTERIES

A. Santoro
and
P. D'Antonio
(Naval Research Laboratory, Washington, DC)
and
S. M. Caulder
(International Lead Zinc Association at the
Naval Research Laboratory, Washington, DC)

A neutron powder diffraction study of α- and β-PbO_2, both chemically prepared and electrochemically formed in cycled battery plates, was carried out to correlate the electrochemical activity of the lead-acid battery with the atomic arrangement of the electrode constitutuents. Our results are consistent with the presence of hydrogen in the structure of β-PbO_2, but the departure of the occupancy factors, for lead and

TABLE 1

Results of the Refinements of the Structure of β-PbO_2 in the Samples Analyzed

Space Group: P4/mmm; Z=2. The figures in parentheses are the standard deviations on the last decimal figure.

Parameter	Chemically Prepared β-PbO_2	Y36	Y3	Jorgensen (7) β-PbO_2:D	Jorgensen (7) β-PbO_2:H	Naidu (13)
x(O)	0.3078(1)	0.3061(2)	0.3052(3)	0.3070(2)	0.3070(2)	
n(Pb)	0.493(2)	0.490(4)	0.477(4)	0.475(5)	0.485(10)	
n(O)	1.014(5)	1.021(4)	1.05(1)			
a	4.9554(1)	4.9608(2)	4.9621(2)	4.9526(1)	4.9500(1)	4.9568(5)
c	3.3861(1)	3.3844(2)	3.3856(2)	3.3789(1)	3.3771(1)	3.3866(2)
c/a	0.6833	0.6822	0.6823	0.6822	0.6822	0.6832
x_m	0.3084	0.3082	0.3082	0.3082	0.3082	0.3083
oxygen B			0.90(9)			
$\beta_{11}=\beta_{22}$(*)	87(3)	91(7)		103(9)	96(8)	
β_{33}	90(9)	103(20)		110(18)	86(17)	
β_{12}	-56(4)	-84(8)		-50(4)	-68(6)	
$\beta_{13}=\beta_{23}$	0.0	0.0		0.0		
Lead B			0.51(5)			
$\beta_{11}=\beta_{22}$	54(3)	70(6)		44(6)	53(7)	
β_{33}	32(7)	73(14)		38(14)	33(15)	
β_{12}	-2(3)	-32(7)		-7(3)	7(5)	
$\beta_{13}=\beta_{23}$	0.0	0.0		0.0		
U	3858(150	4461(280)	3534(450)			
V	1979(55)	1579(105)	2079(190)			
W	1291(15)	1266(30)	1770(40)			

(*) The anisotropic temperature factors are $\beta_{ij} \times 10^4$

TABLE 2

Results of the Structural and Lattice Parameters Refinements of α-PbO_2

$R_N = 11.65$, $R_P = 5.59$, $R_W = 7.63$, $R_E = 3.46$, m = 1

Space Group Pbcn, Z = 4

A) Lattice Parameters

	a	b	c	
Bagshaw et al. (14)	4.993(3)	5.946(2)	5.459(3)	X(+)
Syono et al. (15	4.998(1)	5.958(1)	5.465(1)	X
Y3 (202)*	4.980(9)	5.964(13)	5.473(6)	N
Y3 (130)**	4.986(10)	5.952(9)	5.472(6)	N
α-β (202)*(++)	4.969(6)	5.979(14)	5.482(7)	N
α-β (130)**	4.973(8)	5.961(11)	5.481(10)	N
Annealed	4.967(10)	5.979(20)	5.482(8)	N
Moseley et al. (5)	4.998(1)	5.932(1)	5.441(1)	X
Zaslavskii et al. (16)	4.927	5.927	5.474	X
From neutron profile refinement	4.9627(10)	5.9588(13)	5.4812(8)	N

B) Structure

Lead

	This study	Moseley et al. (5)	Zaslavskii et al. (16)
x	0	0	0
y	0.1596(8)	0.173(7)	0.178
z	1/4	1/4	1/4

Oxygen

	This study	Moseley et al. (5)	Zaslavskii et al. (16)
x	0.2546(12)	0.2(2)	0.276
y	0.4005(7)	0.35(8)	0.410
z	0.4224(7)	0.39(9)	0.425
B	0.07(9)	--	--

U = 43300(4025), V = 21850(1690), W = 6185(230)

* Peak at 20 = 49.48° indexed as 202.

** Peak at 20 = 49.48° indexed as 130.

(+) X and N indicate that the corresponding measurement was made with x-rays and neutrons, respectively.

(++) α-β indicates that the intensities diffracted by β-PbO_2 were subtracted from the powder pattern.

oxygen, from stoichiometric values are not large enough to unambiguously establish whether there are lead or oxygen dificiencies. If the Pb:O ratio corresponds to exact stoichiometry, any hydrogen which is present must be accompanied by a reduction of Pb^{+4}. There is a significant increase in the lattice parameter a of β-PbO_2 in cycled battery electrodes relative to the value found in chemically prepared β-PbO_2. No change in the c parameter, however, was detected. These dimensional changes are consistent with a configuration for hydrogen similar to that observed in the rutile-type structure of SnO_2, in which there are OH^- ions oriented perpendicular to the c axis.

The profile parameters obtained in this analysis show that the crystallites of β-PbO_2 in the positive plate material of a battery cycled three times (Y3) are smaller than those in the chemically prepared compound (∿450 Å versus 800 Å), while there are no significant differences between the latter and β-PbO_2 in the positive plate material of a battery cycled 36 times (Y36). No evidence for the presence of amorphous PbO_2 in the active electrode material has been found. The average structure of α-PbO_2 cannot be accurately determined by profile analysis, at the present time. The difficulties encountered in the refinement may be due to extensive defects, nonspherical crystallites of small size, and/or small departures of the structure from orthorhombic symmetry.

The results of our study are reported in Tables 1 and 2, where they are compared with previously published values.

CRYSTAL STRUCTURE OF AMMONIUM NITRATE: LOW TEMPERATURE PHASE (V)

C. S. Choi and H. J. Prask
(Energetic Materials Division, LCWSL, ARRADCOM, Dover, NJ)
and
(National Bureau of Standards, Washington, DC)

We have completed crystal structure studies of phase IV, II and III of NH_4NO_3 in previous years. This year, we have studied the structure of phase V, the lowest temperature phase, to conclude the structure study of all phases. A deuterated AN sample (D concentration of 90%) was obtained by six cycles of repeated recrystallization from solution with 99.6% D_2O at about 103 °C.

The neutron powder diffraction measurements were made on the high-resolution 5-detector diffractometer at 10K, 78K and from 130K to 270K

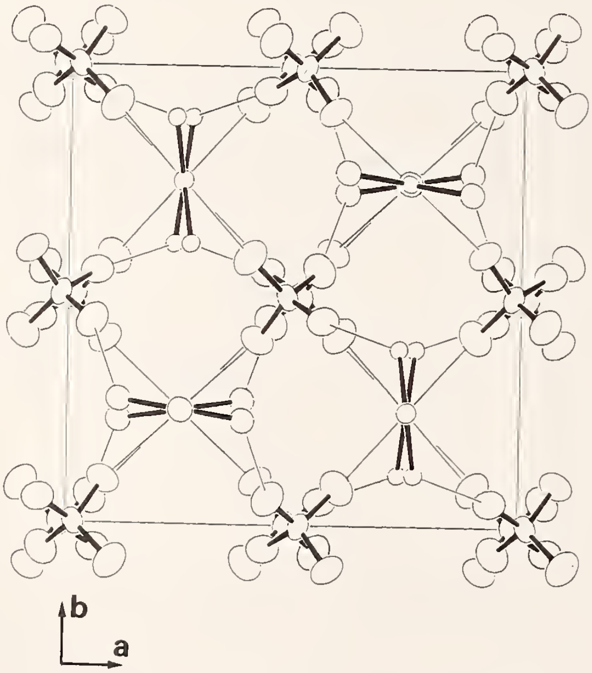

Figure 1. Crystal structure of AN viewed along the C-axis. The unit cell is orthorhombic P ccn with the dimensions, a=7.8850(2), b=7.9202(2), and c=9.7952(2) at 78K.

in 20K steps. We found that the unit cell symmetry is orthorhombic Pccn, and the previously reported tetragonal $P4_2$ is erroneous. The Rietveld profile refinement reduced the residuals to R(integ)=3.63%, R(prof)=2.40%, R_w(ProF)=3.06% and R(expt)=1.88% for the 78K structure. There are two independent sets of three-dimensional H-bond chains which are related mutually by C-glide mirror symmetry. The two H-bond chains are interpenetrating and make a tight VanderWaals contact with very short N···O and O···O intermolecular distances. Figure 1 is the ORTEP drawings to illustrate the H-bonded structure.

The thermal expansion profile of AN was determined as a function of temperature from 10K to 393K, using the unit cell dimensions determined at each temperature by the profile refinement method. Figure 2 is the volumetric expansion expressed in terms of cell volume per unit molecule. Phase V, IV and II are similar in molecular packing (CsCl type), but they differ in the orientation of NO_3 groups. The NO_3 groups in phase IV are packed with their orientation parallel which results in

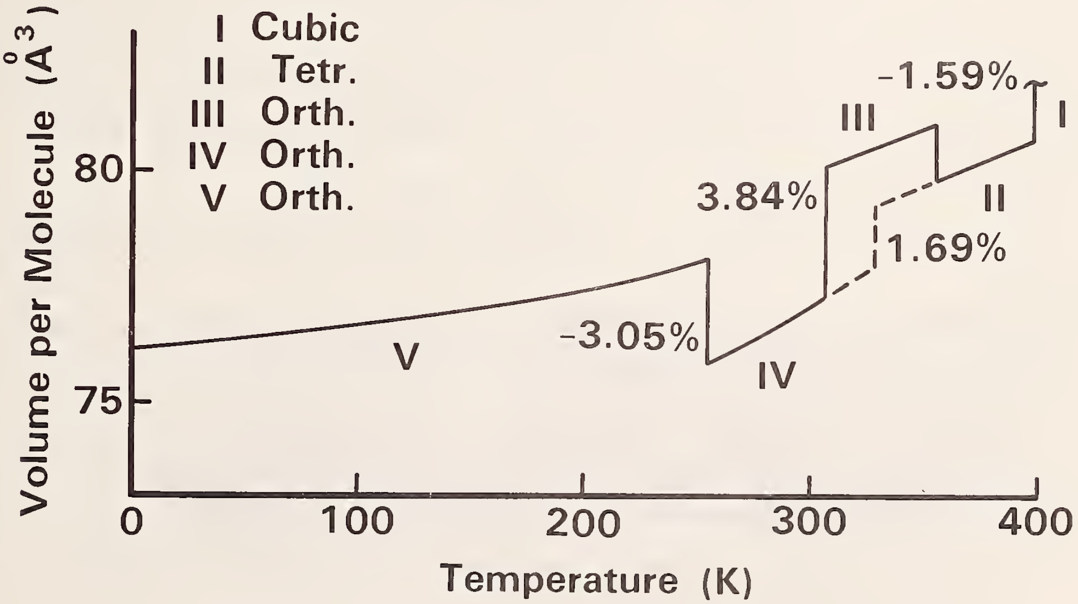

Figure 2. The volumetric thermal expansion of AN as a function of temperature.

maximum density, and is reflected in the specific cell volume curve. The volume change at each transition point is very large, -3.05% at the IV-V and 3.84% at the IV-III transitions.

X-RAY DIFFRACTION STUDIES OF CELLULOSE

H. J. Prask and C. S. Choi
(Energetic Materials Division, LCWSL, ARRADCOM, Dover, NJ)

and

(National Bureau of Standards, Washington, DC)

The two major sources of cellulose for nitrocellulose (NC) production are cotton linters and woodpulp. In general, cotton linters provide a uniform source for NC. However, linters could possibly be in short supply if present production facilities were fully mobilized. In contrast, woodpulp offers a plentiful and less costly source of cellulose. However, woodpulps are considerably less uniform than linters which has led to unacceptable variations in processed NC, particularly in new, continuous nitration production facilities. In the present work we utilize a total-profile analysis of x-ray diffraction data of various cellulose samples to attempt to identify critical feedstock properties for quality control.

Our analysis of cellulose x-ray diffraction patterns includes the following:

1. We constrain the structures for all samples to be monoclinic, but refine lattice parameters;
2. We include principal (equatorial) reflections and weaker (meridional) reflections, the latter scaled to account for orientation effects in the pressed-pellet samples;
3. We make use of an explicit non-crystalline profile obtained from ball-milled cellulose;
4. A peak profile of mixed Gaussian and Cauchy character is

assumed; and

5. The analysis allows for samples of mixed cellulose I and cellulose II composition.

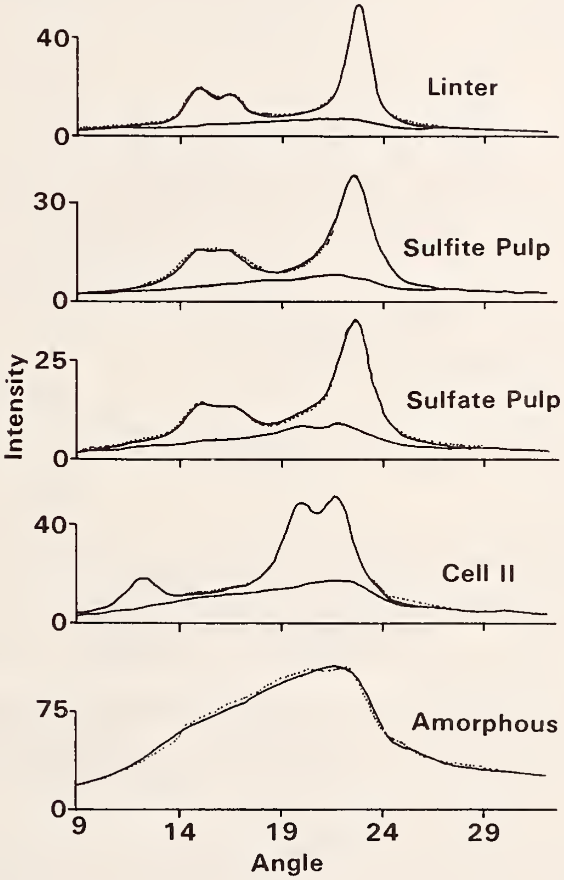

Figure 1. Representative x-ray diffraction patterns of pressed-pellets of various cellulose samples (Cu-Kα radiation). The dots represent the data, the solid lines through the dots are the total-profile fits. The solid lines below the dots (upper four samples) are the combined contribution of Compton scattering, amorphous scattering, flat background and lower-concentration phase (e.g. II in the upper three patterns).

The analytic expression used to fit the total diffraction profile for a predominately cellulose I sample has the form:

$$\begin{aligned} I(\Theta) = {} & P_{BG} + \mathrm{COMP}\,(\Theta) + P_{AM} \cdot \mathrm{AMORPH}(\Theta) \\ & + P^{II} \cdot \mathrm{CELL}(II,\, \Theta,\, WM) + SC \cdot \mathrm{CELL}(I,\Theta) \\ & + \sum_k Q^{Ik}(\Theta) \end{aligned} \tag{1}$$

where

$$\begin{aligned} Q^{Ik}(\Theta) = {} & \sum_k P_H{}^{Ik}(\Theta) \left\{ P_f{}^I \exp \left\{ -\ell n 2 \left[\frac{2(\Theta-\Theta_o)^{Ik}}{P_w{}^{Ik}} \right]^2 \right\} \right. \\ & \left. + \frac{(1 - p_f{}^I)}{1 + \left[2(\Theta-\Theta_o{}^{Ik})/P_w{}^{Ik} \right]^2} \right\} \end{aligned} \tag{2}$$

$$\text{and } \Theta_o{}^{Ik} = \Theta_o{}^{Ik}\,(P_A,\, B,\, P_C,\, P_\beta,\, h^k,\, k^k,\, \ell^k). \tag{3}$$

In the above, Θ is the scattering angle ($=2\Theta_b$) and the Ps are parameters adjusted in the least-square fits. In eqn. (1) the Ps are amplitude parameters for a flat background, amorphous profile, and cellulose II profile (I and II are interchanged in a predominately phase II sample); COMP(Θ) is the Compton scattering component, WM is a multiplicative factor which adjusts all widths of the cellulose II peaks, and SC is an orientation scale factor for meridional reflections in cellulose I which is empirically determined by comparison of measured linter intensities and published fiber structure factors.

The $Q^{Ik}(\Theta)$ correspond to the principal reflections of phase I (i.e. (101), $(10\bar{1})$, (021), and (002) where the chain axis is along b). In eqn. (2), P_H, P_f and P_w are respectively the height, Gaussian fraction, and FWHMs. The Θ-dependence of P_H denotes that angle-dependent corrections such as Lorenz and polarization factors are included. Finally, the Θ_o are peak positions of the principal (h,k,l) reflections of phase I obtained by refining the A and C lattice parameters and the monoclinic

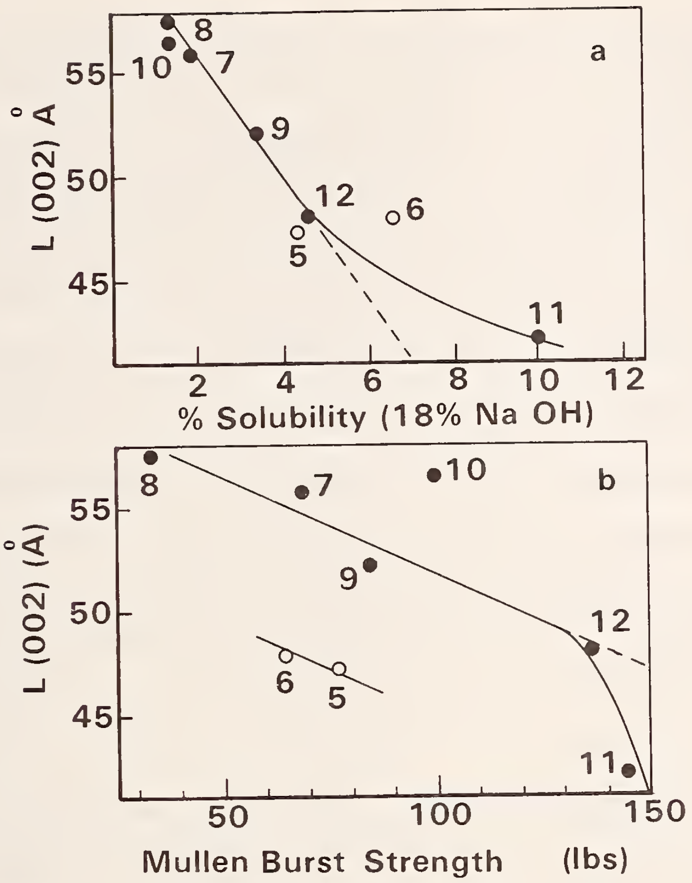

Figure 2. Crystallite (002) dimension vs. %- solubility and Mullen Burst Strength for woodpulps; closed circles = sulfate pulps, open circles = sulfite pulps.

angle, β. The B lattice parameter was not refined because orientation effects reduced non-equatorial reflection intensities.

In figure 1 are shown representative diffraction patterns and least-square fits for linter, sulfite-processed pulp, sulfate-processed pulp, Fortisan (cellulose II), and ball-milled cellulose (the solid line is the profile of six arbitrary Gaussians used to reproduce the pattern). Several points should be noted concerning our total-profile analysis approach. We refine lattice parameters and obtain values in good agreement with accepted values. In contrast to similar efforts (see, for example, refs. 3-5), we calculate relative structure factors from our least-square fit parameters, and find them to be in good agreement with structure factors

Table 1. Celluloses: crystallinity, particle sizes, and shape parameters.

Sample	Type	% Crystallinity	L(002) (Å)
1	I-Linter	49.1±2.0	73.2±0.4
2	I-Linter	50.8±1.5	75.5±0.3
3	I-Linter	44.1±1.6	75.8±0.3
5	I-Sulfite	35.1±2.2	47.2±0.2
6	I-Sulfite	36.0±1.7	47.9±0.2
7	I-Sulfate	32.4±2.0	55.8±0.3
8	I-Sulfate	35.4±1.9	57.5±0.3
9	I-Sulfate	37.2±2.0	52.1±0.2
10	I-Sulfate	32.3±2.1	56.5±0.3
11	I-Sulfate	43?[a]	42.1±0.2
12	I-Sulfate	26.7±3.3	48.1±0.3
4	II-Fortisan	15.4±2.2	61.6±0.6

---

[a] Questionable because of very large FWHMs of principal reflections.

obtained from studies of various cellulose I and II fibers. We also find that for linters (for which features are sharpest) pure Cauchy peak shapes alone will not fit the full diffraction profile (as has been proposed in ref refs. 4 and 5); some explicit amorphous component is required.

In table 1, some of the results for the several samples studied are shown. It should be noted that %-crystallinity is obtained directly from P_{AM} of equation (1) and L(002), which represents crystallite size along [002], is obtained in the usual (approximate) way from the Scherrer equation and the refined P_Ws.

The following tentative conclusions can be drawn from the limited number of samples studied. Within the three sample types, linters and sulfite-processed woodpulp each appear to exhibit fairly uniform properties; sulfate-processed woodpulps show a wide variation in properties. (This is consistent with observations made concerning variability of processed propellants from these classes of feedstocks.) In figure 2, a comparison of "crystallite size" and other measured properties[6] are shown for the woodpulp samples. Sample 11 appears anomalous in both solubility and burst strength; sample 10 in burst strength. With regard to nitration of these samples, it is interesting that both sample 10 and 11 show anomalous changes in viscosity in going from 12.6 to 13.4 wt-% nitrogen. In our measurements, sample 10 is the only one to exhibit a measureable admixture of cellulose II (see "sulfate pulp" in figure 1) and, as mentioned above, sample 11 showed very large FWHMs.

---

1. H. J. Prask and C. S. Choi, "The Correlation of Nitrocellulose Properties and Cellulose Feedstock Structure," *U. S. Army ARRADCOM Tech. Rept.*, in press.

2. J. Mann, *Pure Appl. Chem.* 5, 91-105 (1962).

3. A. M. Hindelah and D. J. Johnson, *Polymer* 13, 423-30 (1972).

4. J. Gjonnes et al., *Acta Chem. Scand.* 12, 489-494 (1958).

5. H. Krassig, *Appl. Poly. Symp.* 28, 777-790 (1976).

6. R. A. Mundy et al., "Improved Nitrocellulose Process Controls," *U. S. Army ARRADCOM Tech. Rept.* ARLCD-CR-80029, Dec. 1980.

HYDROGEN EXCHANGE IN RNASE A: NEUTRON DIFFRACTION STUDY

Alexander Wlodawer and Lennart Sjölin
(National Bureau of Standards, Washington, DC)

and

(National Institute of Arthritis, Diabetes, Digestive,
and Kidney Diseases)

Hydrogen exchange has been studied in a single crystal of RNase A in the course of a neutron structure investigation. Neutron data to 2.0 Å resolution were collected using a flat-cone diffractometer at the National Bureau of Standards Reactor. Fully deuterated synthetic mother liquor (55% t-butanol, 45% D_2O measured pH = 5.25) was added in stages to a vial containing a large ribonuclease crystal. Several complete exchanges of the solvent took place in about six months. Another six months were spent collecting diffraction data. The crystal was kept at room temperature throughout the experiment. Altogether 4132 reflections with $I > 3\sigma(I)$ were observed in the resolution interval of 2-10 Å (51% of the total).

The degree of exchange of amide hydrogens was calculated in a refinement with the neutron data in which the positional and thermal parameters for all atoms were kept constant, while the occupancies were allowed to vary. The refinement was thus constrained for all the parameters other than occupancies and free for the occupancies. All amide hydrogens were formally treated as deuteriums, with the occupancy of 1.0 corresponding to a deuteron and -0.55 to a proton, as indicated by their respective scattering lengths.

The number of parameters in the occupancy refinement was equal to the number of atoms, namely 2360, while the number of observations was 4132. Since the overdetermination by a factor of 1.75 might not have been sufficient in the presence of substantial errors, it was necessary to evaluate the level of confidence in the results. The tests consisted of refining the occupancies of all atoms in the structure without setting any arbitrary upper or lower limits and by monitoring

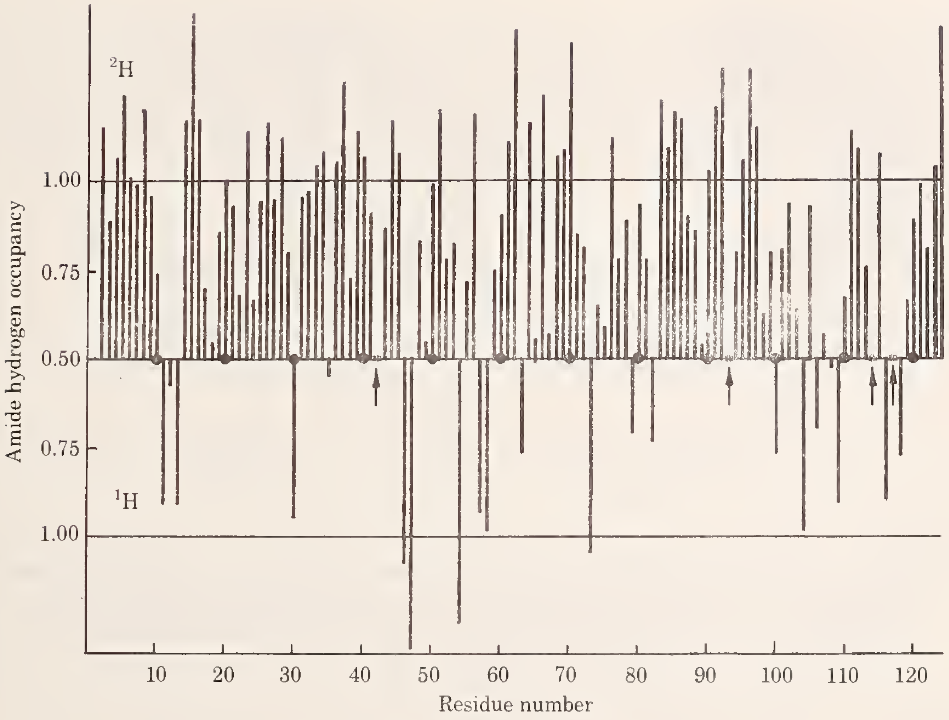

Figure 1. Plot of occupancies of amide hydrogens in RNase as a function of residue numbers. Atoms which are predominantly of deuterium character are plotted above the central line, hydrogens are plotted below mark. Every tenth residue is marked by a dot, arrows point to prolines, which have no amide hydrogens. Scatter of occupancies beyond 1.0 is an indication of errors in their determination; other methods of estimating error levels are discussed in the text.

the behavior of all atoms belonging to the main chain. This refinement clearly does not correspond to a physically meaningful situation and the resulting occupancies of amide hydrogens are not correct, nevertheless, the r.m.s., discrepancies of the occupancies of other main-chain atoms provide a good estimate of the errors associated with the individual estimates of occupancies. Two starting models were used, one with all amide hydrogens assumed to be fully exchanged for deuterium and one in which they were unexchanged. In the first case, the final average occupancies and their r.m.s. deviations for N, CA, HA, O, and D were 1.0 (0.17), 1.08 (0.21), 1.05 (0.20), 1.06 (0.21), and 0.72 (0.41) respectively. The results of the refinement starting from amide hydro-

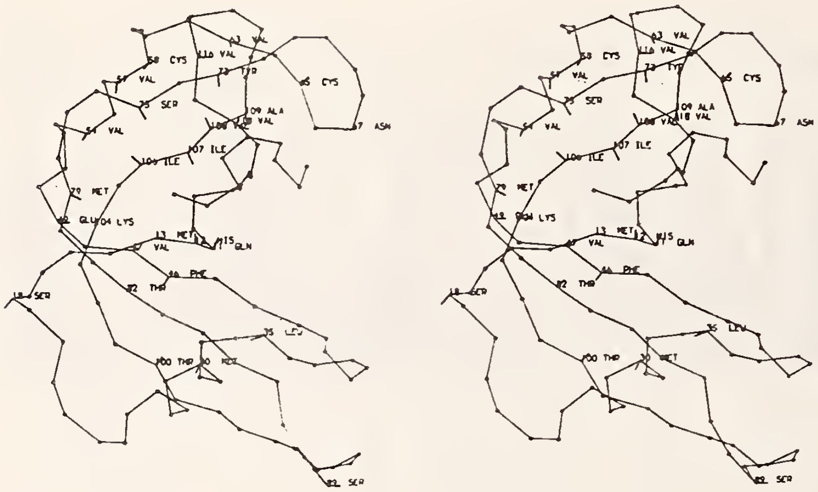

Figure 2. Plot of the positions of all amide nitrogens in the RNase A molecule, as well as of those amide hydrogens which were found to be at least half protected against exchange.

gens were 1.14 (0.19), 1.05 (0.23), 1.07 (0.23), 1.06 (0.23), and 0.31 (0.40).

Final occupancies for amide hydrogens were established on the basis of a refinement in which the upper limit of 1.0 was placed on the occupancies of atoms other than amide hydrogens, and the resulting occupancies of amide hydrogens were divided by 1.06 to compensate for the errors described above. Twelve amide hydrogens were found to be completely protected, six exchanged 25%, and ten were approximately half exchanged. Altogether, about a quarter of the amide hydrogens were not more than half exchanged after approximately one year of exposure to deuterated solvent (figure 1). The distribution of the protected amides in the three-dimensional structure of ribonuclease is shown in figure 2. The information derived from such analysis is usually sufficient to indicate less flexible regions of the protein. The method used here is more straight-forward than chemical analysis. It is also less susceptible to systematic errors, and provides meaningful estimates of random errors, but the confidence which can be placed in the protection of any particular peptide should not be exaggerated, in view of relatively large r.m.s. deviation of calculated occupancies. However, we believe that the results obtained from the crystalline state of RNase are essentially correct for a majority of the amides.

CRYSTALLIZATION OF HEN EGG OVALBUMIN

M. Miller and A. Wlodawer
(National Bureau of Standards, Washington, DC)
and
(Laboratory of Molecular Biology, NIADDK, Bethesda, MD)

Hen ovalbumin, the major component of egg white was obtained in crystalline form almost a hundred years ago and since then it has been readily available in purified form in gram quantities. For that reason it has been used in a large number of studies on physicochemical properties and immunological behavior of proteins. Strangely enough very little is known about secondary and tertiary structure of ovalbumin with all of the information coming from indirect methods, since no x-ray structure is available.

Ovalbumin readily crystallizes from ammonium sulfate or sodium sulfate solutions, but in the previous studies only microcrystals have been reported. When ovalbumin is treated with substilisin, a new crystalline protein, plakalbumin, is formed. A heptapeptide Glu-Ala-Gly-Val-Asp-Alu-Ala (residues 346-352) is released during conversion of ovalbumin to plakalbumin; the resulting two chains can be separated by gel filtration in urea.

In order to be able to study the structure of ovalbumin and plakalbumin by the techniques of x-ray and neutron diffraction, we have grown single crystals of these proteins. Crystals of ovalbumin were grown at 37 °C from 10 to 30 mg/ml of protein solution in cacodylic buffer. Initially crystallization was achieved by vapor equilibration against 50% saturated ammonium sulfate (AMS) in the same buffer (pH 5.0 to 5.4) using the handing drops technique. Crystals were later obtained at pH range of 5.8 to 7.1 by batch method. To the protein dissolved in buffer, saturated AMS solution was slowly added until slight opalescence appeared; the solution was then cleared by centrifugation and set up in sealed vials in 37 °C. Any disturbances such as a shift of temperature, vibrations or even simply examining vials under the microscope in the warm room, resulted in showers of microcrystals.

Plakalbumin crystals were grown at room temperature by a similar batch method from 25 mg/ml protein. The solution of digested ovalbumin was mixed with equal volume of 0.1 M cacodylic buffer pH 5.4, about 60% AMS and 2% methanol.

Crystals of ovalbumin usually appeared after one month and reached their maximum size after several more days. Needless as large as 1.5 x 0.2 x 0.05 mm were obtained at pH 5.4. They belong to space group C2 with a = 116.5 Å, b = 41.8 Å, c = 70.5 Å and β = 101.5°. The assumption that there is one molecule in asymetric unit gave the value of V_m = 2.0 Dalton/A^3, which is in the range observed for other proteins. Crystals obtained at pH 6.7 were usually thicker and their growth was more reproducible, but shifting pH of crystallization to higher values caused a change in the packing of molecules. Crystals obtained at pH 5.8 and higher were triclinic with the following unit cell parameters: a = 62.0 Å, b = 84.3 Å, c = 72.2 Å, α = 87.6°, β = 103.9° and γ = 108/67°. The two crystal forms must be closely related, since the intensities corresponding to the distorted monoclinic lattice can be noticed in the corresponding triclinic projection.

The small size of ovalbumin crystals, poor reproducibility of growth and large asymmetric unit of triclinic crystals make them unsuitable for further x-ray analysis. Crystals of plakalbumin, on the other hand, were larger and easier to obtain. They grew from ammonium sulfate solution in a few days, but were usually twinned. Adding 2% of methanol or ethanol slowed down the process of crystallization to weeks but prevented twinning. These crystals belonged to space group C2 with a = 99.9 Å, b = 102.0 Å, c = 79.3 Å and β = 112.1°.

The crystals grew as rectangular plates with 0.3-0.8 mm sides and were up to 0.2 mm thick. The limit of diffraction observed on still photographs is 2.5 Å. The crystals are stable for up to 100 hours when irradiated using 1200 W sealed x-ray tube.

The crystals of plakalbumin are much more suitable for further x-ray analysis than the crystals of ovalbumin grown by us. The removal of a heptapeptide by subtitisin does not cause significant changes in the structure of ovalbumin, as supported by the fact that the physiochemical studies did not reveal any differences in the behavior of these two modifications of ovalbumin. We are continuing the search of suitable heavy atom derivatives needed for the determination of plakalbumin structure by a method of multiple isomorphous replacement.

HYDROGEN IN METALS--THEORY OF NEUTRON-INDUCED TRANSITIONS TO EXCITED BAND STATES

R. C. Casella

The ongoing program associated with the theory of neutron scattering from tunneling atoms or molecules in solids,[1] particularly the application to hydrogen in metals,[2] has been expanded considerably to include the possible effect of band formation by hydrogen in otherwise pure metals. My prior work has included the theory of inelastic neutron scattering to excited oscillator states from hydrogen trapped in a two-well configuration near an impurity atom (O or N) in b.c.c. metals such as niobium.[3] Experimental evidence[4, 5] for coherence in the tunnel-split ground state of such systems leads me to look for a degree of coherence in the neutron-induced excitations to states which are linear combinations of local excited oscillators for hydrogen, even in relatively pure samples at sufficiently low temperatures. In b.c.c. metals, the hydrogen equilibrium positions are assumed to lie at the tetrahedrally coordinated verticies of the Wigner-Seitz cell, as shown in figure 1. Of course, distortion of the metal-atom positions occurs when the proton (or positive muon) plus its associated

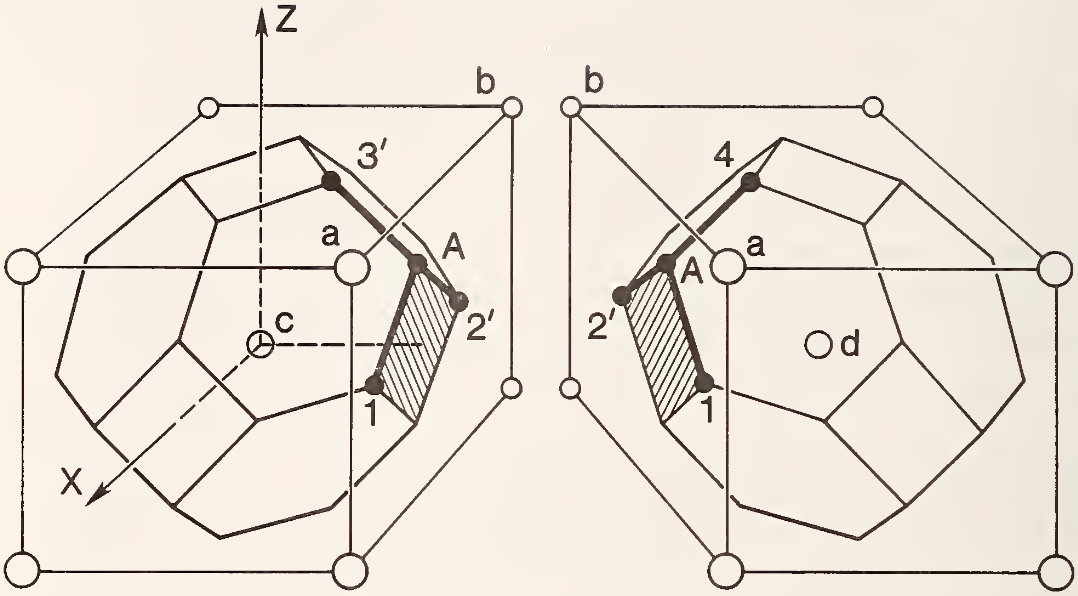

Figure 1. Cut-away view of the hydrogen-site configuration in b.c.c. metals. The hydrogen at site A experiences short-range forces from the metal atoms in the tetrahedral array a, b, c, d, about it. As drawn, atoms c and d are at body centers. The displacements of the metal atoms due to the presence of the hydrogen are not shown. The near-neighbor sites 1, 2', 3', and 4 are also tetrahedrally coordinated about A. All 12 (= 1/2 × 24) vertices in each body-centered cube are energetically equivalent.

electronic cloud occupies a given site (such as position A in figure 1). In particular, the nearest-neighbor metal atoms (at a, b, c, and d in figure 1) are displaced away from the hydrogen, retaining local tetrahedral symmetry. Experimental evidence, especially the relation $\omega_{II} = \sqrt{2}\,\omega_I$, between the first and second neutron-induced excitation frequencies in several b.c.c. systems,[5] suggests a phenomenological model in which, crudely, one may think of the hydrogen as moving harmonically in a three-dimensional local well. (Actually, the coordinated motion of the hydrogen atom plus neighboring metal atoms exhibit the characteristics of harmonic motion.) The hydrogen at A in figure 1 (more accurately, the hydrogen plus its distortion field about A) can tunnel to a nearby position (1, 2', 3', or 4 in figure 1). The ground-state tunnel splitting is enhanced

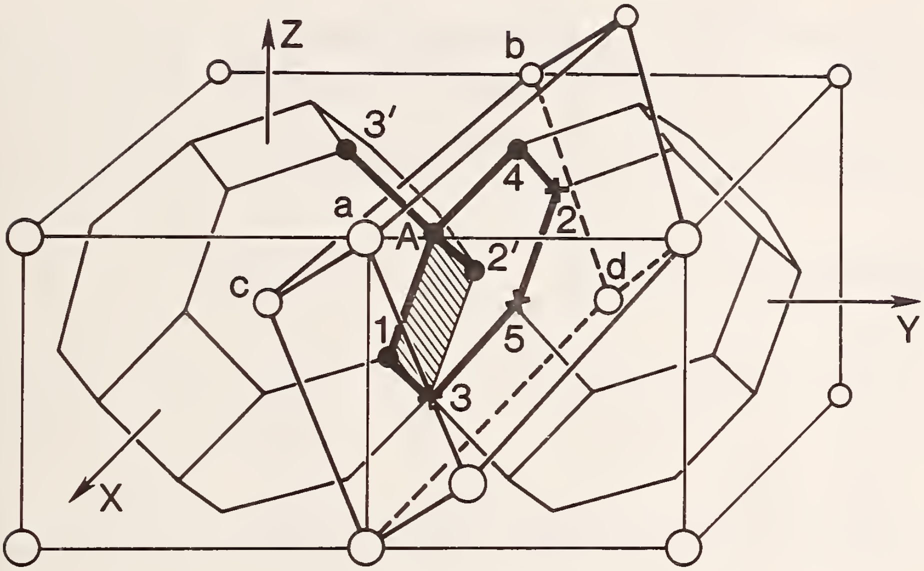

Figure 2. The primitive cell. As shown, the six crystallographically inequivalent sites A, 1, 2, 3, 4, and 5 occur on a hexagon within the cell. As drawn, the near neighbor (relative to A) sites 2' and 3' lie outside the cell. Crystallographically, these are equivalent to sites 2 and 3, and the site 5 is equivalent to a second-near-neighbor of A. (All verticies are equivalent from the point of view of their energetics.) See, also, figure 1.

when a nearby impurity atom lowers the barrier between equivalent sites.[4, 5] It is not unreasonable that hydrogen in a pure metal can tunnel more rapidly among the excited oscillator states than for the ground state, contributing to the inverse lifetime of the local excitation and, hence, to its line width. In the extreme where tunneling can occur coherently between several sites, bands result. A first-principles calculation of the relevant overlap integrals requires a self-consistent calculation of the motion not only of the hydrogen, but also of the surrounding metal atoms. I do not attempt such a calculation, but rather treat the combined system (hydrogen + surrounding displacement field) phenomenologically in an effective rigid-band model. The overlap integrals (which, from symmetry, can be expressed in terms of a few irreducible ones) are treated as parameters ultimately to be determined by experiment. I assume that,

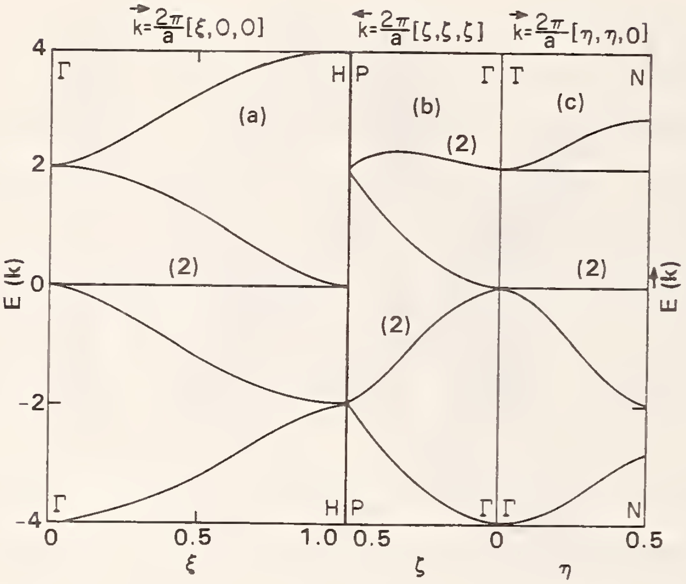

Figure 3. The first set of excitation bands $E(\vec{k})$ which, in the absence of overlap, collapses to a line at $E = \hbar\omega_I = 0$. The energy is measured in units of the single overlap integral H_I. $E(\vec{k})$ is given for (a) $\vec{k}$ along [100], (b) $\vec{k}$ along [111], (c) $\vec{k}$ along [110]. Only nearest-neighbor overlap terms are included. (Energy is measured relative to the first excitation energy $\hbar\omega_I$ of the local oscillator.)

in this model, at least the symmetry of the bands ought be manifest. In particular, the Bloch theorem is effectively recovered, despite self-trapping effects. The domain of validity of this assumption can, in principle, be delineated by experiment. Also, if one treats the inelastic neutron scattering in impulse approximation, then it can happen that the effective final states (intermediate states in a more complete calculation) are virtual rigid-band states, which subsequently decay into local oscillater states. This use of the rigid-band states in impulse approximation for treating the scattering of neutrons from hydrogen in metals is limited to large momentum transfers.

Given the above motivations, I have been engaged in a rather extensive energy-band calculation, involving a tight-binding approximation consisting of Bloch-like states formed by taking linear combinations of the local oscillator states centered at the various b.c.c. sites, such as those labeled A, 1, 2', . . ., in figure 1. There are six inequivalent sites in each unit cell, as shown in figure 2 at A, 1, 2, 3, 4, and 5. Sites 1 and 2 are equivalent to the sites 2' and 3' which are nearest neighbors to A, but lie outside the primitive cell, as drawn. The six inequivalent sites result in 6 × 6 and 12 × 12 secular equations for states formed from

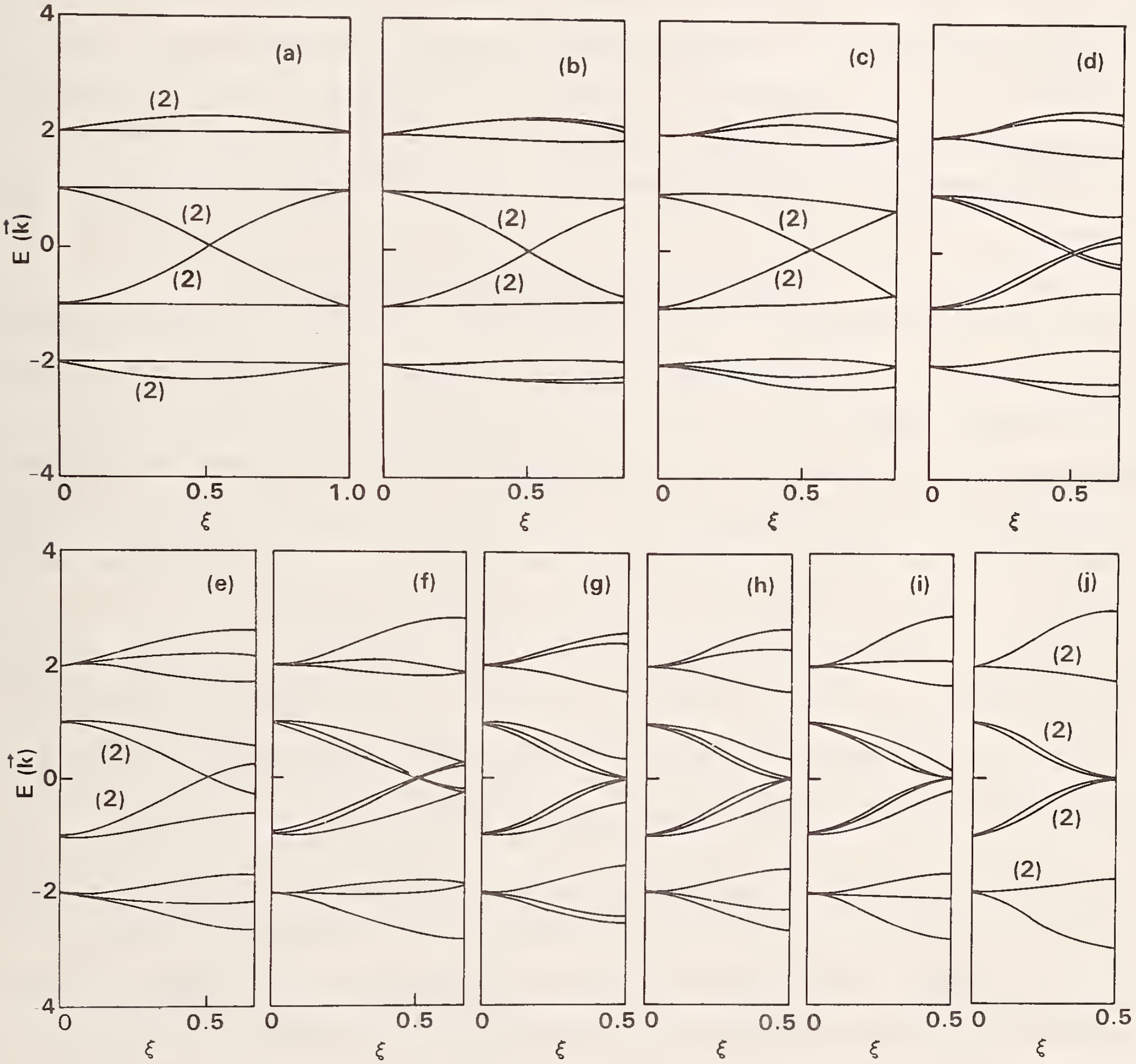

Figure 4. The second set of excitation bonds, $E(\vec{k})$ relative to $\hbar\omega_{II}$. Various slices of the Brillouin zone for $\vec{k}$ along (a) [1, 0, 0], (b) [1, 1/5, 0], (c) [1, 1/5, 1/5], (d) [1, 1/2, 0], (e) [1, 1/2, 1/5], (f) [1, 1/2, 1/2], (g) [1, 1, 0], (h) [1, 1, 1/5], (i) [1, 1, 1/2], (j) [1, 1, 1]. The scale is the (undetermined) parameter, H_{II}. As shown, the second parameter, S = 0.5. (See text.) Doubly-degenerate bonds are denoted by the symbol: (2).

the singly and doubly degenerate local oscillator excitations of frequencies ω_I and ω_{II}, respectively. In nearest neighbor approximation, a common scale, the single irreducible overlap term, can be factored from the secular determinant, all other matrix elements being equal to it apart from phase factors of the type $\exp(i\phi_{ij})$. In this approximation, two such irreducible overlap factors occur in the 12 × 12 determinant. In the latter case, the approximation introduces additional symmetries, such as a pseudo-superlattice effect, mimicing a doubling of the unit cell to a cube containing 12 sites, instead of 6. Also, the approximation introduces an apparent reflection symmetry about the energy $\hbar\omega_{II}$ with eigenvalues occurring in pairs at $\hbar\omega_{II} \pm E$. Preliminary investigation indicates that these artificial symmetries, which are peculiar to the degenerate oscillator excitation (12 × 12 determinant), are a consequence of the nearest-neighbor approximation. Results for the first set of excitation bands in this approximation are shown in figure 3a-figure 3c, where energies are measured relative to the local excitation energy, $\hbar\omega_I$. The unit of energy is chosen to be the single irreducible scale factor, H_I, to be fit by experiment. The second set of excitation bonds, the centroid of which lies above the first by an amount $\hbar(\omega_{II} - \omega_I)$, is shown for several slices in the Brillouin zone in figure 4a-figure 4j. Here, energy is measured relative to $\hbar\omega_{II}$), and the ratio S of the second to the first irreducible matrix element occurring in the 12 × 12 determinant has been set equal to 0.5. The additional pseudo symmetries are exhibited in these figures, where one sees a solution at -E for each solution at E and a pseudo zone boundary at $\xi = 1/2$, which would result from a cubic zone (of half the volume) associated with a cubic cell in real space containing 12 hydrogen sites. (The cubic zone is inscribed in the dodecahedral zone appropriate for the f.c.c. reciprocal lattice belonging to the b.c.c. metals. The two zone boundaries coincide along the cube edge, $\vec{k} = (2\pi/a)[1/2, 1/2, \zeta]$.)

It is planned to include the effects of second-near neighbors and, hopefully, to relate the resulting theoretical model to experiments on inelastic, thermal-neutron scattering from hydrogen-loaded b.c.c. metals, which are being carried out at the NBS Reactor.[5]

---

1. R. C. Casella, *Phys. Rev.* B20, 5318 (1979).
2. R. C. Casella, *J. Physique, Coll.* C6, S42, 923 (1981).
3. R. C. Casella, *Phys. Rev.* B24, 2913 (1981).
4. H. Wipf, et al., *Phys. Rev. Lett.* 46, 947 (1981).
5. A. Magerl, J. J. Rush, and J. M. Rowe (private communication).

RELATIONS BETWEEN FERMION MASSES

R. C. Casella

Work begun on this problem during the latter part of the prior period[1] was completed and published.[2] The main predictions of the model are (i) equality of the (ν_μ, ν_e) and (s, d) mixing angles, (ii) the fermion mass relations,

$$\frac{t - c}{c - u} = \frac{b - s}{s - d} = \frac{\tau - \mu}{\mu - e} = \frac{\nu_3 - \nu_2}{\nu_2 - \nu_1} , \qquad (1)$$

and (iii) a bound on the squared masses of the neutrinos relating possible oscillations among the pairs (ν_μ, ν_e) and (ν_μ, ν_τ), namely

$$\nu_2^2 - \nu_1^2 < 0.063 (\nu_3^2 - \nu_1^2). \qquad (2)$$

In the above, the constituent quark or lepton masses are denoted by their flavor symbols, where (u, d), (c, s), (t, b) and (e, ν_1), (μ, ν_2), (τ, ν_3) are, respectively, the quark and lepton mass eigenstates, which, via Cabibbo rotation, are related to the standard weak isodoublets in the electroweak theory of Glashow, Weinberg, and Salam. To date, relations (1) and (2) remain in approximate accord with experiment. Equation (1) predicts a constituent mass for the t quark in the neighborhood of 27 GeV. Neutrino oscillations continue to elude observation.

---

1. R. C. Casella, *NBS Tech. Note No. 1160*, p. 14, (F. Shorten, Ed., (1982)).
2. R. C. Casella, *Il Nuovo Cimento* 67A, 289 (1982).

CALCULATIONS OF VIBRATIONAL SPECTRA OF SELF-TRAPPED HYDROGEN IN BCC METALS

N. F. Berk

We are presently implementing a theoretical procedure recently reported by H. Sugimoto and Y. Fukai for numerically solving the Schroedinger equation in the Born-Oppenheimer approximation in order to make predictions of the vibrational spectra of self-trapped light interstitials (H) in metals (M). The method assumes a model H-M interaction under the influence of which the metal lattice is allowed to self-consistently relax. Using the theory we plan to study the effects of trapping defects, such as oxygen in Vanadium, on the H-spectra as well as trying to elucidate the mechanisms that determine the location of the defect-induced trapping sites. In addition we hope to study the role of lattice strains, elastic H-H interactions, and time-dependent relaxation effects on the widths of measured vibrational lines in these systems. As the first stages of this program, we have developed numerical procedures for solving the Schroedinger equation for a given potential and for computing the self-consistent lattice equilibrium displacements for a given set of lattice forces and the H-M interaction.

---

1. H. Sugimoto and Y. Fukai, *Phys. Rev.* B670 (1980); *J. Phys. Soc. Japan* 50 (1981).

TRANSLATION-ROTATION COUPLING IN MOLECULAR AND IONIC CRYSTALS

J. M. Rowe and J. J. Rush
and
K. H. Michel
(UIA, Antwerp, Belgium)
and
M. Klein
(NRC, Ottawa, Canada)

Work is continuing on both the theoretical and experimental studies of the $(KCN)_x(KBr)_{1-x}$ system for x = 1.0, 0.95, 0.9, 1.8, 0.5, 1.25, 0.05. Neutron powder diffraction is being used to clarify the nature of the low temperature structures of the mixtures for $x > 0.8$, where preliminary measurements for x = 0.8 have shown the existence of a monoclinic structure, rather than the orthorhombic structure of pure KCN. The samples with x = 0.95, 0.90 and 0.80 will be studied as functions of temperature and cooling rate to attempt to clarify the nature of the transition which occurs at a temperature $T_c \sim 168\ (1-x)$ in these mixtures. It is already clear, however, that strain is a very important variable in these phase transitions as shown by the affects of repetitive cycling on the 168K transition in pure KCN.

As new theory has been developed to explain the absence of observable optic modes in pure KCN and NaCN. This theory is an extension of earlier theories to include the effects of the asymmetry (electrical and mechanical) of the $(CN)^-$ ion. This introduces coupling to modes of ungerade symmetry, a necessary condition for optic mode damping at $q = 0$. Quantitative calculations based upon a microscopic model have shown that this effect is not only sufficient to explain the results, but rather too effective! Thus, we are currently attempting to calculate the effect of a proper self-consistent phonon treatment. The results of this theory will be presented in a paper in preparation. It should be noted that mechanical asymmetry is much more important in this respect than the small electric dipole moment, a conclusion with large implications for the low temperature phase transition (at 85K in KCN).

In addition, new high resolution measurements of the soft mode in pure KCN have been undertaken in an attempt to clarify the situation with respect to the effective quadrupole moment referred to in last year's report. The results, and a representative least squares fit to the model of Sahu and Mahanti[1], are shown in figure 1. For this particular fit, the value of the quadrupole moment used was 1/2 the free ion value. However, the fit is not particularly good at some momentum transfers (q = .3, T = 170K) and some of the parameters found are clearly unphysical. To date, no completely satisfactory fit has been obtained, and we are currently searching for the cause of this. The present position is thus that while the theory gives good qualitative results, it is still lacking quantitatively.

Molecular dynamics simulations are continuing, but several problems persist, closely related to those alluded to above - namely, the selection of a good microscopic force model. A present speculation is that even higher multipole moments are required to reproduce the correct behavior of the $(CN)^-$ ion in this crystal. However, it has not yet been possible to achieve a reliable test of this possibility. If this idea is correct, the apparent reduction of the quadrupole moment needed to give agreement with experiment may in fact be simply a compensation for the neglect of the higher multipole moments.

Finally, both experimental and theoretical studies of the "quadrupole glass" state of mixed crystals continues. Recent articles[2, 3] have questioned the existence of a real transition in these materials, based upon the observed dielectric behavior. However, the alternative description proposed is completely inconsistent with the neutron data, and hence cannot be considered correct. A possible explanation of this discrepancy is that the dielectric constant measurements do not probe the quadrupole order directly, but rather only through its influence on the dipole order. Some support for this hypothesis can be obtained by comparing the observed dielectric behavior with that of pure (KCN) in the lowest temperature ordered phase (T < 85K) as observed by Julian and Luty.[4] The activation energies observed for the mixtures are lower than those seen in KCN (where

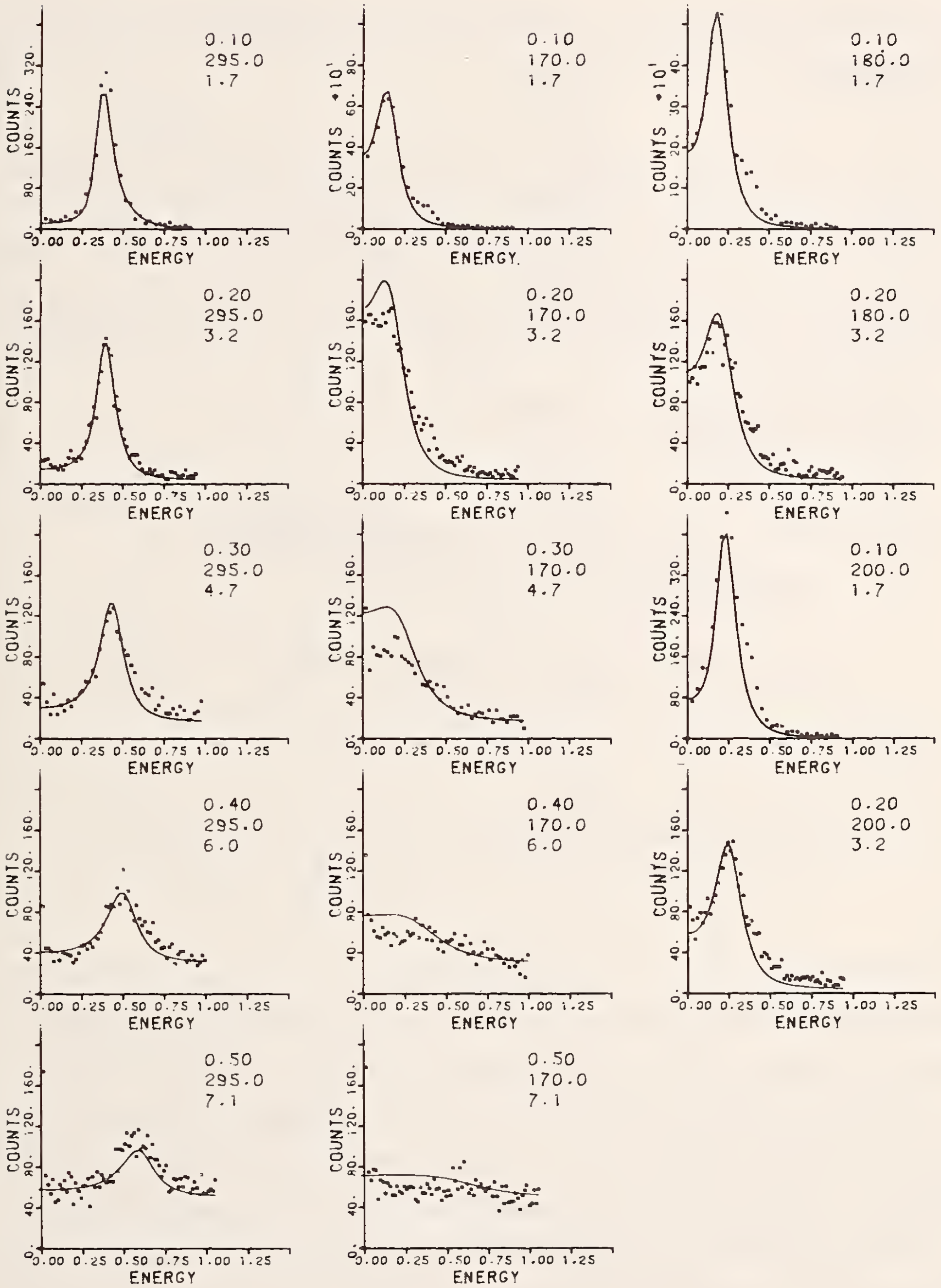

Figure 1. Observed and calculated neutron line shapes for pure KCN at various temperatures and wave vectors along the [100] direction. On each figure, the first number is the wave vector (along [100]), the second is the temperature of measurement, and the third is the "bare phonon" energy in meV. Energies are plotted as fractions of the "bare phonon" energy.

only 180 flips are possible) by an amount not inconsistent with the lower symmetry in pure KCN.

---

1. D. Sohu and S. D. Mahanti (private communication, in press).
2. A. Loidl, R. Feile, and K. Knorr, *Phys. Rev. Letters* 48, 1963 (1982).
3. S. Bhattacharya, S. R. Nagel, L. Fleishman, and S. Susman, *Phys. Rev. Letters* 48, 1267 (1982).
4. M. Julian and F. Lüty, *Ferroelectrics* 16, 201 (1977).

INVESTIGATION OF THE MAGNETIC AND SUPERCONDUCTING TRANSITIONS IN $(Er_{1-x}Ho_x) Rh_4B_4$

J. W. Lynn
(Univ. of Maryland, College Park, MD)
and
(National Bureau of Standards, Washington, DC)

and

R. N. Shelton
(Iowa State University, Ames, IA)

and

C. J. Glinka

We have been studying the pseudoternary alloy $(Er_{1-x} Ho_x)Rh_4B_4$ in the vicinity of the multicritical point at x=0.9 where the ferromagnetic and superconducting phase boundaries converge[1]. For x=0.89, just below the multicritical point, neutron powder diffraction measurements revealed a second order ferromagnetic transition occurring at Tm=5.56K.[2] This transition was notable for the mean-field like temperature dependence of the order parameter and the absence of any observable critical scattering. Most significantly, bulk susceptibility measurements showed that the sample is superconducting over a narrow temperature interval ($\sim$0.2K) centered about T_m thereby implying the coexistence of superconductivity with long range ferromagnetic order.

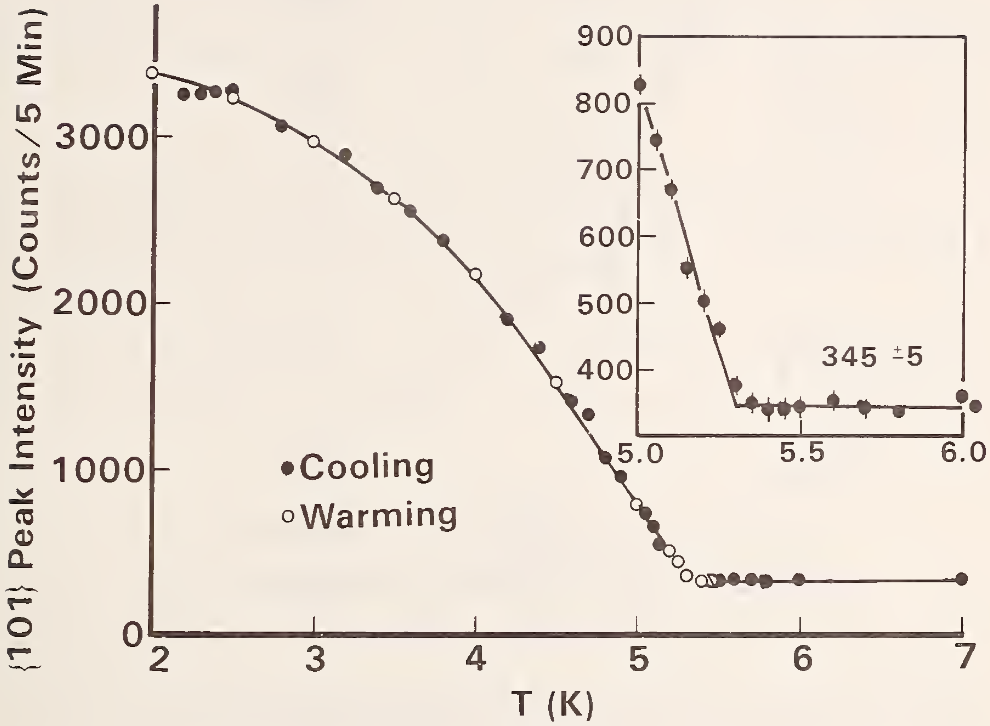

Figure 1. Observed peak intensity of the (101) Bragg peak, demonstrating that there is a ferromagnetic phase transition at 5.3K in $(Er_{.16}Ho_{.84})Rh_4B_4$.

Because the temperature interval where the coexistance appears to occur for x=0.89 is so narrow, measurements have been extended to a sample with x=.84 which has a larger superconducting interval. Bulk susceptibility data for the $(Er_{.16}Ho_{.84})Rh_4B_4$ sample established that at I_{c1}=5.95K the sample becomes superconducting and then at T_{c2}=4.95K reenters the normal state. The (101) Bragg peak intensity displayed in figure 1 exhibits a ferromagnetic transition at Tm=5.3K, well within the boundaries of the superconducting phase. Note that the magnetic intensity is continuous and shows no hysteresis. These data give strong support to the hypothesis that a ferromagnetic component to the magnetization coexists with superconductivity.

An important question to answer is whether there is an oscillatory

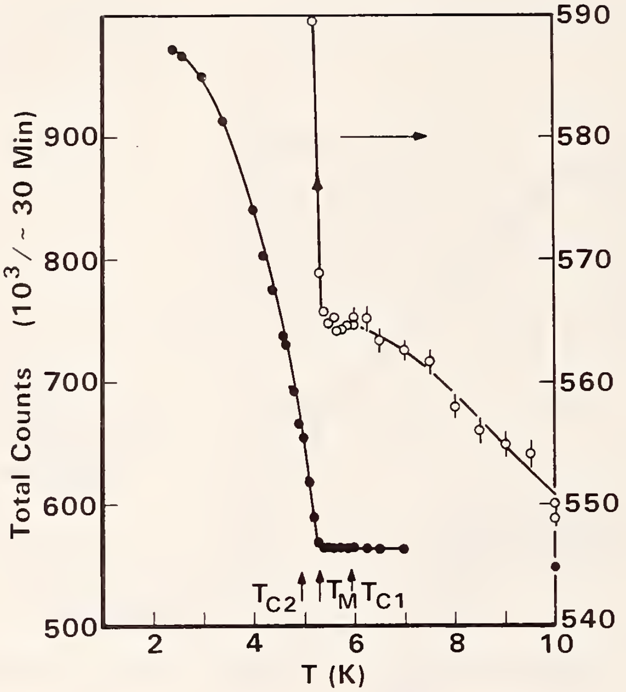

Figure 2. Total intensity of the two-dimensional SANS detector showing the abrupt onset of scattering at small angles at T_m.

component to the magnetization as was observed in ErRh$_4$B$_4$.[3,4] To this end, small-angle scattering data were collected with the new SANS instrument at the NBSR over a Q-range from 0.003 Å^{-1} to 0.1 Å^{-1}. Figure 2 shows the total intensity in the two-dimensional position sensitive detector as a function of temperature. Below the ferromagnetic transition intense small-angle scattering is observed, with an intensity that varies as Q^{-4} at each temperature. This Q-dependence is consistent with the assumption that the scattering originates from domain walls whose widths are large compared to the inverse Q range explored (∿300 Å). No evidence for an oscillatory component to the scattering was observed at any temperature. For temperatures between T_m and T_{c1} we did observe a reduction of the scattering at the smallest wave vectors (<.006 Å^{-1}) consistent with the expected suppression of the paramagnetic scattering due to diamagnetic screening by the superconducting electrons. Further work to observe this effect in other superconductors with magnetic consistuents is now underway.

1. H. B. MacKay, et al *Phys. Rev. Lett.* 42, 918 (1979)

2. J. W. Lynn, R. N. Shelton, H. E. Horng, and C. J. Glinka, (submitted for publication).

3. D. E. Moncton, et. al. *Phys. Rev. Lett.* 39, 1164 (1977).

4. S. K. Sinha, et. al. *Phys. Rev. Lett.* 48, 950 (1982).

FERROMAGNETIC AND SPIN GLASS BEHAVIOR NEAR THE CRITICAL CONCENTRATION IN AMORPHOUS $(Fe_xNi_{1-x})_{75}Gl_{25}$

J. W. Lynn and R. W. Erwin
(Univ. of Maryland, College Park, MD)
and
(National Bureau of Standards, Washington, DC)

and

J. J. Rhyne

and

H. S. Chen
(Bell Laboratories, Murray Hill, NJ)

We are investigating the random amorphous magnetic alloys, $(Fe_xNi_{100-x})_{75}P_{16}Al_3$, just above the critical concentration for long range order ($x_c = 17$) via neutron scattering. It is found that the behavior of the system shifts from ferromagnetic (FM) to spin-glass like (SG) as the temperature is lowered, and a temperature interval within which SG and FM states coexist is indicated. Whether this SG state is a true thermodynamic phase as formulated by Edwards and Anderson[1] or represents a gradual freezing of spins is still an open question.

For the composition x=30, the paramagnetic to FM phase transition is at T_c = 255K as determined by susceptibility data. Measurements of

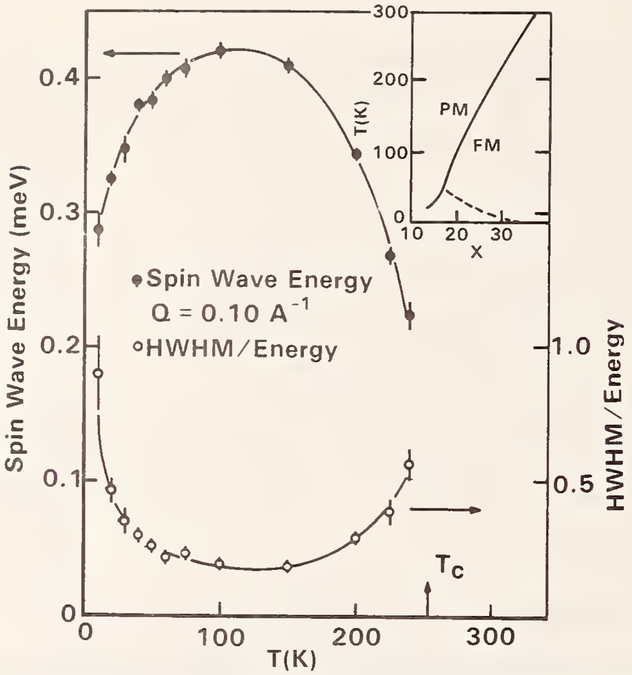

Figure 1. Spin wave energy and intrinsic half-width divided by the energy as a function of temperature. With decreasing temperature the energy and lifetime increase, but then decrease at lower temperatures as the spin-glass state is approached. The solid curves are a guide to the eye. The inset shows the phase diagram for the system as determined by low-field susceptibility and magnetization measurements.[1]

the spin wave (SW) energies and linewidths for this alloy are shown as a function of temperature in figure 1 for a wave vector, $Q = .10\text{Å}^{-1}$ The renormalization of the excitation energies as predicted by SW theory is observed below T_c, but at lower temperatures the SW spectrum begins to collapse.[2] These results are consistent with low-field susceptibility measurements[3,4] which suggest the disappearance of FM long range order at a reentrant temperature, T_R=8K.

Measurements of the temperature dependence of the elastic component of the magnetic scattering establish a spin-freezing temperature, T_f=20K as shown in Figure 2. The spins are at least frozen on a time scale of 4×10^{-9} sec as determined by an upper limit to any intrinsic linewidth of the elastic scattering. Truly elastic scattering [S(E)] would be a direct measure of the SG order parameter as it would imply the existence of an infinitely lived state. We remark that if the system were an ideally random Edwards-Anderson SG, then the intensity of the elastic scattering

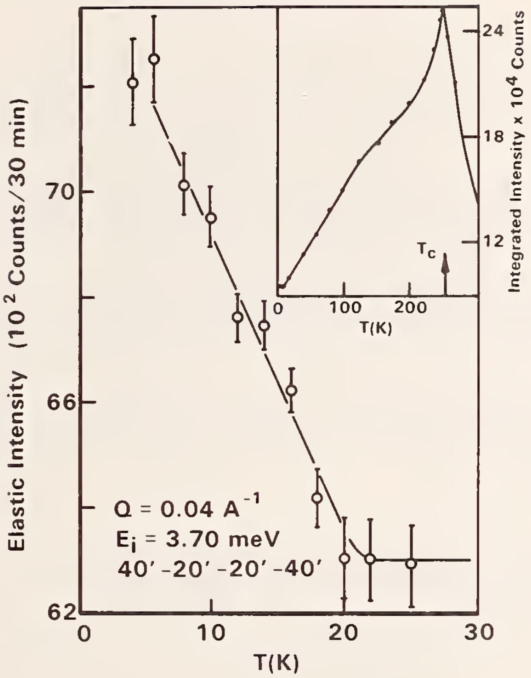

Figure 2. Elastic scattering and the energy integrated (total) scattering as a function of temperature for $Q = 0.04$ Å^{-1}. The elastic component is directly related to the spin-glass order parameter.

would be independent of wave vector. In these relatively concentrated systems, however, we find that there are short-range FM correlations between the spins, which give a wave vector dependence to the elastic scattering. If these frozen spatial correlations are temperature dependent (e.g., the size of an average magnetic cluster is a function of temperature) then the intensity at any particular value of the wave vector would be a product of the order parameter and the static correlation function. We are not able to separate these two contributions at present. Nevertheless, the relatively sharp onset of the elastic scattering is suggestive of the occurrence of a phase transition. The freezing temperature, T_f, obtained is not dependent on the wave vector and is well above the reentrant FM temperature, T_R. We interpret these results as indicating that the SG state develops before the FM state is completely destroyed, so that the two phenomena coexist over a region of temperature. This interpretation is consistent with our inelastic scattering measurements (figure 1) which show that the SW excitations exist below 20 k and become overdamped around $T_R \sim 8$K, and not $T_f \sim 20$K.

---

1. S. F. Edwards and P. W. Anderson, *J. Phys. F.* 5, 965 (1975).

2. J. W. Lynn, R. W. Erwin, J. J. Rhyne, and H. S. Chen, *J. Appl. Phys.* 52, 1738 (1981). Experimental details can be found here.

3. S. M. Bhagat, J. A. Geohegan, and H. S. Chen, *Sol. St. Commun.* 36, 1 (1980); J. A. Geohegan and S. M. Bhagat, *J. Magn. Magn. Mater.* 25, 17 (1981).

4. S. M. Bhagat, J. A. Geohegan, M. L. Spano, and H. S. Chen, *J. Appl. Phys.* 52, 1741 (1981).

SPIN WAVES IN AMORPHOUS $Fe_{1-x}B_x$ ALLOYS

J. J. Rhyne

and

G. E. Fish
(Allied Corporation, Morristown, NJ)

and

J. W. Lynn
(Univ. of Maryland, College Park, MD)
and
(National Bureau of Standards, Washington, DC)

Amorphous alloys of composition $Fe_{1-x}B_x$ can be prepared by melt-spinning techniques throughout the composition range (1,2) from x=0.12 up to about x=0.28. In the vicinity of $x \approx 0.17$, these alloys have been shown to exhibit Invar characteristics (3,4) in which their normal thermal contraction is nearly completely compensated by a large positive magnetostriction. As a function of increasing Boron composition, the Curie temperature increases from 509 K (x=0.12) to 760 K (x=0.28), and a corresponding decrease occurs in the Fe moment from 2.14 μ_B to 1.94 μ_B[1]. The alloys show progressive crystallization at elevated temperatures (2). Initial crystallization temperatures range from 570 K for x-0.12 and increase with boron concentration up to about 685 K for x=0.26. For $x \gtrsim 0.20$, the alloys crystallize below their Curie temperature.

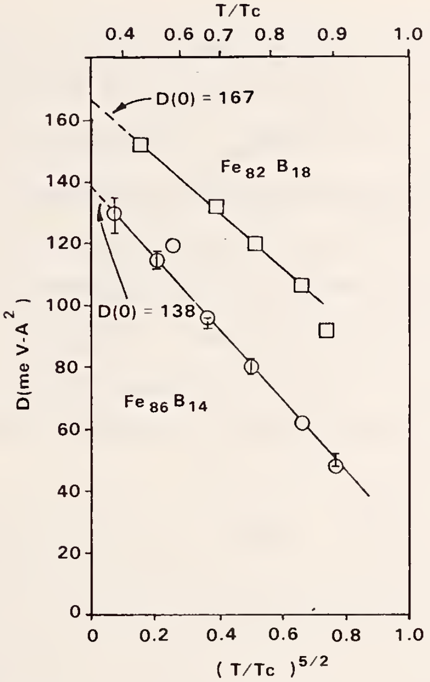

Figure 1. Temperature dependence of spin-wave stiffness for $Fe_{86}B_{14}$ and $Fe_{82}B_{18}$. The data points are the average values for D obtained after resolution correction of the spin-wave energy for $0.06 < q < 0.10$ Å^{-1} ($Fe_{86}B_{14}$) and $q = 0.08$ Å^{-1} ($Fe_{82}B_{18}$). The error bars represent the variation in D obtained from the range of q's measured.

Magnetization measurements (1) have shown a proportionality between the magnetization and $T^{3/2}$, characteristic of linear spin-wave behavior, over an unusually wide range up to $T/T_c \approx 0.33$. From the observed magnetization and the relationship $M(T) = M(0)\ (1-B\ T^{3/2})$ values of the coefficient B have been determined (1). The spin-wave stiffness D predicted by the magnetization can then be calculated from $B = 2.6212 \dfrac{g\mu_B}{M(0)} \left(\dfrac{k_B}{4\pi D}\right)^{3/2}$. The derived values of D can then be compared to those determined directly from the spin-wave dispersion as measured by inelastic neutron scattering, $E = E_g + D(T)\ q^2$, where E_g is the spin-wave energy gap at zero wavevector transfer $q = 0$. For most amorphous alloys, E_g is immeasurably small. Higher order terms in eq. (3) have also been found to be small.

We have performed inelastic neutron scattering on the amorphous alloys $Fe_{86}B_{14}$, $Fe_{82}B_{18}$, and $Fe_{76}B_{24}$, prepared in ribbon form by the inside-roll-chill-block melt-spinning techniques in vacuum. Boron enriched to 98.5 percent ^{11}B was used to reduce the neutron absorption and the ribbons were wound between two aluminum posts to produce a flat plate-like sample of optimum absorption thickness. Neutron data were taken in a vacuum furnace on a conventional triple-axis spectrometer, taking precautions to minimize air and sample-container scattering at the small q required for these studies.

Amorphous alloys require inelastic scattering experiments to be done near the forward beam position ([000] in reciprocal space), and thus neutron energy and momentum conservation conditions place severe limitations on the range of E and q space accessible for measurements. This is particularly critical for measurements on alloys with the larger spin stiffness D. Depending on the alloy and temperature range, useful data were obtained from $q = 0.08 \text{ Å}^{-1}$ up to $q > 0.20 \text{ Å}^{-1}$. Elastic resolution width was approximately 0.8 MeV. Spin waves for both neutron energy gain ($E < 0$) and energy loss ($E > 0$) were easily observable and well resolved up to temperatures where they merge with the central peak (elastic) scattering.

For the $Fe_{86}B_{14}$ alloy, which has a Curie temperature of 556 K, meaningful spin-wave data were obtained over the range from 200 K ($T/T_c = 0.36$) up to 548 K ($T/T_c = 0.99$). For $Fe_{82}B_{18}$ ($T_c = 617$ K), data were taken from room temperature ($T/T_c = 0.48$) up to 548 K ($T/T_c = 0.89$). The spin-wave linewidths observed for all temperatures below 0.9 T_c were that of the instrumental resolution. Above 500 K the $Fe_{86}B_{14}$ alloy, which has the lower Curie temperature, showed distinct linewidth broadening which increased rapidly as T_c was approached. At 513 K the observed width was 1.0 MeV, almost double the instrumental width of 0.55 MeV. (The intrinsic spin-wave width is less than the elastic resolution of 0.8 MeV due to focussing effects.) After resolution corrections were applied, the dispersion data for these alloys were quadratic in q ($E = Dq^2$). The third alloy, $Fe_{76}B_{24}$, ($T_c = 723$ K) exhibits a higher spin stiffness which is almost beyond the range of these neutron experiments. Meaningful results could be obtained only at q = 0.08 Å and for temperatures above approximately 450 K (T/T_c=0.62).

Figure 1 is a plot of the temperature dependence of the values of D for two alloys. As shown, the spin-wave stiffness exhibits the following $T^{5/2}$ renormalization over virtually the entire temperature range studied:

$$D(T) = D(T = 0) \left(1 - a \frac{T}{T_c}\right)^{5/2} \tag{2}$$

The validity of the $T^{5/2}$ relationship over this wide of a temperature region is anomalous and would be expected to result in significant departures of the magnetization from the $T^{3/2}$ low-temperature behavior As mentioned earlier (1,5), these departures are not observed for $T < 0.33\ T_c$. The $(T/T_c)^{5/2}$ dependence of the spin-wave stiffness is consistent with that derived theoretically for a two-magnon interaction for a Heisenberg spin system and is the same behavior seen in crystalline Invar-type alloys $Fe_{65}Ni_{35}$ and Fe_3Pt (6) and in an independent study of the amorphous alloy $Fe_{88}B_{14}$ (7). The $Fe_{76}B_{24}$ alloy data do not appear to follow the $T^{5/2}$ dependence; however, this is not considered significant due to their limited range and lower reliability. The 0 K extrapolated values of D for each alloy and the slope D(0)a of eq. (2) are listed in Table I. For $Fe_{86}B_{14}$, values of D(T = 0) are somewhat higher than that found by Ishikawa (7) et al. with a more rapid decrease of D with temperature than reported in ref. 7. They also find a nonzero value for the gap parameter E_g [eq. (1)] which we do not observe after accurately correcting the raw data for the calculated instrumental resolution. This correction was also verified experimentally by introducing additional vertical collimation. Also included in the table are values of D derived by Hasegawa and Ray (1) from their low temperature magnetization studies which values are in substantial agreement

Table 1. Neutron and Magnetization Determined Values of Spin Stiffness, D, for T = 0 K. The units of D are MeV-Å^2.

	$Fe_{86}B_{14}$	$Fe_{82}B_{18}$	$Fe_{76}B_{24}$	$Fe_{83}B_{16.5}Si_{.05}$
D(T = 0)	113	167	>175*	125 (ref. 8)
(neutron)	118 (ref. 7)			
D(T = 0) (magnet.)	65	71	96	--
D(0)a	115 94 (ref. 7)	90	--	

* Approximate value, limited by energy-momentum restrictions of experiment.

with those from Mössbauer results by Chien et al. (5). Comparison of these values illustrates the second anomaly of $Fe_{1-x}B_x$ spin-wave results. The neutron-determinated D is almost twice as large as that calculated from magnetization. At the same time $D_{neutron}/T_c$ has approximately the same ratio (0.25 for $Fe_{82}B_{18}$ and 0.21 for $Fe_{86}B_{14}$) at room temperature as those found for other amorphous alloys (8) which do not exhibit similar discrepancies in the value of neutron- and magnetization-determined values of D. Similar anomalies have been reported for the $Fe_{65}Ni_{35}$ and Fe_3Pt crystalline alloys (6). These results suggest that both the wide-range of the $(T/T_c)^{5/2}$ dependence of the spin stiffness D and the anomalously small values of D may be intrinsic, but not yet understood, dynamic properties of the magnetic and magneto-elastic interactions peculiar to the Invar state. Preliminary examination of the temperature and q-dependence of the quasi-elastic peak intensity (see Fig. 1) shows that additional magnetic scattering is present and possibly represents a spin diffusion phenomena in these alloys. This is being investigated further as an explanation for the inability of the neutron-determined spin-wave stiffness to account for a significant portion of the reduction in bulk magnetization with temperature.

1. R. Hasegawa and R. Ray, *Phys. Rev.* B20, 211 (1979).
2. R. Hasegawa and R. Ray, *J. Appl. Phys.* 49, 4174 (1978).
3. K. Fukamichi, m. Kikuchi, S. Arakawa, and T. Masumoto, *Solid State Commun.* 23, 955 (1977).
4. K. Fukamichi, H. Hiroyoshi, M. Kikuchi, and T. Masumoto, *J. Mag. Magn. Matls.* 10, 294 (1979).
5. C. L. Chien, D. Musser, E. M. Gyorgy, R. C. Sherwood, H. S. Chen, F. E. Luborsky, and J. L. Walter, *Phys. Rev. B* 20, 283 (1979).
6. S. Ohodera, y. Ishikawa, and K. Tajima, *J. Phys. Soc. Japan* 50, 1513 (1981).
7. Y. Ishikawa, K. Yamada, K. Tajima, and K. Fukamichi, *J. Phys. Soc. (Japan)* 50, 1958 (1981).
8. Summarized in J. J. Rhyne, J. W. Lynn, F. E. Luborsky, and J. L. Walter, *J. Appl. Phys.* 50, 1583 (1979) and in ref. 6.

SPIN DYNAMICS OF $HoAl_2$

J. J. Rhyne

and

N. C. Koon
(Naval Research Laboratory, Washington, DC)

$HoAl_2$ is part of a class of rare earth compounds in which the exchange and crystal field interactions are of comparable magnitude, and thus the magnetic behavior may be expected to be very different from more conventional ordered systems (e.g., rare earth iron compounds) in which the exchange interaction clearly dominates. Neutron inelastic scattering provides direct information on the energies and q dependence of the magnetic excitations, and by analysis of the dispersion curves, rather precise values of the rare earth exchange and crystal field parameters can be determined.

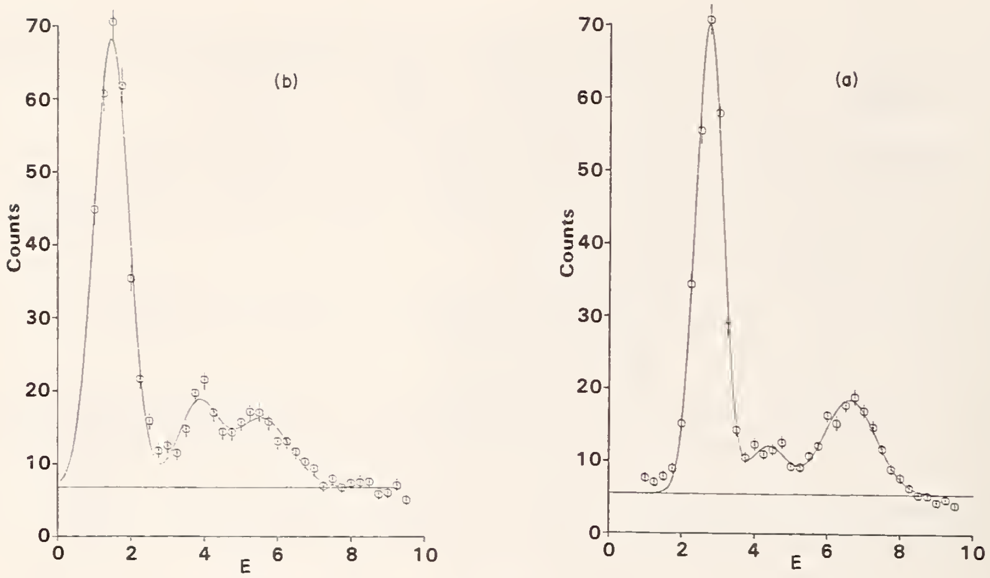

Figure 1. Intensity versus constant-q scan along [q,q,0] at 4K in $HoAl_2$. Data are shown for in-phase modes (left) observable in the zone centered at (2,2,0) and for out-of-phase modes (right) observable at (0,0,2). Three excitations are observable in the energy range studied.

$HoAl_2$ crystallizes in the cubic Laves phase structure (C15) with a lattice parameter of 7.79 A at 4.2 K. The low Curie temperature of 28 K reflects the weak rare earth exchange. The primitive unit cell contains two Ho atoms and thus gives rise to both acoustic (in phase) and optic (out of phase) magnetic modes. There are two distinct Ho-Ho exchange constants, one which couples Ho atoms on the same sublattice (J) and the other which couples Ho atoms on different sublattices (J').

Inelastic scans were taken at 4 K for magnons propagating along all three principal symmetry directions, [q,0,0], [q,q,0], and [q,q,q] and throughout the Brillouin zones centered at (220) and (002). The (220) is an allowed Bragg reflection which arises from only the Ho atoms, while the (002) position is a forbidden lattice reflection. The dynamic structure factor provides a convenient separation of the modes into those resulting from an in-phase precession of the two distinct Ho spins (observable only in the (220) zone), and those resulting from an out-of-phase precession (observable only in the (002) zone).

Figure 1 shows a typical constant q scan of scattered neutron intensity versus energy transfer and the resulting dispersion relations are given in figure 2, for modes propagating in the three symmetry directions. The excitations in the (220) zone are shown by the circle symbols and those in the (002) zone by the square symbols. Error bars are those derived from the least squares fitting of the intensity data. All modes show relatively small dispersion reflecting the weak Ho-Ho exchange interaction. The finite energy gap at q = 0 is a result of the crystal field effect on the spin waves. Significant anisotropy with propagation direction is evident for the higher q.

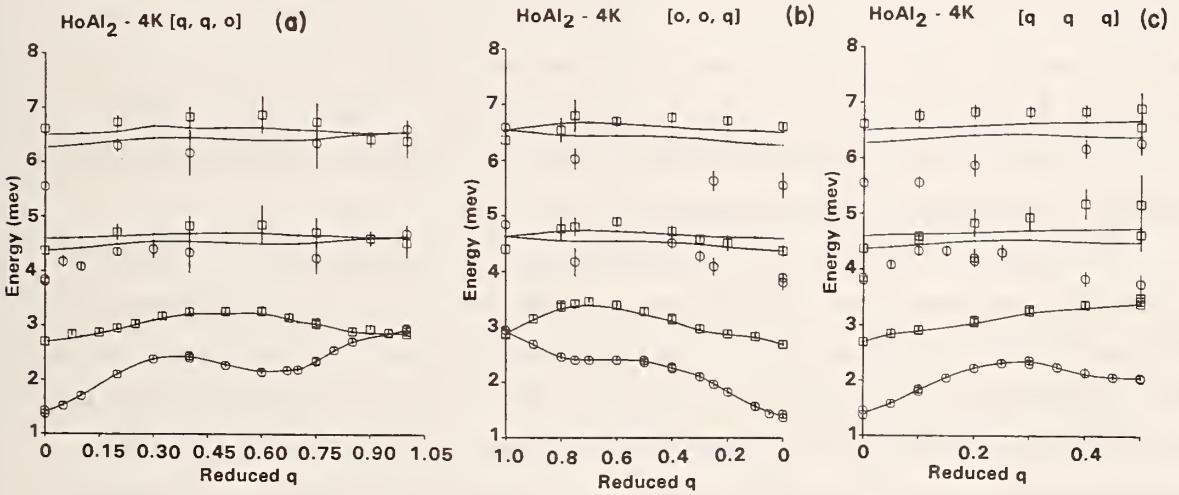

Figure 2. Dispersion curves for $HoAl_2$ at 4K for excitations propagating along all three symmetry directions. The in-phase modes are shown by the circles and the out-of-phase modes by the square symbols. The solid lines are the result of the theoretical fit using $A_4^0 = 1.7$ meV/a_o^4 and $A_6^0 = 0/092$ meV/a_o^6 and $J(0)+J'(0) \cong 0.06$ meV (see text).

The dispersion curves of figure 2 have been analyzed to obtain consistent values of the Ho-Ho exchange parameters and the two crystal field parameters A_4^0 and A_6^0 appropriate to cubic symmetry. The calculated values are given in the caption and the theoretical dispersion curves are shown as the solid lines in figure 2. A Green's function standard basis operator technique in the random phase approximation was used to analyze the data. The low T theoretical neutron scattering cross-section is proportional to a dynamic susceptibility which in turn involves ground state matrix elements $<m|S^{+}|0>$, $<m|S^{-}|0>$, and $<m|S^{z}|0>$ which give rise to transverse excitations (S^{+} and S^{-}) and to longitudinal excitations (S^{z}) respectively. In the low T limit only the S^{-} and S^{+} matrix elements have significant strength in the case of $HoAl_2$, and they have finite values for m = 1,3,5,7,...15 with only the first three values giving rise to experimentally observable scattering as shown in figures 1 and 2. The theoretical relative intensity of the lowest three modes is very sensitive to the values of the crystal field parameters A_4^0 and A_6^0. The relative intensity ratios determined from experiment plus the mode energies at the zone center and boundary enabled a set of crystal field constants A_4^0 and A_6^0 and values of $J(0) \pm J'(0)$ to be determined. These values were then held constant and the q-dependent values of the exchange $J(q)$ and $J'(q)$ were determined from the dispersion of the lowest two modes.

The observation that finite dispersion is observed in all modes immediately indicates that the Ho-Ho exchange interaction is weak but not vanishingly small, in contrast to the case in both rare earth iron and rare earth cobalt Laves phase compounds previously studied by inelastic neutron scattering.[2] In the iron and cobalt materials the rare earth-rare earth exchange interactions were negligibly small as manifested by the absence of dispersion in the rare earth dominated out of phase modes.

---

1. C. M. Williams, N. C. Koon, and B. N. Das, *J. Appl. Phys.* 50, 1669 (1979), and from total neutron scattering measurements in the present study.

2. N. C. Koon and J. J. Rhyne, *Crystalline Electric Field and Structural Effects in f-electron Systems,* edited by J. E. Crow, R. P. Guertin, and T. W. Mahlinsin (Plenum, New York 1980), 125-140.

SMALL ANGLE MAGNETIC SCATTERING FROM AMORPHOUS $TbFe_2$

J. J. Rhyne and C. J. Glinka

Amorphous $TbFe_2$ has a magnetic phase transition at about 135 °C (T_c) to a state which bulk measurements[1] indicate has long-range magnetic order. Small-angle neutron scattering (SANS) measurements made some years ago[2] revealed, however, only a weak, rounded anomaly in the low-angle scattering as a function of temperature in the vicinity of the phase transition. Moreover, below T_c the scattering at the smallest angles continued to increase, which is quite uncharacteristic of a transition to a long-range ordered state. This behavior has been viewed as indicating that the magnetic ordering develops over regions of about 100 Å in linear dimension but no further. As the temperature is lowered below T_c, the degree of order within these regions increases, but the overall sizes of the regions change very little.

Recently the new SANS facility at the NBSR has been used to study the phase transition in $TbFe_2$ at smaller scattering vectors Q than were accessible in the earlier work[2]. An incident wavelength of 6.25 Å, combined with only moderate pinhole beam collimation, was used to cover the Q-range from 0.014 to 0.12 $Å^{-1}$. The temperature dependence of the scattering near T_c for several of the smaller Q-values is shown in figure 1. Here it can be seen that the inflection in the scattering near T_c is most evident at a Q of about 0.03 $Å^{-1}$. At smaller Q's, nearly all indication of an anomaly is obscured by the strong scattering below T_c. This is in contrast to conventional transitions to long-range order which exhibit anomalies which sharpen as Q is reduced.

The Q-dependence of the scattering at selected temperatures both above and below T_c is shown in figure 2 where the inverse intensity I^{-1} is plotted versus Q^2. Above T_c, the scattering is Lorentzian, $I^{-1} \propto (\kappa^2 + Q^2)$ with a correlation range, $\xi = \kappa^{-1}$, which reaches 135 Å at T = 135 °C. Whether or not ξ increases further as the temperature is

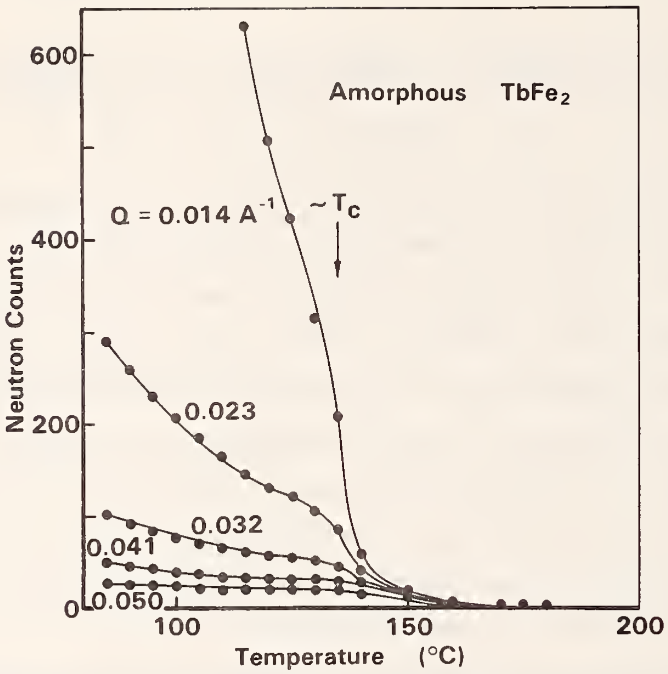

Figure 1. Temperature dependence of the small-angle scattering from $TbFe_2$ in the vicinity of the magnetic phase transition.

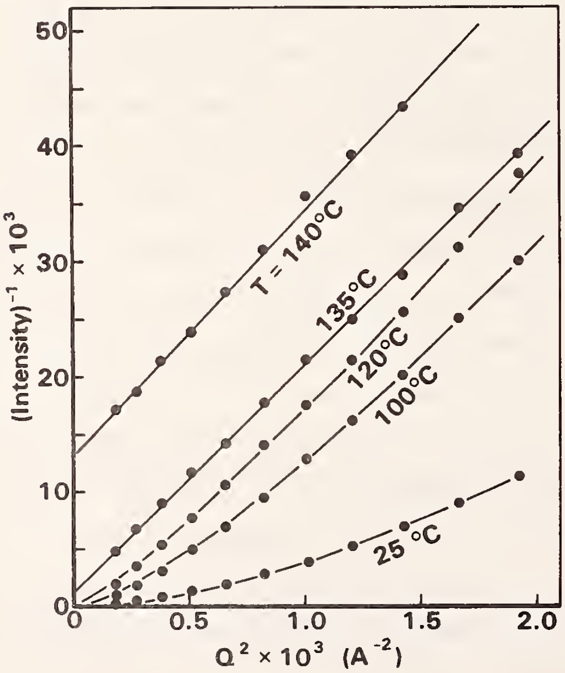

Figure 2. Inverse small angle scattering intensity from $TbFe_2$ plotted versus Q^2 ($0.014 < Q < 0.05$ $\mathring{A}^{-1}$) at selected temperatures above and below T_c. The dashed curves are power law fits ($I^{-1} \propto Q^x$) to the data below T_c.

lowered is difficult to say, since the shape of the scattering gradually changes from Lorentzian to a simple power law, $I^{-1} \propto Q^x$, and appears to diverge at Q = 0 for all temperatures below about 130 °C. At 25 °C, the exponent $x \sim 3$ and changes little at lower temperatures.

The scattering which develops below T_c finally saturates at about 40 K. The shape of this scattering was studied using incident wavelengths between 5 and 8 Å in order to determine if any of this scattering were due to multiple refraction from magnetic domains (beam broadening due to refraction varies as λ^2). The Q-dependence of the scattering was found to be independent of λ, thereby confirming that it arises from diffraction from regions far smaller than typical magnetic domains (typical dimensions of 1-10 μm.). This result and those discussed above agree with earlier measurements and support the hypothesis that finite rather than infinite-ranged magnetic ordering occurs in amorphous $TbFe_2$.

---

1. J. J. Rhyne, J. H. Schelleng, and N. C. Koon, *Phys. Rev.* B10, 4672 (1974).
2. J. J. Rhyne, S. J. Pickart, and H. A. Alperin, *Phys. Rev. Lett.* 29, 1562 (1972).

ADVANCED NEUTRON METHODS

J. M. Rowe, C. J. Glinka, N. Berk
J. LaRock, R. Williams and D. Fravel

1. Small angle Neutron Scattering (SANS)

The new facility for SANS[1] became fully operational in the Fall of 1981 following the installation and calibration of the instrument's 65 cm x 65 cm position-sensitive detector. Figure 1 is an overhead view of the instrument showing the post-sample flight path which houses the detector and the associated data acquisition system. Some minor electronic and computer software problems which arose during the first few months of operation have now been corrected and over the past four months (April-July 1982) the instrument has functioned properly more than 95% of the time. The operating characteristics of the facility, now well established by actual measurements, are summarized in table 1.

Over the past year a number of enhancements to the basic instrument have been added. An automatic multiple sample changer has been installed in the facility's evacuated sample chamber. Up to four samples can be run in any sequence entirely under computer control. A sample stage is available, primarily for polymer and biological specimens, which is equipped with cooling coils and individual heaters and thermocouples for each of four sample positions. To facilitate sample positioning, a low power laser has been built into a rotating beam shutter at the entrance to the pre-sample flight path. The laser can be rotated into the beam at any time to check the alignment of a sample. Computer control of the temperature settings of a closed cycle helium gas refrigerator and an aluminum vacuum furnace has been implemented thereby providing convenient access to temperatures from 10 to 700 K. Horizontal and vertical field electromagnets have also been adapted for use at the facility for measurements in magnetic fields up to 10 kgauss.

Computer software for handling the large data arrays (128 x 128) generated with the area detector has been developed to the point where data sets can be reduced rapidly and interactively, with the aid of a color graphics display terminal, to obtain intensity versus scattering vector curves in a few minutes. This capability significantly improves the efficient use of the facility by enabling users to assimilate and assess data as it is being collected. Further software development directed toward model fitting and extracting particle size distributions from SANS data is planned for the near future.

Since commencing operation, experimental programs in polymers, metallurgy, biology, solid-state physics and nondestructive testing have been initiated. Many of these have involved collaborations with other NBS Divisions (Polymers, Fracture and Deformation and the Metallurgy Divisions), government (NSWC, NRL, NIH) and industrial (e.g., Union Carbide, Exxon, and Allied Corps.) laboratories and several universities (e.g., Maryland, Illinois, and Northwestern).

From these initial efforts a number of promising results have been obtained. For example, a Fracture and Deformation Division study of prototype ceramics which exhibit large, reversible changes in their bulk moduli as a function of temperature gave strong supporting evidence for the hypothesis that these changes are due to the formation of microcracks. In addition to demonstrating the sensitivity of the technique for detecting microcracks, the SANS measurements provided quantitative estimates of the size and number density of the cracks useful for comparison with theoretical calculations.

In another study involving the Fracture and Deformation Division, an important class of maraging steels has been shown to be ideal for studying the effects of deformation on materials with complex microstructures. By applying a saturating magnetic field, the magnetic scattering, which arises from the contrast between non-magnetic precipitates imbedded in the magnetic host material, can be isolated from scattering due to the formation of voids, for example.

In fundamental studies of superconducting materials which contain magnetic constituents, high resolution SANS measurements have yielded the first preliminary indication of the predicted suppression of the long wavelength magnetic fluctuations in the superconducting state.

More detailed descriptions of these and other examples of SANS related projects initiated to date are summarized in following articles in this report.

Table 1. Operating characteristics of the NBS SANS facility

Wavelength:	variable from 5 to 10 Å ($\Delta\lambda/\lambda \sim 0.25$)
Collimation:	single pair of irises or 9 channel converging collimation
Minimum Q:	0.004 $Å^{-1}$ at 6 Å, 0.003 $Å^{-1}$ at 9 Å
Q Range:	0.003 $Å^{-1}$ to 0.6 $Å^{-1}$
Sample size:	0.4 to 2.5 cm diameter
Flux at sample: (10 MW)	10^4 to 3×10^5 n/cm^2-sec depending on slit sizes and wavelength (these fluxes will double at 20 MW)
Detector:	65 x 65 cm^2 position-sensitive counter with 8 x 8 mm resolution

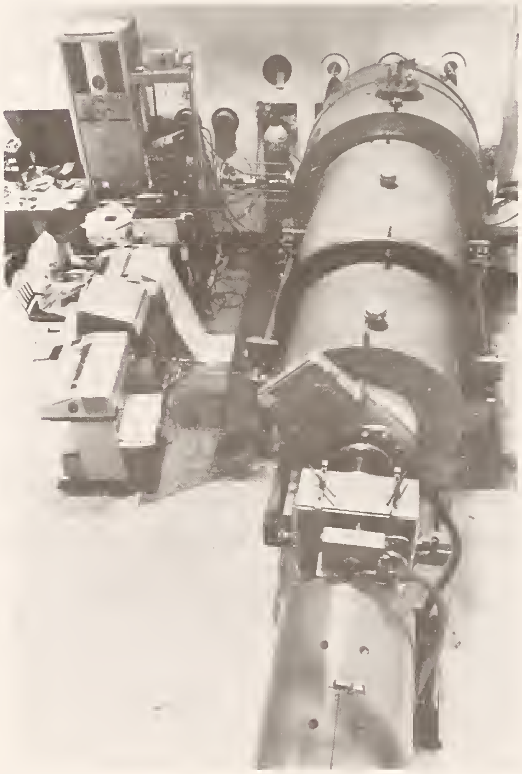

Figure 1. The recently completed small angle neutron scattering instrument showing the post-sample flight path which houses the area detector and the associated data acquisition system.

2. Neutron Time-of-Flight Facility

The NBS time-of-flight (TOF) facility became fully operational during this period. Tests of the resolution and intensity at 6.0, 4.0, and 2.5 Å incident wavelength have confirmed the predicted performance. Data analysis and display programs have been written and tested. Although the background remains higher than desirable, the tests run to date show that the facility is now useable for many experiments. Further developments to further reduce the background are continuing. The data acquisition system includes on-line data display and elementary manipulation, along with a direct link to the VAX computer which allows complete data analysis. As currently configured, the facility comprises 20 banks of two 18" by 1" detectors spanning the angular range from 20° to 106° scattering angle. The incident wavelength can be continuously varied from 1-6 Å, although order contamination is a problem for λ 4A, except at 2.4 and 1.5 Å.

The instrument has been used to measure quasielastic scattering in acetonitrile; diffuse scattering in KCN; the phonon density-of-states in $Vd_{.8}$ and the vibrational density of states on finely divided Pt catalysts.

Future refinements planned for this facility will increase the resolution, decrease the time independent background, and allow data to be taken at lower wave vector transfer.

3. General Instrument Improvements

The triple-axis spectrometer at BT-4 will be extensively modified during the shut down for conversion to 20 MW reactor operation. The modifications will allow higher resolution operation, more rapid conversion to cold neutron studies and lower backgrounds. All of the parts required for this upgrade have been designed and manufactured, and the detailed planning for the conversion is now proceeding.

In the area of sample environmental facilities, a liquid He-3 cryostat has been built and is presently being commissioned. A new, high temperature furnace (∿ 1500 °C) is also under construction.

---

1. C. J. Glinka, Proceedings of the Symposium on Neutron Scattering, Argonne National Laboratory, August 1981 (in press)

INTERNAL EXPANSION FROM BLOCK COPOLYMERS OF h-STYRENE AND d-STYRENE

T. P. Lodge, E. J. Amis, and C. C. Han
(Polymer Science and Standards Division)

and

C. J. Glinka

and

Y. Matsushita, I. Noda, and M. Nagasawa
(Nagoya University, Nagoya, Japan)

The technique of deuterium labelling in SANS makes it possible to investigate the conformational behavior of single molecules or portions of molecules in the presence of many others. This permits experimental results to be obtained which may be compared with theoretical predictions for rather subtle aspects of polymer conformation. In this study this approach has been utilized to investigate the chain length and position dependence of the excluded volume effect; this particular problem has been previously attacked with a variety of techniques including Monte Carlo[1,2], pertubation theory[2,3], and renormalization groups[4,5]. Specifically, the radius of gyration has been determined for a perdeuterated polystyrene of molecular weight about 30,000 dissolved in CS_2, in three different situations: as an isolated molecule, on the end of a larger polystyrene, and in the middle of a larger molecule.

1. Experimental

The three samples were synthesized and characterized as previously described[6]. TUN-01 is a perdeuterated polystyrene of molecular weight 27,000, TUN-14 is a diblock copolymer of perdeuterated polystyrene (M = 27,000) and polystyrene (M = 389,000), and TUN-15 is a triblock with the perdeuterated polystyrene (M = 31,000) sandwiched between two polystyrene ends (M = 140,000 and 122,000). Measurements were made at three concentrations of each sample in CS_2: 0.8%, 1.5%, and 2.5% by weight of polymer. CS_2 was selected because it masks the polystyrene coherent scattering and has no incoherent cross-section. The SANS spectrometer at NBS was used for the study[7]. Incident neutrons of wavelength 5.6 A were employed, with $\Delta\lambda/\lambda = 25\%$. Solutions were contained in a 1 cm path length quartz cell. This arrangement gave an effective q range of 0.014 to 0.13 $\mathring{A}^{-1}$ for these samples; one sample (2.5% TUN-15) was also measured with a high-resolution configuration using a unique focussing collimation system[7]; this extended the effective q range down to about 0.011 $\mathring{A}^{-1}$. Data acquisition is controlled by a dedicated PDP 11/23 computer; data is subsequently transferred to a VAX for analysis. Typical acquisition times were from 8 to 12 hours, depending on sample and concentration.

2. Results and Discussion

For all three samples, the radius of gyration for the perdeuterated blocks were extracted using a nonlinear regression fit to the Debye function. Strictly, this should only be applicable to gaussian chains, whereas CS_2 is a moderately good to good solvent for polystyrene. However, as pointed out by Freed[8], even with fully developed excluded volume the static structure factor S(q) is essentially indistinguishable from the Debye function, if the radius is rescaled. In addition, we have attempted to fit the data to the Ptitsyn Formula[9] with ε either set equal to 0.2 or left floating; no credible fits were obtained. In the Debye function analysis, the baseline was also floated, primarily to account for the small amount of incoherent scattering from the hydrogen present.

Because the data do not extend well into the Guinier region, the extracted values have some sensitivity to the low q limit at which the data are truncated. Thus the fitting was performed after sequentially discarding low q points until the radius values began to change systematically and significantly (1-4%). With the exception of the TUN-15 results, the spread of the values thus obtained is insignificant. Fixed values were obtained by averaging the several individual radii. These results are summarized in Table I, as are the infinite dilution values obtained by least squares. The uncertainties indicated represent the standard deviation which accompanied the average.

In figure 1 the scattering curve for the 2.5% TUN-01 solution (corrected for solvent and cell contributions) is presented. The resulting Debye fit is also shown; the quality of this fit is excellent. The infinite dilution value for R_g of 49.6 Å is in remarkably good agreement with the tabulated value for polystyrene in a theta solvent of about 49 Å[10]. Thus this supports the notion that even in good solvents relatively small polymers do not exhibit much swelling. In figure 2 the scattering curves for the 2.5% TUN-15 solution are shown, for both the regular and the high-resolution runs. The two sets of data have been fitted independently, yielding consistent results; to obtain this plot the high-resolution values have been "normalized" using the intercept and baseline values of the Debye function fits. While the quality of the fit is not as high as with TUN-01, the two separate runs are in very good agreement, and no systematic deviations from the Debye function are apparent.

In figure 3 the extrapolations of R_g to infinite dilution are displayed. The intercept values of R_g are also presented in Table I. Before comparing the results for TUN-14 and TUN-15, it is important to note that the deuterated portions of these two molecules are of different length. If the TUN-15 value of 63.8 Å is scaled to a molecular weight of 27,000, assuming full excluded volume ($R_g \sim M^{0.6}$), a value of 58.7 Å is obtained. This is about 5% greater than the TUN-14 result. In both cases there is considerable swelling relative to the TUN-01 sample. These data represent, as far as we are aware, the first experimental estimate of the so-called "chain end effect" on polymer conformation.

Table I. Values of R_g, A.

	2.5%	1.5%	0.8%	∞ Dilution
TUN-01	37.1 ± 0.3	42.2 ± 0.4	45.6 ± 0.5	49.6
TUN-14	52.1 ± 0.3	53.3 ± 0.1	54.8 ± 0.4	55.9
TUN-15	54.1 ± 1.9	57.4 ± 2.2	50.9 ± 1.2	63.8

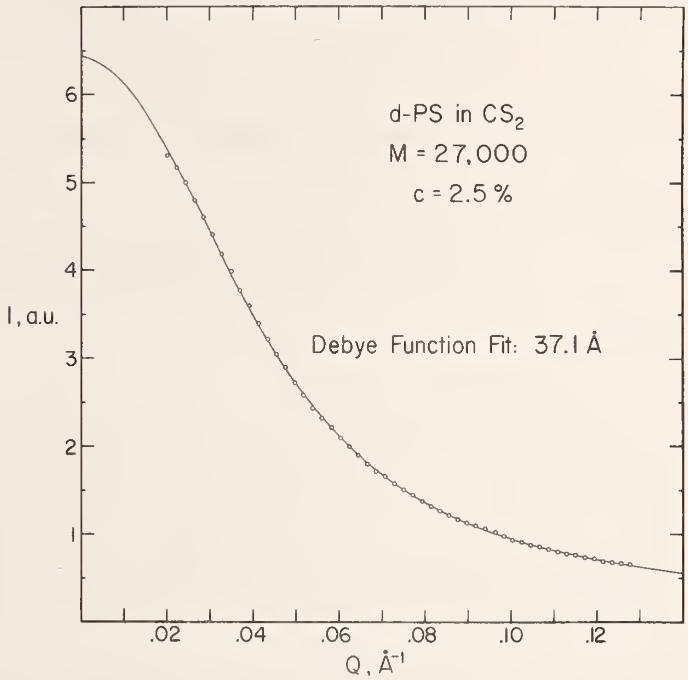

Figure 1. Scattering curve for TUN-01, 2.5% in CS_2. Solid line is Debye function fit.

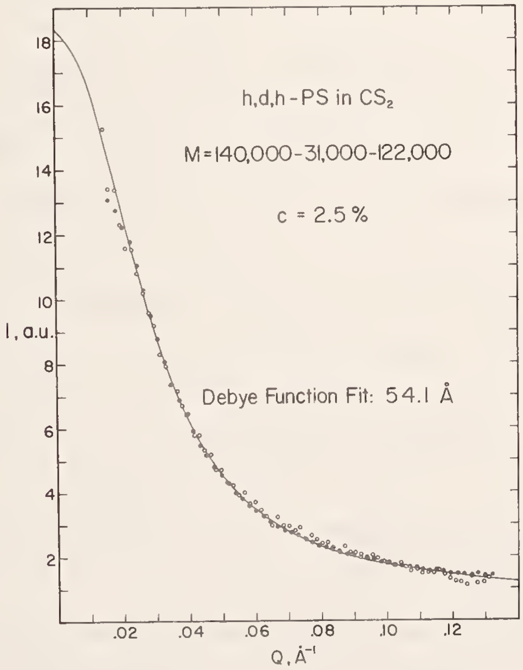

Figure 2. Scattering curves for TUN-15, 2.5% in CS_2: ●-normal resolution, o-high resolution. Solid line is Debye function fit.

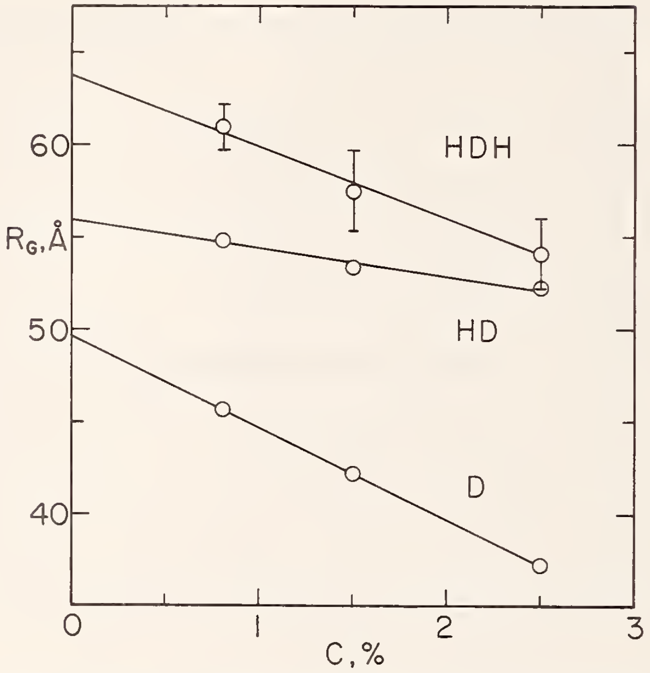

Figure 3. Extrapolation to infinite dilution of R_g values for TUN-01 (D), TUN-14 (HD), and TUN-15 (HDH). Uncertainties indicated as in Table I.

---

1. F. T. Wall and J. J. Erpenbeck, J. Chem. Phys. 30, 637 (1959).

2. A. J. Barrett and W. H. Stockmayer, personal communication.

3. M. Kurata, H. Yunekama, and E. Teramoto, J. Chem. Phys. 28, 785 (1958).

4. J. des Cloizeaux, J. Physique 41, 223 (1980).

5. Y. Oono and T. Ohta, Phys. Lett. 85A, 480 (1981).

6. Y. Matsushita, H. Furuhashi, H. Choshi, I. Noda, M. Nagawawa, T. Fujimoto, and C. C. Han (to be published).

7. C. J. Glinka, Proc. of a Symposium on Neutron Scattering, Argonne National Lab., August 1981.

8. T. Ohta, Y. Oono, and K. F. Freed, Macromolecules 14, 1588 (1981).

9. O. B. Ptitsyn, Zh. Fiz. Khim. 31, 1091 (1957).

10. J. Brandrug and E. H. Immergut, eds. "Polymer Handbook," Wiley: New York, 1975.

STUDY OF POLYMER SURFACTANT COMPLEXES BY SMALL ANGLE NEUTRON SCATTERING

P. S. Leung
(Union Carbide Corporation, Tarrytown, NY)
and
C. Han
(Polymer Science and Standards Division)
and
C. J. Glinka

Subthermal neutrons have an energy and mass appropriate for probing size in the dimensional range of molecular aggregates. The large contrast to neutrons of hydrogen isotopes in hydrogenous materials makes small angle neutron scattering (SANS) unique among scattering techniques and it is particularly useful in separating the contribution of various components in mixed systems. Recently, studies of polymer/surfactant interaction have revealed the presence of molecular complexes between the polymer and the surfactant. The forming of complexes significantly changes the solution properties such as rheology, solubilization, surface activity, etc. However, most available physical measurements cannot distinguish individual contributions in such a mixed system. Thus, the structures proposed have been at best speculative. There have been some initial SANS studies done by groups in France, who used deuterated surfactant and polymer components for this purpose. However, no such study or the interaction of cationic polymer/anionic surfactant systems has been reported so far. Since the latter systems are believed to go through many structural changes depending on the concentration ratio of the two components, we have studied a system containing a cationic polymer and an anionic surfactant in some detail. It was found that a polymer with a rigid extended chain has no significant scattering in the wave vector (Q) range >0.01 $\mathring{A}^{-1}$ due to its large radius of gyration, Rg. By adding a small amount of deuterated anionic surfactant, association occurs leading to significant small angle scattering intensity and corresponding to entities with Rg = 47$\mathring{A}$ (see figure). At surfactant concentrations exceeding the charge neutralization ratio, the deuterated aggragates which form have an Rg of 22Å, which is very close to the size of regular micelles. A somewhat larger polymer segment (Rg=42Å) is simultaneously observed. At even higher surfactant concentrations, a peak appears in the scattering intensity vs. Q plot corresponding most likely to a regular array of micelles. The most probable distance between the surfactant micelles is determined by the balance of free energy of association and the repulsion between the charged miscelles.

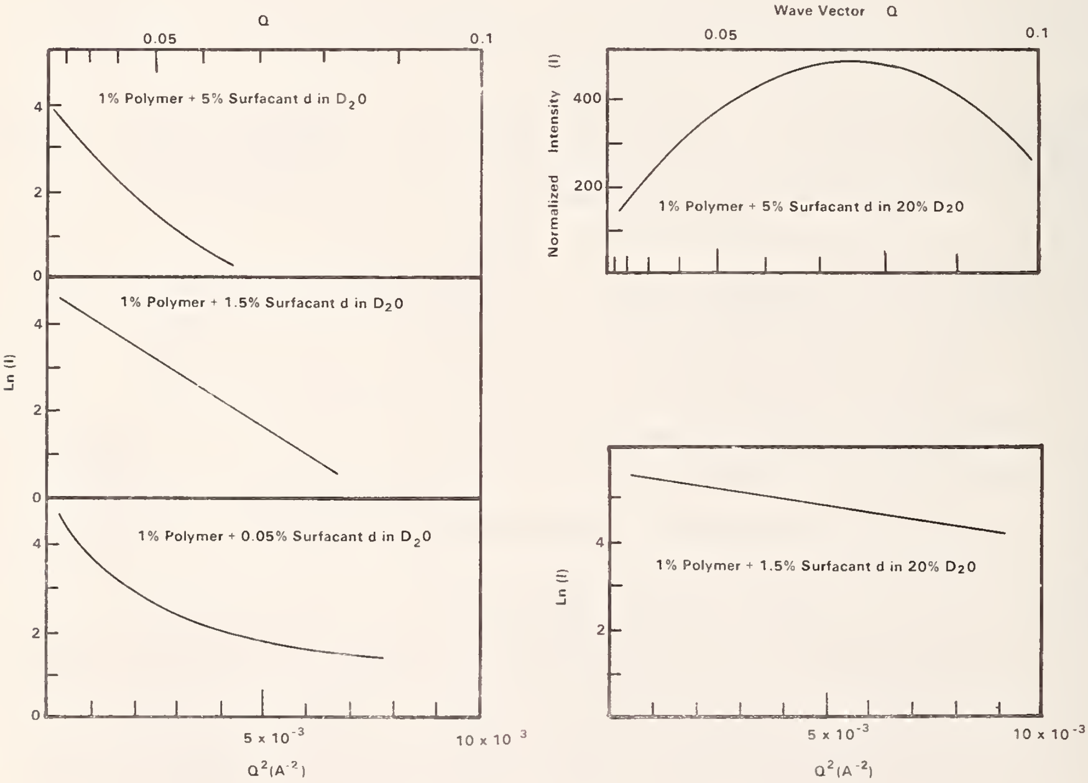

Figure 1. Guinier plot In(I) vs. Q^2 of the radially averaged small-angle scattering from several polymer-surfactant solutions. Contrast matching has been used to study independently the scattering from the polymer (curves on left) and from the surfactant (curves on right).

STRUCTURE FACTOR STUDIES OF A TiCu METALLIC GLASS AS A FUNCTION OF ANNEALING TREATMENT

B. Mozer and S. Singhal
and
A. Maeland
(Allied Chemical Corporation, Morristown, NJ)

Studies were initiated on a two component metallic glass, $Ti_{45}Cu_{45}$, to ascertain what information might be elucidated through small angle neutron scattering (SANS) determinations of the structure factor and through standard neutron diffraction measurements of the structure factor as the alloy is annealed up through the crystalline phase transformation. This particular alloy was fabricated by the Allied Chemical Corporation where its characteristics were determined to be in a state of metallic glass in the physical form of long, thin, narrow ribbons as normally found in the melt spinning methods for producing metallic glass alloys. X-ray diffraction patterns, differential scanning calorimetry, and other standard metallurgical analyses were performed on this alloy in labelling it a well-defined metallic glass.

The titanium alloys, as well as other possible alloy systems that form metallic glasses, can be made in a composition so as to form a "null matrix"[1] neutron scattering system in the liquid state, glassy state, or non-intermetallic crystalline state. Furthermore, this null matrix condition enhances that part of the neutron diffraction associated with short-range order phenomena or microstructure irregularities such as precipitates of 10-1000 Å size as observed in SANS. Neutron diffraction patterns associated with possible short-range orders of various CuTi alloys have been studied with standard neutron diffraction techniques.[2] Very few small angle neutron diffraction measurements have been made on nonmagnetic metallic glasses and only on very complex alloy systems.[3] In these neutron scattering studies, the effects of annealing were not measured.

We prepared a sample in the form of small (1-4 mm^2) pieces from the as-received ribbons of $Ti_{45}Cu_{55}$ to approximate powder sample for the diffraction studies. Cylindrical sample holders of very thin vanadium or copper foil were used to minimize the background scattering from the sample holders. Standard diffraction patterns were taken covering a span of $K = \frac{4\pi}{\lambda} \sin \theta$ from 0.2 Å^{-1} to 6.0 Å^{-1} and small angle scattering patterns were taken covering a span of K from 1.0×10^{-2} Å^{-1} to 1.5×10^{-1} Å^{-1} for the as-received material, the material annealed at 300 °C in vacuum, near the glass transition temperature, for 3 hours, and the materials annealed for 6 more hours at 300 °C.

Figure 1 shows the structure factor in the range 0.2 to 6.0 Å^{-1}. This structure is expected for a glassy system except for the pre-peak at 2.0 Å^{-1} as noted by Sakata et al.[2] With increased time of annealing, the intensity of the pre-peak increases relative to the main peak.

Figures 2, 3, and 4 show constant intensity contour maps for the small angle neutron scattering from the alloy in the as-received condition, after 3 hours of anneal at 300 °C, and after a total of 9 hours of anneal at 300 °C. One notes immediately the strong asymmetry in the scattering. The results in figure 1 are somewhat distorted because we tried to position the beam stop using the scattered beam from the alloy and were unaware of the asymmetry. Consequently, the beam stop was positioned so as to mask the scattering in the upper-half plane. Figures 2 and 3 show the scattering after the respective anneals of 3 plus more hours. In these measurements the beam stop was positioned with a strong symmetric scatterer and the asymmetry in the scattering is well revealed. Preliminary analysis of the scattering patterns indicates microstructure whose dimensions are 150 to 200 Å. The relative intensity of this scattering increases with annealing and the duration of anneal.

The most striking result of the neutron measurements to date on this CuTi alloy is the evidence of the formation of a phase other than the glossy phase in the rapidly solidified sample. This "precipitate" phase is highly oriented along the long dimension of the ribbon. Furthermore, this "precipitate" phase changes with heat treatment and is observed both in the small angle scattering and in the structure observed at larger wave

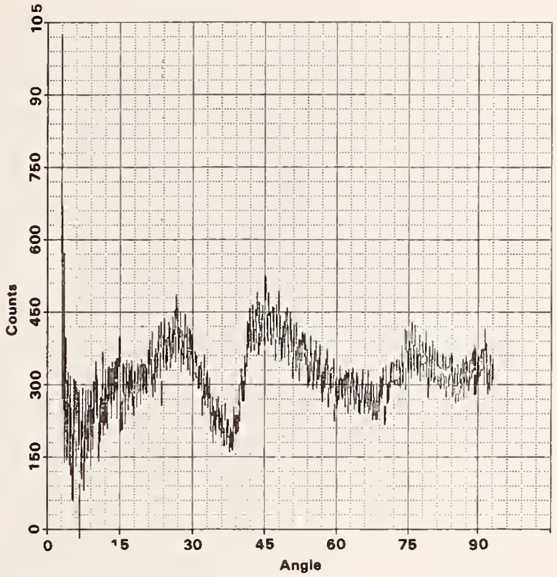

Figure 1. Diffraction data for amorhpous $Cu_{55}Ti_{45}$ alloy after a 3-hour anneal at 300 °C. Neutron wavelength is 1.515 Å and data corrected for container scattering. Note the peak at 27° scattering angle which has been called a chemical short-range order prepeak by Sakata et al.

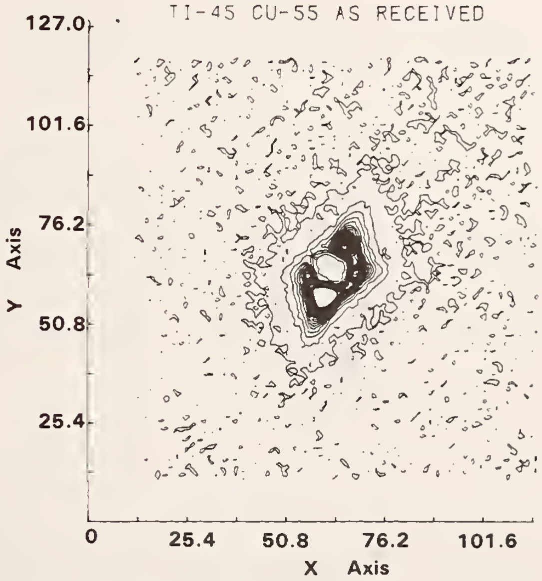

Figure 2. SANS corrected data for amorphous $Cu_{55}Ti_{45}$ alloy in the as-received condition. The asymmetry in the pattern comes from a directionally ordered precipitate phase. The beam stop was misaligned in this pattern and produced a tilt in the asymmetry.

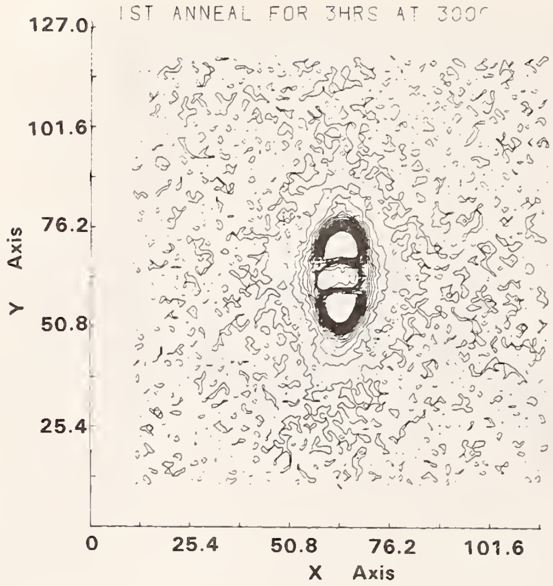

Figure 3. SANS corrected data for amorphous $Cu_{55}Ti_{45}$ alloy after a 3-hour anneal at 300 °C. Note the strong asymmetry in the pattern. The intensity of this pattern is stronger than the as-received sample.

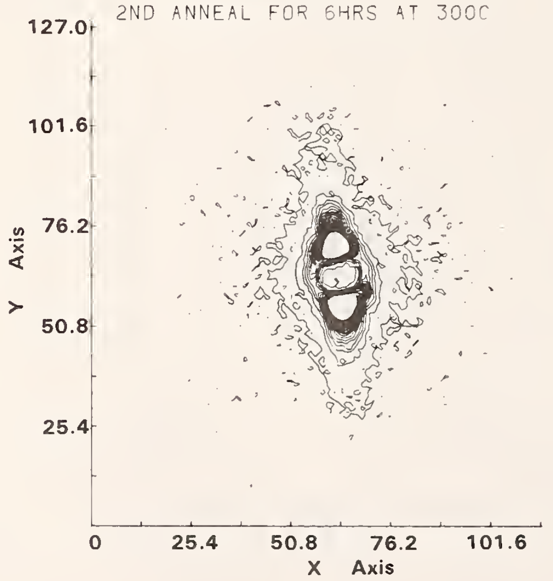

Figure 4. SANS corrected data for amorphous $Cu_{55}Ti_{45}$ alloy after a total of 9-hours anneal at 300 °C. The intensity of this asymmetrical pattern has increased over that of figures 2 and 3.

vector differences. It is important to note that this microstructure may be common to other metallic glass systems and requires a very thorough investigation to help determine manufacturing parameters for the production of metallic glasses. In the future we shall continue our study of the microstructural changes in this alloy as we anneal the sample closer to the crystallization temperature. Other alloys of this system will be investigated to determine if these results are applicable in a general sense. In addition, we are in the process of measuring the thermal properties of this alloy as a function of annealing temperature and duration and we shall characterize this sample using x-ray and other metallographic techniques for intercomparison with our neutron results.

---

1. B. Mozer, D. T. Keating, and S. C. Mass, *Phys. Rev.* 175, 868 (1968).
2. M. Sakata, N. Cowlam, and H. A. Davies, *J. Phys. F: Metal Phys.* 11, 157 (1981).
3. D. E. G. Williams, H. Fujimori, and D. S. Brown, *J. Appl. Cryst.* 15, 206 (1982).

INVESTIGATION OF SiC-Al COMPOSITE MATERIAL BY NEUTRON SCATTERING

H. A. Alperin
(Naval Surface Weapons Center, White Oak, MD)
and
(National Bureau of Standards, Washington, DC)

and

S. P. Singhal
(Fracture and Deformation Division)

We have investigated the feasibility of using neutron diffraction as a tool for the nondestructive evaluation of composite materials. The material selected, SiC fibers in an aluminum matrix, is ideal for this purpose due to the very low aluminum neutron absorption cross section. This makes it possible to observe (111) Bragg reflections from both the fibers and the matrix. Upon application of increasing compressive stress to a cylindrical sample (∿ 1 cm diameter) while it is undergoing neutron scattering measurements, it is possible to accurately measure the change in d-spacing (strain) as a function of applied stress (σ) independently for both the matrix and for the fibers.

$$\Delta d/d = -\nu\sigma/E = -\Delta(2\theta)/2\tan\theta$$

Other bulk measurements only give an average for the composite as a whole.

The required accuracy of the measurement derives from the ability to fit a known function (Gaussian) to the neutron lineshape. With sufficient counting statistics (∿ 4 hrs. for each peak scan) the fit yielded peak positions to an accuracy of ∿ $\pm$ 0.001 degrees (2θ) which gives a change in d-spacing accuracy of ∿ $\pm 1 \times 10^{-4}$ A.

The results are shown in figure 1. For comparison, an identically-shaped rod of 6061 Al was also measured. From the slope and assuming a Poisson ratio $\nu = 0.31$ a Young's modulus $E = 10.9 \times 10^6$ psi (7.5×10^4 MPa) is obtained; this is very close to the value (10.5×10^6 psi) usually quoted for an Al alloy. The stiffening of the Al matrix in the composite is apparent from figure 1 and gives the value $E = 19.5 \times 10^6$ psi. The SiC fibers show a value $E/\nu > 300 \times 10^6$ psi.

Several interesting effects are also observed. One is a relaxation effect observed in the fibers upon repeated measurements over a period of 8 hours at a constant value of stress. The range of variation in d-spacing due to this effect is shown by the cross-hatched bars in figure 1. Another effect is the large initial stiffness shown by both the matrix and the fibers. Neither of these effects are observed in the Al alloy sample. One can see that at the stress levels used in this study (which are in the elastic region) d vs. σ is linear (figure 1). Upon entering into the plastic region at higher stress levels, a departure from this behavior is expected. One can therefore study initiation of failure modes at the SiC-Al interface by extending the measurements to higher stress levels.

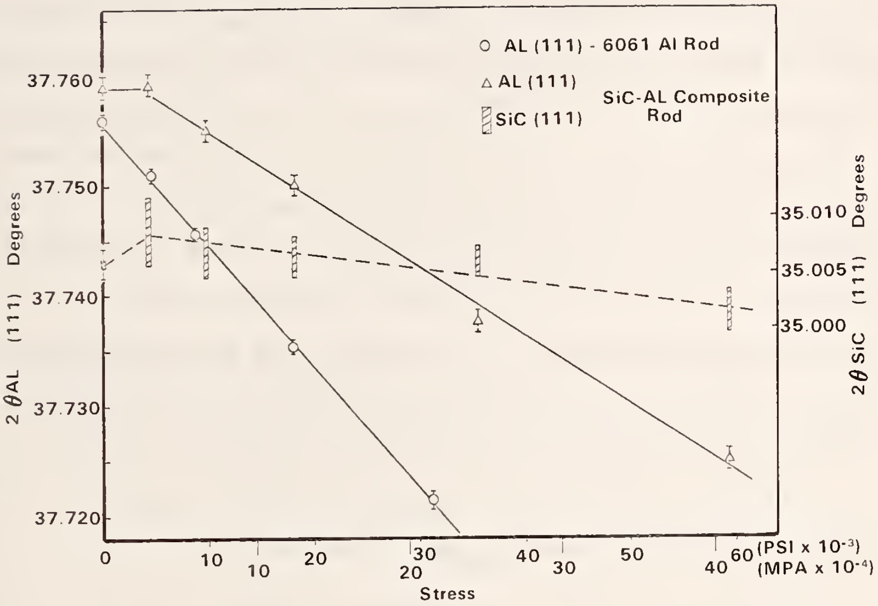

Figure 1. Strain vs stress from Al and S. C Bragg reflections in 6061 Al alloy and S$_i$C-Al composite material.

THE THEORY OF SPINODAL DECOMPOSITION

N. F. Berk

and

S. Singhal
(Fracture and Deformation Division)

and

H. A. Alperin
(Naval Surface Weapons Center, White Oak, MD)
and
(National Bureau of Standards, Washington, DC)

A program is in progress to develop the application of theory to the interpretation of small angle scattering from alloys undergoing spinodal decomposition. Current efforts have focused on the analytical description of Langer, Bar-On, and Miller (LBM) which, even in the simplified form now commonly identified with it, produces a cumbersome set of simultaneous differential equations for the scattering function and the moments of the order parameter distribution function. As part of our own effort, we have implemented a computer solution of these equations and are studying methods to facilitate the comparison of theory with experiment.

In the standard form of the LBM theory, the order parameter distribution function is assumed to be a pair of guassian functions centered on the most probable coarse grain values of the alloy composition. The theory can then be manipulated to give approximate equations of motion for the time evolution of the parameters of the double gaussian ansatz. It does not seem to have been remarked that a consistent set of equations can also be derived for the distribution function on the stronger assumption that the guassians have zero width. For the so called "symmetric" case of an alloy quenched at the critical composition, the small angle scattering intensity is then described by the much simpler set of equations

$$a_t S(q,t) = -q^2(q^2 + a(t))S(q,t) + q^2,$$

$$a(t) = f'(x)/x,$$

$$x^2(t) = 1/q_m \int_o^{q_m} q^2 S(q,t)dq.$$

Here S(q,t) is the scattering intensity as a function of scattering wavevector q and time t, f(x) is the model course grain free energy and x(t) is the composition order parameter. All variables have been expressed in dimensionless form, and q_m, the only "free" parameter, is the inverse measure of the course grain length.

These equations are much simpler than those in the standard form of the theory, yet the solutions exhibit all of the qualitative aspects of the behavior of S(q,t) usually associated with non-linear spinodal decomposition. This suggests that the non-zero width parameter, which seems to contribute in large measure to the complexity of the standard form of the LBM theory, is not essential in determining the scattering "signature" of the decomposition. Moreover, the simplified form is more amenable to the treatment of various model-free energy functions than is the standard form. Preliminary results comparing the Ginsberg-Landau form with the regular solution model indicate that except for the time scale of the evolution, the shape of the scattering curve as a function of q is insensitive to the form of the free-energy function (for the symmetric case).

---

1. J. S. Langer, M. Bar-On, and H. Miller, *Phys. Rev.* A11, 1417 (1957).

NONDESTRUCTIVE EVALUATION OF DISTRIBUTED DAMAGE

E. R. Fuller, Jr., R. J. Fields, E. D. Case, and S. Singhal
(Fracture and Deformation Division)
and
C. J. Glinka

In a number of instances, failure of a structural component results from an accumulation of damage, distributed homogeneously throughout the component, as opposed to the formation and growth of a macrocrack. An example of such a situation is the nucleation and growth of creep cavities in the high-temperature components of energy conversion systems. Another example might be the accumulative damage that occurs in a composite material which is subjected to a fluctuating service stress. An important design consideration in the initial materials selection for such applications is an assessment of the material's failure life, either creep rupture life or fatigue life in the examples mentioned above. Of equal importance, however, in assuring remaining lifetime is a nondestructive assessment of the accumulative damage that has occurred thus far in the service life. If the state of progressive degradation in service can be periodically monitored, the rate of damage accumulation can be determined and actual component lifetime more accurately predicted. Failure due to distributed damage is not necessarily restricted to mechanical failure. In material processing, for example, it is occasionally important to assess the integrity of a body before further processing is warranted.

The objective of this research program is to address these issues by an evaluation of various nondestructive inspection techniques that have potential for monitoring the extent of distributed damage in these materials. Nondestructive techniques are, in general, more desirable than destructive ones because they can be applied to actual operating components without having to replace the component after inspection. However, nondestructive techniques rarely provide direct measurements concerning the microstructural defect associated with the distributed damage. We intend to compare the results of several common nondestructive inspection techniques with direct observational measurements of the size and abundance of defects, thereby increasing the scientific base for these NDE standards. During this first year, the research effort has focused on the detection and characterization of uniformally distributed microstructural damage through the use of the new small-angle neutron scattering (SANS) facility at NBS. Two model systems have been developed and utilized for these studies: (1) creep cavitation damage in 304 stainless steel and (2) uniformally distributed microcracks in a polycrystalline ceramic, yttrium chromite. These studies are described separately below. The small-angle neutron scattering facility is described in a separate report by C. J. Glinka.

1. Cavitation Damage in 304 Stainless Steel

304 stainless steel used in high-temperature applications consists of metal carbides in an austenite matrix. At elevated temperatures, however, the carbide-austenite interface at a grain boundary becomes a preferential site for cavity nucleation. The resulting cavities then grow, link, and ultimately cause failure. The early stages of this process are extremely slow, and the creep cavities, due to their small, size are not easily detectable or quantifiable. It is these early stages of nucleation and cavity growth that are examined in this research through the use of small-angle neutron scattering (SANS).

Since carbide precipitates, as well as creep cavities, give rise to neutron scattering, two requirements must be satisfied for a quantitative evaluation of cavitation damage:

(i) the volume fraction of carbide precipitates should not change significantly during creep and

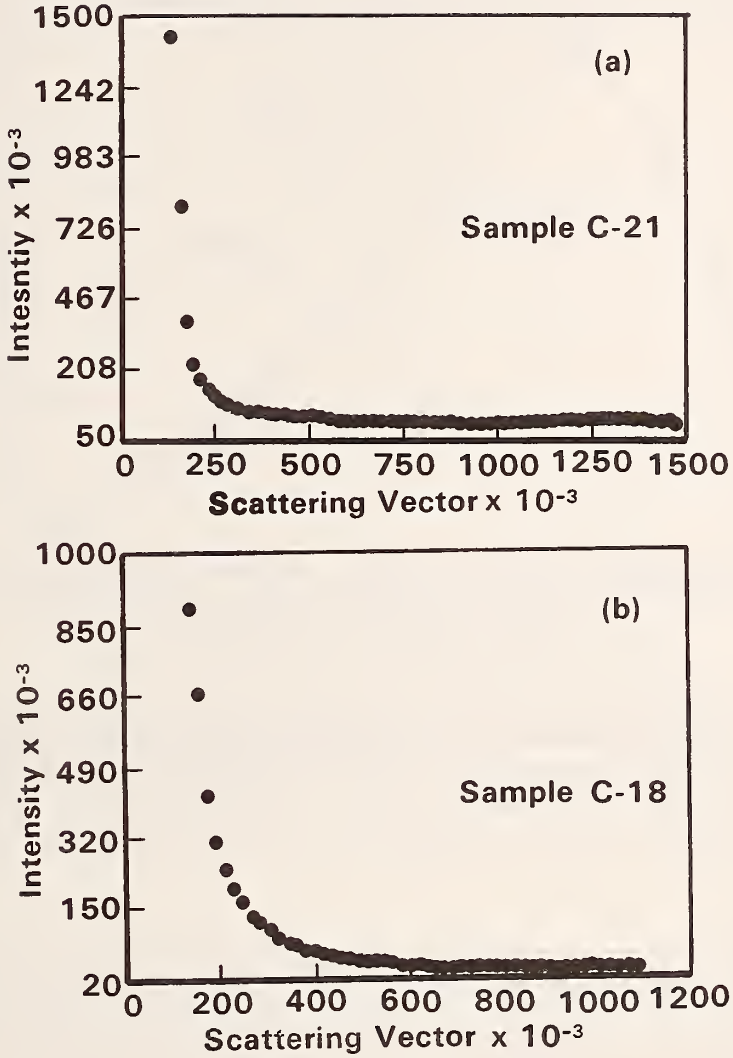

Figure 1. Small-angle neutron scattering intensity versus scattering vector Q for creep cavities (a) in sample C-21 and (b) in sample C-18.

(ii) a reference sample with equivalent carbide structure should be measured and subtracted from the scattering spectrum of the crept sample.

The first condition was achieved in the present study by a "stabilizing" heat treatment of approximately 40 hours at 775 °C prior to the initiation of the creep experiments. This allowed a complete precipitation of carbide thereby stabilizing the volume fraction of carbides. The second

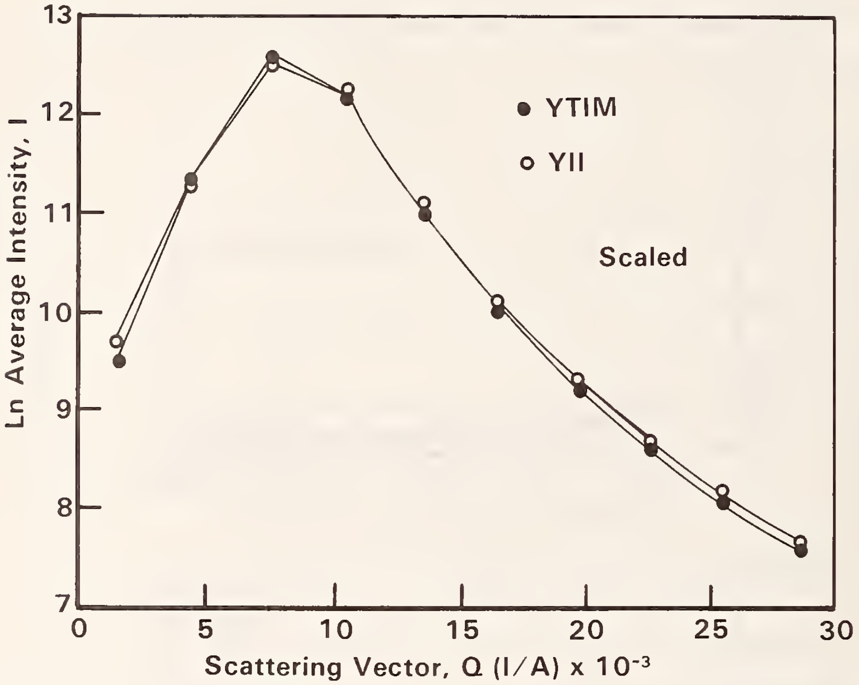

Figure 2. Small-angle neutron scattering intensity versus scattering vector, Q, for two microcracked polycrystalline $YCrO_3$ specimens of different thicknesses. Specimen YTIM is approximately five times thicker than specimen Y11. Similarity between the two curves implies that scattering is predominantly diffractive in nature.

condition was satisfied by a reference specimen which was only heated (and not stressed) along with the crept specimen. Although a number of creep specimens were examined in this study, only two fulfilled this second requirement for a reference sample. These specimens were both crept at 600 °C: one (Sample C-21) at a stress of 145 MPa (21 ksi) for 745 hours and the other (Sample C-18) at a stress of 124 MPa (18 ksi) for 789 hours. The unstressed reference samples for these specimens are designated R-21 and R-18, respectively. The neutron wavelength for these studies was 5.1 Å giving a range of scattering vectors, Q, from 0.014 to 0.16 $\mathrm{\AA}^{-1}$. With this range of Q, contributions from cavities and carbides in the size range of 40 to 450 Å were detected.

The detailed theory and procedure for analyzing the SANS data will be prescribed in a forthcoming publication. A few salient features, however,

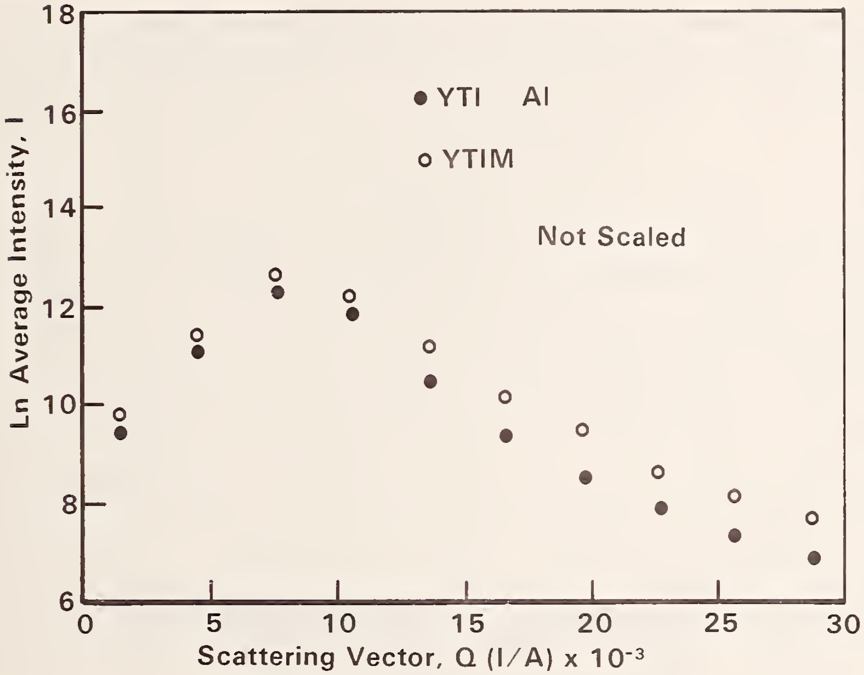

Figure 3. Neutron scattering intensity versus scattering wave vector, Q, for a $YCrO_3$ specimen both in its microcracked state (YT1M) and its healed state (YT1A1).

are described here. If scattering intensity is denoted by I, the differential scattering cross-section is given by

$$dS/d\Omega = cI/t\ M\ T$$

where t is the sample thickness, M is the total monitor count (or scattering time), T is the sample transmission, and c is a combination of experimental constants related to the SANS facility. Creep damage is related to the difference in differential scattering cross-sections between the crept sample (C) and the reference sample (R):

$$[dS_C/d\Omega - dS_R/d\Omega] = c\ [I_C/t_C M_C T_C - I_R/t_R M_R T_R].$$

Accordingly, all intensities in the further discussion have been normalized by sample thickness, transmission, and scattering time.

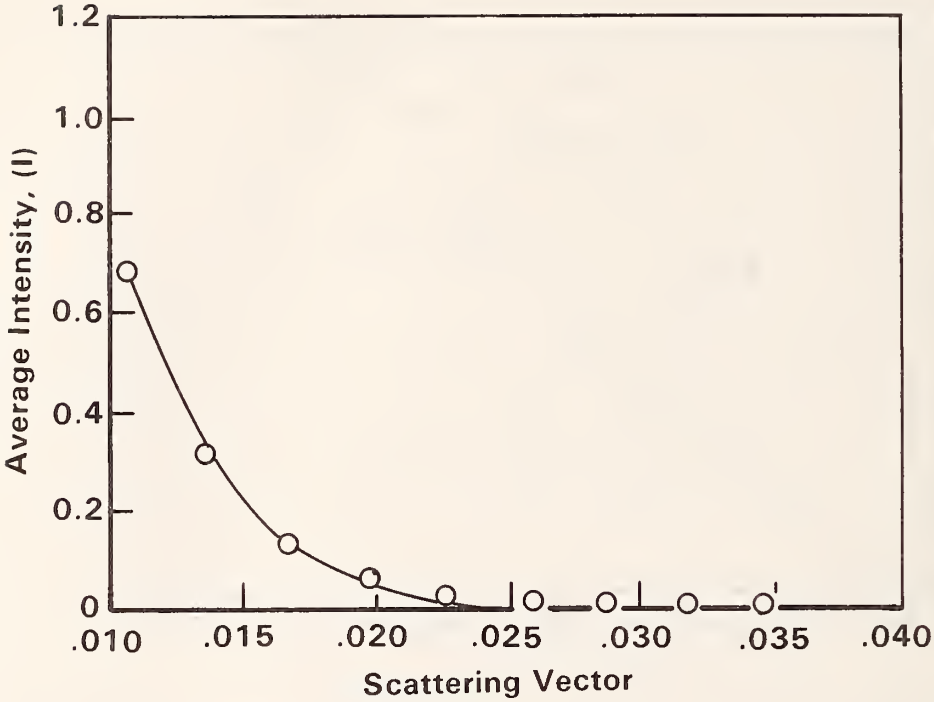

Figure 4. The difference spectrum for the scattering curves plotted in figure 3. The solid line is a fit to a scattering model from a randomly oriented array of thin disks.

The scattering intensity for cavities in sample C-21 [i.e., I (C-21) - I (R-21) is shown in figure 1a, and that for sample C-18 in figure 1b. A visual comparison of these figures indicates that for most scattering vectors Q, the scattering from cavities is larger in sample C-21 than in sample C-18, thus indicating the presence of a higher volume fraction of cavities in sample C-21. A Guinier analysis can be performed on these spectra to obtain an average creep cavity size. Guinier showed that for randomly, distributed, monosized, spherical heterogeneities, the scattering curve near $Q \sim 0$ can be approximated by the relation

$$I = I_o \exp(-R^2Q^2/5)$$

where I_o is the intensity intercept at $Q = 0$ and R is the cavity radius. This expression is valid only when the volume fraction of cavities is small enough to avoid so called "inter-cavity interference."

Guinier plots of the data in figure 1 give a straight line behavior only in the range for Q of 0.01 to 0.025 $\mathring{A}^{-1}$, indicating that the cavities formed during creep cavitation have a range of sizes rather than being one size. To obtain a cavity size distribution will require further analysis, but an average cavity size has been obtained by a least-squares fit to this low Q region. The results are

$$R = 173 \pm 10\ \mathring{A} \text{ for sample C-21}$$

and

$$R = 133 \pm 7\ \mathring{A} \text{ for sample C-18}$$

Thus, sample C-21 not only has a higher volume fraction of cavities but also a larger average cavity size.

Common to various theories of creep cavitation discussed in the literature is the assumption of a two-stage process involving nucleation and growth. In general, the stress level determines both the nucleation and the growth rate; whereas time under load determines the total volume fraction of cavities for that rate. For the present studies, an increase in stress by 20 MPa (3,000 psi) results in larger average cavity size and in greater volume fraction of cavities. Conclusion regarding nucleation, however, require further analyses of size distribution.

Although these analyses are continuing, numerous questions and theoretical obstacles concerning these evaluations have arisen from physical considerations. Chief among these is the fact that cavities always occur on carbides. Accordingly, it may be incorrect to assume that scattering from these two scattering species is independent and uncorrelated. Second, stress induced redistribution of precipitates is possible and will contribute to the apparent creep damage as deduced by SANS. This scattering component will not be correctly evaluated if the scattering cross-section is interpreted as totally due to cavities.

These complications have been neglected in the past year's effort because at present we have no completely satisfactory way to treat them theoretically or to avoid their influence in 304 stainless steel. However, the analyses which have been performed demonstrate that SANS is sensitive to the creep damage in an engineering alloy before this damage is detectable by other techniques, even though an exact interpretation of the data is clouded for a complicated system like 304 stainless steel. Accordingly, it is our intention to better quantify the basic technique by next investigating a simple single phase system for which scattering variations will be solely due to the presence of cavities. Such a material might be OFHC copper which is known to be prone to intergranular cavitation. We may then proceed to the case of a two phase material in which no redistribution of the dispersed phase is possible. Finally, we will return to the complicated case of 304 stainless steel having, perhaps, dealt with some of the theoretical and experimental impediments to a complete analysis of the SANS spectrum.

2. Microcrack Damage in Polycrystalline Ceramics

Microcrack damage in polycrystalline ceramics can degrade the performance of these materials in terms of both their mechanical integrity and their chemical stability (through enhanced permeation of environmental species). Quantitative characterization of this damage is generally done with surface sensitive techniques. Research in this subtask, however, has established, for the first time, the powerful research tool that small-angle neutron scattering (SANS) provides for the characterization of microcracks and crack-like voids in polycrystalline ceramics. SANS has two principle advantages over surface sensitive techniques for this characterization: (1) surface preparation almost invariably damages the specimen surface, thereby complicating the subsequent analysis and

(2) surface stresses are not necessarily the same as those in the bulk, so that surface microcrack sizes and distributions may not be representative. Research has progressed in three areas:

(a) Development of a "Model" Microcracking Ceramic. In order to study the nature of microcracks with a NDE probe, one must be able to distinguish the response due to microcracks from that due to other microstructural features, such as pores or second phase particles. An ideal way to separate these effects is to have a material for which the microcrack number density can be varied independently from other microstructural features. $YCrO_3$ is such a material. It undergoes an apparent phase transformation at ∿ 1100 °C so that it can be readily microcracked by annealing at temperatures slightly above 1100 °C; conversely, these microcracks can be diffusively healed by annealing slightly below 1100 °C. Since the yttrium chromite specimens are initially sintered around 1750 °C, the microstructure (porosity, grain size, etc.) changes little during these anneals, making $YCrO_3$ an ideal "model" material for studying microcracking effects in ceramics.

(b) Determination of the Nature of Neutron Scattering. Since relatively little SANS research has been conducted on polycrystalline ceramics, it is important to establish the extent of refractive neutron scattering, before interpreting scattering results as diffractive in nature. Otherwise, erroneous conclusions could result. This distinction can can be made experimentally by varying either the incident wavelength or the specimen thickness. In both cases, the scattered intensity versus scattering vector should not change for diffractive neutron scattering. For the microcracked $YCrO_3$ specimens considered in this study, the neutron scattering was demonstrated to be predominantly diffractive in nature by varying the neutron wavelength between 6.25 Å and 8.0 Å and by comparing scattering spectrum from specimens with a factor of five difference in thickness (see figure 2).

(c) Analysis of Scattering Data. Figure 3 shows the neutron scattering behavior of a $YCrO_3$ specimen both in its microcracked state

(YT1M) and in its healed state (YT1A1). The difference spectrum is plotted in figure 4. Since the spectrum from the healed state subtracts out the background of microstructural scattering, this difference spectrum represents only the scattering from microcracks. The solid line in figure 4 is a least-squares fit to a model for scattering from a randomly oriented array of thin disks,

$$I(Q) = (A/Q^2) \exp (- H^2Q^2/3),$$

where I is the scattered intensity for a given scattering vector, A is a constant, and H is the thickness of the disk. This model is an asymptotic expression for small Q values. H, as determined from this fit is 170 Å, which is physically reasonable from several independent estimates of the crack opening in such ceramic systems. Further analyses for large scattering vectors indicate that the scattering is from sharp-edged objects, which is consistent with scattering from micro-pores and microcracks. Additional studies with this and other specimens with various thermal annealing treatments further support these results.

In conclusion, it appears that microcrack damage in $YCrO_3$ can be detected using small-angle neutron scattering. Although much more work needs to be done in characterizing the microcrack size, shape, and distribution, the microcrack mouth-opening displacement estimated from SANS data is in general agreement with other, independent measures of crack opening. Finally, although not discussed here, a rapid method for assessing total microcrack damage might be through the use of neutron transmission measurements.

B. NON-RRD PROGRAMS

ACTIVATION ANALYSIS GROUP FY 82

R. Zeisler

The principle objectives of the Activation Analysis Group continue to be the development of nuclear analytical techniques for better sensitivity, higher selectivity, and increased accuracy. A high level of competence has been developed for various reactor-based activation analysis techniques which include instrumental and radiochemical neutron activation analysis (INAA and RNAA), prompt gamma activation analysis (PGAA), and the nuclear track technique (NTT). Non-reactor-based techniques include photon activation analysis (PAA), fast neutron activation analysis, and charged particle activation analysis, which have been used on a more limited scale. With this wide variety of techniques, support is provided for the diversified NBS and other agency programs requiring analytical measurement services. For example, simultaneous multielement determinations over a broad dynamic range in complex matrices as well as highly selective determinations of constituents in the sub-nanogram range have been provided for programs such as Standard Reference Materials, Environmental Measurements, Recycled Oil, Resource Recovery, Nuclear Safeguards, and other disciplinary research programs at NBS.

During the past year, major research efforts have been directed toward the demonstration of multielement capabilities of INAA procedures. With an appropriate combination of PGAA and several INAA determinations, at suitable irradiation and decay intervals, it has been possible to determine more than thirty trace elements in such diverse matrices as liver homogenate, coal, fuel oil, and air particulates. Recent research on instrumental means for background reduction complemented these activities. The evaluation of the newly acquired compton suppressor system for application to multielement determinations resulted in increased sensitivity for several crucial elements. The continuing evaluation of compton suppression techniques using specific detector combinations will provide unique activation analysis sensitivities for such elements as Al, V, Cr, Ni, Zn, and Pt.

Considerable effort has been spent in support of the Pilot National Environmental Specimen Bank (NESB) program. The cryogenic homogenization technique has been improved to accommodate samples up to 1000 g. Sieving experiments at cryogenic temperatures have supported the previous data which had indicated that homogenates processed in the newly developed Teflon disk mills will pass a 40 mesh sieve. The on-going evaluation of the trace element baseline data collected during the first year showed some interesting trends due to the variations in the sample population. For future analyses, a selection of samples which better match epidemiological population data will be considered. Activation analysis data are currently being evaluated to determine the effects of the first year of storage. The second year collection baseline analyses have been initiated using improved instrumental multielement techniques.

The development and installation of the neutron beam depth profiling facility and the first determinations of depth profiles in collaboration with other researchers in the competence program is another important step towards the continuous expansion of research activities. There is a significant potential in exploring this and other "unconventional" activation analysis techniques for future applications especially in the important areas of materials research. To match future needs in high purity materials, gases in metals and distribution of elements, more research must be conducted in the areas of "unconventional" use of reactor neutrons as well as in the use of non-reactor activation sources.

Research efforts during the coming year will focus on the extension of the multielement procedures. For example, the measurements needed to characterize the irradiation facilities after the planned increase of the NBS reactor power to 20 MW will be used to initiate and evaluate "absolute" or monitor activation analysis. This technique will provide results on more elements, since the occurrence of unexpected elements will not preclude their quantitation. For the NESB specimens, an optimized analytical protocol will be developed which can overcome the restrictions of this specific matrix. In the area of non-conventional activation analysis, the use of a fast transfer system for analysis via very short-lived isotopes will be evaluated. It is also anticipated that procedures for the determination of gases in metals will be investigated. However, in this area, access to a source of fast neutrons and/or charged particles is necessary.

1. Improved Radiochemical Procedures for High Sensitivity Measurements of Ultratrace Concentrations of Tin and Mercury

R. R. Greenberg

Although instrumental neutron activation analysis can be used to determine a large number of elements in most matrices, some critical elements are frequently obscured by high background levels of radiation or by interfering elements. With appropriate radiochemical separations, a large number of additional elements can be determined at the ppb and even sub-ppb levels. Tin and mercury are two elements which are of both environmental and biomedical importance. Although radiochemical separation procedures have been previously developed for these elements, recent applications have required better sensitivity and therefore improved separation from interfering elements.

Tin has previously been separated from Orchard Leaves (SRM 1571) with an iodide extraction into toluene. However, approximately one percent of the selenium was found to accompany tin through this procedure which elevated the background level of radiation. Although this did not seriously affect the determination of tin in Orchard Leaves or Citrus Leaves (SRM 172), it did produce serious problems in other materials such as Bovine Liver (SRM 1577) and human livers from the National Environmental Specimen Bank NESB) program. Several modifications in the procedure, including a selenium volatilization step after sample dissolution (using H_2O_2 and HF), a pre-extraction wash with chloroform, and a back-extraction of tin into an aqueous Na_2EDTA solution, reduced the fraction of selenium accompanying tin to ≤ 0.05 percent. With these modifications, the tin content of Bovine Liver (SRM 1577) was found to be 20 ± 3 ng/g (1s for six samples). The tin concentrations in eleven human livers were also determined. Four subsamples of human liver homogenate were analyzed and the precision was better than one percent (1s).

Mercury has previously been separated from a number of matrices by solvent extraction using nickel diethyldithiocarbamate $\pm Ni(DDC)_2 1$ in chloroform. Large fractions (10-50 percent) of copper and bromine accompany mercury and can interfere with the Hg-197 isotope by elevating the background level of radiation. A small fraction of the selenium ($\leq$0.01 percent) also accompanies mercury and directly interferes with the 279 keV γ-ray of Hg-203. Two additional steps were found to greatly improve the separation of mercury from these other elements. The use of a chloroform wash prior to extraction with $Ni(DDC)_2$, and a post extraction wash with aqueous Na_2EDTA reduced the accompanying copper and bromine by a factor of 3-10, and the selenium by a factor of 10-100. With these modifications no selenium could be detected in any of the samples via other, more intense γ-rays. These improvements allowed mercury to be determined in Bovine Livers (SRM's 1577a and 1577b) at the 3-5 ng/g level with uncertainties of only 2-3 percent (1σ) due to counting statistics. SRM 1577 (Bovine Liver) was analyzed as a control and the present value of 16.0 ± 0.3 ng/g (1σ counting statistics) clearly demonstrates the improvement in the method when compared to the previously determined value of 16.8 ± 0.9 ng/g (1σ); the uncertainty due to counting statistics has been reduced by a factor of three.

In summary, the modifications described greatly improved the separation of tin and mercury from the, interfering radionuclides. As a result, the detection limits for both elements were greatly reduced, and the analytical uncertainties due to counting statistics were significantly reduced.

2. I-129 Analysis

G. J. Lutz

A procedure has been developed for the analysis of environmental sample for I-129 at levels below 10^{10} atoms/g (0.2×10^{-12}g/g).

The analysis consists of a pre-irradiation separation, an irradiation in the reactor, and a post-irradiation separation. The pre-irradiation separation involves the combustion of the sample in a stream of oxygen. Exit gases are filtered through quartz wool to trap particulate material and the iodine is collected on an activated charcoal trap approximately seven millimeters in diameter and three centimeters long. This pre-irradiation filtering is necessary to remove cesium, uranium and tellurium which interfere via the reactions $^{133}Cs(n,\alpha)^{130}I$; $^{235}U(n,f)^{129}I(n,\gamma)^{130}I$; and $^{128}Te(n,\gamma)^{129}Te \rightarrow {}^{129}I(n,\gamma)\ ^{130}I$.

The activated charcoal trap is burned in a lower oxygen flow and the iodine is reabsorbed on a smaller charcoal trap. It is desirable to minimize the mass of the charcoal trap to be irradiated in order to reduce the amount of fission product iodine formed from uranium impurities in the charcoal. This fission product iodine is subsequently a counting interference.

It is possible to measure the yield of the pre-irradiation separation in one of two ways. I-125 spike can be added prior to the separation and measured at the end of the separation. Alternatively, if the I-127 content of the sample is known and is sufficiently high, it can be measured by nondestructive neutron activation analysis of the activated charcoal. I-127 almost certainly is a better tracer of I-129 then the I-125 spike is.

The charcoal trap containing the iodine is sealed in quartz under vacuum and irradiated in the rector. The irradiation is usually conducted in RT-4. The neutron flux in this tube is lower than in RT-3 but it is more thermal. This is important as it minimizes the reaction $^{127}I\ (n,2n)^{126}I$. Irradiations are typically conducted for 16 hours. At the end of the irradiation the quartz ampoule is rinsed with acid and cooled in liquid nitrogen. It is then cracked open. Several milligrams of inactive iodine carrier as well as I-125 spike are added to the sample. The major gamma emitting radioactivities are due to bromine, chlorine, and impurities in the charcoal and quartz. The charcoal sample is then burned in a steam of oxygen and exit gases are again passed through a plug of quartz wool and collected onto a trap of hydrated maganese dioxide (HMD). HMD is one of a series of selective ion retention media developed during the past several years. It is usually used for separations from aqueous solutions, but has been applied to gas phase separations. After collection of gases the HMD is heated to a dull red heat. This results in the passage of 80-95% of the iodine while all but one part in 10^4-10^6 of the bronine is retained in the HMD trap.

Efforts have been concentrated on the analysis of two Standard Reference Materials. They are SRM 1648, Urban Air Particulate and SRM 1572 Citrus Leaves. Values in atoms of I-129/gm for SRM-1648 are 1.3×10^9, 2.4×10^9 and 1.7×10^9 atoms/gm. These are not terribly imprecise values as far as I-129 analysis is concerned and agree well with value of 1.5×10^9 obtained at Battelle Pacific Northwest Laboratories.

3. Characterization of Selected Trace Elements in the Chesapeake Bay

R. R. Greenberg, H. M. Kingston, W. S. Liggett, and T. C. Rains

Trace element measurements for a large multi-disciplinary study of the Chesapeake Bay have been completed. As part of this study, water samples were collected at 51 sites, and both the particulate and dissolved fractions were analyzed for Cd, Ce (particulate only), Co, Cr, Cu, Fe, Mn, Mo, Ni, Pb, Sc, Sn, Th, U, and Zn. Two types of samples, surface and bottom were collected and analyzed using specific chemical preconcentration and separation techniques developed for neutron activation analysis (NAA) and graphite furnace atomic absorption spectrometry (GFAAS). The data are the first environmental analyses of this kind to yield a data set at the 95 percent confidence limit that allows rigorous statistical evaluation of elemental relationships.

The concentrations of 14 elements in the dissolved fractions were evaluated by direct comparison with naturally occuring seawater levels. At several locations in the Bay, two toxic elements (lead and tin) were elevated by two orders of magnitude over normal seawater levels. Similar levels of organo-tin were found by other researchers. Most of the dissolved iron concentrations were approximately the same as that found in seawater. However, a number of bottom samples collected at some of the deepest locations had significantly greater iron concentrations. The elevated levels appear to be due to anoxic conditions in the bottom sediments. Similarly, the manganese concentrations had maxima at these same locations. Uranium and molybdenum were found in higher concentrations in seawater than fresh water. As a result, the concentrations of these two elements can be used to trace the seawater content of the water column throughout the Bay. The dissolved thorium concentrations in samples taken near the mouth of the Bay were approximately two orders of magnitude lower than previously reported seawater values. The dissolved concentrations of the remaining elements (Cd, Cr, Co, Cu, Ni, Se, and Zn) appeared to be relatively similar to the levels normally found in seawater.

The information obtained from the raw particulate elemental concentration data has been difficult to interpret in the past. Since the concentrations were reported in elemental mass (ng) per unit volume (mL) of water, the total amount of particulate mass suspended at the time of sample collection strongly affected the results. Variations in current, tide, temperature, biota, wind conditions, etc. can greatly influence the total amount of particulate material suspended in the water column. To circumvent the problem of variable mass loading, a double normalization procedure was used to compute crustal enrichment factors. The concentration of each element in the sample was divided by the concentration of a reference element, in this case scandium, and the resulting value was divided by the ratio of these elements in average crustal material. Scandium was chosen as a reference element because it has essentially no anthropogenic uses and its chemistry is relatively simple (single oxidation state, limited dissolved particulate interactions). The usefulness of this technique can be illustrated by comparing the variability in the cerium concentrations and the cerium enrichment factors (EF). The concentrations varied by a factor of 300 from site to site, while the EFs varied by a factor of 1.5 and the observed standard deviation over the entire Bay was just 10 percent. The EF's for thorium were similar to those of cerium. The environmentally active and anthropogenically abundant elements had significantly more complex ranges and patterns of enrichment factors than the elements used as multiple controls.

Almost all of the iron EF's were similar to those of Ce and Th. However, a few samples had slightly elevated EF's. These samples were collected at some of the deepest locations within the Bay and appear to be linked to anoxic reactions in the sediment at these locations. The enrichment factors for cobalt, manganese, and nickel appeared to trace the flow of Potomac River water for quite some distance down the Bay. This was observed through the elevated EF's for the surface samples as compared to generally uniform EF's for the bottom samples. It was also found that a number of samples had greatly elevated cadmium enrichment factors. This appeared to be a result of crustal weathering of naturally occurring cadmium deposits and not anthropogenic sources. These deposits and their erosion have also been documented by other researchers. The enrichment factors for lead exhibited a great deal of variability; most of the samples had lead EF's approximately five (i.e., five times greater than Pb/Sc ratio for average crustal material). For the elements chromium, copper, and uranium, the enrichment factors appeared similar to naturally occuring material. Molybdenum was below the detectable limits in most samples and tin could not be detected in any of the particulate samples. Zinc suffered from severe blank problems arising from the filter material used; however, samples near the top of the Bay had very high mass loadings and zinc appeared to be slightly enriched.

Although most elements were found at levels that could be explained by natural mechanisms, both dissolved and particulate lead and dissolved tin appeared elevated over normal at some locations. Using enrichment factors, the cobalt, manganese, and nickel clearly traced the flow of the Potomac River; however, it is not clear if the elevated EF's are due to natural or anthropogenic causes. The nature of the samples challenged several existing areas of analytical work. The analysis of ppb and ppt elemental concentrations in a salt matrix led to a new separation preconcentration method for neutron activation analysis. This procedure provides solid resin pellets containing 16 trace elements with no alkali, alkaline earth or halogen element interferences. These pellets are placed directly into the reactor for irradiation. In addition, the statistical evolution of extensive blank data helped to characterize blank behavior at these ultra-trace levels and showed the inadequacies of using a normal distribution. Lastly, the 2-3 orders of magnitude fluctuation of the particulate concentration data led to the application of enrichment factors which have been used in air particulate analyses but had not been applied to a aqueous systems. The choice of a reference element and secondary check elements also proved ideal. This technique provided a means by which the data and its environmental significance could be evaluated based on statistical comcepts. Additional work is currently in progress with the Statistical Engineering Division to investigate additional correlations within these data sets.

4. Determination of Ion-implanted Arsenic in Silicon

R. M. Lindstrom

In support of a program of the Electron Devices Division, measurements were made of the quantity of arsenic in semiconductor silicon. A series of four samples had been ion-implanted at nominal doses from $7x10^{12}$ to $7x10^{15}$ atoms/cm^2. Instrumental neutron activation analysis was used to assay the amount of arsenic in samples of 1 cm^2. All samples were irradiated together for 6 hours in RT3. The results in the table below demonstrate that the dynamic range, sensitivity, and precision of the technique are adequate.

TABLE 1

Arsenic Found

Sample ID	ng	Atoms
3	862 ± 6	$(6.92 \pm .05)x10^{15}$
13	87.5 ± 0.3	$(7.03 \pm .02)x10^{14}$
23	9.37 ± 0.14	$(7.53 \pm .11)x10^{13}$
32	0.600 ±.012	$(4.83 \pm .09)x10^{12}$
97(blank)	<0.006	$<5x10^{10}$

5. Multielement Analysis of Coal Standard Reference Materials

R. M. Lindstrom, R. R. Greenberg, and R. F. Fleming

A series of four coal Standard Reference Materials (SRMs 2682, 2683, 2684, and 2685) are in preparation for use as standards in environmental and energy-related analyses. In addition to certification of sulfur, ash content, and heating value, information will be provided to users on the chemical composition. Nearly thirty major, minor, and trace elements are being determined by a combination of instrumental neutron activation analysis and neutron-capture prompt-gamma activation analysis. A partial list of results is given in the table below.

TABLE 1
Elemental Concentrations in Coal SRMs

Units are μg/g unless % Indicated. Uncertainties quoted are 1s. Basis: dry weight

	SRM 2682	SRM 2683	SRM 2684	SRM 2685
Al(%)	0.462 ± 0.002	0.858 ± 0.005	1.103 ± 0.006	1.669 ± 0.007
As	1.00 ± 0.02	3.64 ± 0.13	3.87 ± 0.14	12.28 ± 0.38
B	39.0 ± 1.3	67 ± 2	114 ± 3	109 ± 5
Ba	382 ± 5	71 ± 3	41.4 ± 2.6	105 ± 6
Br	3.74 ± 0.18	16.85 ± 0.04	10.6 ± 0.5	5.57 ± 0.07
C (%)	76.0 ± 3.8	79 ± 4	68 ± 2	66 ± 3
Ce	9.87 ± 0.08	9.18 ± 0.08	11.5 ± 0.2	17.88 ± 0.18
Co	1.66 ± 0.03	2.22 ± 0.09*	3.85 ± 0.05	4.57 ± 0.06
Cr	15.4 ± 0.3	11.02 ± 0.18	16.8 ± 0.3	22.3 ± 0.4
Cs	–	0.44 ± 0.02	1.15 ± 0.05	1.31 ± 0.07
Eu	0.172 ± 0.005	0.177 ± 0.006	0.226 ± 0.009	0.357 ± 0.004
Fe (%)	0.242 ± 0.003	0.762 ± 0.019	1.454 ± .026	2.396 ± 0.065
H (%)	4.70 ± 0.13	5.0 ± 0.1	4.8 ± 0.1	4.6 ± 0.2
Hf	0.60 ± 0.02	0.418 ± 0.004	0.565 ± 0.012	0.913 ± 0.011
K	117 ± 14	750 ± 10	1969 ± 16	2592 ± 45
La	5.17 ± 0.03	5.05 ± 0.04	6.65 ± 0.10	10.19 ± 0.11
N (%)	0.8 ± 0.3	1.6 ± 0.9	1.6 ± 0.4	1.1 ± 0.3
Rb	–	–	14.6 ± 1.1	16.8 ± 1.3
S (%)	0.447 ± 0.013	1.82 ± 0.05	2.94 ± 0.07	4.64 ± 0.19
Sb	0.189 ± 0.009	0.279 ± 0.008	0.354 ± .008	0.357 ± 0.012
Sc	1.524 ± 0.005	1.941 ± 0.008	2.665 ± .020	3.700 ± 0.019
Se	0.91 ± 0.10	1.23 ± 0.09	1.87 ± 0.16	1.91 ± 0.16
Sm	0.776 ± 0.004	0.859 ± 0.005	1.109 ± 0.012	1.729 ± 0.007
Th	1.532 ± 0.014	1.363 ± 0.011	1.955 ± 0.016	2.66 ± 0.03
U	0.519 ± 0.015	0.418 ± 0.011	0.901 ± 0.010	0.948 ± 0.013
W	1.81 ± 0.03	0.48 ± 0.03	0.562 ± .022	1.18 ± 0.06
Zn	8.6 ± 0.9	9.5 ± 0.6	110 ± 12	17.1 ± 1.1

6. Effect of Natural Isotopic Abundance Variability on the Accuracy of Neutron Activation Analysis

R. F. Fleming and R. M. Lindstrom

Accurate activation analysis requires that the isotopic composition of the sample and standard be the same, or else explicitly known. For monoisotopic elements this requirement is automatically met, and for cases where the activating isotope is of major abundance the fractional change is usually negligible. We are not concerned here with man-made alteration of abundance (e.g. U, Li, B) nor with the uncertainty in the measured value for the abundance. Rather, it is only actual variation in the naturally occuring abundance from sample to sample that is considered. This can be important especially for the lighter elements, which may readily fractionate, and for cases in which chemical reactions or physical processes commonly do not go to completion (i.e. in which the element exists in geochemical or biochemical reservoirs in more than one state), and where the activating isotope is a minor constituent of the element. The example that we have investigated in some detail is sulfur, where a 5-minute S-37 activity is produced from the 0.017% abundant S-36.

Recently Holden[1,2] has published an evaluation of the known variation in nature of isotopic compostion of the elements. Isotopic fractionation of light elements is well documented[3]. Based on this observed natural variability, we list in Table 1 those elements for which measurement by nuclear techniques could result in a systematic bias, and the range of this bias.

Sulfur analysis appears to be an ideal case to investigate experimentally since NAA depending on S-36 should show obvious variation while prompt gamma activation analysis (PGAA) which depends on the capture gammas of S-32 should give consistent results. The wide variation in the isotopic ratios of naturally occurring sulfur was first demonstrated by the McMaster group[4] using mass spectrometric techniques, and has since been documented for thousands of samples.[5,6]

Although careful mass spectrometry can determine the $^{36}S/^{32}S$ ratio directly, the isotopic fractionation of S-34 is typically measured and expressed as

$$\delta^{34}S \equiv \left[\frac{(^{34}S/^{32}S)\ \text{sample}}{(^{34}S/^{32}S)\ \text{standard}} - 1 \right] \text{X}1000, \text{o/oo}. \qquad (1)$$

Meteoritic troilite (FeS) is the usual standard ($\delta^{34} \equiv 0$), since it is believed to reflect the mean solar system abundance and has not been fractionated. Seawater sulfur is uniformly enriched in S-34 by 20 parts per thousand (δ^{34} = +20 o/oo). Volcanic sulfur has a range of δ^{34} from -10 to +10 o/oo, while that in coal and petroleum ranges from -30 to +30 o/oo. The range of published values for δ^{34} is from -53.1 o/oo for a Texas marcasite (FeS_2) to +86.7 o/oo for a barite ($BaSO_4$) from the Japan Sea[1]. Using the theoretical relation for the fractionation of sulfur isotopes[7], we can estiamte the spread in the abundance of naturally occurring S-36.

$$\ln(1 + \delta^{36}S) = (1.90 \pm 0.01)\ \ln(1 + \delta^{34}S),$$
$$\ln(1 + \delta^{33}S) = (1.94 \pm 0.01)^{-1} \ln(1 + \delta^{34}S).$$

This model predicts a maximum difference of 29% in the S-37 specific activity of sulfur samples irradiated under the same conditions. The δ^{34} spread for coal and petroleum is less, but large enough to limit the accuracy of sulfur determination to ±15% regardless of the precision of the measurement.

In this work we demonstrate this systematic error from isotopic variability by determining the S-37 counting rate per unit mass of sulfur produced after irradiation of five δ^{34} standards from McMaster University (the SL-277 series) as well as a galena, a barite and an elemental sulfur standard.(a) Several other sulfurs of unknown isotopic composition including the NBS SRM-371g were also run. The McMaster samples were transposed from Ag_2S to H_2S with HCl, and the H_2S to S with I_2, followed by purification of the product. The volcanic samples and some of the laboratory sulfurs were purified by recrystallization. The samples, weighing from 12 to 90 mg, were irradiated in the NBS reactor, and after a fixed decay time the 3103 keV gamma ray was counted with a germanium detector. Zinc flux monitors were run with each irradiation to measure the constancy of the neutron flux, and small corrections were made for dead-time and pulse pileup.

The resulting decay-corrected counting rates per unit mass of sulfur are given in table 2. There is a 6% difference among sulfurs from commercial suppliers, perhaps a 3% difference among the volcanic sulfurs, and an apparent $\delta^{34}S \cong 0$ for the SRM sulfur. The results for the standards are plotted against $\delta^{34}S$ in figure 1, with each data point representing the average of at least two measurements and the error bars representing counting statistics (1σ) only. The solid line is the predicted curve based on Eqs (2), normalized to the measured activity for sample SL-277-1. The equivalent date for PGAA measurement of the same standards is plotted in figure 2, which exhibits no dependence of specific count rate on fractionation to within the counting uncertainty. One could interpret the combined NAA/PGAA measurement on a sample as being a determination of $\delta^{36}S$ and hence the degree of fractionation. In general, it is more accurate to determine sulfur fractionation by a mass spectrometric measurement of $\delta^{34}S$ however.

In summary, it has been demonstrated that the known isotopic variability of S-36 results in a corresponding inaccuracy in the measurement of sulfur by neutron activation and that this effect is well predicted by the theory. The worst-case limit on the measurement accuracy is ±29%; however this uncertainty can be halved if one uses a standard of known isotopic composition. The Bureau is preparing to issue a sulfur SRM which is certified for isotopic composition. No significant bias exists for PGAA determination of sulfur.

We thank C. E. Rees for providing the five McMaster University interlaboratory standards, I. L. Barnes of NBS for the French and NBS standards, and D. L. Anderson for the University of Maryland for the volcanic sulfurs.

TABLE 1

Natural Isotopic Variability

Element	Isotope : Range	Isotope : Range
Lithium	Li-6 ± 37%	
Boron	B-10 ± 6.2%	
Silicon	Si-30 ± 4.2%	
Sulfur	S-32 ± 0.65%	S-36 ± 29%
Copper	Cu-63 ± 0.38%	Cu-65 ± 0.84%
Selenium	Se-74 ± 1.3%	
Mercury	Hg-202<± 0.6%	Hg-196 ≃ Hg-198/Hg-202=±1.5%
Lead	Pb-204 ± 59%	Pb-202 ± 32%

TABLE 2

Sulfur Irradiation Results

Sulfur Sample	$\delta^{34}S$ o/oo	S-37 Count rate, $sec^{-1} mg^{-1}$	Bias* %
SL-277-1	+ 2.52	4.82 ± 0.03	+0.4
SL-277-2	- 6.46	4.78 ± 0.03	-0.4
SL-277-4	+16.07	4.89 ± 0.03	+2.0
SL-277-9	-19.21	4.66 ± 0.04	-2.9
SL-277-10	-28.5	4.49 ± 0.04	-6.5
Soufre de Lacq	+17.3	5.01 ± 0.02	+4.4
NBS 200 Galena	+ 0.6	4.83 ± 0.04	+0.6
OGS-1 Barite	+20.58	5.02 ± 0.03	+4.6
Volcanic (Hawaii)		4.77 ± 0.03	-0.6
Volcanic (Hawaii)		4.72 ± 0.03	-1.7
Volcanic (St. Helens)		4.87 ± 0.03	+1.5
Lab Grade - A		4.95 ± 0.03	+3.1
Lab Grade - B		4.76 ± 0.03	-0.8
HiPurity - Lot 1		5.05 ± 0.04	+5.3
HiPurity - Lot 2		4.89 ± 0.04	+2.0
NBS SRM-371g		4.83 ± 0.02	+0.6

*The Bias is the inaccuracy which would result if the sample were measured using a standard with $\delta^{34}S = 0$.

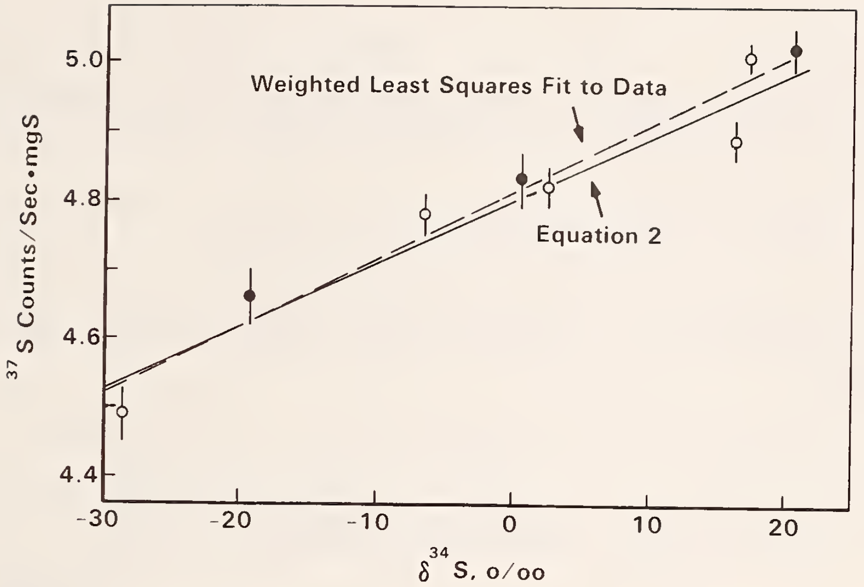

Figure 1. Specific activity of S-37 versus δ S-34.

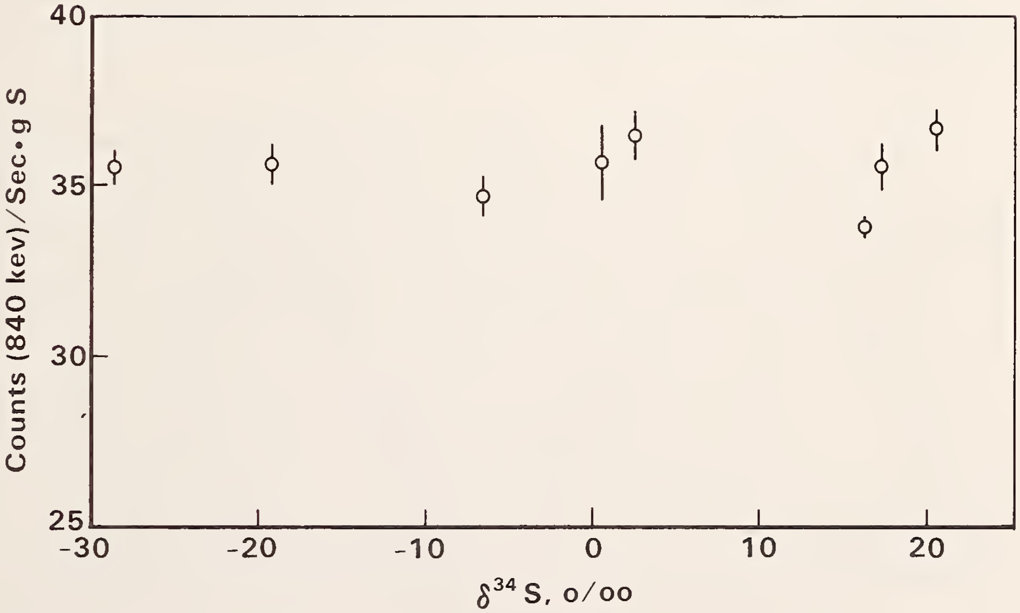

Figure 2. Neutron capture prompt - γ rate versus δ S-34.

---

1. N. E. Holden, "Isotopic Composition of the Elements and Their Variation in Nature: A Preliminary Report," BNL-NCS-50605, Brookhaven National Laboratory (1977).

2. N. E. Holden, "Atomic Weights of the Elements - 1979," *Pure and Applied Chemistry*, 52, 2349 (1980).

3. I. Friedman and J. R. O'Neil, "Composition of Stable Isotope Fractronation Factors of Geochemical Interest," *USGS Paper*, 440-KK (1977).

4. J. Macnamara and H. G. Thode, *Phys. Rev.* 78, 307 (1950).

5. H. Nielsen, Lectures in Isotope Geology, p. 283-312, E. Jäger and J. C. Hunziker, Eds., Spring-Verlag, Berlin (1979).

6. H. R. Krouse, Handbook of Environmental Isotope Geochemistry, p. 435, P. Fritz and J. C. Fontes, Eds., Elsevier Publishing Co. (1980).

7. J. R. Hulston and H. G. Thode, *J. Geophys. Rev.*, 70, 3475 (1965).

7. A Compton Suppression System for Background Reduction and Improved Sensitivity

J. R. Vogt and R. Zeisler

During the past year, a Compton suppression system has been set-up and evaluated for the improvement of analytical sensitivity through background reduction. The system, shown in figure 1, consists of a 25.4 cm (10-inch) long by 23.8 cm (9-3/8 inch) dia. NaI (Tl) annulus and an integral line 7.62 cm (3-inch) by 7.62 cm (3-inch dia. NaI (Tl) well detector used to surround all but the rear of a 19% relative efficient, 1.79 keV (Ge(Li) primary detector. The NaI(Tl) detectors are surrounded by a lead shield that is 10.16 cm (4-inch) thick and has internal dimensions of 40.64 cm (16-inch) by 40.64 cm (16-inch) by 55.88 cm (22-inch) deep. The lead shield is lined with 0.635 cm (1/4-inch) copper sheet. The coincidence circuitry is contained in a 2-wide NIM module (Harshaw NC-26R Anti-Compton Analyzer) which is relatively inexpensive compared to separate NIM modules easy to set-up, and quite stable. The

NC-26R uses amplitude and rise time compensated cross-over (ARC) timing for both the Ge(Li) and NaI(Tl) signals. Coincidence pulses from the NC-26R are fed into the anti-coincidence gate of a Nuclear Data 570 ADC. Adjustments for gating pulse width and delay are contained in the NC-26R. A Berkeley DB-2 random pulse generator is used to correct the gamma-ray photopeak areas for losses due to the coincidence system and pulse pile-up. As can be seen in figure 1, in this system the sample is located inside the NaI(Tl) shield, rather than outside as in same other designs[1]. The interior sample placement is similar to that described by Wagman[2]. Since there is no detection of scattered photons in the forward direction (to the rear of the Ge(Li) detector), the suppression at lower spectral energies is not as good as in systems where the Ge(Li) detector is surrounded more completely.

Figure 2 indicates the Compton suppression obtained with this system for a Cs-137 source. The figure clearly shows the additional suppression of the Compton edge by the central well detector. The

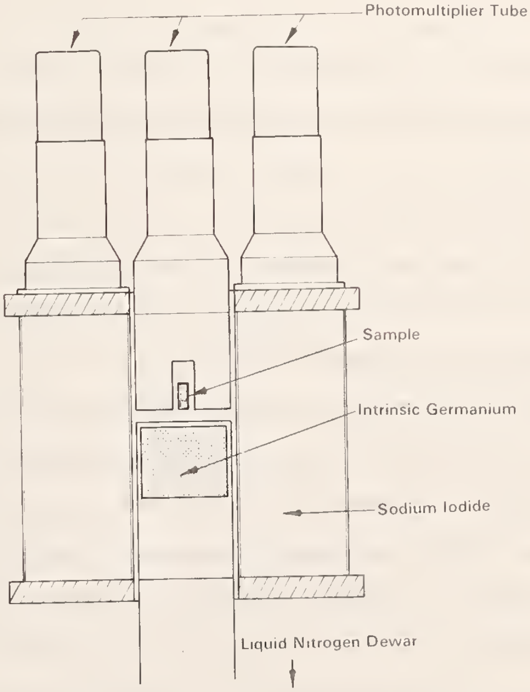

Figure 1. Cross-sectional View of the NBS Compton Suppression System.

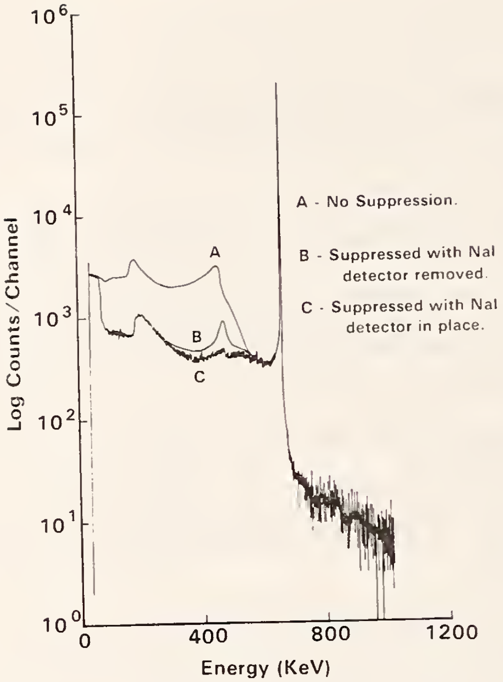

Figure 2. Compton Suppression of CS-137.

suppression is relatively independent of the position of the sample within the well detector. The system increases the peak-to-Compton ratio from 65:1 to 428:1. The suppression factor on the Compton edge is about 7-8, for the middle of the spectrum about 4-5, and at the backscatter peak about 3.5, since the improvement insensitivity follows roughly the square root of the background, the increases in sensitivity for these portions of the spectrum are approximately 2.7, 2.1, and 1.9, respectively.

With the sample inside the NaI(Tl) shield, both coincident photopeaks and Compton events for radionuclides with cascading transitions are suppressed. This effect reduces the spectral background more than simple Compton suppression. Thus the sensitivities of non-coincident gamma-rays are improved, while the sensitivities of coincident gamma-rays are decreased. This can be of benefit in matrices where coincident gamma-rays account for a substantial part of the activity, such as Sc-46 in environmental and geological materials and Na-24 in biological materials.

For example, in SRM 1633 a Fly Ash, the determination of zinc using Zn-65 gives a result of 238.0 ± 3.3 without Compton suppression. The certified value is 220 ± 10. Additional applications for this system are being evaluated.

1. H. J. M. Oarts, C. J. Van der Poel, D. E. C. Scherpenzeel, H. F. R. Archiszewski, and G. A. P. Engelbertink, *Nuc. Instr. Method.* (1980).

2. N. A. Wogman, "Intern. Symp. on Methods of Low-level Counting and Spectrometry, Berlin, 6-10 April 1981, Paper No. IAEA-SM-252125.

8. Facilities for Activation Analysis

R. M. Lindstrom

As a first step in assembling a more powerful and versatile data acquisition and processing system for activation analysis, a PDP 11/44 computer system has been installed. As communication is established with the existing ND6620 and with existing and future multichannel pulse height analyzers, the new computer will begin to perform much of the data processing. The 11/44's faster CPU, larger disks, and more versatile software is expected to improve both the quantity and quality of analysis.

In order to allow the systematic selection of the optimum Ge γ-ray detector for a particular experiment, the efficiency of each detector available was measured by counting a point source of Cs-137 in contact with the end cap. This useful measure of the maximum sensitivity of a detector does not always follow the industry - standard efficiency because of differences in detector dimensions and detector-to-window distances. In the table below, twelve detectors are arranged in increasing order of 0-cm efficiency; the 60-cc detector is much better by this criterion than expected from the standard efficiency.

TABLE 1

Efficiencies of Detectors

Detector Name	0-cm Efficiency (%)	Standard Efficiency (%)	Resolution (keV fwhm)
25 cc	1.61	*	*
Ge(Li) well	1.91	*	2.14
ATF	2.17	10.3	1.99
γX2	2.49	7.6	1.69
γX1	2.50	7.5	1.73
90 cc	2.8	15.6	1.95
66 cc	3.33	14.6	1.88
82 cc	3.33	16.6	1.95
60 cc	3.73	12.2	1.93
104 cc	4.01	21.5	1.76
AMD	4.42	18.1	1.80
131 cc	4.88	30.4	1.78

* Not known.

0-cm Efficiency is the measured number of net photopeak counts per photon emitted by a point source of Cs-137 on the end cap of the detector. The standard efficiency at 1333 keV measured by the manufacturer at 25 cm, relative to that for a 3"x3" NaI detector. The resolution is that measured by the manufacturer at 1333 keV.

NEUTRON-CAPTURE PROMPT GAMMA-RAY ACTIVATION ANALYSIS

D. L. Anderson, G. E. Gordon, W. B. Walters, and W. H. Zoller
(University of Maryland, College Park, MD)

and

R. M. Lindstrom
(Center for Analytical Chemistry)

We have continued to extend and improve the analyses of various types of samples by neutron-capture prompt γ-ray activation analysis (PGAA) which uses a vertical beam tube on top of the NBS reactor.[1] In PGAA, one places the sample in the external neutron beam (of flux $\sim 2\times 10^8$ n/cm^2-sec) and observes prompt γ rays emitted by the various capturing species with a Ge(Li) detector during the irradiation. Unlike the more widely used instrumental neutron activation analysis (INAA), which employs γ rays emitted by radioactive products following irradiations, PGAA can be used to observe elements with reasonable capture cross sections and prompt γ rays of appreciable intensity whether or not capture leads to a radioactive product. Also, in PGAA, the results are available immediately after irradiations, whereas about three weeks are required in INAA to observe all long-lived products. In previous work with NBS SRMs and U.S. Geological Survey standard rocks, we have demonstrated that PGAA can measure the concentrations of the following major and minor elements in most crystal type samples: H, Na, Mg, Al, Si, K, Ca, Ti, V, Mn, and Fe; and the important trace elements B, Co, Cd, N, Sm, and Gd. In biological or other carbonaceous samples (e.g., NBS coals), we observe some of the above plus C, N, S, and Cl. Occasionally other elements are observed in samples of unusual composition such as ores, minerals, manganese nodules, etc. The accuracy of PGAA is so high for many elements, that the method is beginning to be used for routine analyses for certification of some SRMs.[4] The following sections briefly highlight some of our major results from the past year.

1. Assay of Enriched Uranium Fuels

The PGAA technique may ultimately be of considerable value in the assay of various isotopes of heavy elements in safeguards applications. The Livermore group[5] has developed excellent methods that use spectrometry of heavy element x-rays and low energy γ rays that are quite reliable if the heavy elements have been separated from fission products. However, the low energy backgrounds are so enormous in a spent fuel rod, even after two years'cooling, that direct assays of the rods would be impossible with their system. The PGAA technique would have the advantage that it could possibly use γ rays of about 5 MeV from neutron capture in the heavy elements or from very short-lived fission products (few seconds or less) counted between bursts of neutrons in a beam equipped with a chopper. By contrast, most γ rays from long-lived fission products in spent fuel rods have energies of about 1 MeV or less. Thus, one could discriminate strongly against the latter with respect to the ∿5-MeV γ rays by use of thick γ-rays absorbers.

As a first step in testing PGAA as applied to heavy elements, we have irradiated several enriched U-235 SRMs and nuclear fuel pellets supplied by Babcock and Wilcox, Lynchburg, VA. (This project is being performed in collaboration with Dr. Michael Failey of Babcock and Wilcox, a former student of this group, who was heavily involved in development of the PGAA system.) The U-235 isotopic abundance in the SRMs ranged from 0.48 to 93.0%, and for the commercial sintered fuel pellets, it was 3.982%. The counting sequence for these samples was:

1. 5-min count in-beam
2. 1-hr count in-beam
3. 5-min count on an off-line detector
4. 1-hr count on an off-line detector (to observe fission-product γ radioactivity)

The resulting spectra are extremely complicated, with at least 300 γ-ray peaks below 1.5 MeV. Although we have observed clear differences among the spectra taken with samples of various enrichments, the data reduction has only just begun. We are hopeful that some form of this method may be very effective for rapid, nondestructive assay of fuel-pellet enrichments.

2. Burnable Poisons in Nuclear Fuels

Burnable poisons are used in the cores of commercial reactors to help control power distribution at the beginning of each reactor fuel cycle. One method involves the use of solid, cylindrical pellets of sintered Al_2O_3-B_4C mixtures. These pellets are interspersed among the fuel pellets in the assembly. A second method used is the direct addition of Gd to the fuel pellets themselves.

Table 1. Comparison of Boron Analyses in Fuel-Poison Pellets by PGAA and Wet Chemical Techniques

Nominal wt. % B	Observed Wt. % B				
	Wet Chemical Analyses[a]				PGAA
	A1	A2	B1	B2	This work
0.183	0.194	0.197	0.1947	0.1796	0.1815
		0.244			0.1813
					0.1802
0.925	0.898	0.946	-	0.8971	0.8798
1.23	1.137	1.236	-	1.238	1.233
0.2022[c]	0.186	-	-	0.2017	0.2052
1.602[c]	0.905	-	-	1.045	1.565

[a] A and B are different analytical laboratories; 1 and 2 denote analyses separated by a period of months.

[b] Measurements of ^{10}B by PGAA converted to total B using the ratio ^{10}B/total B = 0.1975.

[c] Non-sintered powder mixes of Al_2O_3 and B_4C.

In cooperation with Dr. Michael Failey of Babcock and Wilcox Lynchburg Research Center we have begun to explore the use of PGAA for assay of these burnable poisons using samples provided by Babcock and Wilcox. The initial results, listed in Table 1, indicate that the method would be excellent for the B_4C-Al_2O_3 pellets. The total analysis time for each sample by PGAA was less than 15 min. We obtain excellent reproducibility for the sample analyzed three times and our results appear to be in better agreement with the make-up of the pellets than the wet chemical analyses. By contrast, the wet chemical analyses are much more time consuming and labor intensive, and seem to be less accurate. Thus, the PGAA method is quite promising. A paper covering these results were presented at the Washington American Nuclear Society meeting in November 1982.

Our initial results for Gd-poisoned samples are less encouraging because of the very low levels of GD (<1 ppm) and complexity of the spectra (because of the many fission products formed, see Sect. A above). However, it may be possible to find usable Gd lines in the spectra after more careful study.

We plan to continue these studies during the coming year.

3. Analyses of Reference Materials

We are analyzing several new geological and biological reference materials that were recently released by NBS and the International Atomic Energy Agency (IAEA). The NBS Basalt (SRM 688) and Obsidian (SRM 278) are being certified for most major elements and a number of trace elements.

Table 2 lists the results of our PGAA measurements on the NBS standards, the PGAA results from the University of Missouri, and the NBS values. As is standard geochemical practice, we have calculated the total concentrations based on the assumption of common oxides of the elements, e.g., Na_2O, CaO, Al_2O_3, etc. Our results and those from NBS are excellent for the basalt, but Missouri's exceeds 100% for both standards. The NBS also hits very close to 100% on the obsidian, but our value is somewhat low. Note that we are missing about 0.3% MgO

Table 2. Comparison of Analysis of NBS Rock Standards

Element	Concentration (% unless noted)					
	SRM 688 - Basalt			SRM 278 - Obsidian		
	This work	Univ. of Mo.[a]	NBS certificate[b]	This work	Univ. of Mo.[a]	NBS certificate[b]
H (μg/g)	390±10	-	-	530±45	-	-
B (μg/g)	1.3±0.2	0.88±0.14	-	24.1±0.4	25.2±0.4	(25)[c]
Na	1.61±0.06	1.05±0.07	1.595±0.002	3.51±0.05	2.6±0.2	3.59±0.04
Mg	5.3±0.2	5.7±0.4	(5.1)	-	-	(0.14)
Al	9.18±0.09	9.3±0.2	9.19±0.05	7.55±0.08	7.8±0.2	7.49±0.09
Si	22.39±0.08	24.6±0.6	22.62±0.08	33.1±0.3	36.6±1.3	34.15±0.06
Cl (μg/g)	35.8±0.8	-	-	610±7	640±90	-
K	0.153±0.006	0.17±0.006	0.154±0.006	3.31±0.01	3.44±0.08	3.45±0.02
Ca	8.70±0.09	7.9±0.2	(8.70)	0.71±0.03	0.60±0.10	0.703±0.001
Ti	0.69±0.01	0.72±0.02	0.701±0.006	0.133±0.006	0.145±0.009	0.147±0.004
Mn (μg/g)	1230±40	1120±60	1290±20	380±50	430±70	400±20
Fe	7.03±0.10[d]	7.23±0.17[d]	7.23±0.03[d]	1.39±0.05[e]	1.32±0.17[e]	1.43±0.01[e]
Cd (μg/g)	-	-	-	0.18±0.06	-	-
Nd (μg/g)	-	-	-	30±5	-	-
Sm (μg/g)	2.35±0.02	2.31±0.08	(2.79)	5.45±0.03	5.66±0.10	(5.7)[c]
Gd (μg/g)	2.88±0.10	2.82±0.08	-	4.96±0.08	5.34±0.08	(5.3)[c]
Total (as oxides)	99.4±0.3	103.2±1.5	99.6±0.3	97.3±0.9	103.5±1.5	99.7±0.2

[a] [6].

[b] Values in parantheses are "Information Values", not certified values.

[c] These information values were measured by the Univ. of Missouri group, who cooperated with NBS on certification.

[d] In summing oxides, used NBS result that 82% of Fe is present as FeO.

[e] In summing oxides, used NBS result that 74% of Fe is present as FeO.

Table 3. Preliminary Results from PGAA Studies of New Biological Standards

Element	Concentration (% unless noted)		
	NBS Citrus Leaves (4 samples)	IAEA Cotton Cellulose (6 samples)	IAEA Animal Blood (4 samples)
H	5.96±0.01	6.34±0.10	6.88±0.19
B (μg/g)	64.3±0.6	1.2±0.1	1.4±0.2
C	-	48.0±2.2	-
N	3.62±0.04	-	15.6±0.2
Na	-	-	1.42±0.03
Si	0.19±0.06	-	-
S	0.44±0.02	-	0.71±0.04
Cl (μg/g)	391±6	633±4	14,000±800
K	1.889±0.007	-	0.24±0.02
Ca	3.47±0.05	-	-
Mn (μg/g)	22±6	-	-
Fe	-	-	0.25±0.02

and an unknown amount of P_2O_5. Our values agree very well with NBS, the major exception being Fe in basalt. Our Sm and Gd values agree well with the Missouri values. The Missouri values show some disagreement with the NBS data for Na, Mg, Si, Ca, and Mn. Our values for Si, K, and Ti are low by 3.2, 4.2 and 10% relative to the NBS values, but the agreement is generally quite good.

The Bureau is preparing a new SRM, citrus leaves, to supplement the heavily used orchard leaves (SRM 1571). We have been analyzing the new standard by both INAA and PGAA for as many elements as we can observe. In addition, we are participating in the analysis of two new IAEA standards, cotton cellulose, and animal blood. The PGAA results obtained so far are listed in Table 3. We will do considerably more work on these standards before release of final values.

Table 4. Compositions of Coal and Ashes from Washington State Power Plants

Element	Concentration (% unless noted)			
	Plant #1			Plant #2
	Coal (2 spls)	Precip. ash[a] (2 spls)	Bottom ash[a] (2 spls)	Fly Ash (1 spl)
H	4.31±0.03	0.05±0.02	0.19±0.09	0.05±0.01
B (µg/g)	214±26	2020±170	897±8	142±1
C	51±1	-	-	-
N	1.37±0.01	-	-	-
Na	0.21±0.04	1.5±0.4	1.1±0.3	0.43±0.09
Mg	0.8±0.4	2.0±0.5	1.6±0.3	2.3±0.2
Al	1.63±0.10	12.0±0.1	10.5±0.7	14.6±0.3
Si	2.72±0.07	20.9±0.6	21.7±0.9	24.1±0.2
S	0.59±0.07	0.14±0.01	0.12±0.01	0.13±0.01
Cl (µg/g)	45±15	-	-	-
K	0.11±0.02	0.87±0.05	0.85±0.11	2.60±0.01
Ca	1.24±0.08	9.7±0.5	7.5±0.7	1.04±0.04
Ti (µg/g)	280±5	2480±80	2200±150	7850±25
V (µg/g)	-	455±25	250±50	330±20
Mn (µg/g)	-	260±20	735±50	190±12
Fe	0.46±0.02	3.0±0.2	2.54±0.10	3.81±0.05
Cd (µg/g)	0.30±0.05	0.90±0.19	0.96±0.19	7.4±0.1
Sm (µg/g)	-	70±30	35±4	90±7
Nd (µg/g)	1.14±0.03	10.6±0.1	8.9±0.6	17.0±0.1
Gd (µg/g)	1.0±0.1	9.2±0.2	7.6±0.5	15.1±0.3
Total (as oxides except C, N, H)	72	93	87	95

[a] Corrections for neutron self-shielding by the large amounts of B present in these samples was necessary.

4. Coal and Coal Fly Ash

We have analyzed several coal and coal ash samples during the past year. Typical results from these studies are listed in Table 4: compositions of coal, precipitator fly ash and bottom ash from one plant; and fly ash from a second plant in the State of Washington. We do not understand why we fail to account for 26% of the mass of the coal sample, as we previously reported.

From the summation of oxides, we estimate that the ash content of the coal is 10.5%. Thus, after the combustion process has removed most of the C, H, N, S, and Cl, concentrations of the elements that remain with the ash fractions are increased by factors of about 8.

In general, the results are consitent with those of previous in-plant studies of coal-fired power plants [8, 9]. Most previous studies have been performed with INAA, which does not yield data for about one-third of the elements reported here (although it yields results for 15 to 20 elements not measured by PGAA). One very striking result of this work, which is not observable by INAA, is the enormous boron concentrations of the coal and, especially, the fly ash. This result has previously been noted by other investigators who used PGAA[10,11]. Little is known about the sources of boron in the atmosphere, or even about its atmospheric concentrations. However, judging by the very high boron concentrations in coal fly ash relative to that of soil (∿2000 vs 15 ppm), there is a good chance that coal combustion is the dominant source of boron borne by suspended particles in the atmosphere. If so, boron might serve as an excellent tracer for emissions from coal-fired power plants, which would be of great value in answering such questions as the sources of acidic rainfall and airborne sulfates. During the coming year we will investigate the ability of PGAA to observe boron in atmosphere particle samples.

1. Anderson, D. L. Failey, M. P., Zoller, W. H., Walters, W. B., Gordon, G. E., and Lindstrom, R. M., *J. Radioanal. Chem.*, 63, 97 (1981).
2. Failey, M. P., Ph.D. Thesis, Univ. of Maryland, 1979.
3. Failey, M. P., Anderson, D. L., Zoller, W. H., Gordon, G. E., and Lindstrom, R. M., *Anal. Chem.*, 51, 2209 (1979).
4. This report, Section 5, Activation Analysis Group FY 82.
5. Camp, D. C., Ruhter, W. D., and MacMurdo, K. W., "Determination of Actinide Process and Product Stream Concentrations Off-Line and At-Line by Energy Dispersive X-ray Fluorescence Analysis," *Lawrence Livermore National Laboratory Report* UCRL-85083 (1980).
6. Graham, C. C., Glascock, M. D., Carni, J. J., Vogt, J. R., and Spaulding, T. G., *Anal. Chem.*, 54, 1623 (1982).
7. Germani, M. S., Gokmen, I., Sigleo, A. C., Kowalczyk, G. S., Olmez, I., Small, A., Anderson, D. L., Failey, M. P., Gulovali, M. C. Choquette, C. E., Lepel, E. A., Gordon, G. E., and Zoller, W. H., *Anal. Chem.*, 52, 240 (1980).
8. Gladney, E. S., Small, J. M., Gordon, G. E., and Zoller, W. H., *atmos. Environ.*, 10, 1071 (1976).
9. Klein, d. H., Andren, A. W., Carter, J. A., Emergy, J. F., Feldman, C., Fulkerson, W., Lyon, W. S., Ogle, J. C., Talmi, Y., VanHook, R. I., and Bolton, N. E., *Environ. Sci. Technol.*, 9, 973 (1975).
10. Gladney, E. S., Wangen, L. E., Curtis, D. B., and Jurney, E. T., *Environ. Sci. Technol.*, 12, 1084 (1978).
11. James, W. D., Graham, C. C., Glascock, M. D., and Hanna, A. G., *Environ. Sci. Technol.*, 16, 195 (1982).

SUMMARY OF ACTIVITIES CARRIED OUT BY THE NEUTRON FIELD STANDARDS GROUP

J. Grundl
(Nuclear Radiation Division)

The Neutron Field Standards Group, attached to the Center for Radiation Research (CRR) is engaged in the establishment and application of standard and reference neutron fields as permanent facilities for neutron detector calibrations, neutron dosimetry standardization, and reaction rate cross-section measurement.

One component of this group's activities makes use of the reactor thermal column and the tangential beam tubes where facilities, designed and built by the NFS Group, are in operation. Facility and related capabilities developments for FY 82 are as follows:

1. Installation of a fusion chamber monitor for the cavity fusion source at the reactor thermal column. A specialized fusion chamber of small diameter, purchased in France, was mounted at the entrance penetration of the thermal column cavity. It is now possible to perform time-history fluid monitoring of U-235 fission spectra irradiations. Other notable improvements in the cavity fission source were : (1) experimental examination of flux gradients over the region of detector placement; and (2) receipt of preliminary results of source detector scattering calculations. The latter are part of extensive Monte Carlo calculations being carried out at Los Alamos under joint cooperation and contract.

2. An archive deposit of U-233 is a recent addition to the NBS set of fissionable isotope mass standards. The complex alpha spectrum of U-233 and its daughters and the fact that the deposit is a fluoride compound rather than the usual oxide creates special problems in the mass assay. In order to carry out the thermal-fission component of the assay, fission fragment self-absorption in flouride vs. oxide deposits was investigated in a series of measurements in a thermal beam.

3. The Subcommittee on Standards of CSEWG has explicitly recognized the fission-spectra-averaged cross-section of U-235 in the Cf-252 fission

spectrum as a basic normalization measurement for the U-235 fission cross-section. Remeasurement of this normalization quantity is continuing and included this year fissionable deposit mass intercomparisons at the thermal column. In addition, a re-evaluation of earlier measurements was completed and the result forwarded to CSEWG:

$$\bar{\sigma}_f(\text{U-235}, X_{ef}) = 1216 \pm 19 \text{ mb}$$

There was little changed from the previously published value but the error in the rms sense was reduced by a factor of two. This improvement came from (1) revision of mass scale for NBS fissionable deposits (error reduced to ± 0.75); (2) new detailed monte-carlo scattering calculations for the fission chamber and the fissionable deposit backings carried out at Los Alamos; (3) reduction of the error assigned to the source strength of NBS-I, the National Standard Neutron Source (error reduced to ± 0.9%).

4. The thermal-neutron-radiography facility for diagnostic irradiations of art works is described elsewhere in this report. In cooperation with the Reactor Division and the National Gallery of Art, substantial modifications at the thermal column were designed and fabricated in order to achieve a high intensity flux of thermal neutrons over a large area. The design also made possible rapid recovery of irradiated paintings so that short-lived activities could be included in the post-irradiation diagnostic procedures.

5. The filtered beams of monoenergetic neutrons are used primarily for calibration of neutron personnel dosimetry instrumentation. Flux parameters for the beams were intercompared with those at PTB, the West German Standards Laboratory at Braunschweig. Important improvements in the control system for the dosimetry phantom scanner employed at the filtered beams were completed.

6. Fission cross-section measurements in the thick-shell ISNF were performed for the following isotopes: U-233, Pu-240, Pu-241, and Th-232. Combined with earlier measurements of U-235, U-238, Pu-239, and Np-237, there now exists for ISNF a consistent set of integral fission cross-

section data for essentially all of the fissionable isotopes important for reactor technology. A representative result,

$$\sigma_f(\text{Pu-240, ISNF}) = 824 \text{ mb} \pm 2.8\%,$$

agrees well with the value predicted by ENDF/BV (the U.S. nuclear data file for reactor technology);

$$\frac{\text{Calculated}}{\text{Observed}} = 1.00 \pm 3.0\%$$

A characteristic of this result, identifying it as coming from a standard neutron field, is the inclusion of a component error (in the 3.0% total) uncertainty) for the propagated effect of ISNF spectrum uncertainties.

7. Testing of neutron personnel dosimetry instrumentation continued at a high level making proper institutional use of the filtered beams the thermal column, and the D_2O moderated fission spectrum irradiation facility. Systemmatic performance tests have now been performed on essentially all types of passive neutron dosimeters used in the United States. Calibration of active neutron dosimetry instrumentation parameters and BF_3 counters) for a variety of agencies, laboratories, commercial vendors and most significantly for a suddenly increased number of power reactor operators. See accompanying special report.

8. Neutron fluence standards prepared with the cavity fission source were sent to ORNL for calibration of a new dosimetry counting system. Activation reactions included were In(n,n'), Al(n,α), Ni-58(n,p), and Fe-54(n,p). The counting facility at ORNL will be employed for neutron dosimetry determinations in existing and planned radiations designed to test embrittlement rates in reactor pressure vessel steels.

9. The cavity fission source, after its varied applications to neutron dosimetry calibration, was employed for the first time in a cross-section measurement. The U-235 fission-spectrum-average cross section for the activation dosimetry reaction Ni-58(n,p) was determined in a set of cavity fission sound irradiations. The absolute flux for the experiment was obtained by the method neutron flux transfer from the Cf-252 fission

source using the In (n,n') reaction. The preliminary result of this measurement:

$$\sigma(\text{Ni}, X_{25}) = 101 \pm 3 \text{ mb},$$

caused some spirited discussion if not consternation when reported at the Fourth ASTM-EURATOM Symposium on Reactor Dosimetry in March of this year. This cross section is central for work of dosimetry and the accepted experimental value is some 8% higher than the one above. There is added provacation in the fact that the preliminary NBS value agrees with the calculated spectrum-average cross section whereas the accepted value does not and in fact has been used to challenge the shape of the U-235 fission spectrum.

10. Miscellaneous measurement and related activities make poor material for progress and accomplishment reporting, but unfortunately they constitute a substantial part of the NSF Group effort. Some samples of these activities are: (1) performance test irradiation with thermal neutrons of proton-recoil emulsion detectors; (2) post-irradiation checks of Co-Al and Co-Zr dosimeter wires for validating co-concentrations; (3) revision of ASTM standard on definition of terms used in dosimetry; (4) quality control tests of navy shipboard area monitors; (5) refurbish and check out of fission chambers for CEN/SCK (Belgium) and the University of Arkansas; (6) performance investigation of position-sensitive, proportional counter to be used for linac resonance radiography development.

NEUTRON PERSONNEL DOSIMETER CALIBRATION AND TESTING

R. B. Schwartz
(Nuclear Radiation Division)

The reactor filtered beams, with energies of 2, 24, and 144 keV, together with the beam from the thermal column, were used as part of a complete test of most of the neutron dosimeters used in the United States. Dosimeters from most of the DOE laboratories, as well as from commercial suppliers, were irradiated in each of the reactor beams and with the NBS bare and moderated californium sources. Several dosimeters of each type were irradiated at each facility, at several different dose levels. The data from these irradiations, which are still being evaluated, will allow the accuracy, precision, energy response, and sensitivity of each dosimeter type to be determined. These data will permit the different dosimeters now in use to be accurately compared and evaluated and will serve as a basis for evaluating new dosimeter types under development. This is the first time that such a comprehensive test has been carried out in the United States.

We have also carried out an intercomparison between our filtered beams and the filtered beams at the Physikalisch-Technische Bundesanstalt (PTB) in Braunschweig, Germany. Since NBS and the PTB have the only sets of filtered beams used for instrument calibrations, this constitutes a complete international intercomparison. Preliminary results indicate good agreement between our two laboratories, but the data are still being evaluated.

In addition, we have done numerous irradiations of active instruments (BF_3 counters, remmeters) and passive detectors for several commercial companies, DOE laboratories, the Aberdeen Proving Ground, the Naval Surface Weapons Center, and a university, to calibrate existing instruments and to help develop new ones.

ATMOSPHERIC AND ENVIRONMENTAL STUDIES BY INSTRUMENTAL NEUTRON ACTIVATION ANALYSIS

G. E. Gordon and W. H. Zoller
(University of Maryland, College Park,MD)

We continue to make extensive use of instrumental neutron activation analysis (INAA) to determine concentrations of about 35 elements in samples of atmospheric particulate matter collected from ambient air (now mostly at remote sites such as Hawaii) and in particles released from major sources such as volcanoes. By measuring concentrations of such a large number of elements, we hope to be able to identify contributions from the sources to the atmospheric burden at ambient sampling sites. Examples of three studies are discussed briefly in the following sections.

1. Compositions of Atmospheric Particles at Mauna Loa Observatory, Hawaii

Until recently, there existed no long continuous record of concentrations of elements on particles at a site remote from local activities despite demonstration of the enormous value of the long-term CO_2 record (since 1957) at Mauna Loa Observatory (MLO) in Hawaii for observing CO_2 seasonal variations and long-term increase. Fortunately, since mid-1979, the National Oceanic and Atmospheric Agency (NOAA) has supported weekly collections of filters at MLO and analysis of them by our group using instrumental neutron activation analysis. A distinct diurnal cycle exists at MLO at 3400 m alt, above the marine boundary layer: during the day, warming of the slopes of the mountain causes upslope winds whereas, during the night, cooling of air along the slopes causes downslope winds. Upslope conditions bring up air containing marine aerosol, crustal dust from the island and emissions from the small anthropogenic activity there. Downslope conditions bring down rather clean air from the upper troposphere. A control system alternately activates the pump on one of three filter systems depending on wind conditons and time-of-day to make separate collections of particles from upslope and downslope conditions. The third filter operates when neither condition is clearly established or when a condensation nuclei counter detects high counts due to contamination by motor vehicles, volcanic eruptions, etc.

Average elemental concentrations under various conditions are listed in Table 1. There are huge increases in crustal dust every Spring, apparently because of transport from arid regions of central and eastern Asia. Duce *et al*. [1] previously reported similar incursions of Asian dust at Enewetak Atoll, with concentrations of airborne soil being 2.3 $\mu g/m^3$ in mid-April, 1979. During non-dust conditions at MLO, average Al concentrations are about 7.6 ng/m^3, whereas weekly average concentrations rise to $\gtrsim 250$ ng/m^3 during the dust periods. Upslope samples are similarly affected, but the increases are not as dramatic because of higher normal concentrations.

The downslope data for 1980 are divided into dust and non-dust periods, as differences are so great that yearly averages are strongly influenced by the dust periods for most elements. Average concentrations of many elements are more than an order of magnitude higher during the periods, but there are some exceptions including Br and I, whose concentrations are scarcely affected by the dust, and Na and Se, which are only doubled.

During non-dust periods, downslope concentrations are among the lowest observed anywhere in the world, typically being about a factor of ten greater than at the South Pole for most elements. Thus, these samples represent upper tropospheric air of the North Pacific and as such, will provide a valuable data set for global receptor modeling. As expected, upslope samples have higher concentrations for most elements, major exceptions being Br and I.

Results of preliminary factor analyses of the 1980 downslope data are listed in Table 2. Factor 1 has heavy loadings for most elements and undoubtedly represnets mainly Asian dust. The substantial loadings of some enriched elements, e.g., Zn, As and Sb, do not necessarily indicate that those elements are enriched on Asian soil, as air masses that bring soil from Asia may also bring particles from anthropogenic activities.

Factor 2 has substantial loadings of several marine elements. The loadings for Sb, Yb, and Ta are not understood, Au is discussed below. The heaviest loadings on Factor 3 are those of S and Se. Sulfur is surely secondary, resulting from conversion of SO_2. As Se is in the same chemical group, it is not surprising that it is associated with the S factor. Except for Zn and Na, all elements on Factor 3 are volatile. Factor 4 illustrates experimental artifacts can create a factor. The major loadings are for halogens and ^{7}Be, which have very constant concentrations. This factor may arise because the actual concentrations remain constant, but errors in the volume of air sampled fluctuate, giving an apparent fluctuation of the concentrations. In general, the factor analysis is quite successful, as communalities are close to unity for most elements, major exceptions being Cl and ^{7}Be. The sum of the communalities is 25.6, about 85% of the 30 units of variance. As the dust component accounts for over 18 units of the explained variance, we will run the factor analysis with the dust period excluded to see what factors emerge under normal, cleaner conditions.

Factor analysis also yields the "factor scores", i.e., the strength of each factor during each sampling period. The factor score is centered at zero and has positive values during periods when the factor is stronger than average and negative values when weaker. As expected, Factor 1 has large positive scores for most weeks when the Asian dust was present during April and May. The score for Factor 3, the S and Se factor, was very high for the week of May 27 and several weeks thereafter. Recall that the major eruption of Mr. St. Helens occurred on May 18, 1980. It is tempting to suggest that these elements were picked up from the upper troposhere at Hawaii about one to two weeks after the eruption and remained high for several weeks afterwards; however, more information would be needed to verify the suggestion.

Factor analysis of the 1980 upslope samples at MLO yielded five significant factor, four of which correspond rather closely to the four factors' of the downslope results, although not in the same order.

Factor 3 has no direct counterpart in the downslope data, as it is mainly loaded with Au and W, with minor amounts of V, S, and Ce. We have no idea about its origin; however, Kenneth Rahn (private communication, 1982) observed a factor loaded with Au, Ag and W in an Alaskan data set. Clearly, this factor warrents further investigation. The overall results for the upslope samples are quite acceptable, as the five factors account for 86% of the system variance.

In summary, there are many uncertainties associated with global receptor modeling at this time, but the few results so far obtained are quite encouraging, suggesting the great potential value of further development and use of these methods for gaining a better understanding of the sources and transport particles on a global scale.

2. Airborne Aerosol Measurements in the Quiescent Plume of Mt. St. Helens Volcano

Air-filter samples were collected from the Mt. St. Helens plume with a Lockheed Orion P-3 turbo-prop aircraft during a flight on Sept. 22, 1980, which time the volcano was emitting a stable plume to an altitude of between 2 and 3 km. Four Fluoropore filter samples (1.0-μm pore diam) were taken, two during predominatly cross-plume flight patterns and two when flying coaxially within the plume. The average sampling time was 42 min and the average air volume 5.8 m^3. Fluoropore filters used on the single filter unit have collection efficiencies >99.99% for particles fo diam >0.03 μm (Liu and Lee, 1976). The stacked filter package consisted of two quartz fiber filters (>0.3 μm diam) mounted in a single filter holder, followed by two filter cassettes containing NaOH/flycerol-treated Whatman filters to trap acidic volatile species such as HF, HCl, and SO_2. Two multi-stage series of samples were collected for 30- and 70-min intervals with air volumes of 6.2 and 12.7 m^3, respectively. Blanks were collected for all types of filters by exposing them for only 30 sec.

Results for the Fluoropore filters given in Table 3 represnet blank-corrected concentrations (ng/m^3) of the suspended particulate matter collected in the plume. Blank corrections, calculated from the average of five individual blanks, were insignificant (<10%) for most elements. Also reported are average total sulfur gas concentrations (ppbv) measured during each run by the total sulfur analyzer and the total sulfur (gaseous and particulate) in ng/m^3. Although the plume was very diffuse, even with small sampling volumes, we were able quantitatively to determine 27 elements in the samples due to the low level of impurities in the filter materials and the high sensitivity of INAA. Background aerosols were collected in the vicinity of Mt. St. Helens on other flights. Trace element levels, not shown here, were significantly lower than those measured in the plume.

To identify elements that are enriched in the volcanic plume particles as compared with bulk ash from the May 18 eruption, we calculated the enrichment factors (EF_{ash}) and the average is given in Table 3:

$$EF_{ash} = \frac{(X/Al)_{plume}}{(X/Al)_{ash}} \tag{1}$$

where $(X/Al)_{plume}$ is the concentration ratio of element X to that of Al in the plume and $(X/Al)_{ash}$ is that of a representative ash sample from the volcano. Concentrations for the ash samples were determined by INAA and neutron-capture prompt γ-ray activation analysis (PGAA) of an unleached composite sample collected by the U. S. Department of Agriculture at Pullman, Washington, from the 18 May eruption.

Enrichment factors for the Fluoropore filters are shown in Figure 1 along with those of aerosol particulate samples collected in the stratosphere shortly after the 18 May eruption [2]. Pronounced enrichments relative to ash, up to 10^4, for volatile, non-crustal elements were observed in the quiescent plume. By contrast, EF_{ash} values close to unity were observed for most elements in the plume of the major May 18, 1980 eruption. Those samples were dominated by airborne ash fragments from the mountain's explosive eruption which, in the earlier phases, was primarily of phreatic nature. The huge enrichments of the halogens, W, In, Zn, S, Cd, Se, Sb, Hg, As and Au in the quiescent plume suggest that those elements are associated with higher temperature, more mobile phase being gradually expelled between eruptions without much ash.

Particulate S concentrations based on INAA and IC (as $SO_4^=$) were compared with those of total gaseous sulfur measurements and of acidic sulfur gases as observed by IC analysis of the base-treated filters. Results from the two techniques were in reasonable agreement, as summarized in Table 3, showing that 6+3% of the total S in the plume was borne by particles, the rest being in the form of SO_2 and H_2S based on the total sulfur data from the Meloy Flame Photometric detector.

By normalizing concentrations of enriched elements to that of total S, one can calculate fluxes for other species based upon SO_2 fluxes. Volatile elements with estimated production rates of about a kg/day or greater are listed in Table 4. They include Cl, Zn, As, Hg, Sb, Se, Cd, and Au.

Assuming that the ratio of volitile elements to S in the quiescent emission of Mt. St. Helens is representative, estimates of global inputs of these elements from volcanoes to the atmosphere can be made based on simultaneous total sulfur measurements. Appearing in Table 5, along with daily emission rates, are estimates of the global volcanogenic flux of particulate Cl, Zn, As, Hg, Sb, Se, Cd, and Au, as well as literature values of these species where available. These results compare quite favorably with the previous literature estimates of individual elemental inputs. Clearly, much more detailed chemical information throughout different eruptive cycles of a given volcano is required before reliable assessments of long range effects or future activity can be made.

The data presented here are the result of coordinated sampling by several techniques from a single aircraft sampling platform. We believe that the simultaneous measurement of many bulk and minor constituents from the air represnets the most promising field technique for evaluation of volcanic plumes and theri atmospheric impact.

3. INAA Measurements on Samples from the St. Louis Dichotomous Sampler Network

During 1975-76, atmospheric particulate samples were collected at ten sampling sites in St. Louis as part of the St. Louis Regional Air

Pollution Study (RAPS) [10]. Samples were collected with dichotomous samplers which separated incoming particles into two size fractions: the coarse fraction, with aerodynamic diameters of >2.4 μm and the fine fraction of diameter <0.24 μm. Particles were deposited on 1.2-μm pore-diam cellulose ester membrane filters of 37-mm diam. Characteristics and operation of dichotomous samplers are discussed by Jaklevic et al. About 31,000 of these samples were originally analyzed by Jaklevic et al. by energy-dispersive x-ray fluorescence (XRF) and concentrations of up to 28 elements were measured in each sample.

Recently we obtained 32 of the above samples and 10 filter blanks. We have determined trace element concentrations by instrumental neutron activation analysis (INAA). Our experiments had several purposes: (1) to compare the results of XRF and INAA for the same samples for elements observable by both methods; (2) to determine filter blanks for the 40-odd elements observalbe by INAA in order to establish those that will be measurable above blanks in the filter deposits; (3) to begin to determine typical concentrations in the St. Louis atmosphere of many trace elements obserable only by INAA; and (4) to provide detailed analyses of particulate samples that contain large amounts of material released by a specific source in St. Louis (a pigment plant).

Samples from the entire network were selected for a 12-hr period on the 126th day of 1976 during which the wind direction remained almost contant and from a prevailing wind direction for St. Louis (northwest). In addition, samples taken at various times at Station 118 were analyzed. Most of these samples were heavily influenced by emissions from a pigment plant in the south part of St. Louis, as shown by their generally high concentrations of Ti.

Samples and appropriate standards and flux monitors were irradiated in the National Bureau of Standards (NBS) reactor at a thermal neutron flux of $6x10^{13}$ n/cm^2-sec. Spectra of the γ rays produced by the decay of the induced radioactivity were taken using a Ge(Li) detector coupled to a 4096-channel analyzer system. Two different Tennecomp TP-5000 systems were used, one at NBS for short-lived nuclides and the other at the University of Maryland for long-lived nuclides.

We find that INAA can be used to observe about 35 or so elements in most samples vs. about 20 for most samples by XRF and several that are measureable by both methods can be determined with much greater accuracy by INAA. A number of the elemtns observed by INAA are of considerable value in identifying sources, e.g., Na, Se, As, Sb. However, the cost of analysis per sample, especially in terms of manpower, is far greater for INAA.

In Table 6 we compare the average concentrations of a number of dlements in St. Louis throughout the network on Day 126 of 1976 with those observed by our group in Washington, D. C. during the summer of 1976 [11]. Concentrations of most elements are strikingly similar between the two cities. Major exceptions are Ca, V, Se, and Br. The Ca is in the coarse mode and clearly associated with dust, much of which is gravel or limestone dust. There are many quarries in the St. Louis area. The lowered V concentration surely results from the much lower use of residual oil in St. Louis than in Washington and other Eastern cities. There are many possible sources Se in St. Louis, especially plants that deal with chalcophile metals, e.g., Cu, Zn, and Pb. We don't fully understand the reduced levels of Br. In Table 6 we have listed the XRF values for Pb in St. Louis to give an idea of automotive concentrations. We see that Pb is about the same for the two cities. However, the problem may be that an appreciable amount of Pb is contributed by the two Pb smelters in the area plus other chalcophile element plants.

In Table 7 we compare the results of XRF and INAA for 11 elements in samples for Day 126 throughout the network. We have not included the other samples from Station 118, as they are quite untypical, being heavily loaded with particles from the pigment plant. Despite the fact that uncertainties on many of the individual values are often quite large (e.g., Al by XRF), the agreement between XRF and INAA is suprisingly good for fine-particle samples. Unfortunately, the agreement is poor for coarse particles, the XRF values being up to a factor of 2.2 as large as INAA values. We believe this probably arises because the very largest crutal particles fall off the filters during handling. EPA investigators have found the same problem and are now coating the coarse-particle filters with a light oil to prevent it.

---

1. R. A. Duce, C. K. Unni, B. J. Ray, J. M. Prospero, and J. T. Merrill, *Science,* 209, 1522 (1980).
2. T. Vossler, D. L. Anderson, N. K. Aras, J. M. Phelan, and W. H. Zoller, *Science,* 211, 827 (1981).
3. S. R. Taylor, *Geochim. Cosmochim. Acta,* 28, 1273 (1964).
4. J. S. Fruchter, et al., *Science,* 209, 1116 (1980).
5. National Research Council, *Chlorine and Hydrogen Chloride,* Nat'l Acad. Sci., Washington, (1976).
6. J. O. Nriagu, *Nature,* 279, 409 (1979).
7. P. R. Walsh, R. A. Duce, and J. L. Fasching, *J. Geophys. Res.,* 84, 1719 (1979).
8. B. W. Loo, W. R. French, R. C. Gatti, F. S. Goulding, J. M. Jaklevic, J. Llacer, and A. C. Thompson, *Atmos. Environ.,* 12, 759 (1978).
9. J. M. Jaklevic, R. C. Gatti, F. S. Goulding, B. W. Loo, and A. C. Thompson, *Aerosol Analysis for the Regional Air Pollution Study,* Final Report on Project EPA-IAG-D6-0670, (1981).
10. G. S. Kowalczyk, G. E. Gordon, and S. W. Rheingrover, *Environ. Sci. Technol.* 16, 79 (1982).

SANS STUDIES OF SINGLE CHAIN CONFORMATIONS IN LAMELLAR MICRODOMAINE OF BLOCK COPOLYMERS

T. P. Lodge, E. J. Amis, and C. C. Han
(Center for Materials Science)

and

H. Hasegawa, T. Hashimoto, and H. Kawai
(Kyoto University, Kyoto, Japan)

In this study, SANS technique is used to measure the lateral dimension of deuterated polystyrene block chain in the lamellar microdomain of the mixtures of hydrogenated-styrene/isoprene block copolymers (HSI) and deuterated-styrene/isoprene block copolymers (DSI).

HSI and DSI were synthesized by anionic polymerization. It was intended that these polymers should have exactly the same copolymer composition and degree of polymerization excepting that 98% of the hydrogen atoms of polystyrene block of DSI were replaced by deuterium atoms. Characterization of the polymers were done by osmosis, GPC, and mass analysis. Films were cast from 10% solutions in toluene in Polyflon Petrie dishes at 28 °C. The domain structures were investigated by EM and SANS. The results are shown in figure 1 and figure 2, respectively. All of the samples show well oriented lamellar microdomains and the domain spacings calculated from the peak positions of the SAXS patterns are shown in table 2. The peaks appeared in the through view SAXS profiles indicate that some lamellae are oriented perpendicular to the film surfaces, but their number may be 1/100 of the lamellare parallel to the film surfaces.

SANS experiments were done by using the SANS instrument at NBS. Two scattering geometrics were used for all the specimen. (1) Through view: in this geometry, incident beam is perpendicular to the lamellae. Isotropic scattering patterns were obtained. Difference measurement between different specimen should give the laterial dimension of the d-styrene block. This is shown in figure 3 in the circular averaged form. These data should be compared to the SAXS data in figure 2 which gives similar patterns for different specimen because of the lack of contrast between

Table 1.

		HSI	DSI
Osmo	Number Average Molecular Weight $\overline{Mn}$	75,100	77,600
GPC	Molecular Weight Distribution $\overline{Mw}/\overline{Mn}$		1.15
	Copolymer Composition styrene/isoprene	0.462/0.538[*]	0.522/0.475[**]
	Degree of Polymerization $\overline{Pn}$(st.)/$\overline{Pn}$(iq)	339/584	362/545

---

[*] Mass analysis.

[**] Precursor ($\overline{Mn}$ measurement).

Table 2.

Sample Code	Composition (by wt.) HSI/DSI	domain spacing (edge)	domain spacing (through)	ratio d/dpsi 100% edge	ratio d/dpsi 100% through
50/50	0.500/0.500	398 Å	460 Å	0.995	0.991
75/25	0.750/0.250	398	460	0.995	0.991
87.5/12.5	0.875/0.125	414	445	1.035	0.959
HSI 100%	1.000/0	423	546	1.058	1.177
DSI 100%	0/1.000	400	464	1	1

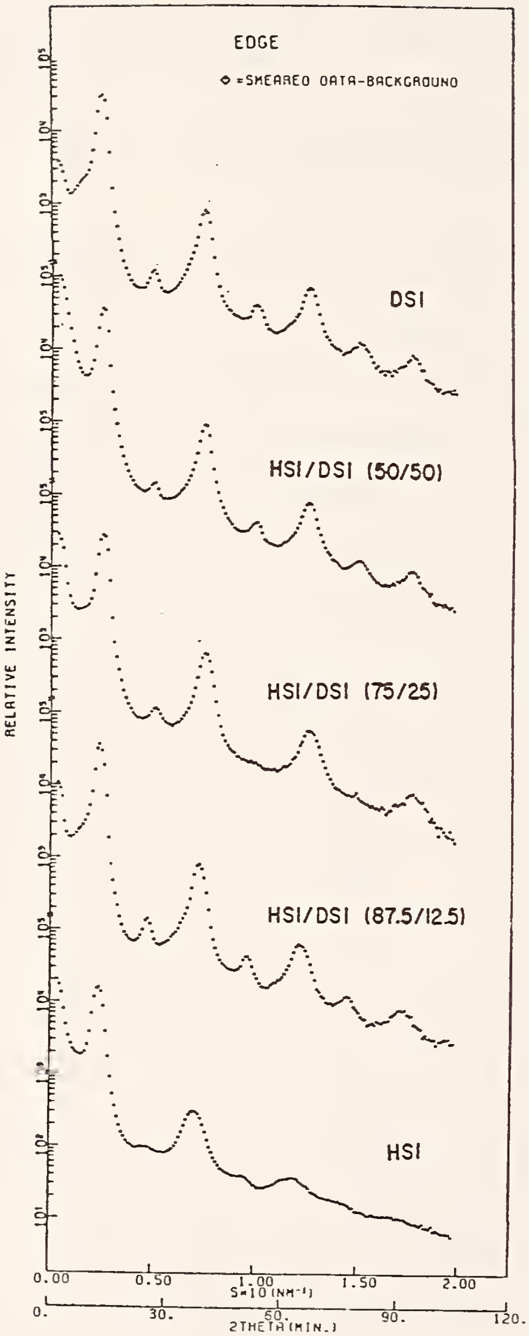

Figure 1. Small angle x-ray scattering of microphase separated polystyrene/polyisoprene lamellae. The ratio of deuterium labeled to hydrogeneous polymers are shown in parenthesis. One-dimensional detector was used which was placed perpendicular to the lamellae.

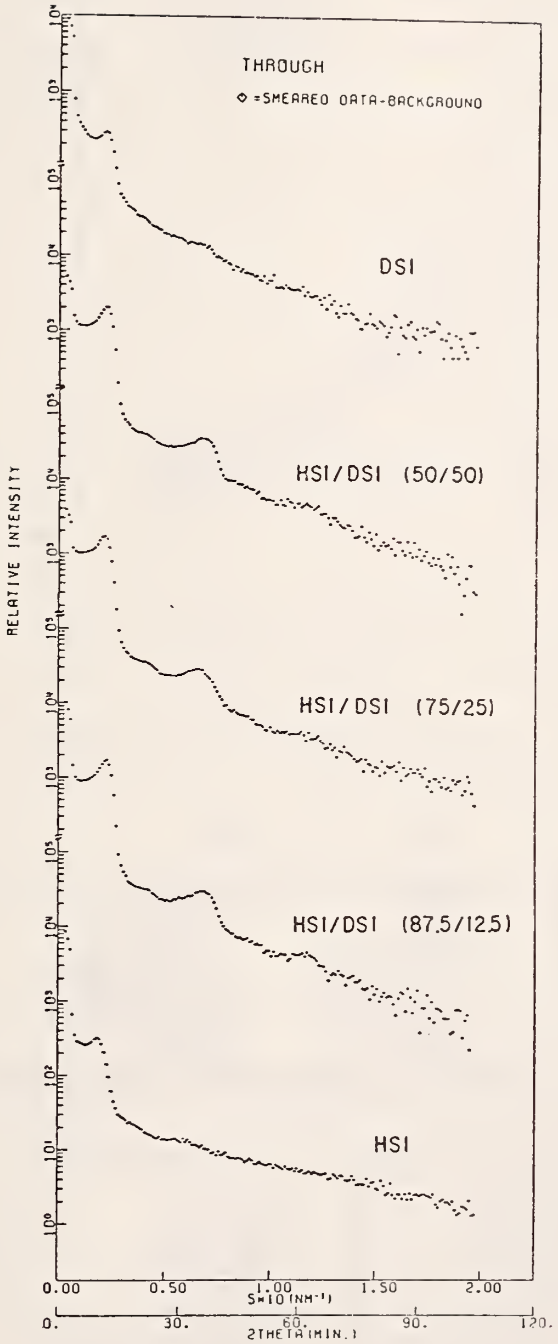

Figure 2. SAXS of PS/PI specimen (as above) in through view.

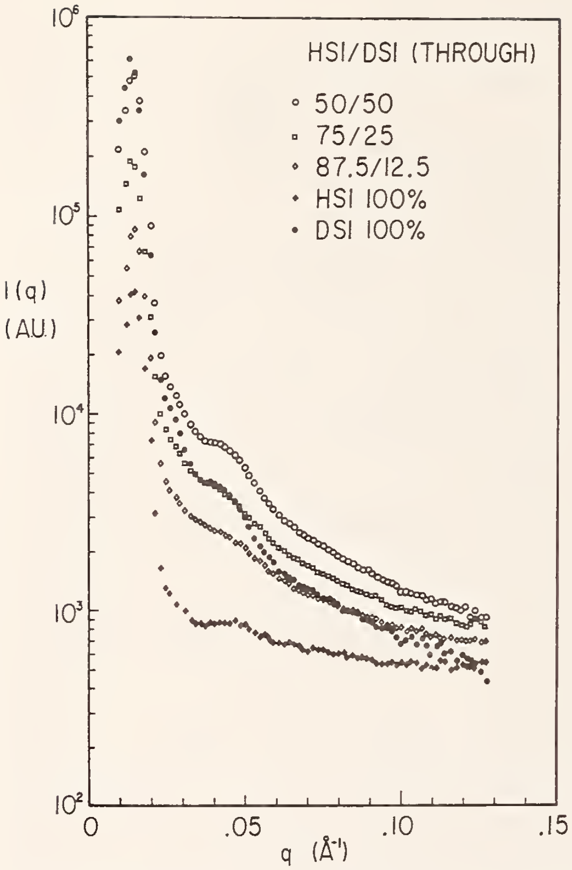

Figure 3. SANS of PS/PI specimen (as above) in through view. Results shown are circular averaged.

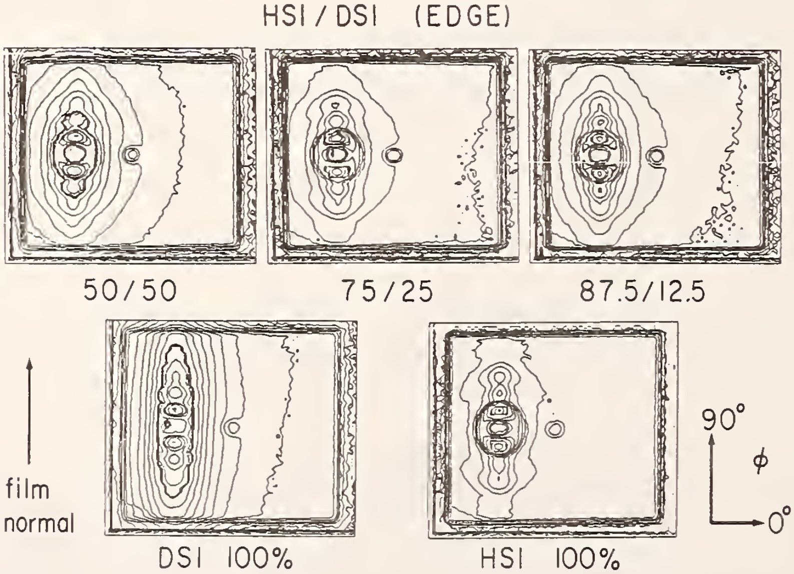

Figure 4. Contour plot of SANS of PS/PI specimen (as above) in edge view.

deuterium labeled and hydrogeneous chains.

(2) Edge View: in this geometry, incident beam is parallel to the lamellae. In other words, almost perfect lamellae are stacked up to macroscopic dimension (∿ 1 cm) and placed parallel to incident beam. Anisotropic scattering pattern was observed on the two-dimensional SANS detector. Strong patterns caused mainly by the repeating distances of the lamellar microdomains are observed in the vertical direction. Very weak diffuse scattering due mainly to the single chain scattering was obtained in the horizontal direction. Contour plots of the edge view patterns are shown in figure 4. The vertical patterns are to be compared with SAXS patterns shown in figure 1. The horizontal pattern, again can be used to deduce single-chain dimension of labeled styrene block.

Detailed analysis of laterial dimension of single-labeled polystyrene block has been carried out. It is clear that single-block laterial dimension of polystyrene in the microphase separated lamella is only about 2/3 of its unperturbed dimension. For example: for the polystyrene with degree of polymerization of 362, the laterial component of the radius of gyration is 20 ± 5 Å compared to unperturbed dimension of 30 ∿ 31 Å. This implies that all the current statistical theories (1,2) of phase separated copolymers have to be modified.

---

1. D. J. Meier, "Block and Graft Copolymers," J. J. Burke and V. Weiss, Eds., Syracuse University Press, Syracuse, NY (1973).

2. E. Helfand and Z. R. Wasserman, "Developments in Block Copolymers," I. Goodman, Ed., Applied Science publishers, Ltd. (in press).

THE NEUTRON ACTIVATION AUTORADIOGRAPHIC STUDY OF PAINTINGS

Y. T. Cheng
(Smithsonian Institution, Washington, DC)

and

I. Schröder, M. Ganoczy, R. S. Carter

The neutron-activation autoradiography project sponsored by the Smithsonian Institution was progressing in two fronts during the past year. The first is the finalization of design concepts from scientists and art conservators. A contract was granted to proceed with the detailed engineering layout of the proposed facility and an estimate of construction costs will be made. The finalized conceptual drawings of the autoradiography facility are shown in figures 1 and 2. The second is the utilization of the present NBSR thermal column for actual painting studies and the preparation of project supporting facilities.

The successful autoradiographic examination of a painting[1, 2] requires that the painting be activated with an adequate thermal neutron fluence ($\sim 1 \times 10^{13} n/cm^2$) and if information about short-lived isotopes (Al, Cr, Ti, etc.) in the painting are to be extracted, then the thermal neutron flux should be as high as possible ($\gtrsim 5 \times 10^9 n/cm^2 sec$). Our initial measurement on the NBSR thermal column indicated it met these requirements. The thermal column also has a very favorable ratio of useful radiation (thermal neutrons) to unwanted ones (fast neutrons, beta, and gamma rays). This is important as the safety of the painting is still the ultimate concern of everyone who is interested in such a facility. After the painting materials are activated, their radiation decay activities are recorded using a solid state (Ge(Li)) detector for gamma spectroscopy and film placed in close contact with the painting for autoradiographic exposures. The gamma spectroscopy is to measure quantitatively the contents of different materials in the painting and the autoradiography is to reveal the relative spatial concentrations of those materials.

The NBSR thermal column at present has a relatively uniform thermal neutron field[3] at the surface which is suitable for activating small

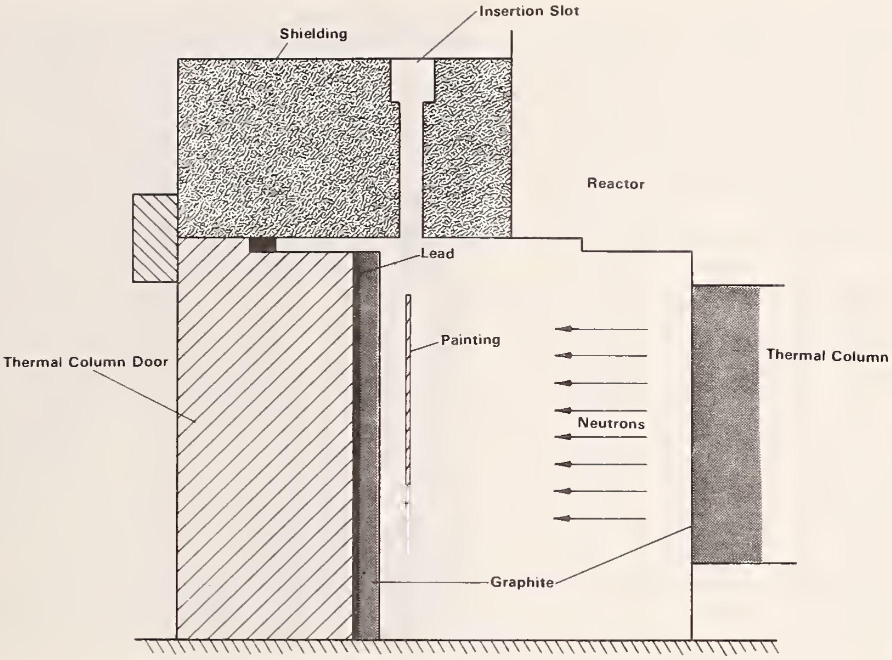

Figure 1. Top view of the proposed NBSR neutron activation autoradiographic facility.

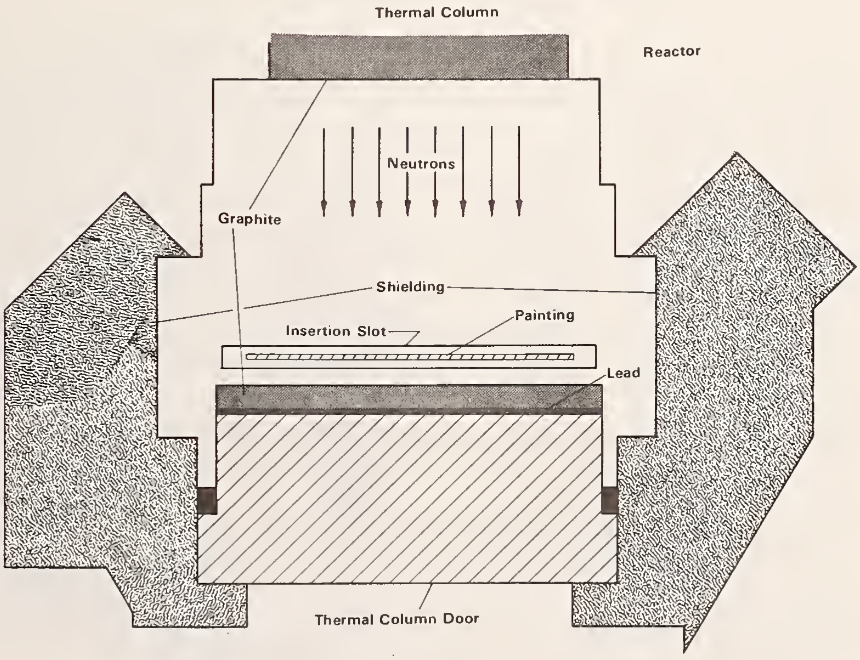

Figure 2. Side view of the proposed NBSR neutron activation autoradiographic facility.

paintings up to 2 1/2' x 2 1/2' in size. Three paintings have thus far been studied using the present thermal column facility. We were approached by the Walters Art Gallery of Baltimore about a late 15th-early 16th century Russian Icon painting panel. The panel is painted on both sides with rich gold inlays. Conventional radiographic techniques failed because of the superposition of the two painting images. It was hoped that neutron activation autoradiography would help to attain clear images of both paintings. Also as part of the inquiry into the methods and materials used in the fabrication of icons of that period, the identification of the pigments in these paintings would add to the knowledge of the palettes used in schools of northern Russian icon painting.

For the security of the painting, a counting and storage room was set up with limited access and the environmental conditions were strictly regulated according to museum standards. The particular icon painting due to its rich content of gold, if not handled properly, might become so active that information about other materials would be obscured. To familiarize ourselves with the general operating procedures such as film handling, proper exposure time, etc., and with the gold problem, an icon was made according to known techniques by the gallery for use as a test painting. It was activated with a thermal neutron flux of $1 \times 10^{10} n/cm^2$ sec for 10 minutes. Eight film exposures and five gamma spectroscopic counts were taken. The time schedule is listed in table 1 along with elements accentuated in the different exposures. The result of the test icon painting showed the time of activation for the real icon should be reduced to 5 minutes. After the activation, the real icon also followed the same schedule as in table 1. Some autoradiographic results are shown in figures 3, 4, and 5.

The third one we have studied is a turn-of-the-century painting by an American painter, Thomas W. Dewing.[4] A project is currently proposed to systematically study as many of his paintings as possible to establish the style and techniques he used. The Dewing painting was activated much the same way as the icons. The counting and autoradiographic process,

Figure 3. Photograph of the painting "Lady with Rose," by Thomas W. Dewing.

Time After Activation 3 min.
Film Exposure Time 6 min.
Prime Elements Exposing the Film

Element	Relative Strength
Co	100
Mn	43
Al	33
Ca	6
Na	5

Figure 4. The 5th autoradiograph of the painting, "Lady with Rose," by Thomas W. Dewing.

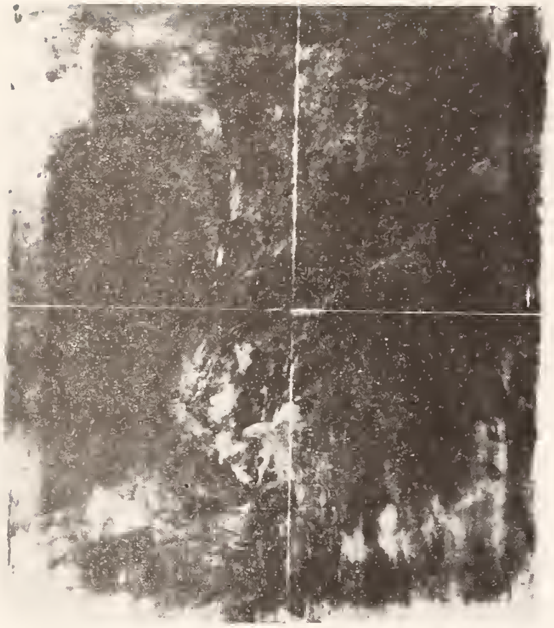

Time After Activation 2.5 hrs.
Film Exposure Time 3.0 hrs.
Prime Elements Exposing the Film

Element	Relative Strength
Mn	100
Na	25
Zn	3
In	1
K	1

Figure 5. The 7th autoradiograph of the painting, "Lady with Rose," by Thomas W. Dewing.

Time After Activation 1 day
Film Exposure Time 1 day
Prime Elements Exposing the Film

Element	Relative Strength
Na	100
Zn	12
K	3
Cd	2
Sb	1

Figure 6. The 9th autoradiograph of the painting, "Lady with Rose," by Thomas W. Dewing.

Table 1. The time sequence of neutron activation autoradiographic studies of paintings.

Time	Event	Optimization of Auto-radiographic Effects
$T_0 = 0$	End of neutron activation	
$T_1 = 5m$	1st film on for 4m	Ag 108 (2.3m) Al 28 (2.3m) Cr 55 (3.6m)
$T_2 = 11m$	1st γ-spectroscopic count for 5m	
$T_3 = 18m$	2nd film on for 15m	S 37 (5.0m) Cu 66 (5.1m) Ti 51 (5.8m) Ca 49 (8.8m) Co 60m (10.5m) Mg 27 (9.5m)
$T_4 = 34m$	3rd film on for 45m	Sb 124m (21.0m) Cl 38 (37.3m) Cd 111m (49.0m)
$T_5 = 1H25m$	2nd γ-spectroscopic count for 30m	
$T_6 = 2H$	4th film on for 3H	Ba 139 (85m) Mn 56 (2.58H) Pb 209 (3.3H) Cd 117m (3.0H)
$T_7 = 5H10m$	3rd γ-spectroscopic count for 3H	
$T_8 = 8H20m$	5th film on for 15H	K 42 (12.5H) Cu 64 (12.8H) Na 24 (15.0H) As 76 (26.7H)
$T_9 = 1D$	4th γ-spectroscopic count for 10H	
$T_{10} = 2D$	6th film on for 3D	Au 198 (2.7D) Hg 197 (2.7D) Sb 122 (2.8D) Ca 47 (4.7D)
$T_{11} = 5D$	5th γ-spectroscopic count for 3D	
$T_{12} = 10D$	7th film on for 14D	P 32 (14.2D) Cr 51 (27.8D)

Table 1. Continued.

Time Time	Event	Optimization of Auto-radiographic Effects
T_{13} = 30D	8th film on for 30D	Hg 203 (47D) Fe 59 (45D) S 35 (87D) Ca 45 (153D) Ag 110m (253D) Fe 55 (2.6Y) Co 60 (5.26Y)

Table 2. Elements present and their relative concentration in the painting Lady with Rose by Thomas W. Dewing detected with neutron activation analysis.

Element	Relative Quantity
Ca	9972
Zn	6120
Al	885.0
K	357.2
Mg	280.7
Cd	115.3
Mn	102.2
Cl	80.2
Na	62.8
Cr	38.8
Co	30.9
Ba	5.8
V	4.2
Cu	2.3
As	0.9
In	0.6
Au	0.3

however, was modified. Instead of counting and exposing film alternately, the counting was being done the same time when the film was being exposed. This enables us to correlate the density on the film more directly and quantitatively with the isotopes measured in the corresponding gamma spectroscopy. Figures 3, 4, 5, and 6 show some of the results from this study. The table on the bottom of each picture list the relative strength of different elements responsible for the film darkening for that particular picture. Table 2 lists all the elements found by the neutron activation method and their relative concentrations in the Dewing painting.

The complete interpretation of the result would involve not only the effort from scientists but also that from painting conservators and art historians. A group of personnel with such specialties is currently being organized for the coming year.

---

1. "Art and Autoradiography: Insights into the Genesis of Paintings by Rembrandt, Van Dyck, and Vermeer," published by the Metropolitan Museum of Art, New York (1982).

2. M. J. Cotter, P. Meyers, L. V. Zelst, C. Olin, and E. V. Sayne, *Applicazione dei Methodi Nucleari nel Campo Delle Opere D'arte*, p. 161-203 (1976).

3. "NBS Reactor: Summary of Activities," *NBS Tech. Note* 1160 (edited by F. J. Shorten, 1981).

C. REACTOR OPERATIONS AND SERVICES

REACTOR OPERATIONS AND SERVICES

The reactor was operated on a normal round-the-clock schedule for the entire year. Other than scheduled shutdowns for maintenance, refueling, testing, and for staff vacation, there were no interruptions in the operating schedule. A program of modernization of reactor components and instrumentation began last year is continuing. Licensing activities to upgrade reactor power to 20 MW and renew the operating license are progressing. A Draft Environmental Impact Statement has been published by the Nuclear Regulatory Commission as required by regulations. A final statement will be issued later this year. The NRC is also preparing a safety evaluation report of the NBS submittals. In this connection NBS provided extensive additional information to NRC to assist in their review. A new license will be issued by the NRC, once the Environmental Impact Statement and the Safety Evaluation Report are published. The new license authorizing increased power and valid for a period of 20 years is expected in early 1983.

Utilization of the reactor continued to be extensive and wide ranging. More than 125,000 instrument hours involving 25 simultaneously operable experimental facilities have been provided to more than 50 organizations from within and outside NBS.

1. Reactor Operations

Over the past year, the reactor was on-line nearly 80 percent of the time and operating at full power 73 percent of the time. This is about the maximum efficiency that can be achieved with the available staff. Once again a remarkable improvement in fuel utilization efficiency was realized by use of new higher loaded elements. An efficiency increase of nearly 50 percent resulting in an average fuel burnup of 65 percent is the best in the history of the facility and has already resulted in a significant fuel cost savings. A summary of the overall operating statistics for the period July 1, 1981 to June 30, 1982 is presented in the following table.

NBSR OPERATING SUMMARY FY 81

No. of days at 10 MW	268
On-line time at 10 MW	73%
Average U-235 burnup	65%
No. of Irradiations	3450
Hours of Irradiations	3100
Hours per Irradiation	0.9

2. Irradiation Service

Heavy utilization of the reactor for activation analysis and irradiation services continued this year. The number of irradiations increased by more than 30 percent. Tens of thousands of specimens, involving foods, drugs, environmental monitoring, geological, and mineral examinations, forensic investigation, and development of standard reference materials were irradiated at the NBS reactor.

3. Engineering Services

In addition to regular engineering and design services provided to reactor operations, experimenters, and users, the engineering staff was involved in a comprehensive program of reactor modernization. The new cooling tower is to be protected against fire by a new fire suppression system for which a contract has been signed to initiate installation. The water treatment building and loading ramp for chemical treatment of the secondary water has been out for bid and is in the negotiation stage. A contract to fabricate new shim arm poison blades has been let. Tooling for this type of control rod was developed and used at Argonne National Laboratory and will be used for this fabrication. Shim arm yokes, arbors and bearings are in the process of fabrication. Redesign of the regulating rod for 20 MW operation has begun which will provide a smoother and more reliable regulating rod operation. A new fuel element contractor has been selected by DOE and has made an NBSR prototype fuel assembly and a production prototype. Fabrication of actual fuel assemblies will begin when parts have been received from the sub-contractor.

REACTOR OPERATIONS AND SERVICES

Extensive effort was expended to implement the modernization program for the reactor instrumentation. This program replaces old equipment with more modern reliable console readout devices. For example; The miniature process recorders provide a faster response indication with the benefit of easy to replace ink cartidges and a much simpler chart roll cassette. The nuclear indication has been expanded to provide the operator with a console meter for each power range and also provides recorded information for both start-up channels and intermediate channels continuously.

The replacement of the nuclear power supplies equal and surpass requirements plus offer over current and over voltage protection. The replacement of individual shim arm position indicators provide the operator with a readout capability to 1/100 th of a degree.

D. SERVICE PROGRAMS

NEUTRON ACTIVATION ANALYSIS AT THE FOOD AND DRUG ADMINISTRATION

W. B. Stroube, Jr. and W. C. Cunningham
(U. S. Food and Drug Administration, Washington, DC)

The Food and Drug Administration (FDA) maintains a neutron activation analysis (NAA) unit in the Reactor Building of the National Bureau of Standards. The neutron activation program at FDA includes both research and analytical support for special projects. Work performed during the past year ranged from routine FDA inter-laboratory quality assurance programs to the study of Spanish cooking oil suspected of being adulterated. Also, a major effort was devoted to the analysis of composited food samples by INAA. The discussion below, which was presented in part at the Annual Meeting of the American Nuclear Society, June 1982 (1), covers some of the findings of the later project.

Food composites were derived from the FY '80 FDA program known as the Total Diet Studies (2), which involves the collection and analysis of foods for selected elements, pesticides and other chemical contaminants. The types and amounts of food collected are based on a 1965 U.S. Department of Agriculture (USDA) survey of food consumed by infants (6 months old), toddlers (2 years old), and adults (teenage male). (The ongoing Total Diet Studies have recently been revised to include analysis of individual foods and reflect current food comsumption data). For the NAA analysis, the homogenized food composites were freeze dried and approximately 300 mg of each was packaged in a polyethylene bag for irradiation. Because the food composites contained substantial amounts of water, the portions analyzed actually represented up to five or six grams of the food composite before freeze drying.

Calcium, Cl, Mg, Mn, Na, and V were found at quantifiable levels in nearly all samples of Cu and K were present at quantifiable levels in many samples.

The elemental abundance ranges for each element, based on wet weight, are given in Table 1. Because of the wide variety of sample matrices

TABLE 1. ELEMENT CONCENTRATION RANGES* IN INFANT AND TODDLER FOOD COMPOSITES (PPM)

Ca	8 - 10,000
Cl	10 - 14,000
Cu	0.06 - 10
K	50 - 10,000
Mg	5 - 11,000
Mn	0.1 - 25
V	0.01 - 0.3
Na	30 - 10,000

*Ranges are for food composites collected during FY'80.

TABLE 2. AVERAGE DIET COMPOSITION

COMPOSITE		INFANT GRAM/DAY	TODDLER GRAM/DAY
1	Drinking Water	237	344
2	Whole Fresh Milk	643	508
3	Other Dairy & Dairy Substitutes	130	69
4	Meat, Fish & Poultry	47	125
5	Grain & Cereal Products	29	116
6	Potatoes	6	35
7	Vegetables	97	73
8	Fruit & Fruit Juices	127	142
9	Fats & Oils	5	14
10	Sugar & Adjuncts	11	30
11	Beverages	21	94

TABLE 3. PERCENT INTAKE OF CALCIUM FOR EACH FOOD COMPOSITE

COMPOSITE	INFANT	TODDLER
2 Whole Fresh Milk	73.8%	64.8%
3 Other Dairy & Dairy Substitutes	14.7	13.8
4 Meat, Fish & Poultry	1.4	4.5
5 Grain & Cereal Products	5.8	9.2
6 Potatoes	0.2	0.4
7 Vegetables	2.2	2.0
8 Fruit & Fruit Juices	1.3	2.5
9 Fats & Oils	0.2	0.3
10 Sugar & Adjuncts	0.2	1.2
11 Beverages	0.2	1.4
Total Calcium, MG/Day	905.	884.

(Table 2), it was difficult to standardize analysis conditions. However, a set of standardized counting geometries relative to the Ge(Li) detectors, and the same irradiation and counting periods were used for all samples, even though there were substantial total activity differences. Results were based on multielement primary standards prepared at the FDA NAA laboratory. For quality assurance purposes, standard precision was checked and accuracy was verified by analyzing several portions of four different NBS biological Standard Reference Materials.

The elemental concentrations were converted to daily intakes using USDA dietary survey consumption data (Table 2). Table 3 gives the percentage intake of Ca from each food group for both infants and toddlers. As predicted, elemental concentrations vary greatly between food groups and the actual daily intake for each element is primarily attributable to only a few of the food groups. For example, more than 3/4 of the Ca daily intake comes from dairy products, whereas meats, grains and vegetables are the primary sources of Na.

1. *Transactions of the American Nuclear Society*, 41, 204-206, 1982.
2. R.E. Duggan and F. J. MacFarland, *Pestic. Monit. J.*, 1, 1-5, 1967.

U.S.G.S. ACTIVATION ANALYSIS PROGRAM

C. A. Palmer, G. A. Wandless, and L. J. Schwarz
(U.S. Geological Survey, Reston, VA)

1. Instrumental Neutron Activation Analysis

The comprehensive and highly automated INAA program at the U.S. Geological Survey analyzes 3,000-4,000 rock and coal samples per year for 24-30 elements. Data provided from these samples are used in a wide variety of geologic studies to support various geologists in their work. In addition to routine analyses and special projects to support U.S. Geological Survey geologists, the project is engaged in a number of independent research projects. These are primarily in four areas: (1) Trace elements in coal minerals (2) equipment and methods development, (3) INAA and radiochemistry of meteorites and lunar samples, and (4) method development for radiochemical separations and applications to terrestrial and extraterrestrial samples.

a. Trace Elements in Coal Minerals

A procedure has been developed for separating low temperature ash from coal into size and density fractions, determining the mineral contents of each fraction by x-ray diffraction analysis and scanning electron microscopy and determining trace element content of each fraction by INAA. A total of 39 elements were determined for these samples because the INAA procedure was expanded to include short lived elements: Al, Ti, V, S, Ca, Mg, Mn, Cl, and Dy. Some fly ash separates were also determined in this manner. Additional INAA was performed on lithologic units of coal.

b. Equipment and Methods Development

Development of methods and equipment for INAA includes the interfacing of optical bar code readers for sample identification to our automatic sample changers. A microcomputer system has been developed for laboratory sample control, and our laboratory balance has been interfaced to the computer. We are investigating the use of pelletization of rock samples in cellulose nitrate for better control of sample counting geometry.

c. INAA of Meteorite Samples

The INAA procedure is being applied to the analysis of antarctic iron meteorites in a cooperative program with the Smithsonian Museum of Natural History. Small metal particles in chondritic meteorite samples have been separated and analyzed by INAA to study the distribution of siderophile elements. Meteoritic metal from lunar soils have been similarly analysed to characterize the source of the metal.

2. Radiochemical Neutron Activation

a. Group Separations

i. Group separations of rare earth elements (REE) U.S.G.S. Standard Rocks

The group separation method is being applied to U.S.G.S. standard rocks in which REE abundances are near or below the limits of detection of our INAA procedure. Group separation is being extended to include the determination of Ba and Sr.

ii. Mafic and ultramafic rocks and separated minerals

We continue to supplement our INAA determinations by group separations in those materials where REE abundances are very low.

b. Ultratrace Determinations of Siderophile and Volatile Elements in Meteorites and in Lunar Rocks

i. Separations

An ion-exchange procedure was developed to separate and determine Pt and Pd by RNAA.

ii. Lunar green glasses

We continue our study of surface-correlated enrichments of volatile and siderophile on lunar green glasses. Bulk volatile and siderophile compositions of surface etched Apollo 15 green glasses (provided by Roman Schmitt of Oregon State University) have been determined. Determination of volatile and siderophile element abundances of unetched green glass specimens is nearing completion.

iii. Lunar ultramafic rocks

Analysis of a suite of lunar dunites for volatile and siderophile elements is nearing completion.

---

1. R. S. Clarke, Jr., E. Jarosewich, J. C. Goldstein, and P. A. Baedecker, "Antartic Iron Meteorites from Allan Hills and Purgatory Peak," *Meteoritics* 15, 273-274.

2. G. A. Wandless and J. W. Morgan, "Analysis of Low Levels of Rare Earths by Radiochemical Neutron Activation Analysis: I - Theoleiitic Basalts," (to be submitted to *Anal. Chim. Acta*).

3. R. Kenneth Petrie and J. W. Morgan, "Union Exchange Separation of Pt and Pd using Perchloric and Hydrochloric Acid Solution," in press, *Radioanl. Chem.*

POSITRON ANNIHILATION IN Cu ALLOYS

L. M. Pecora and A. C. Ehrlich
(Naval Research Laboratory, Washington, DC)

We followed the same experimental methods as reported last year[1] to examine momentum densities ($\rho(p)$) in $Cu_{92.5}Zn_{7.5}$ and $Cu_{75}ZN_{25}$ alloys both in the (110) plane. The data from these experiments was combined with previous runs and momentum densities for $Cu_{1-x}Zn_x$ ($x=0.075$, 0.15, 0.25) were reconstructed[1,2] fermiology of these alloys as well as CuGe alloys of previous experiments were compared to each other as well as to rigid band models based on Cu APW band calculations.[3] Effects of other possible band structure changes in the CuZn alloys $\rho(p)$ were examined. Findings were compared with CuGe and APW results.[4]

1. Fermiology Findings

Using a method of normalization and scaling $\rho(p)$ the Fermi radii for the CuZn and CuGe alloys were calculated in the (110) plane (see Refs. 5 and 6). 3D plots were then made of p_F vs θ and x (alloy electron/atom concentration) as in Figures 1 and 2. One can see the usual trend in the alloys of p_F ongoing from [100] to [110] as is seen in Cu. The major differences occur in the CuGe alloys where the growth of the Fermi surface is slower than rigid band and CuZn alloys and is even negative in some directions (e.g., $\theta=0$, along [100].)

The second 3D plot of each figure shows the deviations from rigid band predictions of the Fermi radii (p_F(alloy)-p_F(rigid band)). These show not only striking variations from what would be expected in a rigid band filling scheme, but also very similar patterns for all concentrations of both alloys, although the absolute values are different. The pattern of these deviations is one of starting from a value along [100] (θ-0°) reaching a maximum near [113] declining to a smaller value near the neck, and increasing from the other side of the neck to the [100] direction [θ-90°].

In an effort to find if this behavior correlated with the characteristics of the wave functions in the conducting band at E_F

we examined the orbital characteristics of the APW wave functions of Cu. One can see from figure 3 that the %d character of the wave functions correlates well with the deviation of p_F(alloy) from p_F(rigid band). In general the larger the d character of a wave function at k_F the more rapid the growth of the Fermi surface in that direction. We can only speculate at this point that somehow these parts of the conduction band with greater d character are sinking with respect to other parts as the solutes are added.

2. Other band structure changes

We examined the CuZn alloys for evidence of s-d hydridization changes.[1,4] We found that in the region of $\rho(p)$ where the CuGe alloys $\rho(p)$'s were shown to change upon addition of Ge, the CuZn alloys $\rho(p)$'s changed only as expected from resolution effects,[5,6] not from any hybridization changes.

3. Publications and presentations

These results were presented at the March 1982 APS meeting in Dallas, Texas as well as at the 6th International Conference on Positron Annihilation in Ft. Worth, Texas.

Three publications have been submitted on this work and past work[1]. Two to the Physical Review[5,6] and one (accepted) as part of a conference proceedings:

(1) L. M. Pecora and A. C. Ehrlich, "Positron Annihilation in Cu and αCuGe Alloys: I. General Results", submitted to Physical Review B.

(2) A. C. Ehrlich and L. M. Pecora, "Positron Annihilation in Cu and αCuGe Alloys: II. Fermiology and Band Structure Changes", submitted to Physical Review B.

(3) L. M. Pecora and A. C. Ehrlich, "2D-ACAR-Reconstruction of Momentum Densities in αCuZn and αCuGe Alloys" to be published in Conference Proceedings" - 6th International Conference on Positron Annihilation, Ft. Worth, TX.

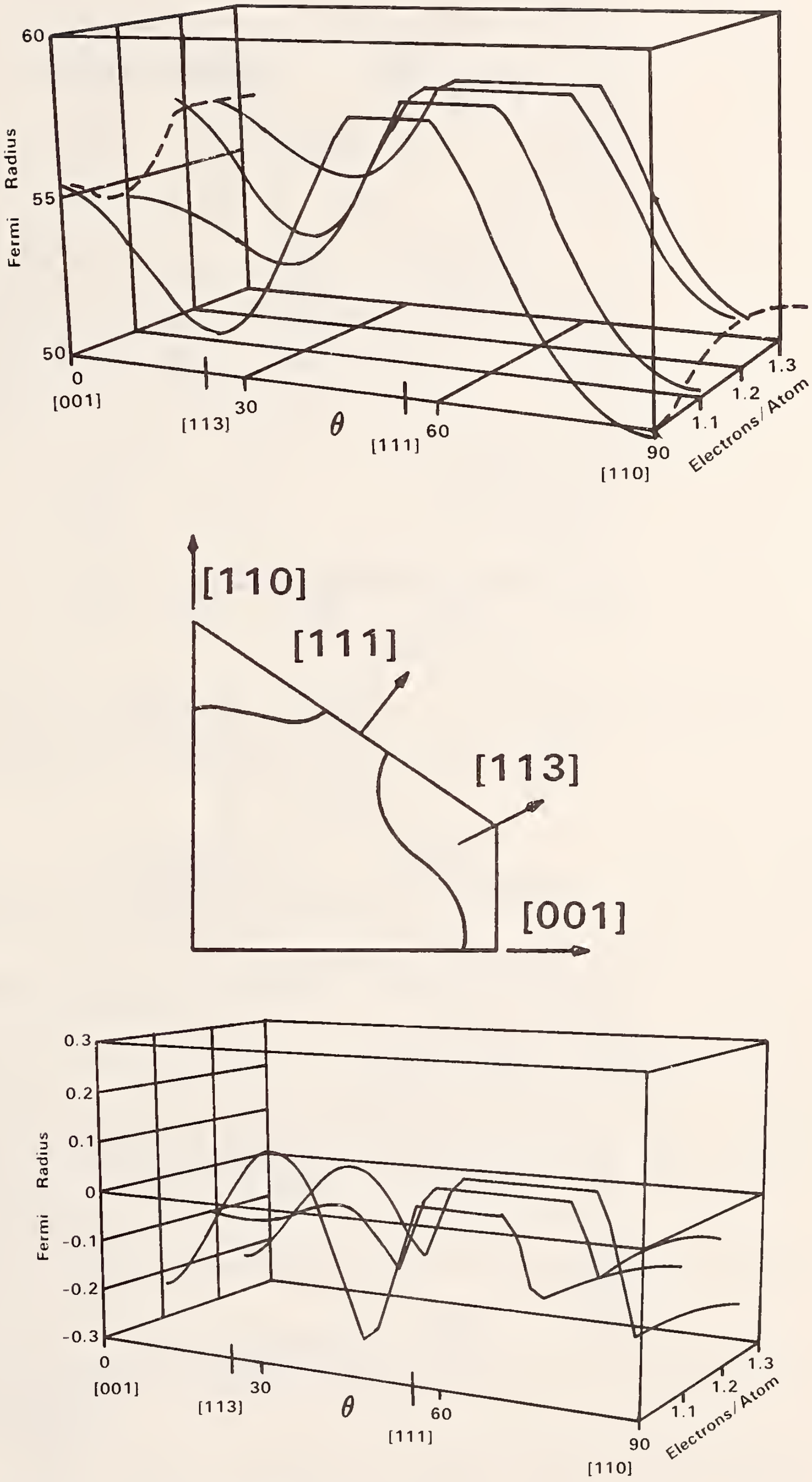

Figure 1. p_F vs θ for $Cu_{1-x}Ge_x$ $(\bar{1}10)$.

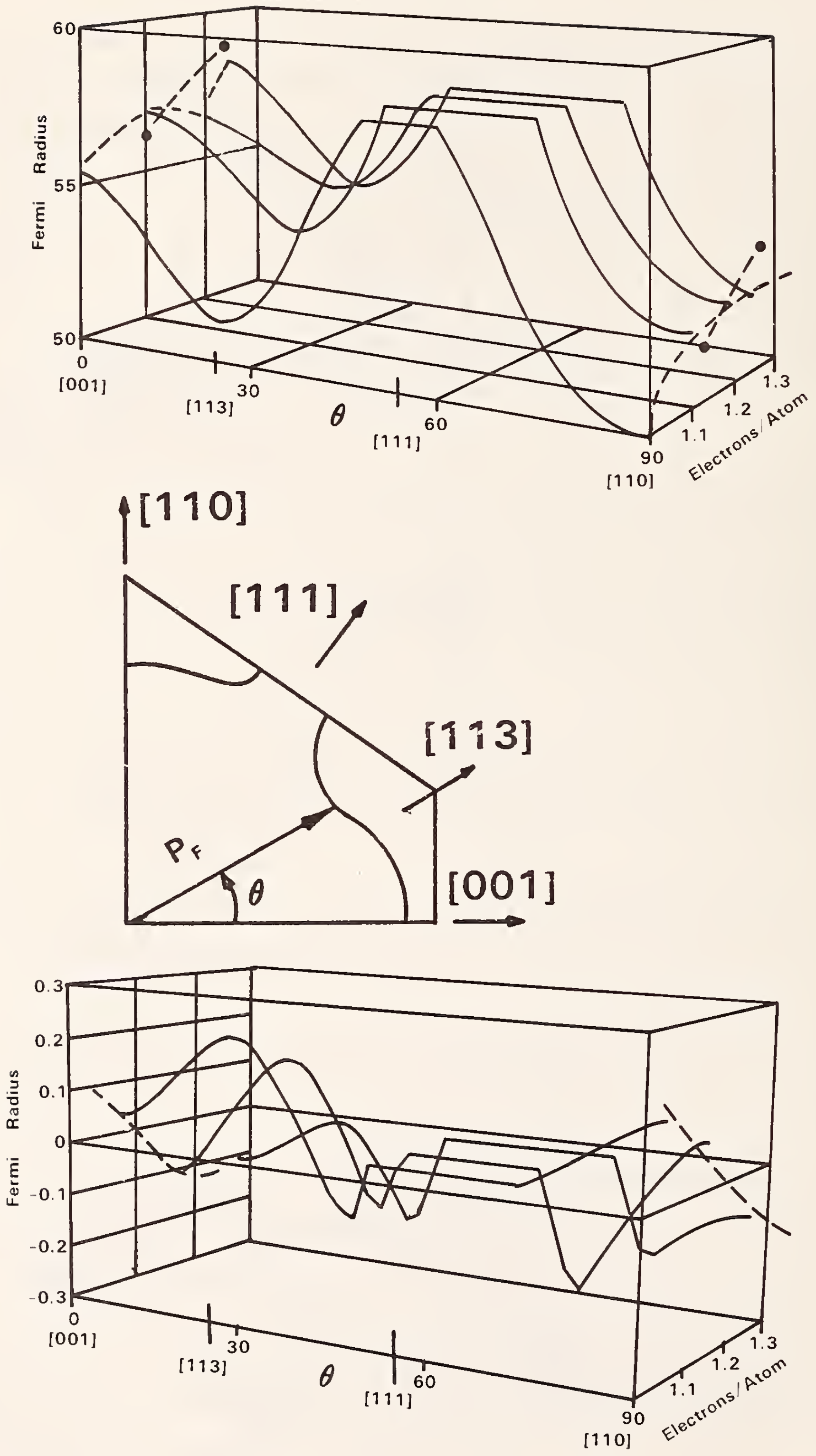

Figure 2(a). Fermi radius vs. angle $Cu_{1-x}Zn_x$ ($\bar{1}10$).
•– – – – –• CPA calculation. R. Prasad, et al., Phys. Rev. 23, 2607 (1981).

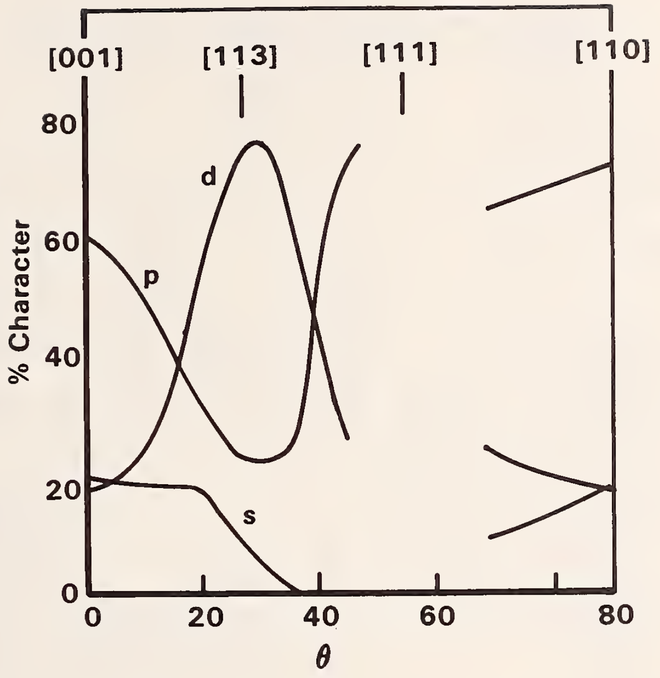

Figure 3. Percent orbital character of the conduction band wave functions at E_F in Cu in the (110) plane.

---

1. L. M. Pecora and A. C. Ehrlich, *NBS Tech. Note No.* 1160, p. 171, F. Shorten, Ed. (1982).

2. L. M. Pecora and A. C. Ehrlich, *Phys. Rev.* B19, 719 (1979)

3. D. A. Papaconstantopoulos, et al, *Phys. Rev.* B15, 4221 (1977)

4. L. M. Pecora and A. C. Ehrlich, *Phys. Rev. Lett.* 46, 1476 (1981)

5. L. M. Pecora and A. C. Ehrlich, submitted for publication to *Phys. Rev B*

6. L. M. Pecora and A. C. Ehrlich, submitted for publication to *Phys. Rev B*

7. L. M. Pecora and A. C. Ehrlich, *Proceedings of the 6th International Conference on Positron Annihilation,* Ft. Worth, TX, to be published.

E. PERSONNEL ROSTER

REACTOR RADIATION DIVISION

566

R. S. Carter, Chief
T. M. Raby, Deputy Chief
*E. C. Maxwell, Admin. Officer
T. Lindstrom, Secretary

Division Staff
R. Casella
B. Mozer
F. Shorten

Reactor Operations
T. M. Raby, Chief
J. F. Torrence, Deputy Chief
C. Harrison, Secretary

Reactor Operators

R. Beasley
M. Bell
N. Bickford
H. Brake
J. Browning
A. Chapman
H. Dilks
L. Lindstrom
W. Mueller
T. Myers
J. Ring
R. Stiber
A. Toth
D. Wilkison

Engineering Services
J. H. Nicklas, Chief
C. Harrison, Secretary

Mechanical Design

E. Guglielmo
J. Sturrock

Electronics

R. Conway
R. Hayes
L. Shuman

Neutron S-S Physics
J. J. Rush, Chief
S. Long, Secretary

Crystallography

C. Choi
D. Fravel (1/2)
J. LaRock (1/2)
E. Prince
W. Rymes (1/2)
A. Santoro
+V. Himes
A. Mighell
J. Stalick
+D. Stakes

Metal Hydrides and Molecular Materials

D. Fravel (1/2)
#H. Prask
J. Rowe (1/2)
W. Rymes (1/2)
#S. Trevino

Magnetic and Amorphous Materials

#H. Alperin
#N. Koon
+J. Lynn
J. Rhyne
#R. Williams

Biological Materials

A. Wlodawer

Advanced Neutron Methods

N. Berk
C. Glinka
J. LaRock (1/2)
J. Rowe (1/2)
S. Singhal, IPA
+R. Tillman

Neutron Radiography

M. Dorsey
M. Ganoczy
#T. Cheng

*Part-time
+WAE, Coop, Stay-in school
#Guest Worker, research assoc.

NON-RRD NBS STAFF LOCATED AT REACTOR

Division 354

J. Arras
P. Cassidy
D. Hoaney
I. Jensen
F. Moore
J. Shubiak

Division 532

R. A. Dallatore
C. Eisenhauer
D. Gilliam
J. A. Grundl
G. Lamaze
L. Li
E. McGarry
I. Schroder
R. Schwartz
W. Slater
V. Spiegel

Division 500

B. Carpenter

Division 551

R. Fleming
K. Fitzpatrick
S. Harrison
J. Langland
R. Lindstrom
G. Lutz
T. Mitlehner
M. Vinocur
J. Vogt
R. Zeisler

GUEST WORKERS AND COLLABORATORS

Division 506

D. Becker

Division 520

E. Kessler

Division 522

R. Dove

Division 532

A. Wasson

Division 533

R. Placious

Division 541

J. Kelly

Division 544

D. Tsai

Division 545

R. Cavanagh

Division 552

S. Wise

Division 553

H. Rook

Division 561

K. Rhyne
R. Roth

Division 562

E. Case
J. Early
R. Fields
E. Fuller

Division 563

E. Amis
R. Bowen
C. Han
T. Lodge
M. Mathew
S. Takagi
R. Waterstrat

Division 564

F. Biancanello
R. Reno
R. Shull

Aberdeen Proving Ground

C. Heimbach

Army Armament Research and Development Command

C. Choi
H. Prask
S. Trevino

Federal Bureau of Investigation

R. Asbery
R. Bilko
J. Haverkost
J. Kilty
R. Kostella
C. Peters
J. Riley
P. Tangren
P. Thompson

Food and Drug Administration

W. Cunningham
W. Stroube, Jr.
J. Tanner

National Gallery of Art

B. Miller
C. Parkhurst

National Institutes of Health

D. Davies
R. Frank

Naval Research Laboratory

P. D'Antonio
A. Ehrlich
M. Fatemi
N. Koon
L. Pecora

Naval Surface Weapons Center

H. Alperin
M. Lia
G. Riel
R. Williams

Smithsonian Institution

M. Blackman
T. Chase
Y. Cheng
J. Mishara
J. Olin
L. Zacherman

U. S. Geological Survey

P. Baedecker
J. Morgan
G. Wandless

PERSONNEL ROSTER

Argonne National Laboratory

T. Brun
O. Hinks
S. Susman

Battelle, N. W.

L. Brackenbush
G. Endres
W. Nicholson

Brookhaven National Laboratory

S. Shapiro

C.R.N.S. Grenoble, France

J. Hodeau
M. Marezio

Institute Laue-Langevin Grenoble, France

A. Magerl

KFA Jülich, Germany

D. Richter

Nuclear Energy Center, Mol, Belgium

A. Fabry

Oak Ridge National Laboratory

F. Kam

University of Alabama

J. Segrest

American University

J. Malamas
R. Segnan

Iowa State University

R. Shelton

Kyoto University (Japan)

H. Hasegawa
T. Hashimoto
H. Kawai

M.I.T.

B. Averbach
L. Schioler
C. Skarda
B. Wuenscher

Northwestern University

J. Lasalle
L. Schwartz

Pennsylvania State University

L. Pilione

State University of New York

H. Herman

Technical University of Munich (Germany)

H. Wipf

University of Antwerp (Belgium)

K. Michel

University of California (Berkley)

R. Bragg

University of Connecticut

J. Budnick

PERSONNEL ROSTER

University of Houston

S. Moss

University of Ife (Nigeria)

A. Oluwole
L. Kehinde

University of Illinois

H. Birnbaum
R. Chasnov
H. Zabel

University of Maryland

D. Anderson
A. Bagheri
D. Ballantine
D. DeMers
D. Delozier
D. Finnegan
S. Fuller
I. Gokmen
F. Geunther
D. Herman
M. Kitto
W. Linthicum
I. Olmer
J. Parrington
J. Phelan
J. Robertson
C. Stone
P. Sheridan
C. Thompson
G. Tuncel
W. Walters
W. Zoller

University of Missouri (Columbia)

D. Alger
W. James

University of Pittsburgh

R. Buttera
S. Malik
H. Smith
W. Wallace

University of Rhode Island

S. Pickart

University of Wisconsin

J. Hinkley
H. Yu

Allied Corporation

G. Fish
R. Hasegawa
A. Maeland

Bell Laboratories

R. Cava
C. Chen

B-K Dynamics

N. Chesser

E. I. DuPont de Nemours Co.

J. Parise

Exxon

D. Lohse

Metronic, Inc.

P. Skarstad

3M Research Laboratory

A. Siedle

PERSONNEL ROSTER

Sandia Corporation

J. Harris

Union Carbide Corporation

E. Goddard

Westinghouse-Hanford Corp.

W. McElroy
J. Rawlins

F. PUBLICATIONS

COLLABORATIVE PROGRAMS

ALEFELD, B., ANDERSON, D. S., HEIDEMANN, A., MAGERL, A., and TREVINO, S. F., "The Measurement of Tunnel States in Solid CH_3NO_2 and CD_3NO_2" *J. Chem. Phys.* (Letter to the Editor) 76, 2758 (1982).

AMMON, H. L., MURPHY, K. C., SJOLIN, L., WLODAWER, A., HOLCENBERG, J. S., and ROBERTS, J. "The Molecular Symmetry of Gluatminase-Asparaginases Rotation Function Studies of the Pseudomonas 7A and Acinetobacter Enzymes," *Acta Cryst.* (in press).

BERK, N. F., ROSENTHAL, J., and YARMUS, L., "Spin Relaxation of Triplet Excitons in Molecular Crystals," *Phys. Rev. B* (in press).

BRUN, T. O., SUSMAN, S., ROWE, J. M., and RUSH, J. J., "Quasielastic Neutron Scattering Study of Ionic Diffusion in β-LiAl," *Solid State Ionics* 5, 417 (1981).

CASELLA, R. C., "Theory of Neutron Scattering from Hydrogen in Metals Involving Transitions to Excited Tunnel Split States," *Phys. Rev.* B24, 2913-2920 (1981).

CASELLA, R. C., "Detection of Impurity Tunneling in Solids Via Coherent Phonon Coupling and Direct Neutron Scattering," *J. Phys.* 42, C6-923-C6-925 (1981).

CASELLA, R. C., "Relations Between Fermion Masses from Effective Potentials in Internal Space," *Il Nuovo Aimento* 67A, 289-297 (1982).

CAVA, R. J., HIMES, V. L., MIGHELL, A. D., and ROTH, R. S., "$FeNb_3Se_{10}$: A New Structure Type Related to $NbSe_3$," *Phys. Rev.* B24, 3634-3637 (1981).

CAVA, R. J., SANTORO, A., MURPHY, D. W., ROTH, R. S., and ZAHURAK, S., "The Structures of Lithium-Inserted Metal-Oxides: $LiReO_3$ and Li_2ReO_3" *J. Sol. St. Chem.* 42, 251-262 (1982).

CAVANAGH, R., KELLEY, R. D., and RUSH, J. J., "Neutron Vibrational Spectroscopy of Hydrogen and Deuterium on Raney Nickel," *J. Chem. Phys.* (in press).

CHEN, H. S., LYNN, J. W., ERWIN, R. W., and RHYNE, J. J., "Spin Wave Excitations in Re-Entry Para-Fero-Spin Class Transition in Glassy $(Fe_xNi_{1-x})_{75}P_{16}B_6Al_3$ Glasses," Proc. of the 4th Intl. Conf. on Rapidly Quenched Metals, 1153-1156 (1981).

PUBLICATIONS

CHOI, C. S. and PRASK, H. J., "Single Crystal Neutron Diffraction Study of Ammonium Nitrate Phase III," *Acta Cryst.* (in press).

CHOI, C. S. and MIGHELL, A. D., "Neutron Diffraction Study of Sodium Sesquicarbonate Dihydrate," *Acta Cryst.* (in press).

CLAUSEN, K., RHYNE, J. J., LEBECH, B., and KOON, N. C., "Temperature Dependence of the Spin-Waves in $ErFe_2$," *J. Phys.* C15, 3587 (1982).

COHEN, J. S. and WLODAWER, A., "Diffraction and NMR Studies of Proteins; an Uneasy Alliance," *Trans. in Biochemical Sciences* (in press).

D'ANTONIO, P., KONNERT, J. H., RHYNE, J. J., and HUBBARD, C. R., "Structural Ordering in Amorphous $TbFe_2$ and YFe_2," *J. Appl. Cryst.* (in press).

DOHERTY, R. M., STEWART, J. M., MIGHELL, A. D., HUBBARD, C. R., and FATIADI, A. J., "The Structure of the 1:1 Molecular Complex of Pyrene and Dicyanomethylenecroconate," *Acta Cryst.* B38, 859-863 (1982).

FERRICK, J. H., RHYNE, J. J., and SEGNAN, R., "Bulk Magnetization of Dysprosium-Scandium Alloys," *J. Appl. Phys.* 53, 2232-2234 (1982).

GLINKA C. J., "The National Bureau of Standards Small-Angle Neutron Scattering Spectrometer," Proc. of the Conf. on Neutron Scattering (in press).

GLINKA, C. J. and BERK, N. F., "The Two Dimensional Position-Sensitive Detector at the National Bureau of Standards SANS Facility," Proc. of the Workshop on Position-Sensitive Detectors (in press).

HARDMAN, K., RHYNE, J. J., PRINCE, E., SMITH, H. K., MALIK, S. K., WALLACE, W. E., "Magnetic and Structural Properties of $Th_6Mn_{23}D_x$ and $Y_6Mn_{23}D_x$," *The Rare Earths in Modern Science and Technology, Vol. III,* edited by G. McCarthy, H. Silber, and J. Rhyne, Plenum Press, New York, pp. 477 (1982).

HARDMAN, K., RHYNE, J., MALIK, S., and WALLACE, W. E., "Site Magnetization of Cubic and Hexagonal $HoMn_2$," *J. Appl. Phys.* 53, 1944-1946 (1982).

HIMES, V. L., MIGHELL, A. D., and DECAMP, W. H., "Structure of Carbamazepine: 5H-Dibenz[b,f]azepine-5-carboxamide," *Acta Cryst.* B37, 2242-2245 (1981).

HIMES, V. L., MIGHELL, A. D., PAGE, S. W., and STACK, M. E., "Structure of Xanthomegnin," *Acta Cryst.* B37, 1932-1935 (1981).

HIMES, V. L., MIGHELL, A. D., STALICK, J. K., and ZON, G., "Structure of Racemic cis-4-Phenylcyclophosphamide," *Acta Cryst.* B38, 1009-1012 (1982).

PUBLICATIONS

HIMES, V. L., MIGHELL, A. D., and SIEDLE, A. R., "Synthesis and Structure of $Cu_5(BTA)_6(\underline{t}\text{-}C_4H_9NC)_4$, a Mixed-Valent Copper-Nitrogen Cluster Containing η^3-Benzotriazolate," *J. Am. Chem. Soc.* 103, 211-212 (1981).

HIMES, V. L. and MIGHELL, A. D., "A Matrix Method for Lattice Symmetry Determination," *Acta Cryst.* A (in press).

HODEAU, J. L., MAREZIO, M., SANTORO, A., and ROTH, R. S., "Neutron Profile Refinement of the Structures of Li_2SnO_3 and Li_2ZrO_3," *J. Sol. St. Chem.* (in press).

LYNN, J. W., SHELTON, R. N., HORNIG, H. E., and GLINKA, C. J., "Investigation of the Magnetic and Superconducting Properties of $Er_{1-x}Ho_x)Rh_4B_4$," *Physica B* (in press).

LYNN, J. W., ERWIN, R. W., RHYNE, J. J., and CHEN, H. S., "Ferromagnetic and Spin Glass Behavior Near the Critical Concentration in Amorphous $(Fe_xNi_{1-x})_{75}G_{25}$," *J. Mag. Magnetic Mtls.* (in press).

LYNN, J. W., ERWIN, R. W., CHEN, H. S., and RHYNE, J. J., "Evolution from Ferromagnetism to Spin-Glass Behavior," *Phys. Rev. Lett.* (in press).

LYNN, J. W., RHYNE, J. J., and BUDNICK, J. I., "Observation of Spin-Waves in Pd (1.5% Fe)," *J. Appl. Phys.* 53, 1982 (1982).

MAGERL, A., ROWE, J. M., RUSH, J. J., WIPF, H., and RICHTER, D., "Influence of Impurities on Local Hydrogen Vibrations in a Niobium Host Lattice," *Intl. Symp. on the Electronic Structure and Properties of Hydrogen in Metals* (in press).

MAGERL, A., RUSH, J. J., ROWE, J. M., RICHTER, D., and WIPF, H., "Local Hydrogen Vibrations in Nb in the Presence of Interstitial (N,O) and Substitutional (V) Impurities," *Phys. Rev. B* (in press).

NICHOLSON, W. L., PRINCE, E., BUCHANAN, J., and TUCKER, P., "A Robust/Resistant Technique for Crystal Structure Refinement," *Progress and Problems in Crystallographic Statistics*, A. J. C. Wilson, ed., International Union of Crystallography (in press).

PRASK, H. J. and CHOI, C. S., "Texture, NDE Characterization 420/00089," *Encyclopedia of Materials Science and Engineering* (in press).

PRINCE, E. and NICHOLSON, W. L., "A Test of a Robust/Resistant Refinement Procedure on Synthetic Data Sets," *Acta Cryst.* A (in press).

PRINCE, E., "Comparison of Profile and Integrated Intensity Methods in Powder Refinement," *J. Appl. Cryst.* 14, 157-159 (1981).

PRINCE, E., "Mathematical Techniques in Crystallography and Materials Science," Springer-Verlag, New York, 192 pp. (1982).

PRINCE, E., "Comparison of the Fits of Two Models to the Same Data Set," *Acta Cryst.* B38, 1099-1100 (1982).

RHYNE, J., HARDMAN, K., MALIK, S., and WALLACE, W., "Magnetic Properties of Cubic and Hexagonal $HoMn_2$," *J. Appl. Phys.* 53, 1944 (1982).

RHYNE, J. J., FISH, G. E., and LYNN, J. W., "Spin Waves in Amorphous $Fe_{1-x}B_x$ Alloys," *J. Appl. Phys.* 53, 2316-2318 (1982).

ROSENTHAL, J., YARMUS, L., and BERK, N. F., "Comments on "Triplet-Exciton Annihilation and Triplet Spin Relaxation in Molecular Crystals," *Phys. Rev.* B24, 1103-1105 (1981).

ROWE, J. M., RUSH, J. J., and MICHEL, K. H., "Comment on Dielectric Susceptibility Measurements in $(KCN)_x(KBr)_{1-x}$ Mixed Crystals," *Phys. Rev. Lett.* (in press).

RUSH, J. J., MAGERL, A., ROWE, J. M., HARRIS, J. M., and PROVO, J. L., "Tritium Vibrations in Niobium by Neutron Spectroscopy," *Phys. Rev.* B24, 4903-4905 (1981).

SANTORO, A., CAVA, R. J., MURPHY, D. W., and ROTH, R. S., "Use of the Pearson Type VII Distribution in the Neutron Profile Refinement of the Structures of $LiReO_3$ and Li_2ReO_3," *Proc. of the Symposium on Neutron Scattering* (in press).

SANTORO, A., ROTH, R. S., and AUSTIN, M., "Powder Neutron Diffraction Study of the Nonstoichiometric Solid Solution of Lithium Tantalate $9LiTaO_3:Ta_2O_5$," *Acta Cryst.* B38, 1093-1098 (1982).

SANTORO, A., "New Developments in Neutron Powder Profile Analysis," *Proc. of the Italian-Yugoslavian Joint Meeting* (in press).

SJOLIN, L. and WLODAWER, A., "Improved Technique for Peak Integration for Crystallographic Data Collected with Position-Sensitive Detectors: A Dynamic Mask Procedure," *Acta Cryst.* A37, 594-604 (1981).

SUSMAN, S., DELBECQ, C. J., BRUN, T. O., and PRINCE, E., "Structure and Conductivity of the NASICON Analog $Na_3Sc_2(PO_4)_3$," *Proc. of the Symp. on Solid Electrolytes* (in press), Montreal, Canada (1982).

THOMLINSON, W., SHIRANE, G., LYNN, J. W., and MONCTON, D., "Neutron Scattering Study of Magnetic Ordering in Ternary Superconductors," Superconductivity in Ternary Compounds, ed. by O. Fischer and N. B. Maple, Springer-Verlag, *Topics in Current Physics Series,* Vol. 2 (1982).

PUBLICATIONS

TSAI, D. H. and TREVINO, S. F., "Thermal Relaxation in a Dense Liquid Under Shock Compression," *Phys. Rev.* A24, 2743 (1981).

WLODAWER, A., "Neutron Diffraction of Crystalline Proteins," *Progress in Biophysics and Molecular Biology*, T. Blundell, ed., Pergamon Press Ltd: Oxford, England (in press).

WLODAWER, A., "A Facility for Data Collection and Processing at the National Bureau of Standards Reactor," *Methods in Enzymology*, H. W. Wyckoff, C. H. W. Hirs, and S. N. Timasheff, eds., Academic Press: New York (in press).

WLODAWER, A. and SJOLIN, L., "Improvement of the Quality of the Data Collected Using a Position-Sensitive Detector," *Nucl. Instrum. Methods* (in press).

WLODAWER, A. and SJOLIN, L., "Application of Joint Neutron and X-ray Refinement to the Investigation of the Structure of Ribonuclease A at 2.0 Å Resolution," *Brookhaven Symposia in Biology*, Upton, NY, Plenum Press (1982).

WLODAWER, A. and SJOLIN, L., "Hydrogen Exchange in RNase A: Neutron Diffraction Study," *Proc. Natl. Acad. Sci. USA* 79, 1418-1422 (1982).

WLODAWER, A. and HENDRICKSON, W. A., "A Procedure for Joint Refinement of Macromolecular Structures with X-ray and Neutron Diffraction Data from Single Crystals," *Acta Cryst.* A38, 239-247 (1982).

WLODAWER, A., BOTT, R., and SJOLIN, L., "The Refined Crystal Structure of Ribonuclease A at 2.0 Å Resolution," *J. Biol. Chem.* 257, 1325-1332 (1982).

WLODAWER, A., SJOLIN, L., and SANTORO, A., "Refinement of the Crystal Orientation Matrix for the Flat-Cone Diffractometer," *J. Appl. Cryst.* 15, 79-81 (1982).

PUBLICATIONS

INDEPENDENT PROGRAMS

ANDERSON, D. L., ZOLLER, W. H., GORDON, G. E., WALTERS, W. B., and LINDSTROM, R. M., "Neutron-Capture Prompt γ-Ray Spectroscopy as a Quantitative Analytical Method," *Neutron-Capture Gamma-Ray Spectroscopy* (in press).

ANDERSON, D. L., PHELAN, J. M., VOSSLER, T., and ZOLLER, W. H., "Neutron-Capture Prompt Gamma-Ray Analysis of Stratospheric and Groundfall Ash Following the Mt. St. Helens Eruption of May 18, 1980," *J. Radioanal. Chem.* 71, 47-58 (1982).

ANDERSON, D. L., FAILEY, M. P., ZOLLER, W. H., WALTERS, W. B., GORDON, G. E., and LINDSTROM, R. M., "Facility for Nondestructive Analysis for Major and Trace Elements Using Neutron-Capture γ-Ray Spectrometry," *J. Radioanal. Chem.* 63, 97-119 (1981).

CUNNINGHAM, W. C. and ZOLLER, W. H., "The Chemical Composition of Remote Area Aerosols," *J. Aerosol Sci.* 12, 367-384 (1981).

FLEMING, R. F., "Neutron Self-Shielding Factors for Simple Geometries," (submitted for publication).

FLEMING, R. F. and LINDSTROM, R. M., "Limitations on the Accuracy of Sulfur Determination by NAA," *Trans. Am. Nucl. Soc.* 41, 223 (1982).

GORDON, G. E., GOKMEN, I., ARAS, N. K., and HENKIN, R. I., "The Use of Stable Isotope Tracers in the Study of Zinc and Selenium Nutrition in Infants," *J. Radioanal. Chem.* 70, 145-161 (1982).

GREENBERG, R. R. and KINGSTON, H. M., "Trace Element Analysis of Natural Water Samples Using Neutron Activation Analysis and Chelation Chromatography," (submitted for publication).

GREENBERG, R. R. and KINGSTON, H. M., "Simultaneous Determination of Twelve Trace Elements in Estuarine and Sea Water Using Pre-Irradiation Chromatography," *J. Radioanalytical Chem.* 71, 147 (1982).

GREENBERG, R. R., KINGSTON, H. M., and RAINS, T. C., "Trace Elemental Characterization of the Chesapeake Bay Water Column," *Transactions of the American Nuclear Society* 41, 201 (1982).

GREENBERG, R. R., ZOLLER, W. H., and GORDON, G. E., "Atmospheric Emissions of Elements on Particles from the Parkway Sewage-Sludge Incinerator," *Environ. Sci. Technol.* 15, 64 (1981).

PUBLICATIONS

HARRISON, S. H. and ZEISLER, R., "Distribution of Pollutant and Essential Elements in Human Livers," *Trans. Am. Nucl. Soc.* 41, 209 (1982).

KINGSTON, H. M. and LUTZ, G. J., "Adsorption and Stability Prior to Analysis of Simulated Nuclear Waste Leachate," (in press).

KINGSTON, H. M., GREENBERG, R. R., BEARY, E. S., HARDAS, B. R., MOODY, J. R., and RAINS, T. C., "The Characterization of the Chesapeake Bay: A Systematic Analysis of Toxic Trace Elements," (submitted for publication).

KOWALCZYK, G. S., GORDON, G. E., and RHEINGROVER, S. W., "Identification of Atmospheric Particulate Sources in Washington, DC Using Chemical Element Balances," *Environ. Sci. Technol.* 16, 79-90 (1982).

ONDOV, J. M., ZOLLER, W. H., and GORDON, G. E., "Trace Element Emissions on Aerosols from Motor Vehicles," *Environ. Sci. Technol.* 16, 318-328 (1982).

PARRINGTON, J. R., ARAS, N. K., and ZOLLER, W. H., "Asian Dust: Seasonal Transport to the Hawaiian Island," (submitted to Science).

PHELAN, J. M., FINNEGAN, D. L., BALLANTINE, D. S., ZOLLER, W. H., HART, M. A., and MOYERS, J. L., "Airborne Aerosol Measurements in the Quiescent Plume of Mount St. Helens: September, 1980," *Geophys. Lett.*, (in press).

VOSSLER, T., ANDERSON, D. L., ARAS, N. K., PHELAN, J. M., and ZOLLER, W. H., "Trace Element Composition of the Mt. St. Hellens Plume: Stratospheric Samples from the May 18th Eruption," *Science* 208, 827-830 (1981).

WISE, S. A., FITZPATRICK, K. A., HARRISON, S. H., and ZEISLER, R., "Operation of the U.S. Pilot National Environmental Specimen Bank Program," Proc. Intern. Workshop on Environmental Specimen Banking and Monitoring as Related to Banking, Saarbrucken, FRG, May 10-15, 1982 (in press).

ZEISLER, R., HARRISON, S. H., and QIAW, S. A., "Analysis of Human Liver Specimens in the U.S. Pilot National Environmental Specimen Bank Program," Proc. Intern. Workshop on Environmental Specimen Banking and Monitoring as Related to Banking, Saarbrucken, FRG, May 15, 1982 (in press).

ZEISLER, R. and GREENBERG, R. R., "Ultratrace Determination of Platinum in Biological Materials Via Neutron Activation and Radiochemical Separation," (in press).

ZEISLER, R. and GREENBERG, R. R., "Procedure for the Determination of the Platinum Baseline in Biological Materials," *Trans. Am. Nucl. Soc.* 41, 219 (1982).

NBS-114A (REV. 2-80)

U.S. DEPT. OF COMM. **BIBLIOGRAPHIC DATA SHEET** *(See instructions)*	1. PUBLICATION OR REPORT NO. NBS TN 1178	2. Performing Organ. Report No.	3. Publication Date June 1983

4. TITLE AND SUBTITLE

NBS Reactor: Summary of Activities July 1981 through June 1982

5. AUTHOR(S)

F. Shorten, Editor

6. PERFORMING ORGANIZATION *(If joint or other than NBS, see instructions)*

NATIONAL BUREAU OF STANDARDS
DEPARTMENT OF COMMERCE
WASHINGTON, D.C. 20234

7. Contract/Grant No.

8. Type of Report & Period Covered

July 1981-June 1982

9. SPONSORING ORGANIZATION NAME AND COMPLETE ADDRESS *(Street, City, State, ZIP)*

National Bureau of Standards
Department of Commerce
Washington, DC 20234

10. SUPPLEMENTARY NOTES

☐ Document describes a computer program; SF-185, FIPS Software Summary, is attached.

11. ABSTRACT *(A 200-word or less factual summary of most significant information. If document includes a significant bibliography or literature survey, mention it here)*

This report summarizes all those programs which depend on the NBS reactor. It covers the period from July 1981 through June 1982. The programs range from the use of neutron beams to study the structure and dynamics of materials through nuclear physics and neutron standards to sample irradiations for activation analysis, isotope production, radiation effects studies, neutron radiography, and nondestructive evaluation.

12. KEY WORDS *(Six to twelve entries; alphabetical order; capitalize only proper names; and separate key words by semicolons)*

Activation analysis; crystal structure; diffraction; isotopes; molecular dynamics; neutron; neutron radiography; nondestructive evaluation; nuclear reactor; radiation

13. AVAILABILITY

☒ Unlimited
☐ For Official Distribution. Do Not Release to NTIS
☒ Order From Superintendent of Documents, U.S. Government Printing Office, Washington, D.C. 20402.
☐ Order From National Technical Information Service (NTIS), Springfield, VA. 22161

14. NO. OF PRINTED PAGES

231

15. Price

$6.50

USCOMM-DC 6043-P80

* U.S. GOVERNMENT PRINTING OFFICE: 1983-0-380-997/5064

NBS TECHNICAL PUBLICATIONS

PERIODICALS

JOURNAL OF RESEARCH—The Journal of Research of the National Bureau of Standards reports NBS research and development in those disciplines of the physical and engineering sciences in which the Bureau is active. These include physics, chemistry, engineering, mathematics, and computer sciences. Papers cover a broad range of subjects, with major emphasis on measurement methodology and the basic technology underlying standardization. Also included from time to time are survey articles on topics closely related to the Bureau's technical and scientific programs. As a special service to subscribers each issue contains complete citations to all recent Bureau publications in both NBS and non-NBS media. Issued six times a year. Annual subscription: domestic $18; foreign $22.50. Single copy, $5.50 domestic; $6.90 foreign.

NONPERIODICALS

Monographs—Major contributions to the technical literature on various subjects related to the Bureau's scientific and technical activities.

Handbooks—Recommended codes of engineering and industrial practice (including safety codes) developed in cooperation with interested industries, professional organizations, and regulatory bodies.

Special Publications—Include proceedings of conferences sponsored by NBS, NBS annual reports, and other special publications appropriate to this grouping such as wall charts, pocket cards, and bibliographies.

Applied Mathematics Series—Mathematical tables, manuals, and studies of special interest to physicists, engineers, chemists, biologists, mathematicians, computer programmers, and others engaged in scientific and technical work.

National Standard Reference Data Series—Provides quantitative data on the physical and chemical properties of materials, compiled from the world's literature and critically evaluated. Developed under a worldwide program coordinated by NBS under the authority of the National Standard Data Act (Public Law 90-396).

NOTE: The principal publication outlet for the foregoing data is the Journal of Physical and Chemical Reference Data (JPCRD) published quarterly for NBS by the American Chemical Society (ACS) and the American Institute of Physics (AIP). Subscriptions, reprints, and supplements available from ACS, 1155 Sixteenth St., NW, Washington, DC 20056.

Building Science Series—Disseminates technical information developed at the Bureau on building materials, components, systems, and whole structures. The series presents research results, test methods, and performance criteria related to the structural and environmental functions and the durability and safety characteristics of building elements and systems.

Technical Notes—Studies or reports which are complete in themselves but restrictive in their treatment of a subject. Analogous to monographs but not so comprehensive in scope or definitive in treatment of the subject area. Often serve as a vehicle for final reports of work performed at NBS under the sponsorship of other government agencies.

Voluntary Product Standards—Developed under procedures published by the Department of Commerce in Part 10, Title 15 of the Code of Federal Regulations. The standards establish nationally recognized requirements for products, and provide all concerned interests with a basis for common understanding of the characteristics of the products. NBS administers this program as a supplement to the activities of the private sector standardizing organizations.

Consumer Information Series—Practical information, based on NBS research and experience, covering areas of interest to the consumer. Easily understandable language and illustrations provide useful background knowledge for shopping in today's technological marketplace.

Order the **above** *NBS publications from: Superintendent of Documents, Government Printing Office, Washington, DC 20402.*

Order the **following** *NBS publications—FIPS and NBSIR's—from the National Technical Information Service, Springfield, VA 22161.*

Federal Information Processing Standards Publications (FIPS PUB)—Publications in this series collectively constitute the Federal Information Processing Standards Register. The Register serves as the official source of information in the Federal Government regarding standards issued by NBS pursuant to the Federal Property and Administrative Services Act of 1949 as amended, Public Law 89-306 (79 Stat. 1127), and as implemented by Executive Order 11717 (38 FR 12315, dated May 11, 1973) and Part 6 of Title 15 CFR (Code of Federal Regulations).

NBS Interagency Reports (NBSIR)—A special series of interim or final reports on work performed by NBS for outside sponsors (both government and non-government). In general, initial distribution is handled by the sponsor; public distribution is by the National Technical Information Service, Springfield, VA 22161, in paper copy or microfiche form.

U.S. Department of Commerce
National Bureau of Standards

Washington, D.C. 20234
Official Business
Penalty for Private Use $300